Near-ultraviolet and visible optical properties of secondary organic aerosols and gas phase species

A thesis submitted to

THE NATIONAL UNIVERSITY OF IRELAND, CORK

Department of Chemistry

for the degree of

DOCTOR OF PHILOSOPHY

by

Eoin Wilson

Based on research carried out in the Department of Chemistry, University College Cork

Supervisor: Dr. Dean Venables

Head of Department: Professor Justin Holmes

University College Cork October 2016

Table of Contents

Declaration

This is to certify that the work I am submitting is my own and has not been submitted for another degree, either at University College Cork or elsewhere. All external references and sources are clearly acknowledged and identified within the contents. I have read and understood the regulations of University College Cork concerning plagiarism.

_____

Eoin Wilson

Acknowledgements

If I was to thanks everyone who has helped me over the last few years, this book would be twice as long as it is.

There is one person who has been instrumental in the work presented here. There is no exaggeration in saying that without him I would certainly not be where I am today. I must express my sincere and unreserved gratitude to Dr. Dean Venables. I began working with Dean during my fourth year project almost 6 years ago. The project was interesting, frustrating, complex and ultimately fulfilling. In that regard it was an eerily accurate introduction to what the next five years of my life would become. Dean was then and remains today a great collaborator. He is always willing to lend a hand and talk through a problem, of which there were many. He also arranged for me to travel to Bayreuth in Germany, Taicang in China and Prague in the Czech Republic which are experiences that I will never forget.

To the CRAC old guard, you have made the last 5 years far more enjoyable than they had any right to be. John 'electric slide' Wenger and John 'mystery tour' Sodeau have thoroughly dispelled the myth of the uptight academic. Ian, Trevor and Dave, you are all great people that I am lucky to call my friends. You've always been there to give me advice and help me when I need it, share a pint with and most importantly, wind up Eoin Mac.

A special thanks must go to Eoin Mac and Jovanna, aka Trunk and Kucken Lederhosen. The two of you are consistently a pleasure to be around. Between Jovanna's incredible baking and Eoin's unrivalled ability to win every quiz he enters, it has been a very fun time indeed. As soon as I came into the CRAC lab you made me extremely welcome and you helped me to get through the last few years. For that I will always be grateful.

I must also thank everyone else in the CRAC family that I have worked with over the last number of years, Paul, Ravi, Ivan, Sak, Rob, Dave H, Ruairi, Paddy, Mike, Shane,

Donovan and everyone else. A big thank you also must go to all the staff in the Chemistry Department.

Left to my own devices I could have very easily completely disappeared in the last few years so I need to thank my friends who have kept me sane, John, Kev, Gav, Cian, Dave, Vera, Shelly, Claire, Conor, Eoin F, Sue and all the DBY lads, thank you all.

Everything that I have done in my life can be traced back to my family. They have always supported me, even if they were convinced that I was becoming a weather man (Brian, I still don't know if you were joking). They have not given me too hard a time for still being in college after 9 years. To Jen, Sue, Emily, Amy, Joe and Molly, I'll always be thankful for your support. Rob, Brian and Luke are the best lot of brothers that I could ask for. I will never be able to express how much I admire and respect my Mam. She has always been there for me, to support me and to guide me. She never stopped believing in me. I can't thank my Mam enough for all that she has done.

To Niamh, you are consistently a source of joy in my life. You have had to put up with a lot while I was undertaking this PhD. I think it might have been more stressful for you than it was for me. You always reassured me when I was worried, cheered me when I was down and focused me when my mind started to wander, and we both know how easily my mind wanders. You mean everything to me, thank you.

Dedication

To my Mam and Dad; without you, none of this would be possible.

Abstract

The interaction of light and gas and particle phase species plays an important role in climate change. Incoherent Broadband Cavity-Enhanced Absorbed Spectroscopy (IBBCEAS) was used to measure the gas phase absorption cross section of a number of atmospherically-relevant species and to investigate the optical properties. The investigated spectral region extended from 325 to 420 nm.

Gas phase absorption cross section spectra of biacetyl, 1-nitronaphthalene, 2-nitrophenol, acetaldehyde and acenaphthylene were measured. The gas phase spectra of 1-nitronaphthalene and acenaphthylene have not previously been reported, while the 2-nitrophenol and acetaldehyde absorption cross sections agreed closely with previous literature values. In addition, the absorption of water in the near-UV region was also investigated. In contrast to a recently report, no water vapour absorption was seen; however, upper limits were established for the water absorption cross section at a resolution of 0.5 nm.

The optical properties of secondary organic aerosols (SOA) formed by ozonolysis of α-pinene were studied. The refractive index values for α-pinene/O_3 SOA ranged from 1.40 at 410 nm to 1.43 at 320 nm, and are broadly consistent with previously reported values. The VOC precursor concentration, relative humidity, and the extent of oxidation were all found to affect the refractive index values.

SOA formed from photochemical reaction of 2-NP was investigated. Nitro-aromatic SOA has been proposed to have a large impact on the UV irradiance in urban areas. The 2-NP loss rate followed second order kinetics which indicated that photolysis was not the only loss mechanism; this finding provided evidence for a proposed mechanism. Addition of acetaldehyde to the reaction suppressed particle formation. Off-line UV/Vis absorption measurements showed that SOA absorption increased towards shorter wavelengths, as is typical of brown carbon. The mass absorption coefficient and imaginary part of the complex refractive index indicate that these SOA species are relatively weakly absorbing.

1. Introduction

1.1. The atmosphere

The atmosphere is the thin layer of gas that surrounds Earth. It is a mixture of different gases, predominantly nitrogen and oxygen which respectively comprise 78 % and 21 % (by volume) of a dry atmosphere. The concentration of these two gases is controlled by geological and biological activity, and human activity has little impact on them. The remaining gases include argon, carbon dioxide (CO_2), water vapour and a large number of trace gases. The concentration of water vapour varies from 0 to 4 % depending on the location, the concentration of argon is 1.28 % while that of CO_2 is currently around 0.04 % (1-3). CO_2 has been, and continues to be, strongly influenced by human activities, primarily combustion.

The atmosphere extends to over 500 km above the surface of the Earth and can be divided into four distinct regions. These are the troposphere, the stratosphere, the mesosphere and the thermosphere (sometimes called the ionosphere). These layers extend from 0-15 km, 15-50 km, 50-85 km and 85-500 km above the surface of the earth respectively, and have characteristic thermal properties. Figure 1.1 shows the temperature change in each of the layers of the atmosphere. As the altitude increases above Earth's surface, the temperature decreases continuously for the lowest 10-15 km. The lower atmosphere is heated by the earth's surface, which is heated by incoming solar radiation. As a result, the temperature decreases as the altitude increases (4). Above the tropopause, the stratospheric ozone layer produces a temperature inversion. Ozone absorbs high energy ultraviolet radiation, which heats the surrounding atmosphere. There is much less ozone in the mesosphere and, coupled with decreased air pressure, results in another decrease in temperature with altitude. In the outermost atmosphere, absorption of solar x-rays by molecules produces another temperature increase in the thermosphere.

Temperature is not the only difference between the atmosphere's regions: they are also characterised by substantial differences in chemical composition, density and transport characteristics. The residence time of molecules in each layer help to dictate the composition of the layers. Most of the mass of the atmosphere is contained in the lower atmosphere, and the troposphere contains 85 % of the total atmospheric mass (5). The turbulent mixing and constant change in the troposphere is indicated in its etymology: '*tropos*' is the Greek word for change. The focus of this work is on how the constituents of the troposphere interact with solar radiation. To address this question, it is first necessary to understand the spectrum of the Sun.

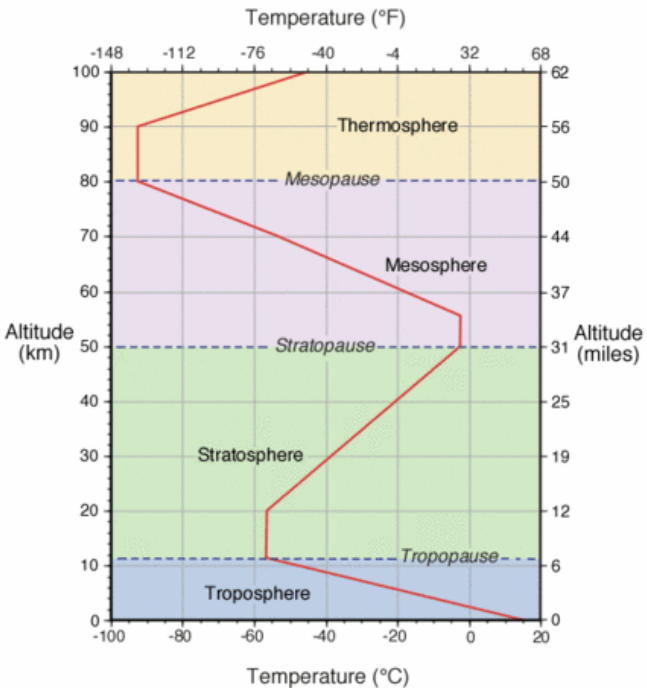

Figure 1.1 Altitude and temperature profile of the different layers of the atmosphere showing the thermal characteristics of each region (Adapted from (6)).

1.2. The Solar Spectrum

The sun has a major impact on the chemical composition of each region of the atmosphere, and the interaction of solar radiation with atmospheric molecules initiates most atmospheric chemistry processes either directly or indirectly. Figure 1.2 shows the solar radiation spectrum at different altitudes in the earth's

atmosphere. The maximum intensity occurs at 550 nm and the top of the atmosphere (TOA) irradiance is about 1360 W m^{-2} (7). The solar radiation at sea level is lower than at the TOA owing to the absorption and scattering of gases and particles. Absorption by atmospheric gases, such as O_2, O_3 and H_2O lead to the sharp drops in the solar radiation spectrum at sea-level shown in Figure 1.2. Different atmospheric constituents have different impacts on solar radiation. Some constituents cause decreases over broad spectral ranges while others have strongly structured spectra. What happens to this light between the outer atmosphere and the surface of the earth is of major interest to atmospheric chemists and climate scientists.

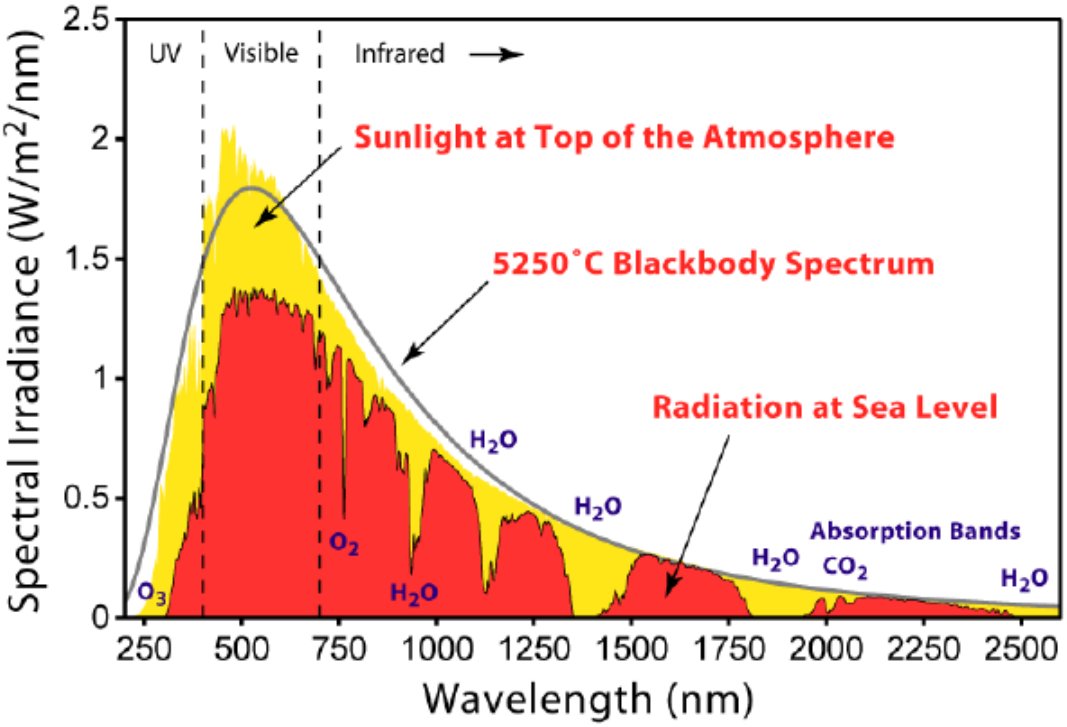

Figure 1.2 Solar radiation spectrum at the top of the atmosphere (TOA) and at sea level. The difference between the two spectra is caused by atmospheric extinction. For comparison, the spectrum of a blackbody is also shown (Adapted from (8)).

1.3. Tropospheric composition

The large number of chemical species present in the troposphere can exist as either gases or particles. Gases range from naturally occurring gases like N_2, to anthropogenic compounds such as chlorofluorocarbons (CFC) (9). Greenhouse gases are a particularly important group of gases because they trap more solar energy in the atmosphere than the much more abundant gases N_2 and O_2. They heat the earth to much higher levels than would otherwise be possible. These greenhouse gases raise the average temperature of the Earth by 30 K (10). Even very small amounts of these species can have an impact on the climate. Trace gases play an important role in the atmosphere, even though they may occur at mixing ratios ranging from parts-per-million (ppm) to parts-per-trillion (ppt) (11).

1.3.1. Trace gases

Trace gases may be inorganic or organic species and arise from diverse sources. Bromine and chlorine, for example, are emitted from the oceans, volcanoes, and biomass burning. These species react with ozone to form BrO and ClO (12). ClO and BrO act as catalysts in the removal of ozone through the ClO_x and BrO_x cycles (13). The combustion of biomass and fossil fuels are a large source of trace gases (14; 15). These combustion emissions can include CO_2, NO_x and NH_3 (16). There has been an increase in levels of CO_2 in the atmosphere. Fossil fuel burning is the largest contributor to CO_2, followed by industrial processes and land use changes (17). Nitrous oxide is emitted from a number of biogenic sources, such as tropical soil which is its largest emission source, and anthropogenic sources, primarily fossil fuel burning and agriculture (18). Methane is estimated to account for up to 20 % of radiative forcing linked to human greenhouse gas (19). Emissions from wetlands account for a large proportion of CH_4 in the atmosphere (20). Fossil fuel burning and animal husbandry account for almost 60 % of the anthropogenic emissions of methane, with the remainder coming from landfills (16 %), biomass burning (11 %), paddy fields (9 %) and biofuels (4 %) (20). Sulphur plays an important role in the formation and growth of aerosol particles. It is emitted from both anthropogenic and biogenic sources. Biogenic sources for various sulphur gases include oceanic

surface water, wetlands, soil, volcanic activity and vegetation, although vegetation is the largest sulphur sink (21). Fuel combustion and industrial activity account for the majority of anthropogenic sulphur species. Fuel combustion accounted for 80 % of anthropogenic sulphur dioxide emissions in the United States, 17.9 % was attributed to industrial activity while the remaining 2 % was from transportation (22). In the Northern Hemisphere anthropogenic sources account for over 80 % of sulphur emissions (23). The oxidation of sulphur gases in the atmosphere lead to the formation of sulphate species. These sulphates can also be emitted from sea spray, soil dust etc. Volatile organic compounds (VOCs) are high vapour pressure organic species. They can become further oxidised in the atmosphere and this can lead to particle formation. The global annual VOC flux has been estimated at 1150 Tg C yr^{-1}. Isoprene is the largest contributor to VOCs in the atmosphere, accounting for 44 %. The remainder consists of monoterpenes (11 %), reactive VOCs (22.5 %) and other VOCs (22.5 %). Biogenic emissions of VOCs exceed anthropogenic sources. Woodlands account for 75 % of global isoprene and monoterpenes and 66 % of other VOCs. Crop land, shrubs and oceans account for the remainder of biogenic emission sources (24). Anthropogenic sources include transportation, landfills and industrial activity (25).

1.3.2. Aerosols

In addition to gases, the atmosphere contains large amounts of particulate matter, or aerosols. Aerosols are a suspension of solid or liquid particles in a gas. These particles span a size range from 0.002 to 100 μm, i.e. five orders of magnitude (26). The lower limit of this size range is only an approximation because there is no fine line over which a small cluster of molecules becomes a particle. Size and mass, as well as chemical composition and particle morphology, are all important characteristics of particles and influence how a particle can interact with other species in the atmosphere and with incoming solar or outgoing terrestrial radiation.

The size of particles has been described as the most important factor in terms of their effect in the atmosphere (26). Particles are generally divided into coarse particles, which have diameters greater than 2.5 μm, and fine particles, with

diameters below 2.5 µm. Fine particles can be further subdivided into the accumulation range (0.08 to 1-2 µm) and the Aitken nuclei range (0.01 to 0.08 µm). Furthermore, particles with diameters below 0.01 µm are often referred to as ultrafine or nucleation mode particles, Figure 1.3. These nucleation mode particles occur in the greatest number in the atmosphere and mostly consist of sulphate, nitrates, and organic compounds (27). The size of the particles affects their residence time in the atmosphere. Nucleation mode particles typically have very short residence times due to fast coagulation processes. This agglomeration of nucleation mode particles results in their growth into Aitken mode particles (28). Like nucleation mode particles, Aitken mode particles have short lifetimes, on the order of minutes. These particles can grow into the accumulation mode either through self-coagulation or through agglomeration into larger particles (26). Coarse particles cannot stay in suspension for long, as they require strong air currents to remain in the air to overcome gravitational settling. Measurements have found significant atmospheric lifetime differences based on particle sizes for silt particles. Particles of 1.5 µm have a lifetime of 179 hours while those of 8 µm have only a 28 hour lifetime (29). Conversely, very small particles coagulate rapidly to form larger particles. For this reason, the size range that is most important for atmospheric chemistry is 0.002 to 10 µm. Particles in the accumulation mode account for approximately 5 % of the total number of particles but up to 50 % of the total mass. These are generally removed by rainout, when these ultrafine particles are scavenged by rain water and fall to the earth as precipitation (30). Fine particulates account for a large percentage of total particle number and mass, with contributions of up to 30 % in non-urban and 50 % in urban environments (26).

Aerosols in the atmosphere can be categorised as either being directly emitted particles (primary emissions), or as secondary aerosols, which are formed in the atmosphere from processing of condensable gases. Emission sources for primary particles can be anthropogenic or biogenic. Anthropogenic sources include vehicle emissions, waste incineration, home heating, industrial activity and shipping (31-34). Natural sources include volcanic activity, sea salt and wind-blown mineral dust (35; 36). Bioaerosols also contribute to primary aerosols and may arise from

bacteria, fungi, viruses, as well as organic debris (37; 38). The interaction of wind on continental land masses or ocean surfaces is the most important natural source of primary aerosols, and mineral dust is one of the largest contributors to particulate matter in the atmosphere (39).

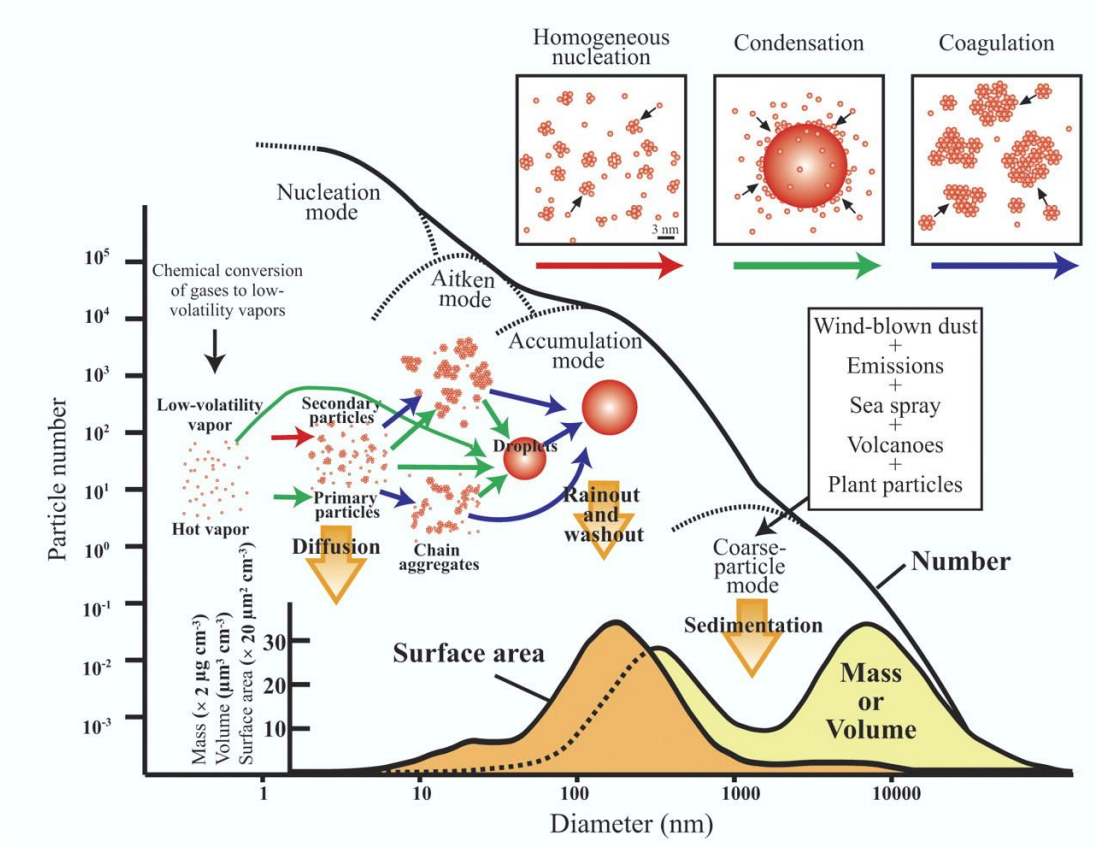

Figure 1.3 Schematic of the size distribution of atmospheric particles (Taken from(27)).

Gas phase species in the atmosphere can undergo continuous chemical reactions. If this processing produces sufficiently low vapour pressure species, the gases will begin to form particles. These are known as secondary aerosols. An example of this is the formation of ammonium sulphate. Ammonia is released as a gas from agricultural sources throughout the world (40). It reacts with sulphuric acid to form either ammonium hydrogen sulphate, Reaction 1.1, or ammonium sulphate, Reaction 1.2:

$$NH_3 + H_2SO_4 \rightarrow NH_4HSO_4 \quad \textbf{(R 1.1)}$$

$$2NH_3 + H_2SO_4 \rightarrow (NH_4)_2SO_4 \quad \textbf{(R 1.2)}$$

This process results in particles from 0.1 to 1 µm (41). Sulphate particles constitute a large percentage of secondary particles in the atmosphere (37 %). Other components of fine aerosols include organic carbon (24 %), ammonium (11 %), elementary carbon (5 %), nitrates (4 %) and others (19 %), as shown in Figure 1.4 (42). Organic carbon is also a major component of fine aerosol and depends strongly on location. It has been estimated that 20 to 50 % of the fine aerosol mass at continental mid latitudes and up to 90 % in tropical forested areas is due to organic material (43-45). Secondary organic aerosols (SOA), which result from the oxidation of volatile organic compounds (VOCs), account for a large portion of the organic carbon (46; 47). For this reason, they have been the focus of a large number of studies. Aromatic hydrocarbons, cycloalkanes and cyclic alkenes can all be oxidised to form secondary organic aerosols (SOAs) (48; 49). The type of SOA varies depending on location. Biogenic SOA estimates are in the order of 12 to 70 Tg yr^{-1} and arise from the processing of biogenic VOCs (BVOCs) (50). Isoprene, terpenes and sesquiterpenes are the BVOCs that are most prevalent in rural environments due to emission from vegetation. Oxidation is one of the primary reaction routes for unsaturated compounds such as monoterpenes (51). For example, 80 % of atmospheric losses of α-pinene are due to reaction with ozone (52).

With such a vast and varied collection of gases and particulate matter in the atmosphere, there will inevitably be interactions between these species and light. Any compound that affects the light balance has a potential impact on photochemical processes as well as climate forcing.

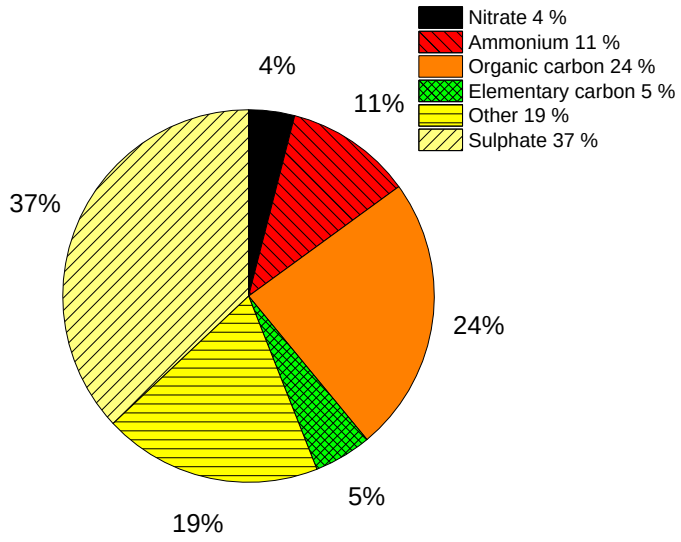

Figure 1.4 Composition of fine aerosol particulates over continental land masses. (Adapted from (42)).

1.4. Extinction: Scattering and absorption

As light passes though the atmosphere, it interacts with both gases and particles which change the amount of light that reaches the surface of the earth. The Beer-Lambert law describes the change in intensity of incident light:

$$\log\left(\frac{I}{I_0}\right) = \varepsilon . c . L \qquad \textbf{(1.1)}$$

where I_0 is the intensity before and I is the intensity after any interactions, L is the path length of the light beam (cm), $\boldsymbol{\varepsilon}$ is the molar extinction coefficient (L mol^{-1} cm^{-1}) and c is the concentration (mol L^{-1}). The extinction coefficient is a measure of the total light reducing effect of the sample. In the atmosphere, the extinction coefficient (b_{ext}) is composed of contributions from extinction caused by gases and extinction caused by particles. Extinction arises from the two contributions of scattering and absorption:

$$b_{ext} = b_s + b_{abs} \qquad \textbf{(1.2)}$$

where b_s denotes the extinction arising from scattering and b_{abs} denotes that from absorption processes.

When light is scattered, its direction of propagation is altered. Light scattering in the atmosphere is generally elastic in nature. This means that the energy, and therefore the wavelength of the light, is not affected by the scattering. Although inelastic scattering also occurs, for instance, Raman scattering, it is a very weak phenomenon and of minor importance in the atmosphere. When an electromagnetic wave interacts with a particle or gas, it can induce a dipole moment, Figure 1.5. This induced dipole moment is an electromagnetic radiation source. The interaction between this electromagnetic source and the incident light causes scattering. Scattering depends on the wavelength of the light compared with the size of the particle. For species that are much smaller than the wavelength of light, Rayleigh scattering dominates, whereas Mie scattering dominates for species of comparable size to the wavelength (53). For light in the ultraviolet and visible (UV/Vis) region (190-750 nm), Rayleigh scattering relates to species with diameters less than 0.03 µm and Mie scattering dominates for particles between 0.03 µm and 10 µm (26). As gas molecules are very small compared to the wavelengths of light in the UV/Vis region (190-750 nm), Rayleigh scattering is prevalent. Rayleigh scattering accounts for the blue colour of the sky, because shorter wavelengths are scattered much more efficiently than longer wavelengths. Scattering of light by particles (Mie scattering) has a major impact on the distribution of light in the atmosphere. Studies have shown that particles in the size range of 0.1 to 1 µm have the greatest impact on light scattering (54; 55).

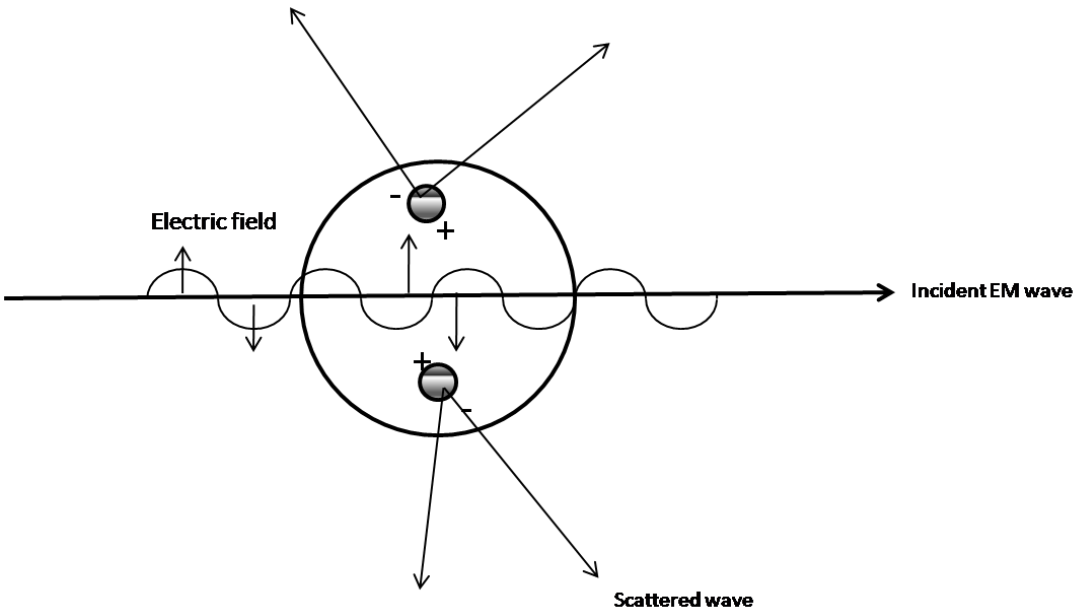

Figure 1.5 Schematic depiction of light scattering by an induced moment due to an incident electromagnetic wave (Adapted from (56)).

Absorption of light results in annihilation of the photon and transfer of the photon's energy to the absorbing molecule. This energy can alter the rotational, vibrational, or electronic energy of the molecule. The energy levels of molecules are quantized and it takes a photon of specific energy to cause the increase to a higher energy level. The energy difference between two molecular energy levels must match the energy of the photon, which is related to its wavelength:

$$E = \frac{hc}{\lambda} \qquad \textbf{(1.3)}$$

where *E* is energy, *h* is Planck's constant, *c* is the speed of light and $\boldsymbol{\lambda}$ is the wavelength of light. A molecule may have a broad or structured spectrum and each species absorbs light in a unique manner. The absorption cross section of a molecule characterises the likelihood of the molecule absorbing a photon of a given wavelength, and is expressed as the effective area (units of cm^2 $molecule^{-1}$) over which a molecule absorbs light. In addition to identifying and quantifying a species, the absorption cross section can be used to calculate its photolysis rate when the photolysis quantum yield is known. Photolysis can occur when light in the UV/Vis region of the spectra has sufficient energy to break chemical bonds in a molecule:

$$A + h\upsilon \rightarrow \text{products} \quad \textbf{(R 1.3)}$$

The rate at which the concentration of compound A decreases is described as

$$\frac{d[A]}{dt} = J[A] \quad \textbf{(1.4)}$$

where *J* is the photolysis rate coefficient and [A] is the concentration of substance A. Photolysis rates depend on the molecular properties of absorption cross section, *σ*, and photodissociation quantum yield, *Φ*, and on the spectral actinic flux, *F*. These properties are wavelength dependent, and J is the integral of these properties over all relevant wavelengths:

$$J = \int \sigma(\lambda, T)\Phi(\lambda, T)F(\theta, \lambda)d\lambda \quad \textbf{(1.5)}$$

Photolysis quantum yield, in nominal units of molecules photon^{-1}, can be defined as the probability that an absorbed photon will cause the molecule to dissociate. Actinic flux, in units of photons cm^{-2}s^{-1}, represents the amount of light available to a molecule at a point in the atmosphere and includes both direct and indirect light. Actinic flux depends on location, season, meteorology, and time of day. It can be determined either by direct measurements or by spherically integrating the irradiance values. Irradiance is easier to measure directly and there is a method for converting it into usable actinic flux values (57).

The photolysis rate of a species contributes to its overall atmospheric lifetime, which is the time taken to reduce its concentration to 1/e of its initial concentration (58; 59). The absorption cross sections of a number of atmospheric species, particularly those with a relatively low vapour pressure, are either unknown or rather uncertain. Chapter 3 of this thesis therefore focuses on determining the absorption cross sections of a number of atmospherically-relevant species.

Visibility

Light extinction is related to visibility in the atmosphere. Visibility is one of the most readily perceived effects of atmospheric constituents on light. The Koschmieder equation is used to relate the extinction coefficient to visibility (60):

$$V_r = \frac{3.92}{<b_{ext}>} \quad \textbf{(1.6)}$$

where V_r is visibility and b_{ext} is the extinction coefficient. The extinction coefficient is averaged over the range of visible wavelengths but it is normally measured at 550 nm. Visibility has been measured in many locations including Central Europe, North America and Asia and has been used to estimate atmospheric extinction (61-65). The different contributions for scattering and absorption for gases and particles to light in the atmosphere have been studied. For example, a monitoring campaign in Denver, Colorado determined that Rayleigh scattering by gases and absorption by nitrogen dioxide each accounted for 7 % of total extinction. A further 29 % of extinction was due to particle absorption with the remaining 64 % attributed to scattering by aerosols (66). Extinction by particles was therefore much larger than that from gases. Similar contributions to extinction from gases and particles were found in California (67). An example of reduced visibility due to light scattering is shown in Figure 1.6.

Figure 1.6 Reduced visibility in Beijing as a result of extinction of light (68).

Complex Refractive Index

The absorption and scattering characteristics of particles are governed by their complex refractive index. The refractive index (RI) of a material is the ratio of the speed of light in a vacuum to that of the target material:

$$n = \frac{c}{v} \quad \textbf{(1.7)}$$

where *n* is the refractive index, *c* is the speed of light in a vacuum and *v* is the velocity of light in the target medium. RI values are wavelength dependent (69-71). If a species also absorbs light, the RI becomes complex in nature and is known as the complex refractive index (CRI). The CRI is described by:

$$n^* = n - ik \quad \textbf{(1.8)}$$

where n^* is the CRI, *n* is the real part of the CRI, which is associated with scattering, and *k* is the imaginary component of the CRI, which is associated with absorption. The CRI is an important property of a species because it can be used to determine its effects on radiative forcing.

1.5. Climate effects

The radiative balance is a measure of the amount of solar radiation entering and exiting the earth's atmosphere. Any phenomenon that affects this balance is said to have a radiative forcing effect, and changes in the radiative balance alter the earth's climate (1; 72; 73). The direct and indirect radiative forcing effects caused by tropospheric aerosols, the radiative forcing effects of particulates formed from biomass burning events, the radiative forcing of absorbing aerosol species and the influence of black carbon on aerosol models have all been reviewed in detail (45; 74-78). Major contributions to radiative forcing are shown in Figure 1.7. The radiative forcing effect of some change can be positive, in which case it has a heating effect on the climate, or it can be negative, in which case it has a cooling effect. Since 1750, concentration levels of carbon dioxide, methane and nitrous oxide have increased (79-83). Due to the increase in concentration of these gases, their radiative forcing effects, owing to their absorption of longer wavelength radiation, have increased by +1.66, +0.48 and 0.16 Wm^{-2}, respectively (84). These compounds have strong, positive radiative forcing effects. They are part of the long-lived greenhouse gases group and their effects are known to a high degree of scientific certainty.

Compared to gases, aerosols generally have a large negative radiative forcing effect and result in a net cooling effect on the environment. This is largely due to their scattering of light and contribution to cloud formation and albedo. In the latter case, particles act as cloud condensation nuclei (CCN), that is, as initial sites for condensation of water vapour into cloud droplets. These droplets can affect the lifetime, droplet size, and composition of clouds, which are good reflectors of light (26; 85-87). The best estimate for the radiative forcing of particles is -0.35 (-0.85 to +0.15) W m^{-2} for the direct effects of absorption and scattering of light. A further -0.45 (-1.2 to 0.0) W m^{-2} has been attributed to the indirect radiative forcing effects of particles, that is, to aerosol/cloud interactions (88). The combined aerosol radiative forcing effect of atmospheric particles is therefore -0.9 (-1.9 to 0.1) W m^{-2}. This has the same magnitude (but opposite sign) as the radiative forcing effects of both methane and nitrous oxide. Secondary organic aerosols (SOA) account for a portion of these effects, -0.03 (-0.27 to +0.20) W m^{-2}. While the effects for SOA are reported to be minor in relation to total aerosol, they have a large uncertainty associated with their measurements. There is also a large degree of uncertainty associated with the radiative forcing effects of aerosols in general. Between 2005 and 2011 the total measured anthropogenic radiative forcing effect increased by 44 % (88). This has been attributed in part to the decrease in estimated forcing by aerosols.

For a long time, the effects of aerosols on radiative forcing were thought to be largely negative due to their strong scattering effect. While this is still the case, there has been a growing awareness of the importance of aerosol absorption (89-93). The strongest absorbing component in atmospheric aerosols is black carbon (BC) (94). BC is formed during incomplete combustion from sources such as vehicle emissions, industrial activity, energy production and residential heating (95). BC absorbs solar radiation across a broad spectral range and has a strong, positive radiative forcing effect that, per unit mass, is up to 680 times larger than that of CO_2 (95; 96). As a result, its contribution to radiative forcing is comparable to that of CH_4 and second only to CO_2 (97; 98). Due to the various emission sources, BC concentrations are highly variable across the globe (99-105). Besides existing in

atmospheric particles, BC also deposits on snow banks, where it darkens the surface of the snow. The resulting decrease in albedo produces a higher rate of melting of the snow (106).

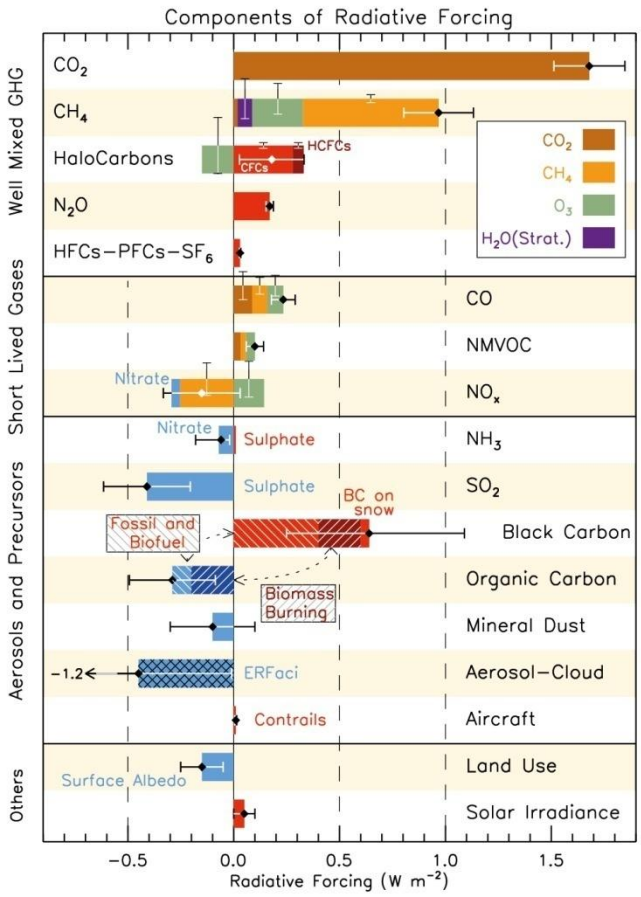

Figure 1.7 IPCC radiative forcing estimates and associated uncertainties in 2013 relative to 1750 (From (88)).

While BC has been the primary area of study of absorbing atmospheric aerosols, recently there has been an increase in interest in other absorbing organic matter in particles. The most important of these is brown carbon (BrC), which is sometimes referred to as HULIS (humic-like substances) or light absorbing carbonaceous matter (LAC) (107). BrC is characterised by a strong increase in light absorption from the visible to the UV (107-110). Due to the increased absorption of light at shorter wavelengths, Angstrom exponent (AE) values have been used to

differentiate between BC and BrC. BC tends to have AE values of 1, whereas BrC can have much higher values (111). Angstrom Exponent is a power law which can be used to determine the extinction at a given wavelength. This will be discussed in greater detail at a later point. The imaginary part of the CRI of BrC also increases towards shorter wavelengths.

BrC may be emitted directly into the atmosphere as a result of biomass burning, forest fires, residential solid fuel burning and biogenic sources such as plant debris and humic material, and it can also be formed through further processing of gas species in the atmosphere to become SOA (112-120). The radiative forcing effect of BrC is estimated to range from + 0.1 to + 0.25 W m^{-2}, making it comparable with nitrous oxide (96; 121). When BrC was included in some climate models, it changed the effect of organic carbon from having a net negative radiative forcing affect to a positive effect (121). Slight changes in the imaginary part of the refractive index can change the sign of the radiative forcing affect. Bond and Bergstrom reported that the simple forcing efficiency, which they describe as direct forcing in watts per gram, for a particle with a diameter of 150 nm, at a wavelength of 550 nm, is negative if the CRI is 1.55 + 0.05i but positive if it is 1.55 + 0.06i (122). This means that species that form BrC can have a potentially large climate effect. Reducing the large uncertainty associated with radiative forcing of aerosols is needed to better constrain estimates of the earth's radiative balance. Many studies have measured the radiative forcing effects of aerosols (74; 123-125). Direct radiative forcing effects are determined using three parameters: the extinction coefficient, the single scattering albedo and the scattering phase function (74). The single scattering albedo (SSA) is a measure of the ratio of scattering to extinction. A value of unity indicates a purely scattering species. The scattering phase function determines the angular distribution of scattered radiation (126).

The models used to calculate radiative forcing can be determined in two ways. Models either use direct measurements of spectral, temporal and spatial dependencies of all optical properties needed, or they calculate these properties based on averaged physical property data from a number of sources. The measurement method is the most direct, for example, in the case of the extinction

coefficient of humic-like substances with a cavity ring-down spectrometer (127). However, the sheer quantity of data needed makes computing the optical properties the best approach at present (128). By applying Mie theory to particles with a specific refractive index and measured size distribution, these parameters can be estimated. Mie theory was developed by Gustav Mie in 1908, although essentially the same calculations had been published by Ludvig Lorenz in 1890 (129; 130). Mie theory provides an analytical solution to Maxwell's equations for the scattering of electromagnetic radiation by particles in terms of an infinite series (131; 132). When using Mie theory a number of assumptions are applied to the particles, including; they are assumed to be spherical and homogeneous, the resulting scattering is elastic and that the optical properties are fully described by the complex refractive index. A number of light scattering theories have been set forth for particles that are non-spherical in nature, although it is still customary to use Mie theory when determining scattering of atmospheric species (53; 133-136).

The refractive index is an essential pre-requisite for applying Mie theory to model radiative forcing. Studies have shown that a change in the refractive index value from 1.4 to 1.5 results in a decrease in radiative forcing by 12-19 % in non-absorbing aerosols, such as the SOA studied later in this work (89; 137; 138). There are a number of different techniques that have been used to measure the refractive index and other optical properties of atmospheric particles, as well as the absorption cross sections of molecules. These have been described in aerosol optical property measurement reviews (139; 140). Some of these techniques will be discussed in the following section before introducing incoherent broadband cavity-enhanced absorption spectroscopy (IBBCEAS), the technique that was primarily used in this work.

1.6. Measurement of sample extinction

Optical spectroscopic techniques are by far the most widely used method of trace gas monitoring. This is due to their high sensitivity, wide applicability, and

quantitative results. Techniques that incorporate optical spectroscopy make choices on the light source and the wavelength range of light, the physical principle of detection (absorption or emission), and arrangement of the light path. Trace gas and aerosol monitoring techniques include tuneable diode laser spectroscopy, photoacoustic spectroscopy, light detection and ranging (LIDAR), laser-induced fluorescence (LIF), differential optical spectroscopy (DOAS) and cavity ring-down spectroscopy (CRDS) (141-154).

Measuring the extinction of atmospheric samples is challenging because of the extremely low concentrations of atmospheric gases and particles, which in turn give rise to small absorption and scattering of gases and particles. The most successful approach to this problem is to artificially extend the pathlength of light through the sample by using an optical cavity. An optical cavity consists of an arrangement of highly reflective mirrors that allows a photon or beam of light to circulate in a closed path. The first spectroscopic use of optical cavities was based on cavity ring-down spectroscopy (CRDS). In the following, we briefly consider the CRDS principle of measurement as it is the forerunner of the method used in this study as well as other optical cavity methods.

CRDS was developed by O'Keefe and Deacon in 1988 (155). A laser pulse is introduced into an optical cavity containing a sample. The pulse is reflected between a set of highly reflective mirrors, which extends the pathlength of the light in the cavity. A small fraction of the pulse is lost through the mirrors after each pass. Depending on the reflectivity of the mirrors used, a cavity of 1 m in length could have an effective pathlength of tens of kilometres. The extended pathlength allows for much more sensitive measurements than single pass instruments (156; 157). Moreover, it is the rate of change of intensity that is monitored in CRDS, so the measurements are independent of the initial intensity (158). This improves sensitivity as light source variability is unimportant; such fluctuations in source intensity often limit the sensitivity of absorption techniques (159). The CRDS pulse intensity decreases exponentially in a cavity:

$$I(t) = I_0 e^{\left(\frac{-t}{\tau_0}\right)} \quad \textbf{(1.9)}$$

where *I(t)* is the intensity at a given time, *t* is time, and τ_0 is the "ring-down" time, which is the characteristic time it takes the intensity to fall to 1/e of its initial intensity, I_0. For a sample with negligible extinction, the only losses are due to light exiting the mirrors during each pass. When an absorbing species is present there are additional loss processes:

$$I(t) = I_0 e^{(\frac{-t}{\tau} - \alpha c t)} \quad \textbf{(1.10)}$$

where τ is the ring-down time in the sample filled cavity, α is the absorption coefficient and *c* is the speed of light. The absorption coefficient can be then determined from Equation 1.9 and Equation 1.10:

$$\alpha = \frac{\frac{1}{\tau} - \frac{1}{\tau_0}}{c} \quad \textbf{(1.11)}$$

By taking these measurements at different wavelengths a spectrum can be recorded. However, this approach has the disadvantage of requiring a tuneable laser system, and laser systems with broad spectral coverage are expensive. A basic schema for a CRDS set up, the relative time profiles of light loss, and a sample absorption spectrum are shown in Figure 1.8.

Most CRDS work has focused on gas phase molecules, although recently there has been increased interest using the technique for aerosol optical measurements. It has been used to determine the complex refractive index, the extinction cross section and extinction coefficient of both bulk aerosol and single aerosol particles (127; 160-162). While CRDS is well established and has been used in a wide number of studies, a newer spectroscopic technique was used in this study, namely, incoherent broadband cavity-enhanced absorption spectroscopy (IBBCEAS).

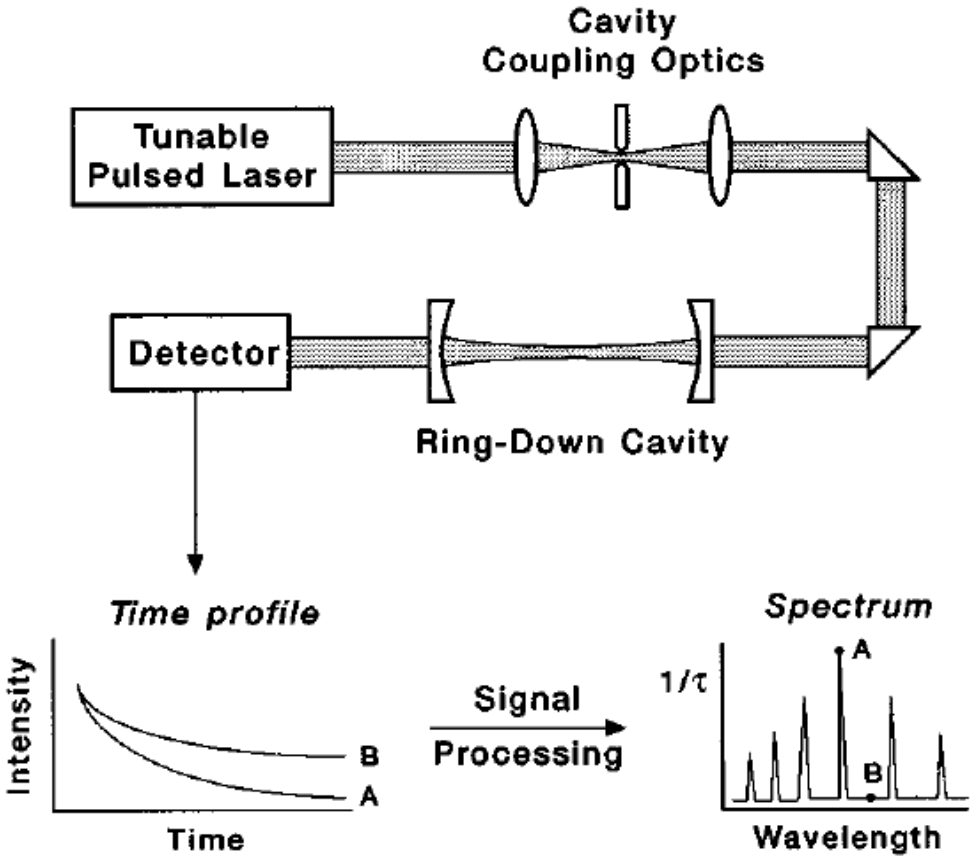

Figure 1.8 Schema of typical CRDS experiment. Figure from Zalicki et al. (163).

1.7. Cavity-enhanced absorption spectroscopy

While CRDS is well established and has been used in a wide range of applications, other spectroscopic developments following CRDS have used optical cavities to achieve enhanced absorption sensitivity. The foremost of these methods is cavity-enhanced absorption spectroscopy (CEAS). CEAS is a spectroscopic method based on measurement of the time-integrated intensity transmitted through a high finesse optical cavity. As in CRDS, photons trapped in the cavity typically undergo multiple passes through the sample to produce sensitive extinction measurements. The very high number of reflections through a high finesse optical cavity results in measurements that are usually much more sensitive than single or multipass

techniques. The light source is typically a CW-laser and need not be pulsed. Disadvantages of CEAS include spectral structure arising from the axial modes of the cavity. These need to be removed through averaging or careful experimental design. CEAS has been extensively used in the study of trace gases, gas phase kinetics and molecular dynamics (164-166). CEAS, which uses a laser to measure extinction at a single wavelength at a time, is the direct forerunner of the spectroscopic technique used in this study, namely, incoherent broadband cavity-enhanced absorption spectroscopy (IBBCEAS).

1.8. Incoherent broadband cavity-enhanced absorption spectroscopy (IBBCEAS)

The principle spectroscopic technique used in this work was incoherent broadband cavity enhanced-absorption spectroscopy (IBBCEAS), which is an optical cavity method descending from CRDS. IBBCEAS is a spectroscopic technique that has been widely utilized in atmospheric chemistry. It is a non-invasive, in-situ monitoring technique with a wide range of applications. IBBCEAS was developed in 2003 by Ruth and co-workers, who demonstrated its utility by measuring the absorption spectrum of molecular oxygen and that of gaseous azulene between 628 and 670 nm (167). Since then it has been used primarily for monitoring atmospheric trace gases, both in the field and in laboratory experiments. More recently, the use of IBBCEAS in aerosol experiments has been growing (168-174). In the following, the measurement principle of IBBCEAS will be described, and a description of the experimental IBBCEAS system used in this work will be presented in Chapter 2.

In IBBCEAS, as in other optical cavity methods, an optical cavity is created by highly reflective dielectric mirrors, usually placed facing one another. The dielectric mirrors are highly reflective and are generally greater than 99 % reflective over their maximum reflectivity region. A beam of light is directed through one mirror and light in the cavity is trapped between the mirrors. The multiple reflections of light through the sample increase the pathlength, which allow the measurement of

much smaller extinctions than would be the case for a single pass through the sample.

When studying compounds with broad absorption bands or when monitoring multiple species simultaneously, a wide spectral range is often of greater importance than high spectral resolution. Fiedler et al. stated that the IBBCEAS technique can be utilised in principle from the deep-UV to the far-IR (190 nm – 10 µm) (167). Some example gas phase experiments that have been undertaken using the IBBCEAS technique are listed in Table 1.1. This table is not an exhaustive list, but simply illustrates the diversity of measurements and target gases studied with IBBCEAS, as well as the different spectral ranges used.

Most IBBCEAS instruments have used relatively narrow spectral ranges. The two most common light sources used have been arc lamps and LEDs. LEDs are stable, relatively cheap and are available at a number of different wavelength ranges. They often do not require further optical filtering. However, their output covers relatively narrow spectral ranges, extending normally to just 15-40 nm. This is a disadvantage when monitoring compounds with broad absorption spectra or when monitoring multiple species concurrently. In contrast, the arc lamp is an extremely broadband light source with output from 185 to 2000 nm. The broad spectral range is better suited to monitoring multiple species. The wavelength range must be tailored to the experiment through the use of spectral filters and adds complexity to the instrument. Most of the experiments mentioned in Table 1.1 take place at wavelength ranges greater than 400 nm. Nonetheless, the near UV/Vis region is important for tropospheric chemistry. However, applying the method at shorter wavelengths is challenging owing to the more limited selection and performance of optics such as filters and dielectric mirrors, the lower brightness of light sources, and the lower efficiency of detectors.

Table 1.1 Examples of studies based on IBBCEAS, showing the diversity of target species, spectral regions and resolution, and light sources used.

Reference	Target species	Light source	Region (nm)	Resolution (nm)
Fiedler et al. (167)	O_2, azulene	Xe arc lamp	628-670	0.026
Langridge et al. (175)	NO_2, NO_3 and H_2O	LED	625-681	0.38
Chen et al. (176)	O_3, acetone, 2-butanone and 2-pentanone	75 W Xe arc lamp	335-375	0.3-0.7
Washenfelder et al. (177)	Formaldehyde and NO_2	Laser-driven arc lamp	315-350	0.47
Kennedy et al. (178)	N_2O_5 and NO_3 NO_3 NO_2	Three LEDs	615-706 639-680 410-482	0.9 0.75 0.4
Venables et al. (179)	NO_3, NO_2, O_3 and H_2O	75 W Xenon arc lamp	625-705	0.3
Gherman et al. (180)	HONO NO_2	LED	362-379	0.35 0.5
Vaughan et al. (181)	I_2,OIO,IO	150 W Xe arc lamp	525-555 420-460	0.4 0.2
Wu et al. (182)	NO_2	LED	450-490	0.9
Aalto et al. (183)	CO_2, CH_4	Supercontinuum source	1590-1700	0.1
Johansson et al. (184)	I_2	LED	500-550	0.5

IBBCEAS is a relatively new technique compared to some of the more established atmospheric monitoring methods. There have therefore been a number of intercomparisons to validate its accuracy and performance. Langridge et al. compared IBBCEAS measurements with those of a CRDS for NO_2, and against a commercial hygrometer for monitoring the concentration of water vapour (175).

Although the IBBCEAS and the CRDS measured signals in different spectral regions (625-672 nm and 558-570 nm, respectively), there was exceptionally good agreement in determining the concentration of NO_2 and the relative humidity. Another study compared the concentration of NO_2 as determined by IBBCEAS and a traditional chemiluminescence detector (185). Again, this showed exceptional agreement between both techniques. Large intercomparison experiments have shown excellent agreement between IBBCEAS and a variety of other methods for determining NO_3, NO_2, and aerosol extinction (170; 185; 186).

Besides being a useful laboratory tool, IBBCEAS has also been deployed during field campaigns. Its relatively low cost and ease of set up have allowed it to become a valuable field instrument. A three-channel IBBCEAS was installed aboard an atmospheric research aircraft to measure NO_3, N_2O_5, H_2O and NO_2 (178). To combat the vibrations from the airplane, the cavities were mounted on an anti-vibration plate. NO_2 levels were compared with an on board chemiluminescence detector and once again displayed extremely good agreement between the measurements. It was also successfully used to monitor a time series of NO_2 over the course of the flight. During the RHaMBLe campaign in Brittany, France, the concentration of NO_3 plus the concentration of N_2O_5 that had been thermally decomposed into NO_3 were measured (181). An advantage of cavity-based methods is that they allow pre-processing of samples. The sum of NO_3 and N_2O_5 concentrations were also measured from the roof of the BT Tower in London in the same way as described above (187).

In recent years aerosol optical properties have been an increasing area of experimentation and the IBBCEAS technique has been applied to several aerosol studies. Established techniques, such as nephelometers, only record scattering at a few wavelengths, whereas IBBCEAS has the ability to perform in-situ, continuous, broadband extinction measurements (70; 188; 189). Table 1.2 shows that, although there have been some measurements in the near-UV, they usually incorporate dual cavities and are not fully continuous over their range due to the use of two cavities. Bluvstein et al. studied the optical properties and single scattering albedo of ambient aerosol, Suwannee river fulvic acid and Pahokee peat fulvic acid (169).

They combined an IBBCEAS, a photoacoustic cell coupled with a CRDS and a nephelometer. This allowed them to report results from 300-650 nm. Only the IBBCEAS measurements were over a continuous range, 315-345 and 360-390 nm. All other measurements are single wavelengths. Having an in-situ, non-invasive, broadband monitoring technique should contribute to a better understanding on the interaction between gases, particles and light.

Table 1.2 List of IBBCEAS aerosol measurements.

Reference	Measurement	Light source	Region (nm)	Resolution (nm)
Washenfelder et al. (168)	Polystyrene latex spheres (PSLs), ammonium sulphate (AS), Suwannee River fulvic acid, nigrosin dye	LED	360-390 385-420	N/A
Varma et al. (170)	AS	Xe arc lamp	610-720	0.4
Bluvshtein et al. (169)	Ambient aerosol, Suwannee river fulvic acid, Pahokee peat fulvic acid	Laser driven Xe arc lamp	315-345 360-390	0.5
Zhao et al. (171)	PSLs, AS	LED	445-480	0.4
Flores et al. (172)	SOA from α-pinene ozonolysis	LED	360-390 390-420	N/A
Varma et al. (174)	AS	Short-arc Xe lamp	620-720	0.6
Varma et al. (170)	AS	Short-arc Xe lamp	687	0.6
Wilson et al. (173)	SOA from photolysis of 2 nitrophenol	Xe arc lamp	320-410	0.4

1.9. Aims of this work

This work focuses on using an IBBCEAS system in the near-UV and at blue wavelengths to investigate the absorption spectra of gases and the optical properties of secondary organic aerosol particles. The near-UV region has received relatively little attention, but is important in the troposphere because the high energy associated with these wavelengths initiates many atmospheric photochemical reactions. These short wavelengths are also strongly associated with brown carbon absorption.

Chapter 2 describes the atmospheric simulation chamber and instrumentation, as well as the setup, calibration and validation of the IBBCEAS system. The determination of the absorption cross section of several atmospherically relevant compounds is presented in Chapter 3. This includes several gas phase absorption cross sections recorded for the first time. These absorption cross sections are useful in identifying and quantifying gas phase compounds. In Chapter 4, the optical properties of a biogenic SOA system are investigated. The ozonolysis of α-pinene was chosen as a representative system for purely scattering biogenic SOAs. The optical properties presented include the extinction, single scattering albedo, Angstrom exponent and complex refractive index. The effects of concentration, OH scavengers and elevated levels of water on the optical and physical properties of the SOA are also investigated.

Chapter 5 contributes to the growing interest in the effects of absorbing aerosols in the atmosphere, especially in urban areas, by studying SOA formed by the photolysis of 2-nitrophenol. Such nitroaromatic species have been identified as having a major impact on levels of UV light in urban environments due to their ability to absorb as well as scatter light (190). The mass absorption coefficient, CRI, and SSA for these particles are presented, and the effect of changing the reaction pathway via the addition of OH scavengers, Criegee intermediate scavengers, and NO_2, is investigated. These chapters illustrate not only the application of IBBCEAS in a number of measurements but also provide valuable information on the optical

properties of different particles and the absorption spectra of several gases of relevance to the atmosphere.

References

1. Seinfeld JH, Pandis SN. 2016. *Atmospheric chemistry and physics: from air pollution to climate change*. John Wiley & Sons
2. Randall D. 2010. The Composition of Air. *Carbon* 39:1.28
3. Rambler MB. 1989. *Global ecology: Towards a science of the biosphere*. Elsevier
4. 2016. *Atmo336 - Fall 2012*. http://www.atmo.arizona.edu/students/courselinks/fall12/atmo336/lectures/sec1/structure.html
5. Jacob D. 1999. *Introduction to atmospheric chemistry*. pp 17. Princeton University Press
6. 2016. *7(b) The Layered Atmosphere*. http://www.physicalgeography.net/fundamentals/7b.html
7. Kopp G, Lean JL. 2011. A new, lower value of total solar irradiance: Evidence and climate significance. *Geophysical Research Letters* 38
8. Campillo C, del Henar Prieto M, Fortes R. 2012. *Solar radiation effect on crop production*. INTECH Open Access Publisher
9. McCulloch A, Midgley PM, Ashford P. 2003. Releases of refrigerant gases (CFC-12, HCFC-22 and HFC-134a) to the atmosphere. *Atmospheric Environment* 37:889-902
10. Mitchell JF. 1989. The "greenhouse" effect and climate change. *Reviews of Geophysics* 27:115-39
11. Wang W, Yung Y, Lacis A, Mo Ta, Hansen J. 1976. Greenhouse effects due to man-made perturbations of trace gases. *Science* 194:685-90
12. Gerlach TM. 2004. Volcanic sources of tropospheric ozone-depleting trace gases. *Geochemistry, Geophysics, Geosystems* 5
13. KUTZBACH JE. 1961. Chlorine Monoxide Radical, Ozone, and HydrogenPeroxide: Stratospheric Measurements by Microwave Limb Sounding. *Science* 214:2
14. Marland G, Boden T, Andres R, Brenkert A, Johnston C. 2007. Global, regional, and national fossil fuel CO2 emissions. *Trends: A Compendium of Data on Global Change*:37831-6335
15. Andreae MO, Merlet P. 2001. Emission of trace gases and aerosols from biomass burning. *Global Biogeochemical Cycles* 15:955-66
16. Yokelson RJ, Burling I, Urbanski S, Atlas EL, Adachi K, Buseck P, Wiedinmyer C, Akagi S, Toohey D, Wold C. 2011. Trace gas and particle emissions from open biomass burning in Mexico. *Atmospheric Chemistry and Physics* 11:6787-808
17. Quéré CL, Andres RJ, Boden T, Conway T, Houghton R, House JI, Marland G, Peters GP, Van der Werf G, Ahlström A. 2013. The global carbon budget 1959–2011. *Earth System Science Data* 5:165-85
18. Vitousek PM, Matson PA. 1993. Agriculture, the global nitrogen cycle, and trace gas flux. In *Biogeochemistry of Global Change*:193-208: Springer. Number of 193-208 pp.
19. Nisbet EG, Dlugokencky EJ, Bousquet P. 2014. Methane on the rise—again. *Science* 343:493-5
20. Bousquet P, Ciais P, Miller JB, Dlugokencky EJ, Hauglustaine DA, Prigent C, Van der Werf GR, Peylin P, Brunke EG, Carouge C, Langenfelds RL, Lathiere J, Papa F, Ramonet M, Schmidt M, Steele LP, Tyler SC, White J. 2006. Contribution of anthropogenic and natural sources to atmospheric methane variability. *Nature* 443:439-43
21. Bates T, Lamb B, Guenther A, Dignon J, Stoiber R. 1992. Sulfur emissions to the atmosphere from natural sourees. *Journal of Atmospheric Chemistry* 14:315-37

22. Husar RB. Atmospheric sulfur behavior in power plant and regional plumes. *Proc. Man's Impact on the Troposphere: Lectures in Tropospheric Chemistry*, *1978*, 1:319: National Aeronautics and Space Administration, Scientific and Technical Information Office
23. Spiro PA, Jacob DJ, Logan JA. 1992. Global inventory of sulfur emissions with 1× 1 resolution. *Journal of Geophysical Research: Atmospheres* 97:6023-36
24. Guenther A, Hewitt CN, Erickson D, Fall R, Geron C, Graedel T, Harley P, Klinger L, Lerdau M, McKay W. 1995. A global model of natural volatile organic compound emissions. *Journal of Geophysical Research: Atmospheres* 100:8873-92
25. Piccot SD, Watson JJ, Jones JW. 1992. A global inventory of volatile organic compound emissions from anthropogenic sources. *Journal of Geophysical Research: Atmospheres* 97:9897-912
26. Finlayson-Pitts BJ, Pitts Jr JN. 1999. *Chemistry of the upper and lower atmosphere: theory, experiments, and applications*. Academic press
27. Buseck PR, Adachi K. 2008. Nanoparticles in the atmosphere. *Elements* 4:389-94
28. Hobbs PV. 2000. *Introduction to atmospheric chemistry*. Cambridge University Press
29. Tegen I, Lacis AA. 1996. Modeling of particle size distribution and its influence on the radiative properties of mineral dust aerosol. *JOURNAL OF GEOPHYSICAL RESEARCH-ALL SERIES*- 101:19,237-19,44
30. Andronache C. 2004. Precipitation removal of ultrafine aerosol particles from the atmospheric boundary layer. *Journal of Geophysical Research: Atmospheres* 109
31. Mohr C, Huffman JA, Cubison MJ, Aiken AC, Docherty KS, Kimmel JR, Ulbrich IM, Hannigan M, Jimenez JL. 2009. Characterization of Primary Organic Aerosol Emissions from Meat Cooking, Trash Burning, and Motor Vehicles with High-Resolution Aerosol Mass Spectrometry and Comparison with Ambient and Chamber Observations. *Environmental Science & Technology* 43:2443-9
32. Schauer JJ, Kleeman MJ, Cass GR, Simoneit BRT. 2002. Measurement of Emissions from Air Pollution Sources. 5. C1−C32 Organic Compounds from Gasoline-Powered Motor Vehicles. *Environmental Science & Technology* 36:1169-80
33. Dentener F, Kinne S, Bond T, Boucher O, Cofala J, Generoso S, Ginoux P, Gong S, Hoelzemann J, Ito A. 2006. Emissions of primary aerosol and precursor gases in the years 2000 and 1750 prescribed data-sets for AeroCom. *Atmospheric Chemistry and Physics* 6:4321-44
34. Lei Y, Zhang Q, He KB, Streets DG. 2011. Primary anthropogenic aerosol emission trends for China, 1990–2005. *Atmos. Chem. Phys.* 11:931-54
35. Schauer JJ, Rogge WF, Hildemann LM, Mazurek MA, Cass GR, Simoneit BR. 1996. Source apportionment of airborne particulate matter using organic compounds as tracers. *Atmospheric Environment* 30:3837-55
36. Allen A, Oppenheimer C, Ferm M, Baxter P, Horrocks L, Galle B, McGonigle A, Duffell H. 2002. Primary sulfate aerosol and associated emissions from Masaya Volcano, Nicaragua. *Journal of Geophysical Research: Atmospheres* 107:ACH 5-1–ACH 5-8
37. Després V, Nowoisky J, Klose M, Conrad R, Andreae M, Pöschl U. 2007. Characterization of primary biogenic aerosol particles in urban, rural, and high-alpine air by DNA sequence and restriction fragment analysis of ribosomal RNA genes. *Biogeosciences* 4:1127-41
38. Möhler O, DeMott P, Vali G, Levin Z. 2007. Microbiology and atmospheric processes: the role of biological particles in cloud physics. *Biogeosciences* 4:1059-71

39. Calvo A, Alves C, Castro A, Pont V, Vicente A, Fraile R. 2013. Research on aerosol sources and chemical composition: past, current and emerging issues. *Atmospheric Research* 120:1-28
40. McGinn SM, Janzen HH. 1998. Ammonia sources in agriculture and their measurement. *Canadian Journal of Soil Science* 78:139-48
41. Zhuang H, Chan CK, Fang M, Wexler AS. 1999. Size distributions of particulate sulfate, nitrate, and ammonium at a coastal site in Hong Kong. *Atmospheric Environment* 33:843-53
42. Heintzenberg J. 1989. Fine particles in the global troposphere a review. *Tellus B* 41:149-60
43. Putaud J-P, Raes F, Van Dingenen R, Brüggemann E, Facchini M-C, Decesari S, Fuzzi S, Gehrig R, Hüglin C, Laj P. 2004. A European aerosol phenomenology—2: chemical characteristics of particulate matter at kerbside, urban, rural and background sites in Europe. *Atmospheric environment* 38:2579-95
44. Saxena P, Hildemann LM. 1997. Water absorption by organics: Survey of laboratory evidence and evaluation of UNIFAC for estimating water activity. *Environmental science & technology* 31:3318-24
45. Kanakidou M, Seinfeld J, Pandis S, Barnes I, Dentener F, Facchini M, Dingenen RV, Ervens B, Nenes A, Nielsen C. 2005. Organic aerosol and global climate modelling: a review. *Atmospheric Chemistry and Physics* 5:1053-123
46. Cappa CD, Che DL, Kessler SH, Kroll JH, Wilson KR. 2011. Variations in organic aerosol optical and hygroscopic properties upon heterogeneous OH oxidation. *Journal of Geophysical Research: Atmospheres* 116
47. Kroll JH, Seinfeld JH. 2008. Chemistry of secondary organic aerosol: Formation and evolution of low-volatility organics in the atmosphere. *Atmospheric Environment* 42:3593-624
48. Grosjean D, Seinfeld JH. 1989. Parameterization of the formation potential of secondary organic aerosols. *Atmospheric Environment (1967)* 23:1733-47
49. Grosjean D. 1992. In situ organic aerosol formation during a smog episode: estimated production and chemical functionality. *Atmospheric Environment. Part A. General Topics* 26:953-63
50. Hallquist M, Wenger J, Baltensperger U, Rudich Y, Simpson D, Claeys M, Dommen J, Donahue N, George C, Goldstein A. 2009. The formation, properties and impact of secondary organic aerosol: current and emerging issues. *Atmospheric Chemistry and Physics* 9:5155-236
51. Atkinson R, Arey J. 2003. Gas-phase tropospheric chemistry of biogenic volatile organic compounds: a review. *Atmospheric Environment* 37:197-219
52. Griffin RJ, Cocker III DR, Seinfeld JH, Dabdub D. 1999. Estimate of global atmospheric organic aerosol from oxidation of biogenic hydrocarbons. *Geophysical research letters* 26:2721-4
53. McCartney EJ. 1976. Optics of the atmosphere: scattering by molecules and particles. *New York, John Wiley and Sons, Inc., 1976. 421 p.* 1
54. Sinclair D. 1950. Optical properties of aerosols. *Handbook on aerosols*:81-96
55. Waggoner A, Charlson R. 1976. Measurements of aerosol optical parameters. *Fine Particles*:511-34
56. Hahn DW. Light scattering theory.
57. Kylling A, Webb AR, Bais AF, Blumthaler M, Schmitt R, Thiel S, Kazantzidis A, Kift R, Misslbeck M, Schallhart B, Schreder J, Topaloglou C, Kazadzis S, Rimmer J. 2003. Actinic flux determination from measurements of irradiance. *J. Geophys. Res.-Atmos.* 108:ACH 11 1-0

58. Saiz-Lopez A, Saunders R, Joseph D, Ashworth S, Plane J. 2004. Absolute absorption cross-section and photolysis rate of I 2. *Atmospheric Chemistry and Physics* 4:1443-50
59. Plum CN, Sanhueza E, Atkinson R, Carter WPL, Pitts JN. 1983. Hydroxyl radical rate constants and photolysis rates of alpha-dicarbonyls. *Environmental science & technology* 17:479-84
60. Horvath H. On the applicability of the Koschmieder visibility formula. *Atmospheric Environment (1967)* 5:177-84
61. Chang D, Song Y, Liu B. 2009. Visibility trends in six megacities in China 1973–2007. *Atmospheric Research* 94:161-7
62. Groblicki PJ, Wolff GT, Countess RJ. 1981. Plumes and Visibility Measurements and Model Components-Supplement Visibility-reducing species in the denver "brown cloud"—I. Relationships between extinction and chemical composition. *Atmospheric Environment (1967)* 15:2473-84
63. Horvath H. 1995. Estimation of the average visibility in central Europe. *Atmospheric Environment* 29:241-6
64. Nam-Jun B, Yong Pyo K, Kil Choo M. 1996. Fourth International Conference on Atmospheric Science and Applications to Air QualityVisibility study in Seoul, 1993. *Atmospheric Environment* 30:2319-28
65. Lee KH, Wong MS, Kim K, Park SS. 2014. Analytical approach to estimating aerosol extinction and visibility from satellite observations. *Atmospheric environment* 91:127-36
66. Groblicki PJ, Wolff GT, Countess RJ. 1981. Visibility-reducing species in the Denver "brown cloud"—I. Relationships between extinction and chemical composition. *Atmospheric Environment (1967)* 15:2473-84
67. Larson SM, Cass GR. 1989. Characteristics of summer midday low-visibility events in the Los Angeles area. *Environmental science & technology* 23:281-9
68. BBCworld. 2016. *Beijing releases air pollution data - BBC News*. http://www.bbc.com/news/world-asia-china-16665360
69. Chang H, Charalampopoulos T. Determination of the wavelength dependence of refractive indices of flame soot. *Proc. Proceedings of the Royal Society of London A: Mathematical, Physical and Engineering Sciences*, *1990*, 430:577-91: The Royal Society
70. Nakayama T, Sato K, Matsumi Y, Imamura T, Yamazaki A, Uchiyama A. 2012. Wavelength dependence of refractive index of secondary organic aerosols generated during the ozonolysis and photooxidation of α-pinene. *Sola* 8:119-23
71. Nakayama T, Sato K, Matsumi Y, Imamura T, Yamazaki A, Uchiyama A. 2013. Wavelength and NO_x dependent complex refractive index of SOAs generated from the photooxidation of toluene. *Atmospheric Chemistry and Physics* 13:531-45
72. Haywood J, Ramaswamy V, Soden BJ. 1999. Tropospheric aerosol climate forcing in clear-sky satellite observations over the oceans. *Science* 283:1299-303
73. Kaufman YJ, Fraser RS. 1997. The effect of smoke particles on clouds and climate forcing. *Science* 277:1636-9
74. Haywood J, Boucher O. 2000. Estimates of the direct and indirect radiative forcing due to tropospheric aerosols: A review. *Reviews of geophysics* 38:513-43
75. Andrews E, Ogren J, Bonasoni P, Marinoni A, Cuevas E, Rodríguez S, Sun J, Jaffe D, Fischer E, Baltensperger U. 2011. Climatology of aerosol radiative properties in the free troposphere. *Atmospheric Research* 102:365-93
76. Reid JS, Eck TF, Christopher SA, Koppmann R, Dubovik O, Eleuterio D, Holben BN, Reid EA, Zhang J. 2005. A review of biomass burning emissions part III: intensive

optical properties of biomass burning particles. *Atmospheric Chemistry and Physics* 5:827-49
77. Stier P, Seinfeld JH, Kinne S, Boucher O. 2007. Aerosol absorption and radiative forcing. *Atmospheric Chemistry and Physics* 7:5237-61
78. Koch D, Schulz M, Kinne S, McNaughton C, Spackman J, Balkanski Y, Bauer S, Berntsen T, Bond TC, Boucher O. 2009. Evaluation of black carbon estimations in global aerosol models. *Atmospheric Chemistry and Physics* 9:9001-26
79. Keeling CD, Bacastow RB, Bainbridge AE, Ekdahl CA, Guenther PR, Waterman LS, Chin JF. 1976. Atmospheric carbon dioxide variations at Mauna Loa observatory, Hawaii. *Tellus* 28:538-51
80. Siegenthaler U, Sarmiento J. 1993. Atmospheric carbon dioxide and the ocean. *Nature* 365:119-25
81. Stauffer B, Fischer G, Neftel A, Oeschger H. 1985. Increase of Atmospheric Methane Recorded in Antarctic Ice Core. *Science* 229:1386-8
82. Blake DR, Mayer EW, Tyler SC, Makide Y, Montague DC, Rowland FS. 1982. Global increase in atmospheric methane concentrations between 1978 and 1980. *Geophysical Research Letters* 9:477-80
83. Machida T, Nakazawa T, Fujii Y, Aoki S, Watanabe O. 1995. Increase in the atmospheric nitrous oxide concentration during the last 250 years. *Geophysical Research Letters* 22:2921-4
84. Solomon S, Qin D, Manning M, Chen Z, Marquis M, Averyt K, Tignor M, Miller H. 2007. Contribution of working group I to the fourth assessment report of the intergovernmental panel on climate change, 2007. Cambridge University Press, Cambridge
85. Cruz CN, Pandis SN. 1997. A study of the ability of pure secondary organic aerosol to act as cloud condensation nuclei. *Atmospheric Environment* 31:2205-14
86. Novakov T, Penner J. 1993. Large contribution of organic aerosols to cloud-condensation-nuclei concentrations.823-6
87. Lohmann U, Feichter J. 2005. Global indirect aerosol effects: a review. *Atmospheric Chemistry and Physics* 5:715-37
88. Myhre G, Shindell D, Bréon F-M, Collins W, Fuglestvedt J, Huang J, Koch D, Lamarque J-F, Lee D, Mendoza B. 2013. Anthropogenic and natural radiative forcing. *Climate change* 423
89. Kim H, Barkey B, Paulson SE. 2010. Real refractive indices of α-and β-pinene and toluene secondary organic aerosols generated from ozonolysis and photo-oxidation. *Journal of Geophysical Research: Atmospheres* 115
90. Kim H, Barkey B, Paulson SE. 2012. Real refractive indices and formation yields of secondary organic aerosol generated from photooxidation of limonene and α-pinene: the effect of the HC/NO_x Ratio. *The Journal of Physical Chemistry A* 116:6059-67
91. Kim H, Paulson SE. 2013. Real refractive indices and volatility of secondary organic aerosol generated from photooxidation and ozonolysis of limonene, α-pinene and toluene. *Atmospheric Chemistry and Physics* 13:7711-23
92. Saleh R, Hennigan C, McMeeking G, Chuang W, Robinson E, Coe H, Donahue N, Robinson A. 2013. Absorptivity of brown carbon in fresh and photo-chemically aged biomass-burning emissions. *Atmospheric Chemistry and Physics* 13:7683-93
93. Schnaiter M, Linke C, Möhler O, Naumann KH, Saathoff H, Wagner R, Schurath U, Wehner B. 2005. Absorption amplification of black carbon internally mixed with secondary organic aerosol. *Journal of Geophysical Research: Atmospheres* 110

94. Novakov T, Ramanathan V, Hansen J, Kirchstetter T, Sato M, Sinton J, Sathaye J. 2003. Large historical changes of fossil-fuel black carbon aerosols. *Geophysical Research Letters* 30
95. Bond TC, Sun H. 2005. Can Reducing Black Carbon Emissions Counteract Global Warming? *Environmental Science & Technology* 39:5921-6
96. Change IC. 2013. The physical science basis. Contribution of working group I to the fifth assessment report of the intergovernmental panel on climate change. *K., Tignor, M., Allen, SK, Boschung, J., Nauels, A., Xia, Y., Bex, V., Midgley, PM, Eds*:1535
97. Jacobson MZ. 2000. Physically-based treatment of elemental carbon optics: Implications for global direct forcing of aerosols. *Geophysical Research Letters* 27:217-20
98. Sato M, Hansen J, Koch D, Lacis A, Ruedy R, Dubovik O, Holben B, Chin M, Novakov T. 2003. Global atmospheric black carbon inferred from AERONET. *Proceedings of the National Academy of Sciences* 100:6319-24
99. Novakov T, Hegg DA, Hobbs PV. 1997. Airborne measurements of carbonaceous aerosols on the East Coast of the United States. *Journal of Geophysical Research: Atmospheres* 102:30023-30
100. Putaud JP, Van Dingenen R, Mangoni M, Virkkula A, Raes F, Maring H, Prospero J, Swietlicki E, Berg O, Hillamo R. 2000. Chemical mass closure and assessment of the origin of the submicron aerosol in the marine boundary layer and the free troposphere at Tenerife during ACE-2. *Tellus B* 52:141-68
101. Ramanathan V, Crutzen PJ, Lelieveld J, Mitra A, Althausen D, Anderson J, Andreae M, Cantrell W, Cass G, Chung C. 2001. Indian Ocean Experiment: An integrated analysis of the climate forcing and effects of the great Indo-Asian haze. *Journal of Geophysical Research: Atmospheres* 106:28371-98
102. Chameides WL, Yu H, Liu S, Bergin M, Zhou X, Mearns L, Wang G, Kiang C, Saylor R, Luo C. 1999. Case study of the effects of atmospheric aerosols and regional haze on agriculture: An opportunity to enhance crop yields in China through emission controls? *Proceedings of the National Academy of Sciences* 96:13626-33
103. Kaufman Y, Hobbs P, Kirchhoff V, Artaxo P, Remer L, Holben B, King M, Ward D, Prins E, Longo K. 1998. Smoke, Clouds, and Radiation-Brazil (SCAR-B) experiment. *Journal of Geophysical Research: Atmospheres* 103:31783-808
104. Kaneyasu N, Murayama S. 2000. High concentrations of black carbon over middle latitudes in the North Pacific Ocean. *Journal of Geophysical Research: Atmospheres* 105:19881-90
105. Bodhaine BA. 1995. Aerosol absorption measurements at Barrow, Mauna Loa and the south pole. *Journal of Geophysical Research: Atmospheres* 100:8967-75
106. Hadley OL, Kirchstetter TW. 2012. Black-carbon reduction of snow albedo. *Nature Clim. Change* 2:437-40
107. Andreae M, Gelencsér A. 2006. Black carbon or brown carbon? The nature of light-absorbing carbonaceous aerosols. *Atmospheric Chemistry and Physics* 6:3131-48
108. Lack D, Langridge J. 2013. On the attribution of black and brown carbon light absorption using the Ångström exponent. *Atmospheric Chemistry and Physics* 13:10535-43
109. Moosmüller H, Chakrabarty R, Ehlers K, Arnott W. 2011. Absorption Ångström coefficient, brown carbon, and aerosols: basic concepts, bulk matter, and spherical particles. *Atmospheric Chemistry and Physics* 11:1217-25
110. Bahadur R, Praveen PS, Xu Y, Ramanathan V. 2012. Solar absorption by elemental and brown carbon determined from spectral observations. *Proceedings of the National Academy of Sciences* 109:17366-71

111. Kirchstetter TW, Novakov T, Hobbs PV. 2004. Evidence that the spectral dependence of light absorption by aerosols is affected by organic carbon. *Journal of Geophysical Research: Atmospheres* 109:208
112. Chakrabarty R, Moosmüller H, Chen L-W, Lewis K, Arnott W, Mazzoleni C, Dubey M, Wold C, Hao W, Kreidenweis S. 2010. Brown carbon in tar balls from smoldering biomass combustion. *Atmospheric Chemistry and Physics* 10:6363-70
113. Lack DA, Richardson MS, Law D, Langridge JM, Cappa CD, McLaughlin RJ, Murphy DM. 2012. Aircraft instrument for comprehensive characterization of aerosol optical properties, Part 2: black and brown carbon absorption and absorption enhancement measured with photo acoustic spectroscopy. *Aerosol Science and Technology* 46:555-68
114. Bond TC. 2001. Spectral dependence of visible light absorption by carbonaceous particles emitted from coal combustion. *Geophysical Research Letters* 28:4075-8
115. Andreae MO, Crutzen PJ. 1997. Atmospheric aerosols: Biogeochemical sources and role in atmospheric chemistry. *Science* 276:1052-8
116. Rizzo LV, Artaxo P, Mueller T, Wiedensohler A, Paixao M, Cirino GG, Arana A, Swietlicki E, Roldin P, Fors EO. 2013. Long term measurements of aerosol optical properties at a primary forest site in Amazonia. *Atmospheric Chemistry and Physics* 13:2391-413
117. Rizzo LV, Correia AL, Artaxo P, Procópio AS, Andreae MO. 2011. Spectral dependence of aerosol light absorption over the Amazon Basin. *Atmospheric Chemistry and Physics* 11:8899-912
118. Updyke KM, Nguyen TB, Nizkorodov SA. 2012. Formation of brown carbon via reactions of ammonia with secondary organic aerosols from biogenic and anthropogenic precursors. *Atmospheric environment* 63:22-31
119. De Haan DO, Corrigan AL, Tolbert MA, Jimenez JL, Wood SE, Turley JJ. 2009. Secondary organic aerosol formation by self-reactions of methylglyoxal and glyoxal in evaporating droplets. *Environmental science & technology* 43:8184-90
120. Powelson MH, Espelien BM, Hawkins LN, Galloway MM, De Haan DO. 2013. Brown carbon formation by aqueous-phase carbonyl compound reactions with amines and ammonium sulfate. *Environmental science & technology* 48:985-93
121. Feng Y, Ramanathan V, Kotamarthi V. 2013. Brown carbon: a significant atmospheric absorber of solar radiation? *Atmospheric Chemistry and Physics* 13:8607-21
122. Bond TC, Bergstrom RW. 2006. Light absorption by carbonaceous particles: An investigative review. *Aerosol science and technology* 40:27-67
123. Sokolik IN, Toon OB. 1996. Direct radiative forcing by anthropogenic airborne mineral aerosols. *Nature* 381:681-3
124. Charlson RJ, Schwartz S. 1992. Climate forcing by anthropogenic aerosols. *Science* 255:423
125. Jacobson MZ. 2001. Global direct radiative forcing due to multicomponent anthropogenic and natural aerosols. *Journal of Geophysical Research: Atmospheres* 106:1551-68
126. Kiehl J, Briegleb B. 1993. The relative roles of sulfate aerosols and greenhouse gases in climate forcing. *Science* 260:311-4
127. Dinar E, Riziq AA, Spindler C, Erlick C, Kiss G, Rudich Y. 2008. The complex refractive index of atmospheric and model humic-like substances (HULIS) retrieved by a cavity ring down aerosol spectrometer (CRD-AS). *Faraday discussions* 137:279-95
128. D'Almeida GA, Koepke P, Shettle EP. 1991. *Atmospheric aerosols: global climatology and radiative characteristics*. A Deepak Pub

129. Mie G. 1908. Beiträge zur Optik trüber Medien, speziell kolloidaler Metallösungen. *Annalen der physik* 330:377-445
130. Lorenz LV. 1890. Upon the light reflected and refracted by a transparent sphere. *Vidensk. Selsk. Shrifter* 6:1-62
131. Hulst HC, van de Hulst HC. 1957. *Light scattering by small particles*. Courier Corporation
132. Bohren C, Huffman D. 1983. Absorbing and scattering of light by small particles. *Wiley Interscience* 13:123-7
133. Wriedt T. 1998. A review of elastic light scattering theories. *Particle & Particle Systems Characterization* 15:67-74
134. Kahnert FM. 2003. Numerical methods in electromagnetic scattering theory. *Journal of Quantitative Spectroscopy and Radiative Transfer* 79:775-824
135. Shettle EP, Fenn RW. 1979. Models for the aerosols of the lower atmosphere and the effects of humidity variations on their optical properties, DTIC Document
136. Twomey S. 1977. The influence of pollution on the shortwave albedo of clouds. *Journal of the atmospheric sciences* 34:1149-52
137. Marshall SF, Covert DS, Charlson RJ. 1995. Relationship between asymmetry parameter and hemispheric backscatter ratio: implications for climate forcing by aerosols. *Appl. Opt.* 34:6306-11
138. Andrews E, Sheridan PJ, Fiebig M, McComiskey A, Ogren JA, Arnott P, Covert D, Elleman R, Gasparini R, Collins D. 2006. Comparison of methods for deriving aerosol asymmetry parameter. *Journal of Geophysical Research: Atmospheres* 111
139. Moosmüller H, Chakrabarty R, Arnott W. 2009. Aerosol light absorption and its measurement: A review. *Journal of Quantitative Spectroscopy and Radiative Transfer* 110:844-78
140. McMurry PH. 2000. A review of atmospheric aerosol measurements. *Atmospheric Environment* 34:1959-99
141. Zahniser MS, Nelson DD, McManus JB, Kebabian PL, Lloyd D. 1995. Measurement of trace gas fluxes using tunable diode laser spectroscopy [and discussion]. *Philosophical Transactions of the Royal Society of London A: Mathematical, Physical and Engineering Sciences* 351:371-82
142. Werle P, Mücke R, Slemr F. 1993. The limits of signal averaging in atmospheric trace-gas monitoring by tunable diode-laser absorption spectroscopy (TDLAS). *Applied Physics B* 57:131-9
143. Podolske J, Loewenstein M. 1993. Airborne tunable diode laser spectrometer for trace-gas measurement in the lower stratosphere. *Appl. Opt.* 32:5324-33
144. Herrmann K. Tunable Diode Laser Spectroscopy.
145. Bernegger S, Sigrist M. 1990. CO-laser photoacoustic spectroscopy of gases and vapours for trace gas analysis. *Infrared Physics* 30:375-429
146. Sigrist MW. 2003. Trace gas monitoring by laser photoacoustic spectroscopy and related techniques (plenary). *Review of scientific instruments* 74:486-90
147. Harren FJ, Mandon J, Cristescu SM. 2000. Photoacoustic spectroscopy in trace gas monitoring. *Encyclopedia of Analytical Chemistry*
148. Müller JF. 1992. Geographical distribution and seasonal variation of surface emissions and deposition velocities of atmospheric trace gases. *Journal of Geophysical Research: Atmospheres* 97:3787-804
149. Garstang M, Scala J, Greco S, Harriss R, Beck S, Browell E, Sachse G, Gregory G, Hill G, Simpson J. 1988. Trace gas exchanges and convective transports over the Amazonian rain forest. *Journal of Geophysical Research: Atmospheres* 93:1528-50
150. Pundt I, Mettendorf K-U, Laepple T, Knab V, Xie P, Lösch J, Friedeburg C, Platt U, Wagner T. 2005. Measurements of trace gas distributions using long-path DOAS-

tomography during the motorway campaign BAB II: experimental setup and results for NO_2. *Atmospheric Environment* 39:967-75

151. Wittrock F, Oetjen H, Richter A, Fietkau S, Medeke T, Rozanov A, Burrows J. 2004. MAX-DOAS measurements of atmospheric trace gases in Ny-Ålesund-Radiative transfer studies and their application. *Atmospheric Chemistry and Physics* 4:955-66
152. Brown S, Stark H, Ravishankara A. 2002. Cavity ring-down spectroscopy for atmospheric trace gas detection: application to the nitrate radical (NO3). *Applied Physics B* 75:173-82
153. Romanini D, Kachanov A, Sadeghi N, Stoeckel F. 1997. CW cavity ring down spectroscopy. *Chemical Physics Letters* 264:316-22
154. Jongma RT, Boogaarts MG, Holleman I, Meijer G. 1995. Trace gas detection with cavity ring down spectroscopy. *Review of scientific instruments* 66:2821-8
155. O'Keefe A, Deacon DA. 1988. Cavity ring-down optical spectrometer for absorption measurements using pulsed laser sources. *Review of Scientific Instruments* 59:2544-51
156. von Bobrutzki K, Braban CF, Famulari D, Jones SK, Blackall T, et al. 2010. Field inter-comparison of eleven atmospheric ammonia measurement techniques. *Atmospheric Measurement Techniques* 3:91-112
157. Romanini D, Lehmann K. 1993. Ring-down cavity absorption spectroscopy of the very weak HCN overtone bands with six, seven, and eight stretching quanta. *The Journal of chemical physics* 99:6287-301
158. LaFranchi B. 2003. Cavity Ring Down Spectroscopy: History, Fundamentals, and Applications. *Chemistry* 226:1-18
159. Wheeler MD, Newman SM, Orr-Ewing AJ, Ashfold MN. 1998. Cavity ring-down spectroscopy. *Journal of the Chemical Society, Faraday Transactions* 94:337-51
160. Pettersson A, Lovejoy ER, Brock CA, Brown SS, Ravishankara A. 2004. Measurement of aerosol optical extinction at 532nm with pulsed cavity ring down spectroscopy. *Journal of Aerosol Science* 35:995-1011
161. Abo Riziq A, Erlick C, Dinar E, Rudich Y. 2007. Optical properties of absorbing and non-absorbing aerosols retrieved by cavity ring down (CRD) spectroscopy. *Atmospheric Chemistry and Physics* 7:1523-36
162. Smith JD, Atkinson DB. 2001. A portable pulsed cavity ring-down transmissometer for measurement of the optical extinction of the atmospheric aerosol. *Analyst* 126:1216-20
163. Zalicki P, Zare RN. 1995. Cavity ring-down spectroscopy for quantitative absorption measurements. *The Journal of chemical physics* 102:2708-17
164. Vaughan S, Canosa-Mas CE, Pfrang C, Shallcross DE, Watson L, Wayne RP. 2006. Kinetic studies of reactions of the nitrate radical (NO_3) with peroxy radicals (RO_2): an indirect source of OH at night? *Physical Chemistry Chemical Physics* 8:3749-60
165. Courtillot I, Morville J, Motto-Ros V, Romanini D. 2006. Sub-ppb NO_2 detection by optical feedback cavity-enhanced absorption spectroscopy with a blue diode laser. *Applied Physics B* 85:407-12
166. Neil SR, Maeda K, Henbest KB, Goez M, Hemmens R, Timmel CR, Mackenzie SR. 2010. Cavity enhanced detection methods for probing the dynamics of spin correlated radical pairs in solution. *Molecular Physics* 108:993-1003
167. Fiedler SE, Hese A, Ruth AA. 2003. Incoherent broad-band cavity-enhanced absorption spectroscopy. *Chemical Physics Letters* 371:284-94
168. Washenfelder R, Flores J, Brock C, Brown S, Rudich Y. 2013. Broadband measurements of aerosol extinction in the ultraviolet spectral region. *Atmospheric Measurement Techniques* 6:861-77

169. Bluvshtein N, Flores JM, Segev L, Rudich Y. 2016. A new approach for measuring the UV-Vis optical properties of ambient aerosols. *Atmos. Meas. Tech. Discuss.* 2016:1-27
170. Varma RM, Ball SM, Brauers T, Dorn H, Heitmann U, Jones R, Platt U, Pöhler D, Ruth AA, Shillings A. 2013. Light extinction by secondary organic aerosol: an intercomparison of three broadband cavity spectrometers. *Atmospheric Measurement Techniques* 6 3115-30
171. Zhao W, Xu X, Dong M, Chen W, Gu X, Hu C, Huang Y, Gao X, Huang W, Zhang W. 2014. Development of a cavity-enhanced aerosol albedometer. *Atmospheric Measurement Techniques* 7:2551-66
172. Flores J, Zhao D, Segev L, Schlag P, Kiendler-Scharr A, Fuchs H, Watne Å, Bluvshtein N, Mentel TF, Hallquist M. 2014. Evolution of the complex refractive index in the near UV spectral region in ageing secondary organic aerosol. *Atmos Chem Phys Discus* 14:4149-87
173. Wilson EM, Chen J, Varma RM, Wenger JC, Venables DS. A novel, broadband spectroscopic method to measure the extinction coefficient of aerosols in the near-ultraviolet. *Proc. AIP Conf. Proc*, *2013*, 1531:155-8:
174. Varma RM, Venables DS, Ruth AA, Heitmann U, Schlosser E, Dixneuf S. 2009. Long optical cavities for open-path monitoring of atmospheric trace gases and aerosol extinction. *Appl. Opt.* 48:B159-B71
175. Langridge JM, Ball SM, Shillings AJ, Jones RL. 2008. A broadband absorption spectrometer using light emitting diodes for ultrasensitive, in situ trace gas detection. *Review of scientific instruments* 79:123110
176. Chen J, Venables DS. 2011. A broadband optical cavity spectrometer for measuring weak near-ultraviolet absorption spectra of gases. *Atmospheric Measurement Techniques* 4:425-36
177. Washenfelder R, Attwood A, Flores J, Rudich Y, Brown S. 2015. Broadband cavity enhanced spectroscopy in the ultraviolet spectral region for measurements of nitrogen dioxide and formaldehyde. *Atmospheric Measurement Techniques Discussions* 8:41-52
178. Kennedy O, Ouyang B, Langridge J, Daniels M, Bauguitte S, Freshwater R, McLeod M, Ironmonger C, Sendall J, Norris O. 2011. An aircraft based three channel broadband cavity enhanced absorption spectrometer for simultaneous measurements of NO_3, N_2O and NO_2.
179. Venables DS, Gherman T, Orphal J, Wenger JC, Ruth AA. 2006. High sensitivity in situ monitoring of NO3 in an atmospheric simulation chamber using incoherent broadband cavity-enhanced absorption spectroscopy. *Environmental science & technology* 40:6758-63
180. Gherman T, Venables DS, Vaughan S, Orphal J, Ruth AA. 2007. Incoherent broadband cavity-enhanced absorption spectroscopy in the near-ultraviolet: application to HONO and NO2. *Environmental science & technology* 42:890-5
181. Vaughan S, Gherman T, Ruth AA, Orphal J. 2008. Incoherent broad-band cavity-enhanced absorption spectroscopy of the marine boundary layer species I_2, IO and OIO. *Physical Chemistry Chemical Physics* 10:4471-7
182. Wu T, Zhao W, Chen W, Zhang W, Gao X. 2009. Incoherent broadband cavity enhanced absorption spectroscopy for in situ measurements of NO_2 with a blue light emitting diode. *Applied Physics B* 94:85-94
183. Aalto A, Genty G, Laurila T, Toivonen J. 2015. Incoherent broadband cavity enhanced absorption spectroscopy using supercontinuum and superluminescent diode sources. *Optics Express* 23:25225-34

184. Johansson O, Mutelle H, Parker AE, Batut S, Demaux P, Schoemaecker C, Fittschen C. 2014. Quantitative IBBCEAS measurements of I_2 in the presence of aerosols. *Applied Physics B* 114:421-32
185. Fuchs H, Ball SM, Bohn B, Brauers T, Cohen R, Dorn H, Dubé W, Fry J, Häseler R, Heitmann UM. 2010. Intercomparison of measurements of NO_2 concentrations in the atmosphere simulation chamber SAPHIR during the NO_3 Comp campaign.
186. Dorn H, Apodaca R, Ball SM, Brauers T, Brown S, Crowley J, Dubé W, Fuchs H, Häseler R, Heitmann UM. 2013. Intercomparison of NO_3 radical detection instruments in the atmosphere simulation chamber SAPHIR.
187. Benton A, Langridge J, Ball S, Bloss W, Dall'Osto M, Nemitz E, Harrison R, Jones R. 2010. Night-time chemistry above London: measurements of NO_3 and N_2O_5 from the BT Tower during REPARTEE-II. *Atmospheric Chemistry and Physics Discussions* 10:14347-86
188. Nakayama T, Matsumi Y, Sato K, Imamura T, Yamazaki A, Uchiyama A. 2010. Laboratory studies on optical properties of secondary organic aerosols generated during the photooxidation of toluene and the ozonolysis of α-pinene. *Journal of Geophysical Research: Atmospheres* 115
189. Hao L, Romakkaniemi S, Yli-Pirilä P, Joutsensaari J, Kortelainen A, Kroll J, Miettinen P, Vaattovaara P, Tiitta P, Jaatinen A. 2011. Mass yields of secondary organic aerosols from the oxidation of α-pinene and real plant emissions. *Atmospheric Chemistry and Physics* 11:1367-78
190. Jacobson MZ. 1999. Isolating nitrated and aromatic aerosols and nitrated aromatic gases as sources of ultraviolet light absorption. *Journal of Geophysical Research: Atmospheres* 104:3527-42

2. Experimental Methods

2.1. Introduction

Atmospheric simulation chambers are used to further the knowledge of complex atmospheric processes. These chambers allow much greater control over the chemical composition and physical properties of a sample than would be possible in the real atmosphere. Controlled variables include relative humidity and temperature, photolysis rate, and initial chemical composition. Atmospheric chambers (sometimes called smog chambers) first came into use in the 1950's. There is a long and well documented history of the use of such chambers to study important atmospheric processes such as gas phase chemical mechanisms, aerosol formation from gaseous precursors, absorption cross section measurements, and the formation of ozone and secondary organic aerosols (1-6). The following chapters focus on direct spectroscopic measurements of the absorption cross sections of a number of atmospherically relevant gas phase compounds and optical properties of secondary organic aerosols. These measurements were performed inside an atmospheric simulation chamber.

2.2. Atmospheric Simulation Chamber

The atmospheric simulation chamber used for these measurements is located in the Centre for Research into Atmospheric Chemistry (CRAC) laboratory in the Chemistry Department of University College Cork (UCC). A detailed description of the chamber has been given previously and is summarised here (7). The chamber comprised a quasi-cylindrical bag that is 4.1 m in length with a diameter of 1.1 m and a volume of approximately 3.9 m^3. The bag material was fluorinated ethylene propylene (FEP), which is chemically inert and minimises surface reactions, while also

transmitting visible and ultraviolet light, Figure 2.1. The FEP cylinder was surrounded by aluminium panelling to exclude ambient light from the chamber. The chamber was filled with dry air that had been passed through an air purification system. The purification system (Zander KMA 75) lowered the mixing ratios of NO_x and non-methane hydrocarbons to less than 10 ppbv by passing the air through a series of scrubbers; water vapour was also removed to lower the relative humidity in the clean chamber to about 0.03 %. Purge air inlet lines combined with an extractive exhaust allowed the chamber contents to be replaced with clean air.

The chamber was at ambient atmospheric pressure (ca. 101 kPa). 36 fluorescent lamps surrounded the chamber: 18 lamps with maximum emission at 254 nm (40 W Philips TUV) and 18 lamps with emission maximum at 360 nm (40 W Philips TL05). These lamps were used for photolysis and oxidation experiments. The temperature and the relative humidity were continuously monitored by a dew point meter (Vaisala DM70). There was no temperature control in the chamber. The chamber has a typical temperature of 19-21 °C all year round. Over the course of an experimental day (9:00 to 16:00) the temperature usually increased by 2 °C. When chamber lights were turned on, the temperature inside the chamber rose. This increase in temperature was related to the length of time the lights were on. Over a one hour period, the lights would increase the temperature in the chamber by about 8 °C.

After each experiment, the chamber was cleaned by flushing with purified air for at least 8 hours. As large amounts of gases and particles were present after many experiments, additional measures were taken to clean the chamber volume and walls. A large amount of ozone was added to the chamber and the chamber lamps were turned on. This is a standard method for cleaning simulation chambers (8). However, some wall contaminants were difficult to remove due to the age and condition of the chamber. NO_2 was regularly added to the chamber as a calibrant gas and remained on chamber walls at low levels even after extensive flushing. To reduce NO_2 contamination on walls, high levels of water vapour were sometimes added to the chamber to convert residual NO_2 to HONO, which was then removed more easily from the chamber during flushing.

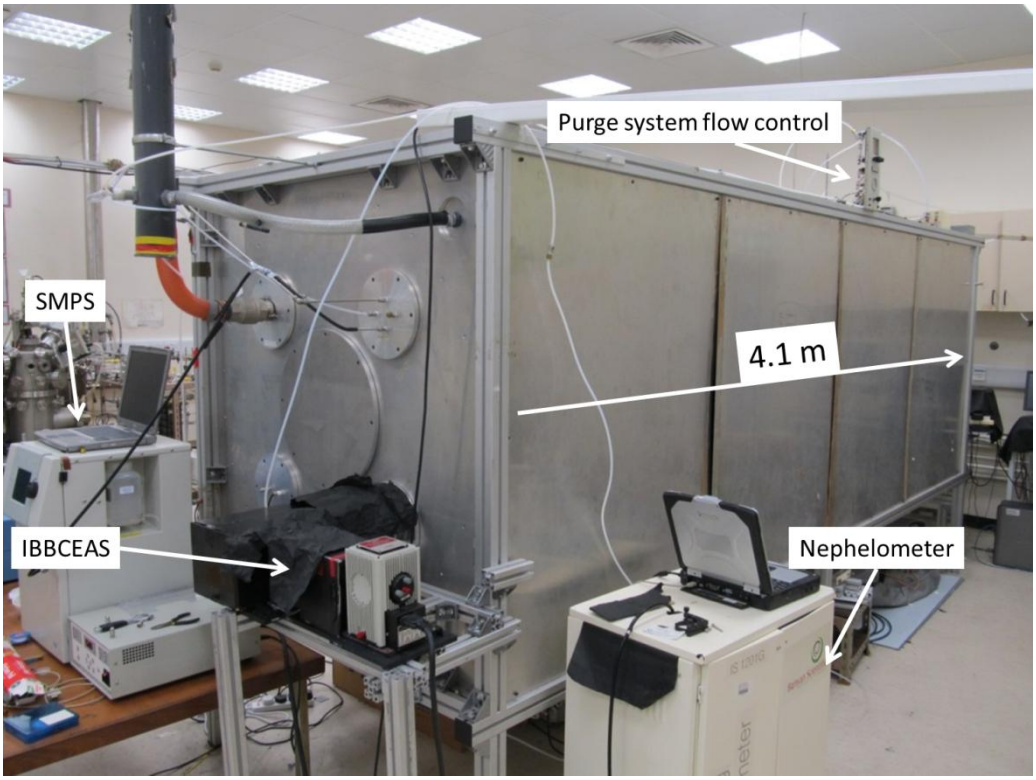

Figure 2.1 Photograph of the CRAC laboratory atmospheric simulation chamber with associated instruments: Incoherent Broadband Cavity-Enhanced Absorption Spectroscopy (IBBCEAS), nephelometer, and Scanning Mobility Particle Sizer (SMPS).

2.2.1. Standard chamber instrumentation

Ozone monitor

The mixing ratio of ozone in the chamber was monitored by a Thermo Scientific model 49i ozone analyser (O_3). This instrument had a measurement range from 0.05 ppbv to 200 ppmv and a precision of 1 ppbv. A time resolution of 20 seconds could be achieved. The measurement principle is based on absorption of 254 nm radiation, which occurs close to the maximum absorption for ozone in the Hartley band. Other compounds absorbing strongly in this region, including some of the aromatic compounds used in this research, gave rise to a spurious signal in the ozone monitor. Scientific insight and careful experimental control is therefore needed in interpreting the ozone monitor output.

NO_x monitor

The mixing ratios of NO_x, NO and NO_2 in the chamber were monitored by a Thermo Scientific model 42i ($NO-NO_2-NO_x$) analyser. The measurement range is 0-100 ppmv with a precision of ± 0.4 ppbv and a response time of 40 seconds. The NO_x measurement is based on the intensity of the chemiluminescent reaction of NO with ozone to determine the amount of NO present. All other NO_x species are converted to NO on a molybdenum catalytic converter and are therefore indirect measurements. The instrument was calibrated using purified laboratory air for the zero point and calibrant gas from a cylinder containing a known, certified concentration of NO in a matrix gas (Air Liquide 99.99 % purity).

Scanning Mobility Particle Sizer (SMPS)

The evolution of the aerosol particle number, mass, diameter, volume and surface area in the chamber was monitored using a TSI SMPS model 3034. This instrument measured particles in the size range of 10 to 487 nm and up to a total aerosol concentration of 10^7 particles cm^{-3}. The SMPS took 3 min to scan sequentially across the size range. The mass of particles was determined from the measured volume of particles and the particle density, which is set by the user. Therefore it is necessary to choose the most appropriate density based on the available literature. In general, reported densities for SOA vary from 0.9 to 1.6 g cm^{-3} (9). The density of secondary organic aerosols can change slightly over the course of an experiment, although this effect was not treated in our calculations. The densities used for each experiment were consistent with those used in reported literature and are given in the appropriate chapters.

2.3. Incoherent Broadband Cavity-Enhanced Absorption Spectroscopy

2.3.1. Instrument description

The primary instrument used in this study was an Incoherent Broadband Cavity-Enhanced Absorption Spectroscopy (IBBCEAS) system. It was installed directly

across the 4.1 m length of the CRAC chamber. The optical cavity in the IBBCEAS instrument was formed by two highly reflective mirrors, which enhance the sensitivity to light losses in the sample by reflecting light multiple times between the mirrors, thereby increasing the pathlength of broadband light through the sample. The IBBCEAS mirrors were supplied by Layertec GmbH: they were 25.4 mm diameter, fused silica, plano-concave (5.0 m radius of curvature) substrates and had a dielectric coating with an average reflectivity of 99.6 % between 290-450 nm on the concave surface.

The mirrors were placed inside flexible mounts attached to the chamber. The mounts extended 32.5 cm from each end of the chamber. The total distance between the two reflective mirror surfaces was 475 cm, but the distance through the sample was 410 cm owing to the purged volume around the mirrors. Two micrometers on the mirror mounts allowed the angle of the mirrors to be adjusted and the cavity to be aligned, Figure 2.2. These mounts were connected to the chamber via KF25 vacuum connections to prevent leaks. To prevent contamination of the cavity mirror surfaces by gases or the deposition of particles, a flow of purified air was passed over the mirrors at a rate of 0.6 L min^{-1} per mirror. The airflow to the purge system and the chamber flush are connected to the same air supply. When the flush was on, the rate of air flow over the mirrors dropped from 1.2 L min^{-1} to 0.2 L min^{-1}. If the flush needed to be turned on during an experiment, a nitrogen gas cylinder was connected to the purge to ensure that the purge flow rate over the mirrors remained constant.

The light source used in the IBBCEAS was a 75 W Osram XBO Xenon short-arc lamp which emitted light from 200 to 1300 nm, Figure 2.3. The wavelength range of this study was from 320 to 420 nm, covering most of the near UV and some of the visible spectrum. Arc lamps allow a degree of versatility in the experimental set up. LEDs have previously been used for IBBCEAS studies, and while these are a cheaper alternative light source, they transmit light over much narrower spectral ranges and are not very bright below 365 nm (10).

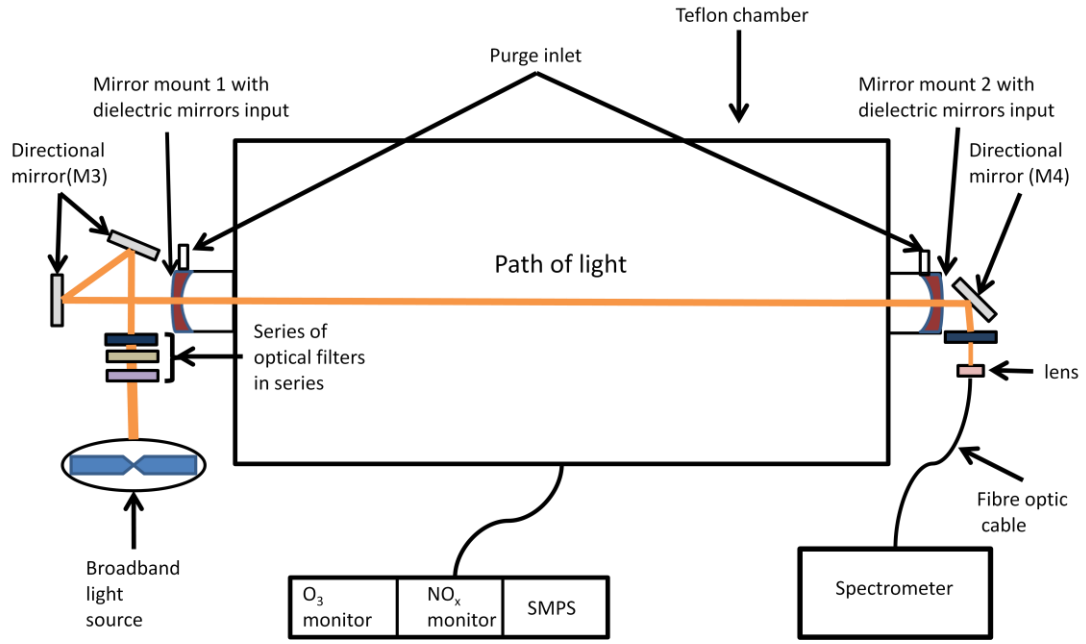

Figure 2.2 Schema of the IBBCEAS optical system across the chamber.

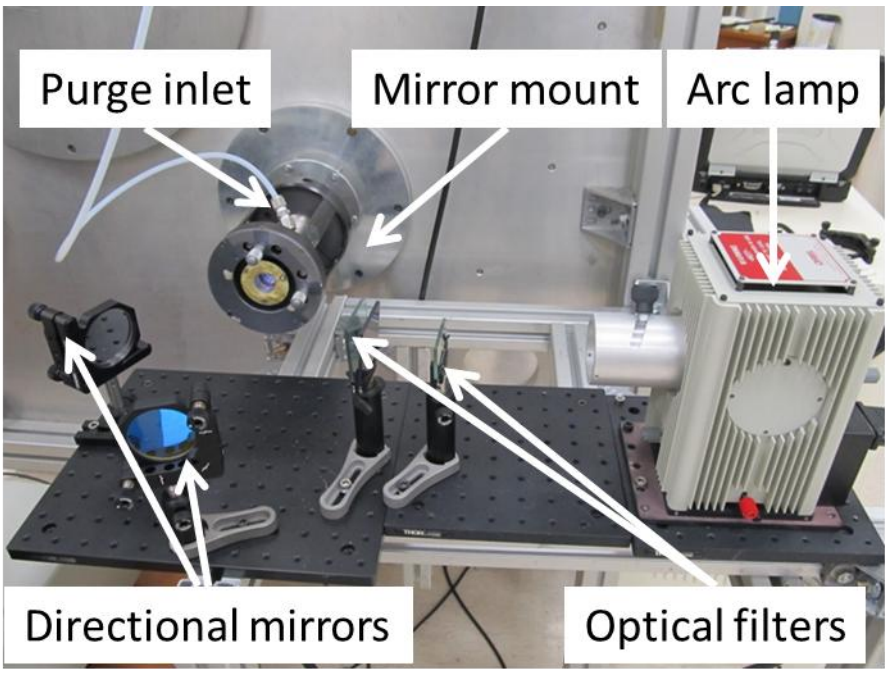

Figure 2.3 A close-up photograph of the lamp and filters at the optical entrance to the cavity. The lamps and components were mounted onto a breadboard attached to the chamber and floor with a series of metal profiles.

An enhanced aluminium mirror and a CVI Melles-Griot UR 2.00 UV cold mirror (M3) were used as positioning mirrors to direct the light beam through the first dielectric

mirror, into the chamber, and through the second dielectric mirror. This was reflected off another aluminium coated mirror (M4) and focused through a UV fused silica plano-convex lens (35.1 mm) into an Andor optical fibre. The optical fibre was connected to a Shamrock SR-163 spectrometer with a DU420A-BU2 CCD. The grating in the spectrometer was a 1200 lines mm^{-1} grating with a 300 nm blaze wavelength, giving spectral coverage of about 120 nm in the near-ultraviolet.

2.3.2. Optical alignment and spectral filtering

The sensitivity of the IBBCEAS system derives from the extended pathlength of the light in the cavity arising from multiple reflections of the broadband light between the two dielectric mirrors. To maximise the number of reflections, the mirrors need to be aligned to ensure that light is reflected accurately from one mirror to the other. A brief description of the alignment procedure is given here.

The two mirror mounts, all the filters and a number of the aluminium side panels of the chamber were removed. An iris was placed over both openings in the chamber. The two external, positioning mirrors were used to direct a laser beam through the centre of the two irises; the beam was then reflected off M4 and focused into the fibre cable, Figure 2.2. Once this path height was established the M2 mirror mount was re-attached. With this mount and associated mirror in place, the mount was adjusted to reflect the light back on itself and through the opening on the opposite side of the chamber. Once the light path through the centre of the opening was established, mirror mount M1 was re-attached. The mirror alignment was again adjusted to direct the light path back along itself. This reflection, back and forth, of the light path between the dielectric mirrors, creates an aligned optical cavity. As the mirror separation was relatively long, the optical cavity could be aligned relatively straightforwardly.

It was also necessary to spectrally filter the broadband light source to remove unwanted wavelengths. Light outside of the region of interest adversely affects the spectra by adding to background light in the spectrograph. The dielectric mirrors of the optical cavity reflect over 99 % of photons between from 300 to 450 nm, but transmit up to 95 % of light outside of this range. As a consequence, light outside of

the spectral region of interest is transmitted efficiently through the optical cavity to the spectrometer. Even though spectral dispersion by the grating in the spectrometer removes most unwanted wavelengths, scattering and multiple reflections within the spectrometer itself result in some light getting to the detector and contributing to background levels. A secondary reason for filtering is to prevent the detector from saturating.

In order to reduce extraneous light, several optical filters were used to narrow the wavelength range of light in the optical system. Optical filtering across the very broadband output of the arc lamp is difficult to achieve, particularly in the near-UV where the choice of optical filters and other optical components is limited. No single filter was adequate across the lamp output spectrum, so several filters in series were used to remove undesired wavelengths from the optical system. These filters were Schott KG2, KG3 and BG3 and Edmund Optics NT47-256; transmission spectra of these filters are displayed in Figure 2.4.

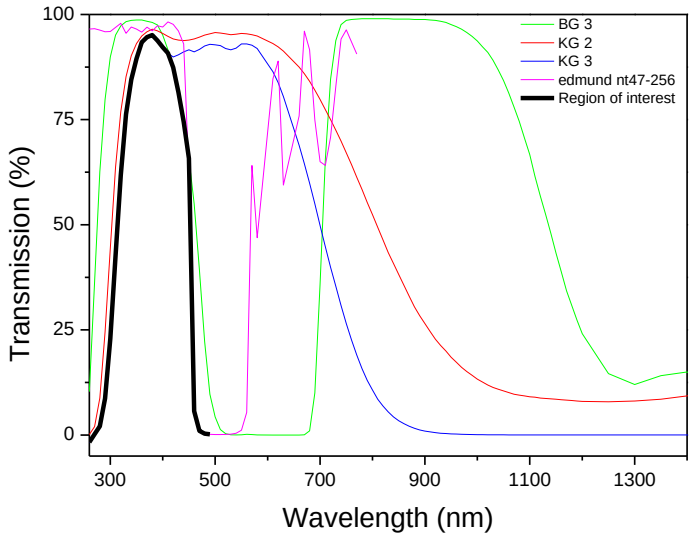

Figure 2.4 Transmission spectra of the filters used in the IBBCEAS system. The combination of the different light filters allowed most wavelengths outside of the region of interest to be eliminated.

With these filters in place, most wavelengths outside of the high reflectivity range of the optical cavity were removed from the system. Some longer wavelengths,

particularly between 700 and 820 nm, were attenuated less efficiently. No way was found to remove these wavelengths with standard commercially available filters at that time.

The transmission spectrum through the cavity after filtering is shown in Figure 2.5. The structure evident in the transmission spectrum arises mostly from the cavity mirror reflectivity spectra. The light intensity through the cavity drops rapidly below 360 nm and is indistinguishable from the baseline below 300 nm.

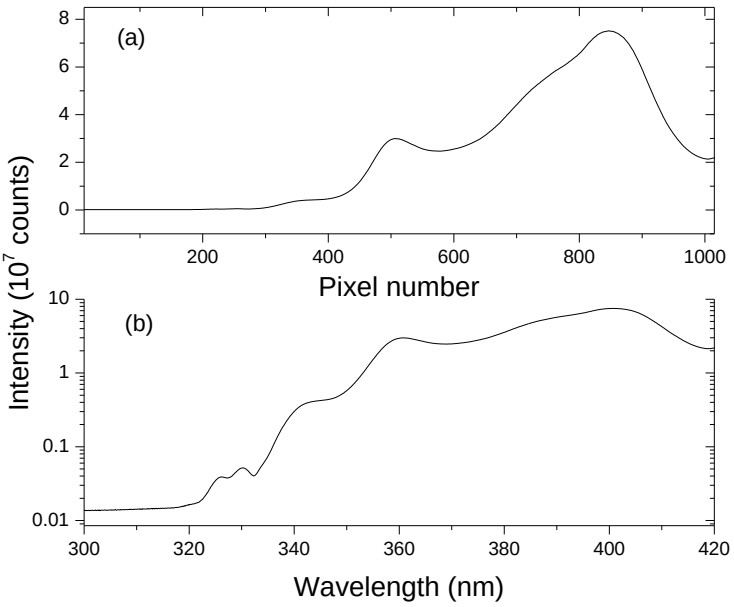

Figure 2.5 IBBCEAS light intensity spectrum through the clean chamber. (a) shows the linear intensity curve. The logarithmic intensity curve (b) shows where significant intensity is available in the spectrum. (a) and (b) show the same light output. The pixel number and corresponding wavelength is shown on the x-axis.

2.3.3. Wavelength calibration and instrument resolution

The spectrometer records intensity of the light against pixel number of the CCD detector. The wavelength window of the spectrometer was calibrated by mapping each pixel number to a corresponding wavelength value. A reference spectrum was obtained from a low pressure mercury/argon lamp, which emits several strong mercury and argon atomic emission lines across the ultraviolet and visible spectral

region. The emission lines from the calibration lamp are much narrower than the resolution of our spectrograph and have well characterised emission wavelengths, allowing the wavelength scale of the spectrometer to be calibrated accurately and the resolution of the instrument to be determined.

Light from an Ocean Optics HG-1 mercury/argon calibration lamp was coupled into the fibre cable and into the spectrograph. The resulting atomic emission spectrum Figure 2.6 was used for the wavelength calibration.

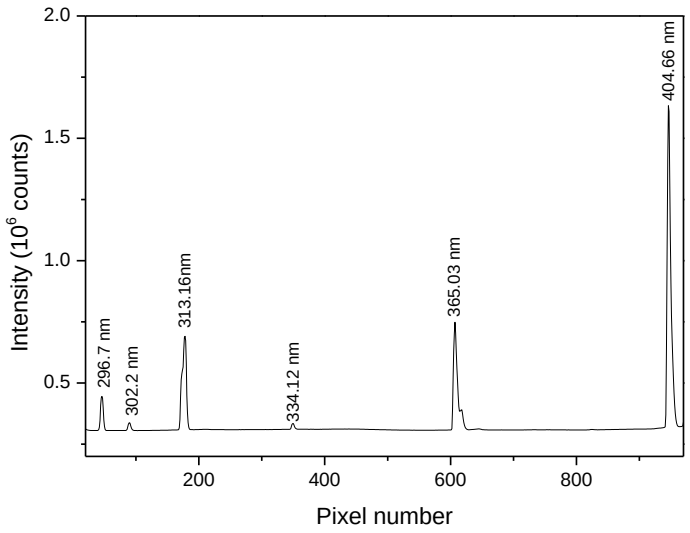

Figure 2.6 Atomic emission spectrum of the Hg-Ar lamp, showing the positions of the seven emission lines used to calibrate the spectrograph wavelength scale.

The Andor CCD software was used to assign the pixel numbers of each of the peaks to their corresponding wavelengths. The seven emission lines wavelengths and pixel positions in the atomic emission spectrum were fitted by a second-order polynomial fit, Figure 2.7. The R^2 value of 0.99998 for the pixel-wavelength mapping indicated the excellent agreement between the pixel positions across the wavelength region. The uncertainty in wavelength position after the calibration was the standard deviation for the linear fit. It was determined to be 0.13 nm.

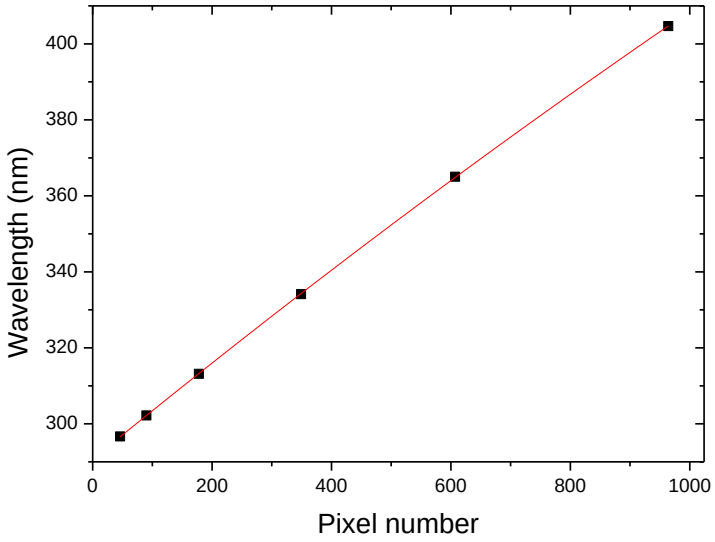

Figure 2.7 Linear regression of the pixel number/wavelength mapping of the peak maxima for six emission lines from the atomic emission lamp spectrum in Figure 2.6.

The spectral resolution of a spectrograph depends on the width of the entrance slit, the focal length, the size and dispersion of the diffraction grating and the detector pixel width. The spectral resolution for our IBBCEAS system was also determined using the calibration lamp. A Gaussian fit was applied to the atomic emission lines to determine the Full Width at Half Maximum (FWHM) of the line as observed through the spectrometer, Figure 2.8. The resolution of the spectrometer quoted by the manufacturers was 0.19 nm at 546 nm when used in conjunction with a CCD with pixel width of 13.5 µm and a 10 µm entrance slit. The CCD used in this work had a greater pixel width of 26 µm, while the width of the entrance slit was determined by the 100 µm diameter of the fibre bundle. With our spectrograph configuration, the measured resolution at 296.75 nm was 0.5 nm. Knowing the resolution of our spectrometer allows us to convolute higher resolution absorption cross section spectra from the literature to closely approximate the spectra recorded with our instrument. Origin graphing software was used for convolutions. Figure 2.9 illustrates the loss of finer detail from the original spectra after the convolution.

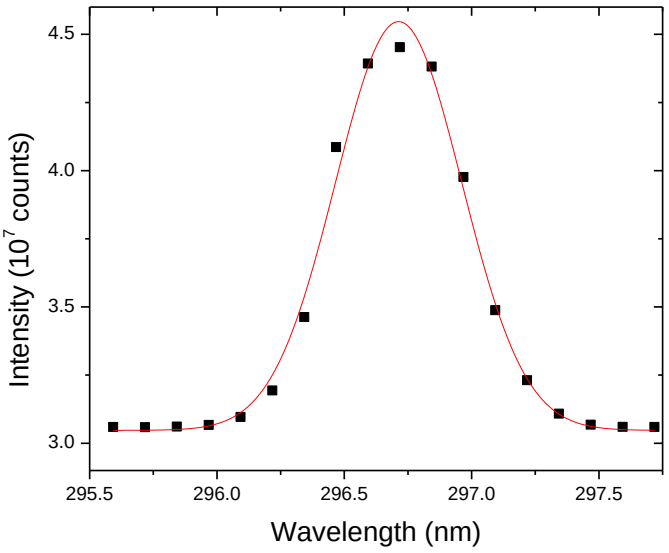

Figure 2.8 The black symbols show the measured atomic emission line spectrum of Hg through the Andor spectrometer. The red line is a Gaussian fit to the experimental spectrum. The resolution of the spectrometer is indicated by the FWHM of the peak. The width of this peak was also representative of emission lines at longer wavelengths.

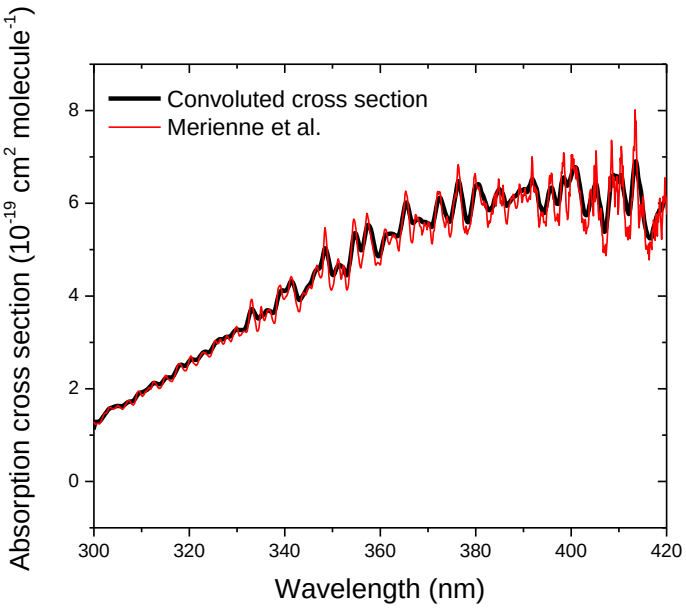

Figure 2.9 Comparison between the raw NO_2 absorption cross section from Merienne (red) and the processed, convoluted data (black) (11). Some of the sharper features in the original, higher resolution spectrum are not present in the convoluted spectrum.

2.3.4. Spectrometer

When using the IBBCEAS system, a number of steps were taken to ensure data quality. The effects of dark current in the CCD need to be minimized in the spectrometer. Dark current occurs due to thermally generated charge in the silicon lattice of the CCD, which increases strongly with temperature. The temperature of the spectrometer was kept at -40 °C over the course of each experiment to minimise the dark current. The spectrometer software enables the exposure time, number of accumulations and number of spectra recorded to be set. Each spectrum for these experiments was recorded over a 30 s period. This corresponded to 1261 accumulations of a 0.0084 s exposure each.

The optical filters that were in place in this system completely removed light below 300 nm. However during experimental monitoring it was noted that there was a measured intensity below 300 nm. This was assumed to be the result of longer wavelength light that had not been fully attenuated, affecting the spectrometer, through scattering or reflections within the spectrometer. The changes in intensities between 290 to 300 nm were used as a baseline for these experiments. The measured intensities between 290 and 300 nm were averaged and this was removed from the measured intensity at all other wavelengths. This can be seen in Figure 2.10. This was assumed to correct for possible changes in light intensity over time.

The above procedure assumed that the baseline changed uniformly across the spectrum. This is not necessarily the case and could introduce uncertainties in the measured spectra. In future work, drifts in the lamp spectrum could be monitored separately (for example, by having a split fibre optic cable that would measure the raw output of the light before passing through the chamber). This approach would allow spectral variations in the lamp output to be accounted for and more accurate absorption measurements to be made.

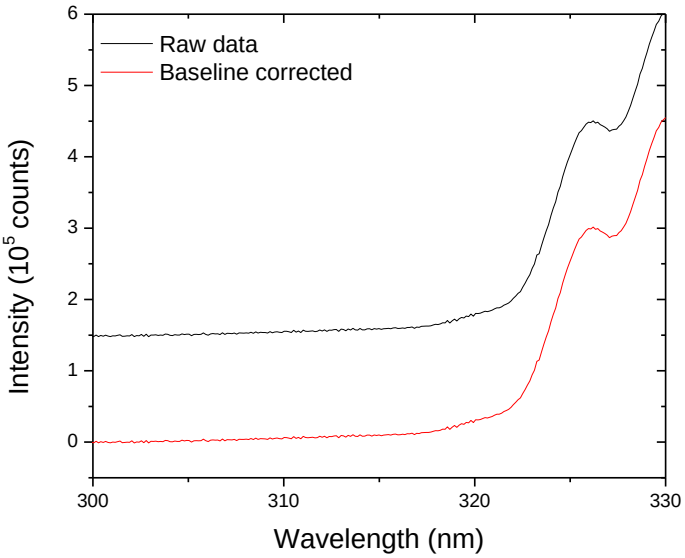

Figure 2.10 The difference between the raw data and the same data after the baseline correction is applied is shown here and shows the shift in intensity to zero below 300 nm.

2.4. Mirror reflectivity calibration

The IBBCEAS system can record very sensitive extinction measurements due to its artificially extended pathlength. The enhanced sensitivity of these measurements relies on a pair of highly reflective mirrors, whose reflectivity must be calibrated before quantitative measurements can be made. The high mirror reflectivity increases the path length of the optical cavity. This is known as the effective pathlength, L_{eff}:

$$L_{eff} = \frac{L}{1-R} \qquad (2.1)$$

where *L* is the length of the cavity and *R* is the mirror reflectivity. Based on the mirror manufacturer's reflectivity specifications, the 4.10 m long cavity would have an effective pathlength of up to 1333 m at 350 nm. In practice, optical cavities do not usually achieve this level of performance (Figure 2.11). The reflectivity of the mirrors was calibrated for each experiment to ensure that systematic errors from changes in the cavity alignment did not affect measurements. Several calibration approaches were used throughout this study and are described below.

The mirror reflectivity can be determined by measuring the absorption caused by a known concentration of an absorbing species with a well-documented absorption cross section. An absorbing species causes the intensity of the light transmitted through the cavity to drop. By measuring the intensities before and after the absorption, the mirror reflectivity can be retrieved from the absorption of a single compound using the following equation:

$$(1 - \mathrm{R})_{\lambda} = \frac{(\mathrm{NL}\,\sigma)}{\left(\frac{\mathrm{I}_0 - \mathrm{I}}{\mathrm{I}}\right)} \qquad \textbf{(2.2)}$$

where *R* is the mirror reflectivity, *N* is the number density of the calibration compound in the sample, *L* is the length through the chamber, *σ* is the absorption cross section, I_0 is the intensity of the light in a clean chamber and *I* is the intensity measured with the absorbing compound present. The mirror reflectivity therefore can be determined straightforwardly if the compound has a well-defined absorption cross section and its number density is known.

The number density can be measured with another instrument, or calculated from the amount of calibration compound added to the chamber volume, which must also be known. Although the volume of the chamber had previously been determined to be 3910 L, the FEP bag did not have a rigid shape and could change shape and volume during the flushing and use of the chamber. To compensate for any variation in chamber volume, *V*, the volume was taken into account in some experiments using a modified version of Equation 2.2:

$$\mathrm{V}(1 - \mathrm{R})_{\lambda} = \frac{(\mathrm{nL}\,\sigma)}{\left(\frac{\mathrm{I}_0 - \mathrm{I}}{\mathrm{I}}\right)} \qquad \textbf{(2.3)}$$

Here *V (1-R)* is the property calibrated and *n* is the number of molecules. This new formula was applied to absorption cross section measurements in which a known amount of sample was added to the chamber.

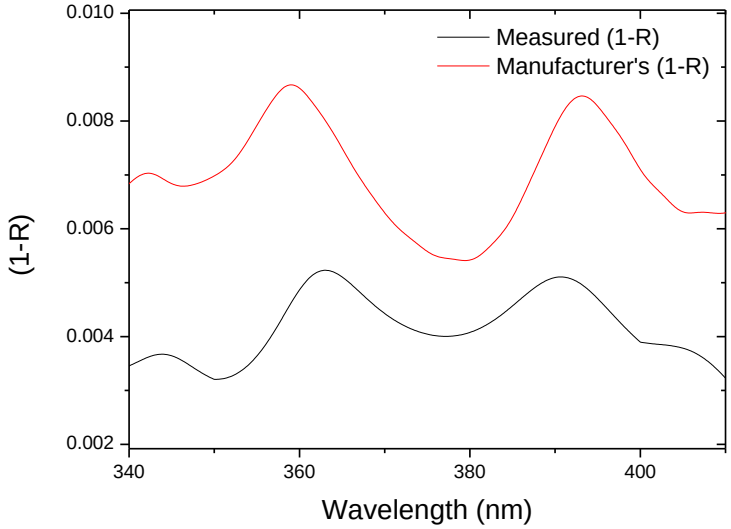

Figure 2.11 Manufacturer's (red) and measured (black) mirror reflectivity spectra, shown as (1 – R) in which higher reflectivities have lower values. The shape of the two reflectivity spectra match, although measured mirror reflectivities are lower than the manufacturer's values.

2.4.1. Nitrogen dioxide absorption

Nitrogen dioxide absorbs strongly across ultraviolet and visible wavelengths and has a characteristic, structured absorption. It is volatile (21 °C boiling point), readily available and is easily added into the chamber by injecting the gas through a septum into the chamber (12).

Spectra of the clean chamber were recorded for approximately 20 minutes prior to sample or calibrant addition. These spectra were used to determine I_0. NO_2 was added to the chamber from a gas tight syringe. NO_2 was added twice to test the reproducibility of the reflectivity determination. NO_2 absorbs light in a very structured way; this structure can be seen in Figure 2.12.

The scan number for I_0 and I were chosen based on the time profile of the fractional intensity change at a given wavelength, Figure 2.13. The two additions of NO_2 to the chamber are readily seen. The NO_2 mixing ratio in the chamber was stable for reasonably long times under most circumstances.

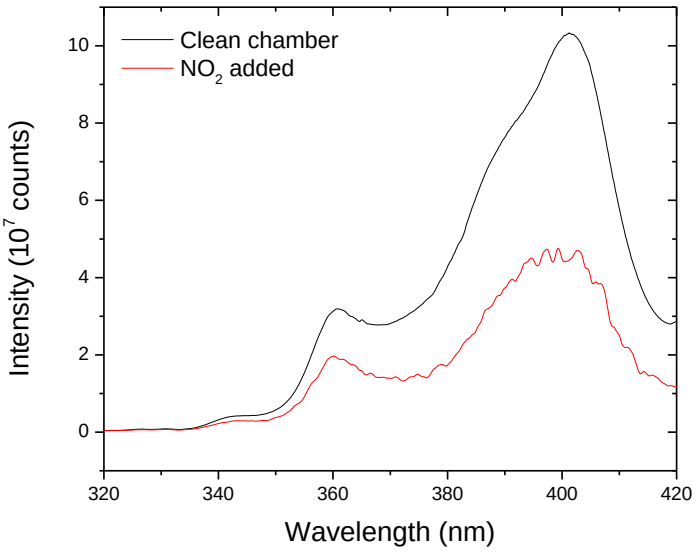

Figure 2.12 Spectra before (in black) and after (red) the addition of NO_2 into the chamber. Some of the structure of the NO_2 absorption in Figure 2.9 is visible in the small-scale structure in the red spectrum.

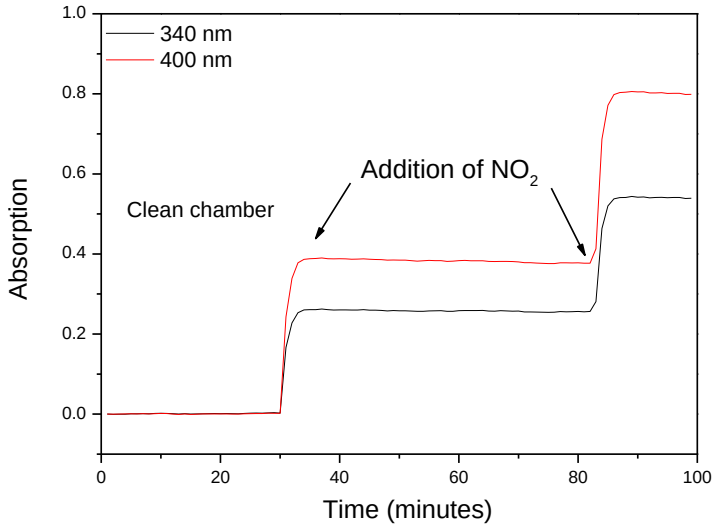

Figure 2.13 Time profile of the fractional intensity change in the chamber at two representative wavelengths, 340 nm and 400nm, showing the double addition of NO_2. The fractional intensity change differs between the two wavelengths but occurs simultaneously, as expected.

The reflectivity of the mirrors was calculated using Equation 2.3. The NO_2 concentration in the chamber was measured with the chemiluminescent NO_x detector. However, calibration with NO_2 had several disadvantages. This approach did not give a reliable measurement when other NO_x species were present. Moreover, chemiluminescent NO_x measurements are known to be subject to interferences (13). In addition, the NO_x detector was not operational for the majority of the experiments described. For this reason the absorption from NO_2 was used as a relative calibration in conjunction with an absolute calibration from another species.

2.4.2. Methyl vinyl ketone absorption

Owing to the disadvantages of NO_2 for calibration, a more reliable calibration compound was sought. Methyl vinyl ketone (MVK) was identified as a suitable calibration compound. It is a stable compound with a low boiling point (84 °C) allowing an accurate amount of MVK to be added to the chamber using the impinger (Section 2.6). MVK has a strong absorption across much of the region of interest, Figure 2.14. Its absorption is broad, reducing the need to convolute the spectra. Disadvantages of MVK are that its absorption drops to zero above 400nm, so MVK and NO_2 were used together to give an accurate, robust mirror reflectivity calibration that extended across the operating spectral window of the IBBCEAS system.

Mirror reflectivity calibrations based on MVK and NO_2 (using the chemiluminescent NO_x detector) produce consistent spectral features, but the absolute values of the mirror reflectivities varied (Figure 2.15). As discussed above, the NO_x detector is prone to interferences from other absorbing species, whereas the amount of MVK added was known to a high degree of accuracy, allowing a higher degree of certainty in the mirror reflectivity determination. The procedure followed therefore used MVK to calibrate the mirror reflectivity at 360 nm. A relative reflectivity spectrum was then determined using NO_2. This relative NO_2 reflectivity spectrum was smoothed and then scaled to match the absolute MVK reflectivity at the

selected wavelength. This approach gave an accurate absolute reflectivity measurement spanning the full wavelength range of the IBBCEAS spectrometer

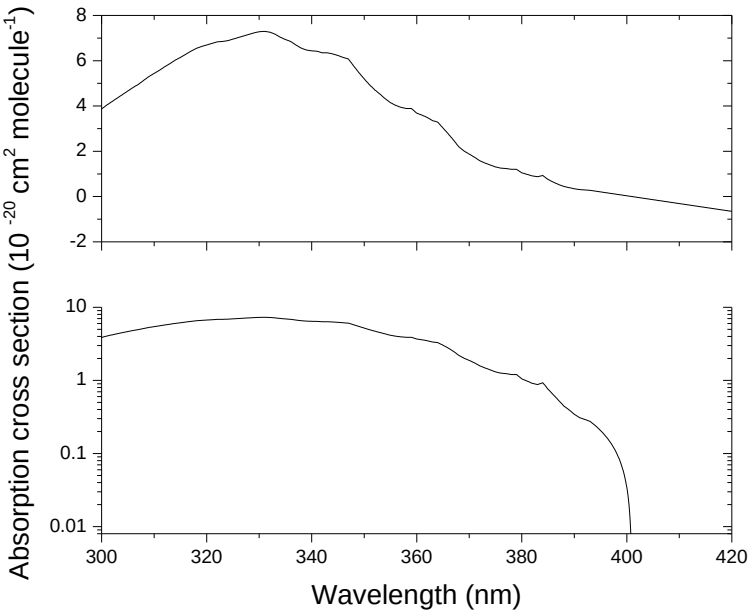

Figure 2.14 IUPAC recommended absorption cross section of MVK, as determined by Gierczak (14).

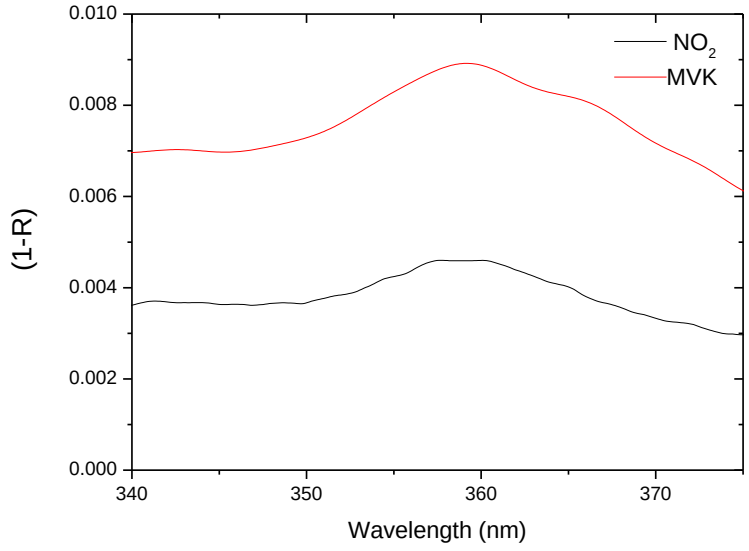

.

Figure 2.15 Mirror reflectivity spectrum determined by MVK (red) and NO_2 (black). Both calibrants give the same mirror reflectivity shape but the magnitudes differed.

2.4.3. Biacetyl absorption

For a number of experiments, high levels of ozone were present in the chamber. As ozone reacts rapidly with MVK across its double bond, a different calibration compound was needed. Biacetyl was found to be a suitable alternative: like MVK, it absorbed strongly in the near-UV, was sufficiently stable to be stored for long time, and volatile enough (boiling point of 88 ° C) to be easily added to the chamber. However, there are fewer biacetyl literature cross section values than for MVK and some differences in their shapes were noted particularly at shorter wavelengths (15; 16). These differences will be addressed in Chapter 3.

2.4.4. Calibration of mirror reflectivity before and after experiments

Mirror reflectivities were initially calibrated at the start of each experiment. The chamber had to be cleaned after these calibrations and prior further measurements. This procedure was time-consuming and there were concerns that the chamber was not thoroughly cleaned prior to introducing reactants. If so, the presence of residual compounds could potentially affect the experiment. Moreover, it was possible that mechanical vibrations while flushing the chamber could affect the alignment of the optical system. For these reasons it was preferable to calibrate the reflectivity after each experiment.

Before modifying the operating procedure, mirror reflectivity calibrations carried out at the start and at the end of the experiment were compared. The test case used was the formation of secondary organic aerosol (SOA) by the photolysis of 2-nitrophenol (2NP). The mirrors were calibrated in the morning and the chamber was then flushed with clean air for 4 hours. 2NP was added to the chamber, the chamber lights were turned on, and SOA was formed. These particles caused extinction in the chamber. After several hours the mirrors were re-calibrated using the same calibration process as the earlier calibration.

The two calibrated reflectivity spectra are compared in Figure 2.16. The overall shape of the reflectivity is the same for the morning and afternoon calibration.

However, there is a 15 % difference in the actual values. This was attributed to small changes in the optical alignment over the experimental period of 8 hours. Since most experiments were significantly shorter in duration than this experiment, changes in alignment were expected to be correspondingly smaller and the calibration was expected to be significantly more stable. Therefore, the post-experiment calibration timing was adopted.

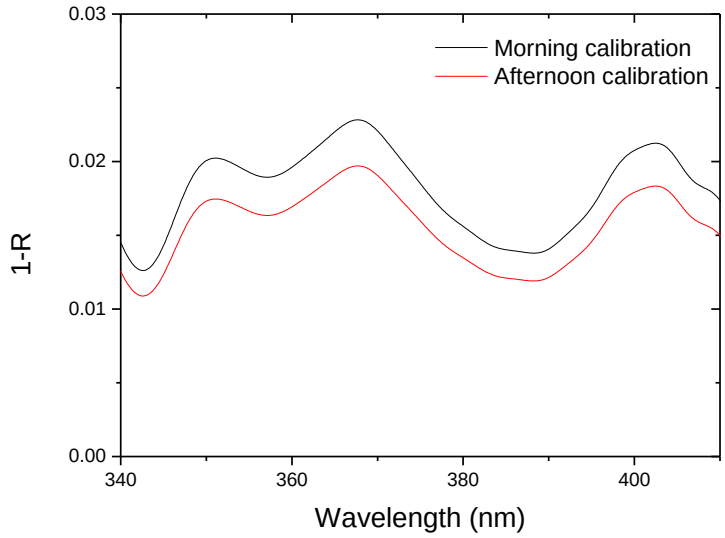

Figure 2.16 Mirror reflectivity spectra based on calibrations prior to (black) and after (red) an experiment in which SOA was formed. The shape of the reflectivity spectrum is the same for the morning and afternoon, with a 15% difference in the magnitude in the (1 – R) values.

2.4.5. Linearity of measured extinction

The concentration of absorbing or scattering species present in an optical cavity is known to reduce the effective pathlength of light in the cavity (17). When an absorbing compound is added rapidly to the chamber, the increase in sample absorption is quantified as the difference in absorption in the sample before and after the additional absorbing species was added:

$$\Delta\text{abs} = \text{abs}_{\text{after}} - \text{abs}_{\text{before}} \qquad \textbf{(2.4)}$$

This expression expands to:

$$\Delta\text{abs} = \left(\frac{I_0 - I_a}{I_a}\right) - \left(\frac{I_0 - I_b}{I_b}\right) \quad \textbf{(2.5)}$$

where I_0 is the intensity of light before any additions to the chamber, I_b is the intensity of light immediately before an addition of an absorbing species and I_a is the intensity of light after the addition on an absorbing species. Chen and co-workers, (6), showed that this equation simplifies to

$$\Delta\text{abs} = \left(I_0 \left(\frac{I_b - I_a}{I_b I_a}\right)\right) \quad \textbf{(2.6)}$$

When Equation 2.6 is substituted into Equation 2.3 we get

$$V(1 - R)_\lambda = \frac{(nL\sigma)}{\left(\frac{I_0 (I_b - I_a)}{I_b I_a}\right)} \quad \textbf{(2.7)}$$

This modification of the absorption calculation, to correct for the changing effective path length, should maintain the linear relationship between measured absorption and concentration. To test whether the measured extinction in the IBBCEAS system across the chamber was indeed linear, multiple additions of methyl vinyl ketone (MVK) were added to the chamber (Figure 2.17). A linear fit of the first three points had an r^2 value of 0.999. When compared with the fit for all 5 points, some deviation from linearity is evident at higher absorptions. The relationship between concentration and fractional intensity change becomes nonlinear for larger extinctions. In practice the relationship is linear up to a fractional intensity change of approximately 2.0, with retrieved values underestimated by about 15 % when the fractional intensity changes were 2.5.

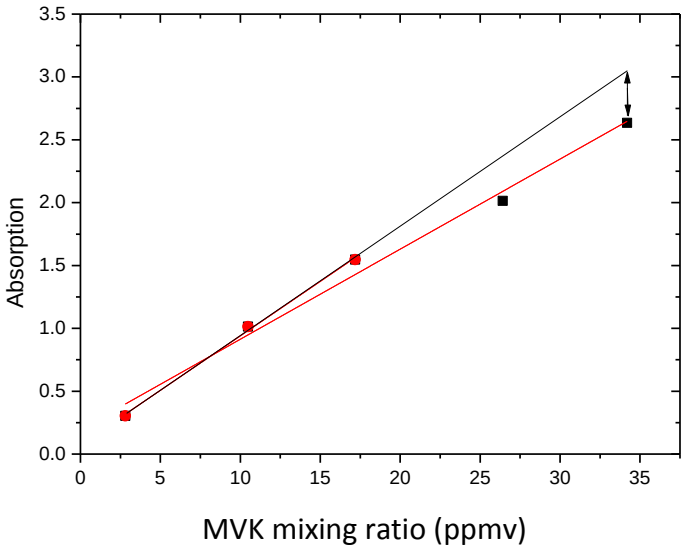

Figure 2.17 Relationship between the absorption (at 360 nm) and mixing ratio of MVK for a number of additions of MVK. The linearity breaks down when the absorption (or extinction) exceeds 2.

2.5. Validation of IBBCEAS

The IBBCEAS measurements were validated by comparing the absorption cross section determined for a well-known absorbing compound against reported literature data. Benzaldehyde was chosen as reference because it is volatile and has a structured absorption in the region of interest. The absorption cross section was determined using the IBBCEAS chamber system and compared to published spectra(6; 18). The compound was added to the chamber using the impinger method (Section 2.6) and the mirror reflectivity was calibrated. The absorption cross sections (σ) from the literature were compared to the cross section determined from this, Figure 2.18. There is a very close match between our values and those of Chen et al., especially below 370 nm. There are slightly higher values above 380 nm in the Chen data compared to that of this work. However, above 380 nm benzaldehyde has almost no absorption. The results from Xiang et al. only report values every 5 nm. As such, their spectrum does not capture the finer spectral structures. There is a good match below 355 nm and above 370 nm. The cross section determined via the IBBCEAS match previously reported cross sections

in both shape and magnitude, indicating the IBBCEAS system's ability to perform accurate measurements.

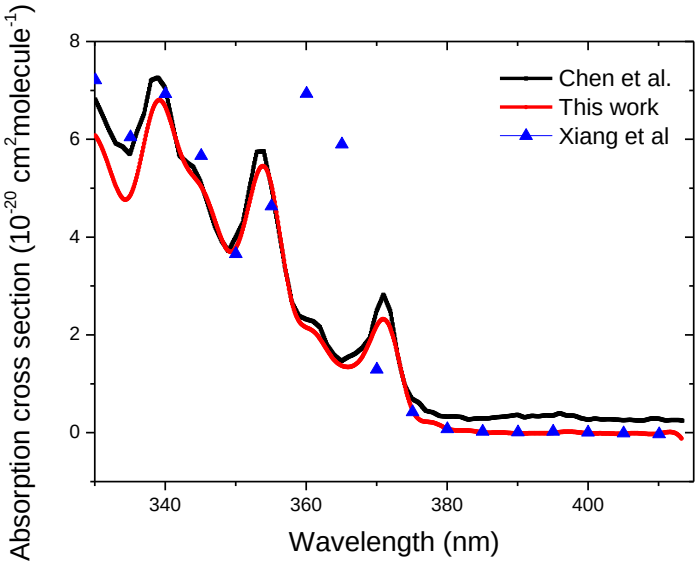

Figure 2.18 Absorption cross section of benzaldehyde determined in the chamber compared to literature cross sections of Chen et al. and Xiang et al. (6; 18).

2.6. Standard experimental procedure

The routine of most of the experiments discussed here followed a similar process: the empty chamber was monitored; one or more species were added to the chamber, the mirror reflectivity calibration was undertaken and the chamber was cleaned. The Xenon short-arc lamp of the IBBCEAS system was turned on and allowed to warm-up for 1 hour to ensure stable output of light. Prior to recording spectra through the chamber, the light beam into the cavity was blocked and a background spectrum was measured. The chamber was sealed tightly and the spectrometer covered to reduce the intrusion of ambient light into the spectrometer. The background spectrum was subtracted from spectra measured during the experiment. The first 20 minutes of spectra were of the clean chamber and were used to define the reference intensity, I_0, for the measurements. After this initial period, the calibration compound or sample was added to the chamber.

A glass impinger and glass vial were used for the addition of liquid and solid compounds, Figure 2.19. A known amount of the compound was added to a pre-weighed vial and the vial was connected to the impinger assembly. The exact mass of the compound in the chamber was determined from the difference in mass of the vial and impinger before and after the sample addition. The impinger was connected through a flange in the chamber side and secured with Swagelok fittings. The vial and impinger were then carefully heated with a heat gun. Care was taken to avoid overheating, which could result in pyrolysis, thermal decomposition, or the formation of particles. The whole impinger was heated evenly to prevent condensation of low volatility compounds onto cold surfaces. The vial and impinger were heated until the compound was fully in the gas phase. A stream of purified air carried the evaporated compound into the chamber. Not all the calibrants needed pre-treating to add to the chamber. Nitrogen dioxide is already a gas at room temperature and pressure; it was injected directly into the chamber.

In order to ensure the atmosphere inside the chamber was homogeneous in nature, two fans inside the chamber were turned on when a species was added. This speeded up the mixing of the chamber contents. However, the fans also increased the rate of wall losses and were therefore only turned on for 5 minutes before and after the introduction of sample compounds.

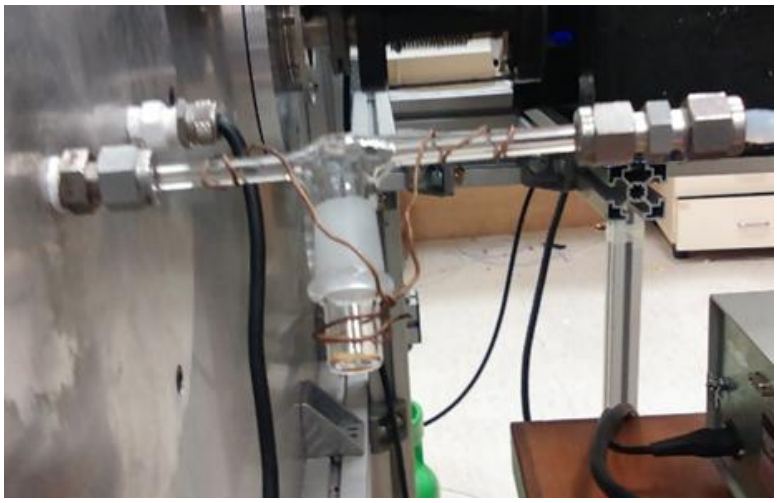

Figure 2.19 Close-up photograph of the glass impinger system connected to the side of the chamber (left side of picture). The sample is held in the glass vial underneath the impinger. The inlet air line is to the right.

For a number of experiments the relative humidity in the chamber needed to be increased. To increase the relative humidity inside the chamber, deionised water was heated in a three necked round bottom flask that was submerged in a water filled beaker on a hot plate, Figure 2.20. The heated sample water evaporated into a stream of dry air and passed through a water trap to ensure that no liquid water entered the chamber. It took approximately 90 minutes to raise the relative humidity of the chamber to 70 %. This process did not raise the temperature of the chamber appreciably.

Figure 2.20 The apparatus shown above allows the RH in the chamber to be increased in a controlled manner. The inlet on the left has laboratory air constantly flowing through it. This takes any water vapour directly out the outlet on the right, through a water trap, into the chamber.

2.6.1. Filter sample extraction

Numerous filter samples were collected for off line analysis. Ultra-high resolution mass spectrometry (UHRMS) was used to analyse the chemical composition of some chamber particles, while UV/Vis spectra of filter samples were used to study particle absorption. The resolution of the UHRMS was sufficiently high to determine

the stoichiometric formula for the components of the sample. UV/Vis spectrometry was used to measure the absorption caused by the species formed in the chamber. The filter holder was connected to the chamber via a denuder. A pump was used to extract sample air at a flowrate of typically 21 L min^{-1} from the chamber, Figure 2.21. The sample was passed through a denuder to remove any gas phase species present in the sample, and then through a heat-treated, grade 2500 QAT-UP 47 mm filter. The filters that were used were heated to 400 °C in a furnace for an 8 hour period to remove any impurities from the filter. Particulate matter was deposited onto the filters. The filters were wrapped in foil, sealed in Ziploc bags and stored in a freezer until further analysis.

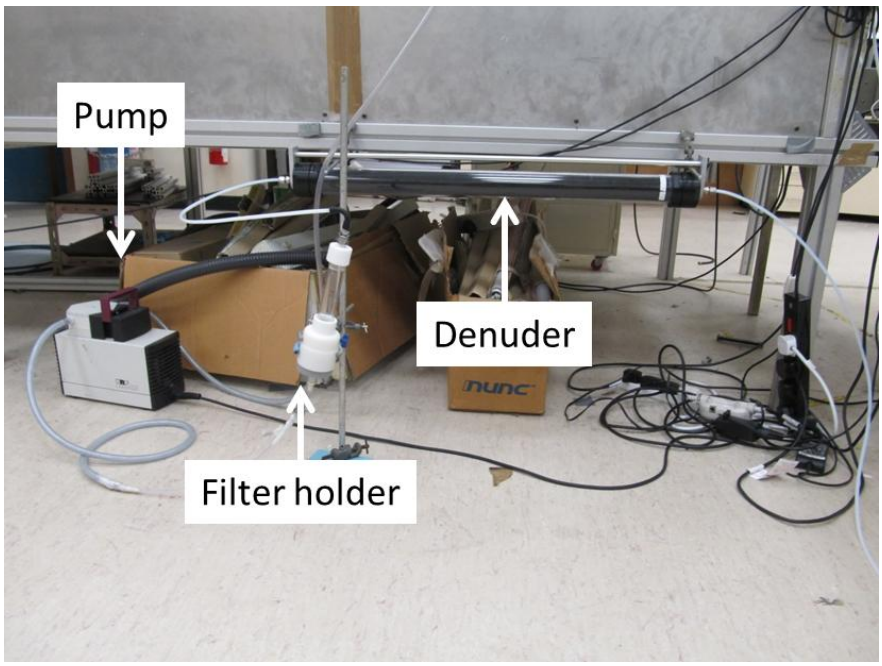

Figure 2.21 Set up used for collecting filter samples. The pump draws air from the chamber, through the denuder, and then the filter inside the filter holder. The flow rate of the extraction was set to 21 L min^{-1} and was checked at the beginning and end of each collection.

References

1. Akimoto H, Hoshino M, Inoue G, Sakamaki F, Washida N, Okuda M. 1979. Design and characterization of the evacuable and bakable photochemical smog chamber. *Environmental Science & Technology* 13:471-5
2. Carter W, Atkinson R, Winer A, Pitts J. 1982. Experimental investigation of chamber-dependent radical sources. *International Journal of Chemical Kinetics* 14:1071-103
3. Jeffries H. 1985. *Outdoor Smog Chamber Experiments to Test Photochemical Models: Phase II*. US Government Printing Office
4. Leone JA, Flagan RC, Grosjean D, Seinfeld JH. 1985. An outdoor smog chamber and modeling study of toluene–NO_x photooxidation. *International journal of chemical kinetics* 17:177-216
5. Stern JE, Flagan RC, Grosjean D, Seinfeld JH. 1987. Aerosol formation and growth in atmospheric aromatic hydrocarbon photooxidation. *Environmental science & technology* 21:1224-31
6. Chen J, Wenger JC, Venables DS. 2011. Near-ultraviolet absorption cross sections of nitrophenols and their potential influence on tropospheric oxidation capacity. *The Journal of Physical Chemistry A* 115:12235-42
7. Thüner LP, Bardini P, Rea GJ, Wenger JC. 2004. Kinetics of the Gas-Phase Reactions of OH and NO_3 Radicals with Dimethylphenols. *The Journal of Physical Chemistry A* 108:11019-25
8. Henry KM, Donahue NM. 2011. Effect of the OH radical scavenger hydrogen peroxide on secondary organic aerosol formation from α-pinene ozonolysis. *Aerosol Science and Technology* 45:696-700
9. Chen X, Hopke P. 2009. Secondary organic aerosol from α-pinene ozonolysis in dynamic chamber system. *Indoor Air* 19:335-45
10. Langridge JM, Ball SM, Shillings AJ, Jones RL. 2008. A broadband absorption spectrometer using light emitting diodes for ultrasensitive, in situ trace gas detection. *Review of scientific instruments* 79:123110
11. Merienne M, Jenouvrier A, Coquart B. 1995. The NO2 absorption spectrum. I: Absorption cross-sections at ambient temperature in the 300–500 nm region. *Journal of atmospheric chemistry* 20:281-97
12. Giauque W, Kemp J. 1938. The Entropies of Nitrogen Tetroxide and Nitrogen Dioxide. The Heat Capacity from 15 K to the Boiling Point. The Heat of Vaporization and Vapor Pressure. The Equilibria N_2O_4= $2NO_2$= 2NO+ O_2. *The Journal of Chemical Physics* 6:40-52
13. Dunlea E, Herndon S, Nelson D, Volkamer R, San Martini F, Sheehy P, Zahniser M, Shorter J, Wormhoudt J, Lamb B. 2007. Evaluation of nitrogen dioxide chemiluminescence monitors in a polluted urban environment. *Atmospheric Chemistry and Physics* 7:2691-704
14. Gierczak T, Burkholder JB, Talukdar RK, Mellouki A, Barone S, Ravishankara A. 1997. Atmospheric fate of methyl vinyl ketone and methacrolein. *Journal of Photochemistry and Photobiology A: Chemistry* 110:1-10
15. Plum CN, Sanhueza E, Atkinson R, Carter WP, Pitts JN. 1983. Hydroxyl radical rate constants and photolysis rates of alpha-dicarbonyls. *Environmental science & technology* 17:479-84
16. Horowitz A, Meller R, Moortgat GK. 2001. The UV–VIS absorption cross sections of the α-dicarbonyl compounds: pyruvic acid, biacetyl and glyoxal. *Journal of Photochemistry and Photobiology A: Chemistry* 146:19-27

17. Platt U, Meinen J, Pöhler D, Leisner T. 2009. Broadband Cavity Enhanced Differential Optical Absorption Spectroscopy (CE-DOAS)–applicability and corrections. *Atmospheric Measurement Techniques* 2:713-23
18. Xiang B, Zhu C, Zhu L. 2009. Gas-phase absorption cross sections of 2-nitrobenzaldehyde and benzaldehyde in the 285–400nm region, and photolysis of 2-nitrobenzaldehyde vapor at 308 and 351nm. *Chemical physics letters* 474:74-8

3. Gas phase absorption cross sections

3.1. Introduction

The electronic and nuclear structure of a molecule dictates how strongly light is absorbed and at what wavelengths the absorption occurs. The unique spectrum of this absorption is described by the absorption cross section, which can be used to identify a molecule and to quantify its concentration. Moreover, when the photolysis quantum yield is known, the absorption cross section is needed to determine the photolysis rate for the compound in a given radiation field.

The absorption cross section spectrum of a molecule differs somewhat depending on whether the molecule is in the gas phase or dissolved in a solvent. When a compound is in solution, the solvent interacts with it and alters its energy levels and broadens spectral features. Solvent interaction with the absorbing molecule affects the frequency, intensity or shape of the absorption and is termed solvatochromism (1). The polarity of the solvent influences these changes by altering the interaction, particularly with the excited state (2). This solvent interaction often lowers the energy required for a transition and produces a shift in the absorption spectra. When the excited state energy is lowered, the position of the absorption is red-shifted and is called a bathochromic shift (1). For example, the absorption peak of azobenzene occurs at 336 nm in acetonitrile but at 356 nm in dimethylformamide (3). This shift of 20 nm is large enough to significantly alter the amount of solar radiation that azobenzene would absorb in the near-UV, and could also affect the photolysis rate.

This chapter presents measurements of the gas phase absorption cross sections of a number of important atmospheric species. The 6 compounds that were studied were biacetyl, 1-nitronapthalene (1-NN), 2-nitrophenol (2-NP), acetaldehyde,

acenaphthylene and water. These are all compounds of atmospheric interest, either as major constituents of the atmosphere, as for water, as directly emitted species like biacetyl and the aromatic compounds, or as atmospheric oxidation products, like ethanal. These absorption cross sections are needed to quantify these species, calculate photolysis rates, and model their influence on radiative transfer.

There have been very few values reported for the vapour pressure of acenaphthylene. There is also very little agreement between these measurements which range from 9.12×10^{-4}, 6.8×10^{-4}, 3.6×10^{-3} and 1.67×10^{-2} mmHg (4-7). As acenaphthylene goes into the chamber easily and remains there in the gas phase for an extended period of time then we believe that the higher vapour pressures reported are more accurate.

Table 3.1 Molecular structures, purities, suppliers, and vapour pressures (at 25 °C) of the compounds measured in this chapter.

Name	Structure	Purity	Source	Vapour pressure (mmHg)
biacetyl	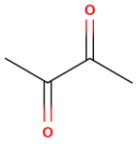	97 %	Sigma Aldrich	68.03
1-nitronaphthalene	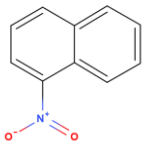	99 %	Sigma Aldrich	5×10^{-4}
2-nitrophenol	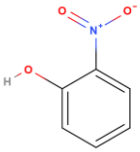	≥ 99 %	Fluka Analytical	0.113
acetaldehyde	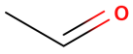	≥ 99.5 %	Fluka Analytical	740
acenaphthylene	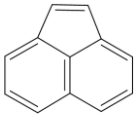	2 different purities: 75 % with 25 % acenaphthene and ≥ 99 %	Sigma Aldrich	9.12×10^{-4}
water		N/A	Purified deionised water	23.8

3.2. Biacetyl

There are a number of sources through which biacetyl is introduced into the atmosphere. It is formed by direct emissions from medium duty truck diesel engines and cigarette smoke (8; 9). Biacetyl is also formed as a product of ring cleavage of the NO_x-air photooxidation of aromatic hydrocarbons (10; 11). One of its major tropospheric loss processes is photolysis (12). It has four main photolysis products: carbon monoxide, ethane, methane, and acetone, which are all greenhouse gases (13).

Due to its broad absorption in the near-UV/Vis, its high vapour pressure, and its chemical stability, biacetyl was also one of the compounds used to calibrate the mirror reflectivity of the IBBCEAS system (as described in Chapter 2). As such, it is important to establish accurate values of the biacetyl absorption cross section. Three different experiments were undertaken to determine the absorption cross section of biacetyl. Mixing ratios between 5.97 and 7.6 ppmv of biacetyl were used for these experiments. These experiments allowed us to test the repeatability of the results obtained. We also checked the linearity of the IBBCEAS system to ensure that the results were not affected by instrumental artefacts or unexpected dimerization of the sample.

3.2.1. Results

Before the absorption cross section was determined, the linear relationship between concentration and absorption was examined. Over the course of a single experiment five different concentrations of the compound were added to the atmospheric simulation chamber. The temporal dependence of light intensity at 360 nm over the entire experimental period is shown in Figure 3.1.

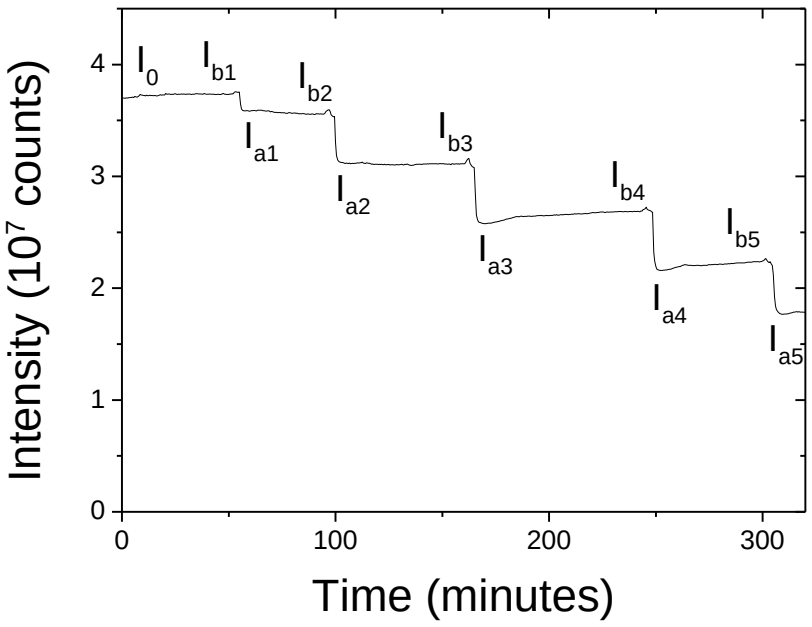

Figure 3.1 Temporal dependence of the intensity of light at 360 nm showing the initial reference intensity, I_0, and the intensities before, I_b, and after, I_a, addition of known volumes of biacetyl.

Each drop in intensity relates to an increase in the mixing ratio of biacetyl in the chamber. Initially the resulting intensity is stable after each addition. However, once the biacetyl concentration builds up following each addition, some of the biacetyl begins to partition to the walls. This can be seen by the slight increase in intensity between (for example) I_{a4} and I_{b5} in Figure 3.1. For this reason the intensity used to calculate the absorption was taken within a minute of each addition. This allowed time to ensure that biacetyl was homogeneously distributed within the chamber. The absorption was calculated using Equation 2.6.

Figure 3.2 shows that there is a linear relationship between absorption and concentration. The r^2 values reported indicate a high level of goodness of fit and the y-intercepts are close to zero. The linearity is slightly worse at shorter wavelengths because this is where the least light is present in our system. The low level of light, seen below 340 nm in Figure 2.5, results in smaller decreases in intensity and changes in the background light levels, which reduces the accuracy of absorption measurements at these wavelengths. Moreover, the absorption cross section of

biacetyl is quite weak below 350 nm, further complicating measurements in this spectral region.

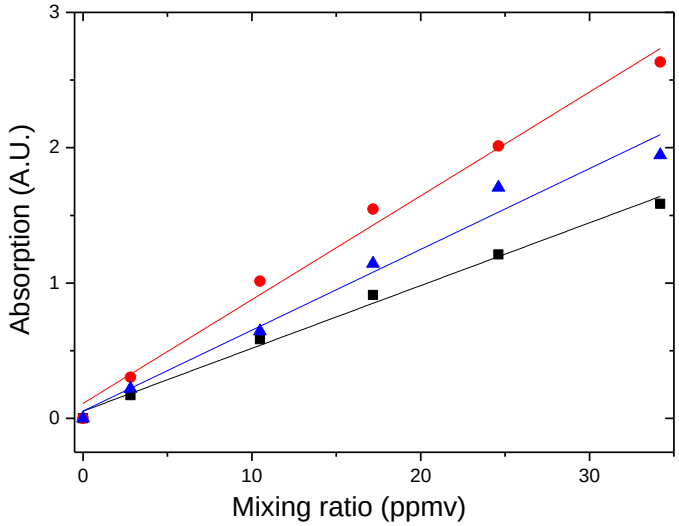

Figure 3.2 The linearity of the measured absorption in the chamber as a function of biacetyl mixing ratio is shown for the multiple additions of biacetyl. Three wavelengths are shown: 340 nm (black), scaled by a factor of 10, 380 nm (blue) and 405 nm (red). The r^2 values are 0.990, 0.997 and 0.995, respectively.

Equation 2.7 describes the relationship between the absorption measured with the IBBCEAS and the values for the absorption cross section. Rearranging the formula in terms of the absorption cross section gives:

$$\sigma = \frac{V(1-R)(I_0\frac{(I_b-I_a)}{(I_b*I_a)}}{nl} \qquad (3.1)$$

where σ is the absorption cross section (cm^2 $molecule^{-1}$), V is the volume of the chamber, R is the mirror reflectivity, I_0 is the intensity before any compound is added, I_b is the intensity before the compounds of interest was added, I_a is the intensity after the compound is added, n is the number of molecules of the absorbing compound and l is the length of the cavity (cm). The mirror reflectivity is determined for each experiment.

The absorption cross section was determined for the three concentrations of biacetyl and is shown in Figure 3.3. There was good agreement between the values despite the different concentrations and the measurements being taken on different days, showing the good repeatability of the results.

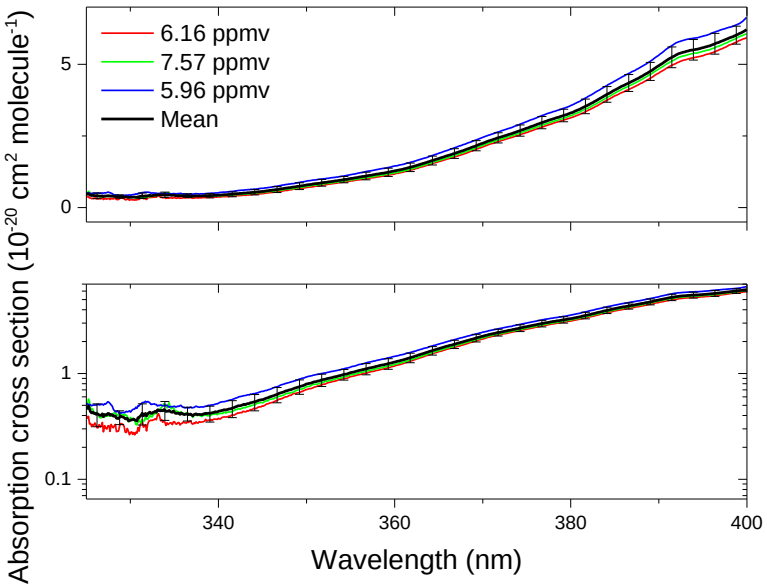

Figure 3.3 The absorption cross section spectrum of biacetyl determined from three different experiments. The average of the measured spectra is shown in black.

The absorption cross section increases strongly in going from shorter to longer wavelengths. Figure 3.3 shows that there is a 20-fold increase in absorption between 330 nm and 400 nm. The errors bars present in the above graph are based on the standard deviation of the averaged results. The consistency of the measurements is apparent. There is a standard deviation of 16 % at 340 nm and 6 % at 400 nm between the three measurements.

There have been a few measurements of the biacetyl absorption cross section reported in the literature. These are compared to the results of this work in Figure 3.4. The overall shape of the absorption spectrum in Figure 3.4 agrees very well with the other absorption cross section spectral shape. The magnitude of our measured cross-section is somewhat higher than literature spectra. As can be seen

in the log plot in Figure 3.4, with the exception of the values by Plum et al. below 350 nm, our values are higher than previously reported values. The values by McMillan et al. arise from a personal communication to the editor of a photochemistry textbook from 1966 (14). As such, it was not possible to assess the quality of the data. The measurement by Horowitz et al. was taken under 0.5-1.0 Torr of pressure (15). This is far lower than the ambient pressure (ca. 760 Torr) during our measurements, although the pressure should not strongly affect the magnitude of the absorption cross section in this spectral region. Increased pressure can cause a broadening of narrow spectral features, e.g. for vibrational absorption lines (16). The measurements made by the Plum group were taken in an atmospheric simulation chamber at 298 ± 2 K and 3-13 Torr (12). There is therefore no clear and apparent reason for the increase in the magnitude of the cross section, but we note that the spectrometer has been validated against a structured compound, benzaldehyde. As a consequence, there is some confidence in the reasonableness of our values.

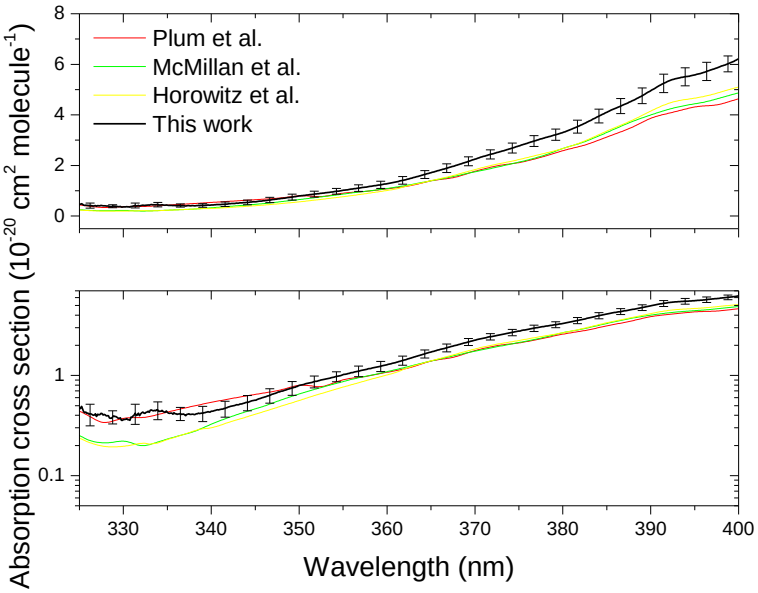

Figure 3.4 A comparison of the absorption cross section spectra of biacetyl measured in this work and in other studies [7, 8, 9].

3.3. 1-Nitronaphthalene

1-nitronaphthalene (1-NN) is a polycyclic aromatic hydrocarbon (PAH) composed of two connected benzene rings and a nitro group in the 1 position. It has been observed in the atmosphere in a number of locations all over the world, including California, Marseille, Birmingham and Damascus (17-19). One of the reasons that 1-NN has been so widely studied is that it has well documented effects on human health. Studies have shown that 1-NN has carcinogenic properties and also increases the mutagenic activity of the atmosphere (20; 21). Nitro-PAHs, including 1-NN, have been found to increase the mutagenicity occurring in the modified *Salmonella typhimurium* assay used. This test is widely used to determine the tendency of a chemical to cause mutations in DNA (22). Nitro-PAHs and amino-PAHs alter the cytokine and chemokine responses in human bronchial cells, and 1-NN has also been found to cause pulmonary and hepatic toxicity in rats (23; 24).

As 1-NN has potential to adversely impact public health, there have been widespread studies of its sources and abundance. 1-NN is amongst the most abundant nitro-PAHs in the atmosphere. The major contribution of 1-NN to the atmosphere comes from the exhaust of light and heavy diesel engines (23-26). There has been some concern that the PAHs measured in diesel exhaust were not a real product but an artefact (27). This has led to precautions being taken in a measurement campaign for nitro-PAHs. Sampling was carried out in a busy road tunnel and in the city centre in Birmingham, UK and also on the roof of a 20 m high building in the centre of Damascus, Syria (17). A study has found that the amount of nitro-PAHs formed as artefacts during the sampling process is only 2-3 % (19). Gas chromatography has been used to confirm the presence of 1-NN and 2-NN in diesel emissions (28). Measurements in Redlands, California recorded 1-NN at 424 pg m^{-3} and 1906 pg m^{-3} for day and night time levels respectively, while measurements in Marseilles in July 2004 showed that 1-NN accounted for 30-50 % of the total nitro-PAH concentration (19; 29). Sample sites included an urban environment, a suburb and the countryside. As expected, concentration differences were found

between the three locations with the urban at 208 pgm^{-3}, sub-urban 176 pgm^{-3} and rural 9.7pgm^{-3} (19). These results would reflect the contribution of diesel engines to 1-NN concentrations. 1-NN can form in the atmosphere as a product of the reaction between naphthalene and OH or NO_3 in the presence of NO_2 or from dye manufacture (25; 30). As photolysis is one of main loss processes for 1-NN in the troposphere, the absorption cross section for the compound in the gas phase is an important property, along with the quantum photolysis yield, in determining the lifetime and radiative contributions of 1-NN (21).

3.3.1. Results

1-NN is a yellow solid at room temperature, with a melting point between 59-61 °C and a boiling point of 304 °C. Large crystals can form during storage. In our experiments, the crystals were crushed using a pestle and mortar before putting into the impinger. This ensured the largest possible surface area and aided in vapourising the sample. Owing to its very low vapour pressure, however, 1-NN proved difficult to add to the chamber and it deposited quickly to the walls (Table 3.1). As the concentration of 1-NN in the gas phase decreased rapidly, its absorption was determined at the time immediately after the addition as the I_b (Figure 3.5). This did not allow the compound to be fully homogeneously distributed in the chamber nor did it account for losses during the addition of 1-NN. A number of different concentrations of 1-NN were used to calculate the cross section. Owing to the uncertainty in the concentration of gas phase 1-NN, the uncertainty in the magnitude (but not the spectral shape) of the absorption cross-section is correspondingly large. Figure 3.5 shows the absorption time profile following multiple successive additions of 1-NN to the chamber. The absorption starts to fall immediately following each addition, and the rate of the decrease is more rapid at higher concentrations. This drop in absorption is due to the loss of gas phase 1-NN to the chamber surfaces.

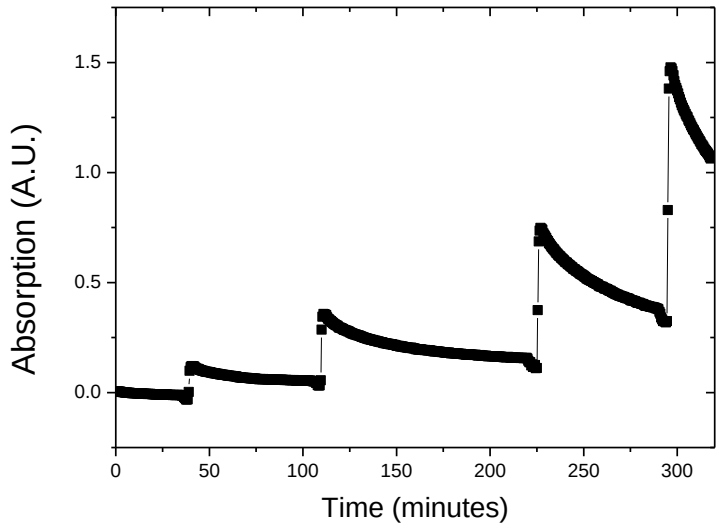

Figure 3.5 Time profile for absorption at 345 nm for four additions of 1-NN. The rate of loss of 1-NN to chamber surfaces increases at higher concentrations of gas phase 1-NN, as indicated by the higher absorption.

Figure 3.6 shows the variation in measured absorption cross sections of 1-NN. The spectral shape is consistent across all the measurements, with maxima at shorter wavelengths, a shoulder at 340 nm and a tail that tends towards zero above 400 nm. This large absorption is typical of nitrated aromatics as the nitro group shifts the absorption of the benzene ring to longer wavelengths. The loss of 1-NN to the chamber walls would lead to an overestimation of the number of molecules of gas phase 1-NN, and would thereby artificially lower the value for the cross section. For this reason, the highest measured cross section (for the addition of 112 ppbv in Figure 3.6) is likely to be closer to the true value of the absorption cross section. The standard deviation is between 6 and 14 %, at 340 and 400 nm, respectively, of the mean absorption cross section, despite a range of additions that span almost an order of magnitude in concentration. Considering the challenges of introducing 1-NN into the chamber and the rapid changes in absorption following the introduction, we consider the mean spectrum to be a reasonable estimate of the 1-NN absorption cross section within its stated uncertainty. Nevertheless, over-estimating the concentration of 1-NN in the chamber is likely to give our

measurements a negative bias that should be borne in mind when using this cross section.

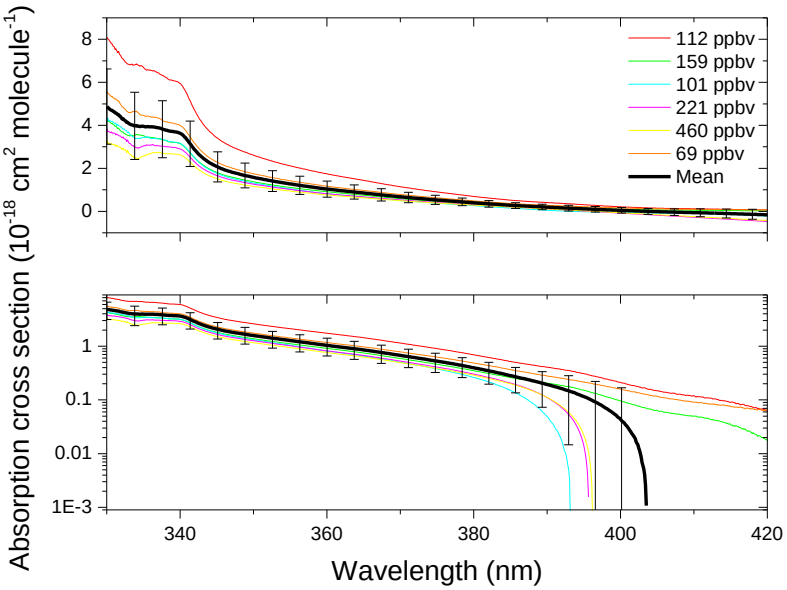

Figure 3.6 Absorption cross section spectrum of 1-NN obtained in multiple experiments. The mean of the spectral measurements is shown in black.

A series of UV/Vis solution phase measurements were also made for this compound. A 2.8 x 10^{-4} M stock solution of 1-NN and hexane was made in a volumetric flask and sonicated for 5 minutes to ensure the total dissolution of 1-NN. From the stock solution, five different concentrations were created with 80, 60, 40 and 20% stock solution and the remainder was made up with the hexane solvent. Measurements of samples in quartz cuvettes were carried out in a Thermo Scientific Evolution 60 UV/Vis spectrometer. Each measurement consisted of a reference measurement of pure hexane along with one of the samples. After each sample was measured, the resulting absorbances were plotted against concentration for each wavelength (Figure 3.7).

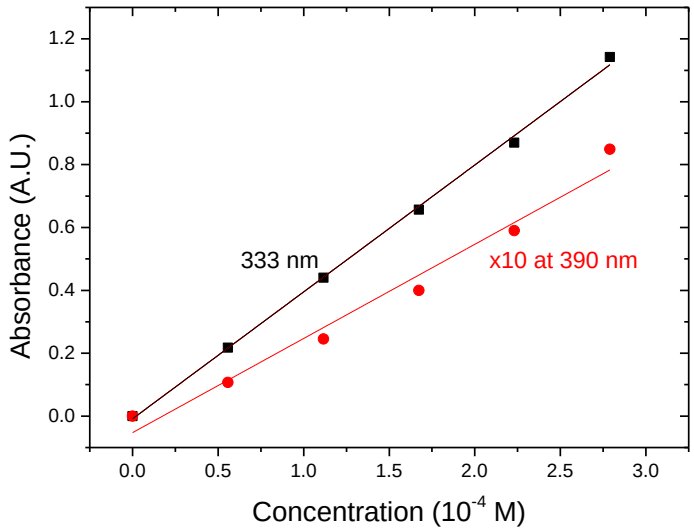

Figure 3.7 Absorbance of 1-NN in hexane for five different concentrations in solution. The graph represents the absorbance at 333 nm, which is close to the absorption maximum, and at 390 nm, at which absorption is an order of magnitude weaker. The r^2 values for the linear fits are 0.999 and 0.988, respectively.

As shown in Figure 3.7, there is a linear relationship between absorbance and concentration in accordance with the Beer-Lambert law. For solution spectra, this relationship is conventionally written as:

$$A = \log_{10} \frac{I_0}{I} = \varepsilon l c \qquad (3.2)$$

where A is absorbance, I_0 is the intensity of the reference and I is the intensity through the sample, ε is the molar absorption coefficient (L mol^{-1} cm^{-1}), l is the length of the cuvette (1 cm), and c is the concentration of the sample ($molL^{-1}$). The molar absorption coefficient is determined by the slope of this line. This property can be expressed as an absorption cross section (σ), which is more commonly used to describe the gas phase absorption of a compound:

$$\sigma = \frac{\ln 10 \varepsilon}{N_a} \qquad (3.3)$$

where N_a is the Avogadro's number. The gas and solution phase absorption cross sections are compared in Figure 3.8. The shape of the absorption is similar, including shoulders at 340 nm (gas) and 360 nm (hexane) and a gradual decrease in

absorption towards longer wavelengths. There is a significant difference between the magnitude of the gas and solution phase absorption cross section, with the gas phase cross section a factor of 2 to 4 smaller than the solution phase. The maximum of the solution phase measurement appears at 325 nm, but no maximum is evident in the gas phase within the spectral range of the IBBCEAS system. As the maxima was not determined in the gas phase we cannot be sure that the solution phase measurement is not red shifted.

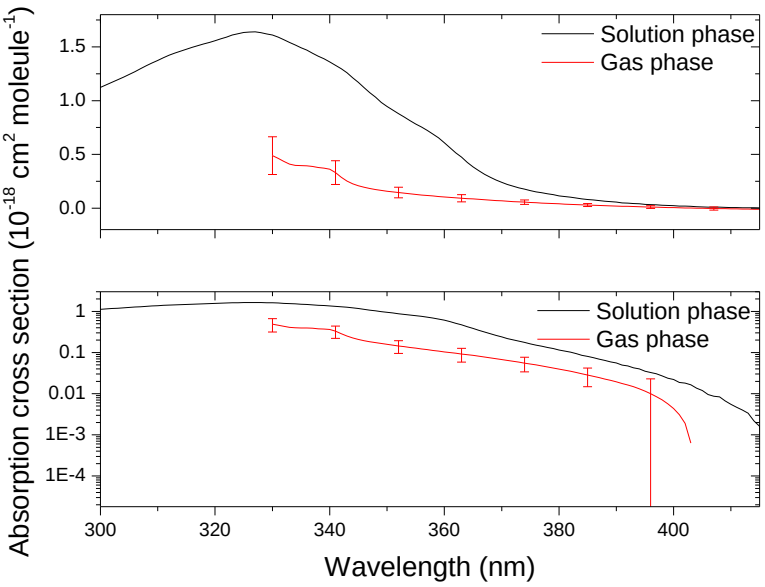

Figure 3.8 The gas phase and solution phase absorption cross section for 1-NN. The difference in magnitude between the two is apparent.

Zugazagoitia et al. have reported the solution phase cross section of 1-NN in a number of different solvents (31). These solvents ranged from non-polar (cyclohexane) to more polar solvents such as methanol, pentanol and acetonitrile. Our spectrum in hexane is compared to their spectrum in cyclohexane in Figure 3.9. The magnitudes of the absorption cross sections are very similar at the maxima. The absorption spectrum of Zugazagoitia and co-workers extends to longer wavelengths, probably a result of the slightly higher polarity of cyclohexane compared to hexane used in our study. In both cases, the solution phase absorption cross sections are appreciably larger than the gas phase cross section shown in Figure 3.6.

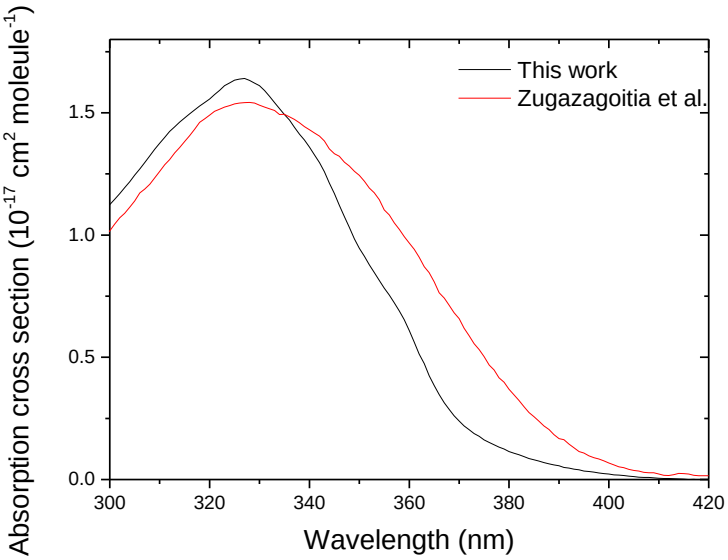

Figure 3.9 The 1-NN/hexane solution absorption cross section is compared here to that reported by Zugazagoitia et al. for 1-NN in cyclohexane(31).The magnitudes of the absorption maxima agree closely, although a slight red shift is seen in the cyclohexane solution. The polarities of hexane and cyclohexane are 0.1and 0.2, respectively.

As discussed above, obtaining a consistent absorption cross section for gas phase 1-NN was subject to significant negative bias owing to fast deposition to the walls. Nevertheless, the observed difference in magnitude of between the gas phase and solution cross section is probably too large to arise from this source, and the gas phase absorption cross section of 1-NN is still expected to be significantly lower than that of the solution phase. As a consequence, calculating the photolysis lifetime of 1-NN on the basis of the solution phase cross section would considerably underestimate the photolytic lifetime of the species and demonstrates the value of the gas phase absorption cross sections.

3.4. 2-Nitrophenol

Like 1-NN, 2-nitrophenol (2-NP) has a long history of being monitored in the atmosphere. It was first observed in rainwater in 1975 (32). 2-NP has phytotoxic properties, and causes headaches, respiratory problems and a reduction in the oxygen-carrying capacity of blood (33-35). Direct emission sources for 2-NP include

coal and wood combustion, and production of pharmaceuticals, disinfectants and explosives (33). A significant portion of the 2-NP in the atmosphere has been attributed to vehicle emissions. Nojima et al. measured 2-NP mixing ratios of 3.1 ppbv in petrol engine exhausts and 6.4 ppbv in diesel engine exhausts (36). By monitoring the ratio of benzene, a known tracer of exhaust emissions, to 2-NP at the source and in the atmosphere, the 2-NP was deemed come from vehicular exhausts. In addition, atmospheric nitration of phenols is an indirect source of 2-NP, occurring either via night-time reaction with NO_3 radicals (37; 38).

The concentrations of 2-NP changes dramatically with location and local sources have a major impact on the prevalence of a compound. A number of monitoring campaigns have been undertaken in a variety of locations. In Portland, Oregon, 2-NP was found at average concentrations of 58.5 ng L^{-1} and 24 ng m^{-3} in rain and air respectively over a seven day period (39). In contrast, a much lower gas phase concentration of 0.8-6.4 ng m^{-3} was observed at Great Dun Fell, a remote monitoring site in the English Pennines. These concentrations were lower than other European sites, likely owing to the site's remoteness (40-42).

The photophysical properties of 2-NP and other nitrated aromatics have received significant interest (43-45). The relatively long wavelength absorption of 2-NP is due to a combination of the delocalisation of the electrons around the benzene ring and the influence of the lone pairs on electrons on the OH and nitro groups. Some researchers have suggested that photolysis of 2-NP could alter the concentration of nitrous acid, HONO, in the atmosphere (43). The formation of HONO has previously been observed in the solution phase (46). Measured concentrations of HONO in the atmosphere exceed predicted concentrations based on known sources and sinks, and photolysis of 2-NP was proposed as a new gas phase source for HONO (43; 47). HONO is important in atmospheric chemistry because it is a photolytic precursor for the OH radical. Other researchers have observed instantaneous formation of HONO after the photolysis of 2-NP in a reaction flow tube (43). In addition, Chen et al. have proposed that the large absorption by 2-NP may have a significant impact on the available actinic flux when 2-NP concentrations are high. This attenuation of the actinic flux would slow primary photochemical processes, particularly in urban

environments (42). For these reasons the near-UV absorption cross section of 2-NP remains an important property that determines its environmental fate and impact.

3.4.1. Results

A number of experiments were carried out to determine the absorption cross section of 2-NP. Six different mixing ratios (41, 59, 81, 100, 126, 200 ppbv) were used to ensure that there was no concentration or other systematic effects in the measurements. Unlike 1-NN, there were no issues adding the 2-NP to the chamber in a reliable and consistent way because the vapour pressure of 2-NP is much greater than that of 1-NN. Figure 3.10 shows the linear relationship between the mixing ratio of 2-NP and its absorption. There is no evidence for concentration effects, such as dimerization, present during these experiments. These absorptions were used to calculate the absorption cross section.

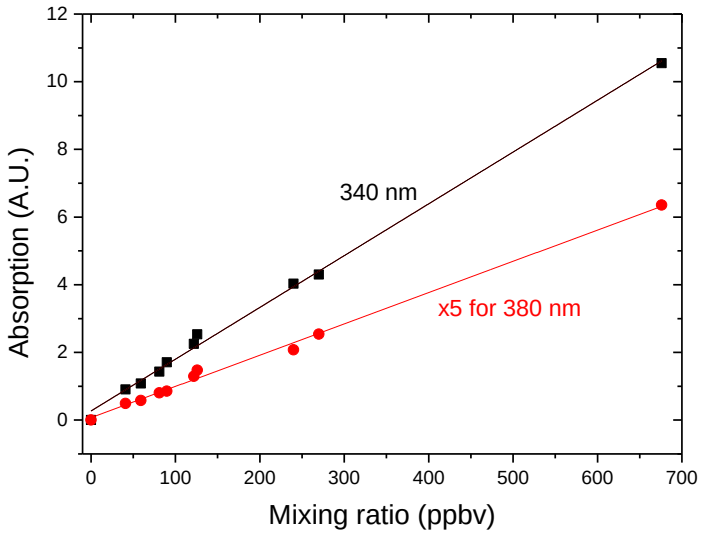

Figure 3.10 Mixing ratio dependence of the absorption of gas phase 2-NP at 340 nm (black squares) and 380 nm (red circles). The r^2 values of the linear fit were 0.999 (340 nm) and 0.998 (380 nm). Both wavelengths exhibit a strong linear relationship between mixing ratio and absorption.

The absorption cross section of 2-NP has an absorption maximum at 339 nm and the absorption tails off quite slowly at longer wavelengths, extending into the

visible, Figure 3.11. The magnitude of the absorption is very large near the maximum and is comparable to ozone at its absorption maximum at 254 nm (48).

There is a small drop in the absorption between 330 and 335 nm, although this feature is less certain owing to the weak light levels in the IBBCEAS system at this wavelength. A solution phase absorption cross section was measured in hexane in a similar fashion as for 1-NN. Its linear absorbance and concentration relationship is displayed in, Figure 3.12, and the gas and solution phase absorption cross section are compared in Figure 3.13. The magnitudes of the solution and gas phase cross sections are quite similar at their respective maxima. The absorption bands have similar shapes and no fine vibronic structures. The solution phase measurement is red shifted by about 20 nm relative to the gas phase. As the IBBCEAS measurements are of the gas phase compound, the observed shift in the solution spectra indicate the effect of the solvent molecules on the energy levels of the ground and excited states of 2-NP. The solution phase absorption cross section spectrum of 2-NP is therefore a poor approximation of the position and magnitude of that in the gas phase, highlighting the importance of measuring the gas phase absorption spectrum of species that occur to a significant extent as gases with sufficient vapour pressure.

There is only one previously recorded gas phase absorption cross section value for 2-NP in this region, which was made in our group using a modified IBBCEAS system, Figure 3.14 (42). One reason for the lack of other measurements is that the low vapour pressure of the compound results in large wall losses in typical flow spectrometers, making it difficult to estimate the concentration. The overall shape of the two cross sections is similar, although the magnitude of our spectrum is somewhat lower than that of the measurements reported by Chen et al. There are also two small shoulders in the measurements made by Chen et al. at 354 and 373 nm that are not evident in either our gas phase or solution phase spectra. Chen et al. state that these features do not correspond to artefacts arising from mirror structure. However, on the basis of our results for the 2-NP SOA where some residual mirror structure is apparent, it is possible that small artefacts from the mirrors may be responsible for these shoulders.

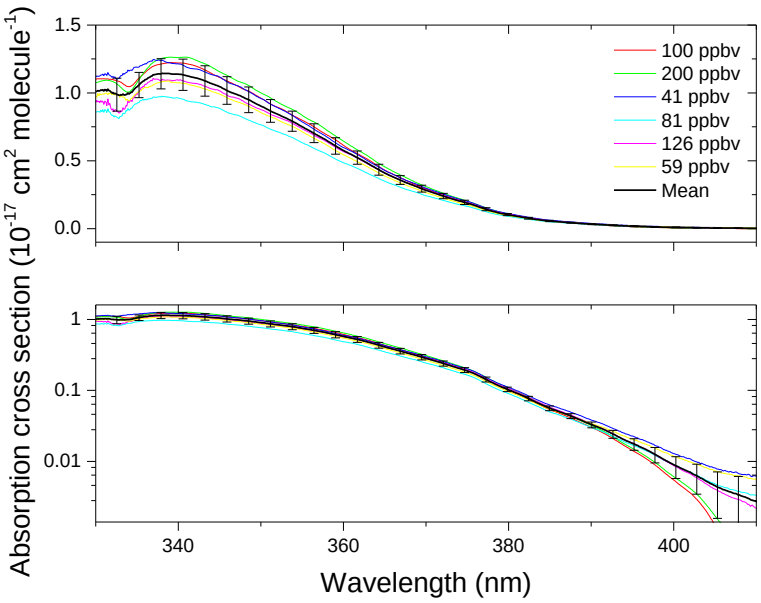

Figure 3.11 Absorption cross section spectra for the six measurements of 2-NP, along with the mean and standard deviation of the measurements.

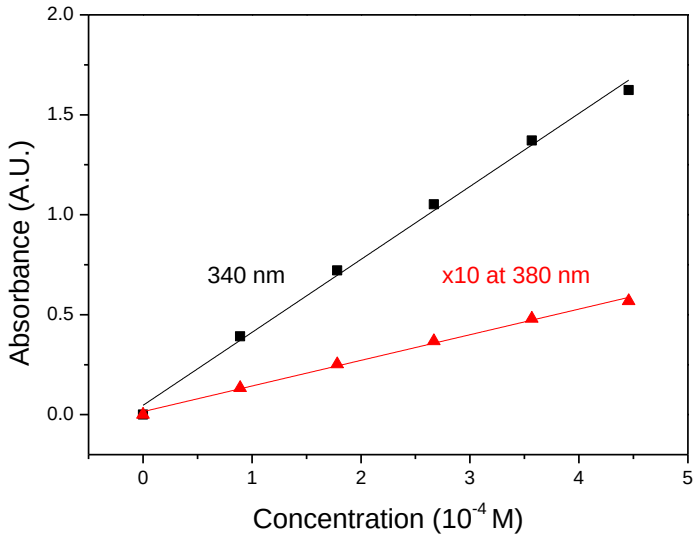

Figure 3.12 Absorbance vs concentration for 2-NP/hexane solution at 340 nm (black) and 380 nm (red). Values of r^2 for the linear regression were 0.997 (340 nm) and 0.998 (380 nm).

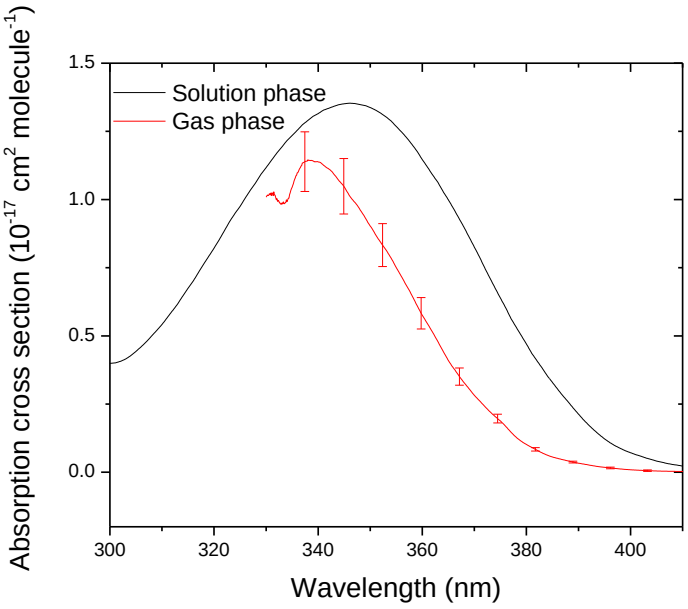

Figure 3.13 Comparison of the cross section of 2-NP in the gas phase (red) and in solution phase in hexane (black).

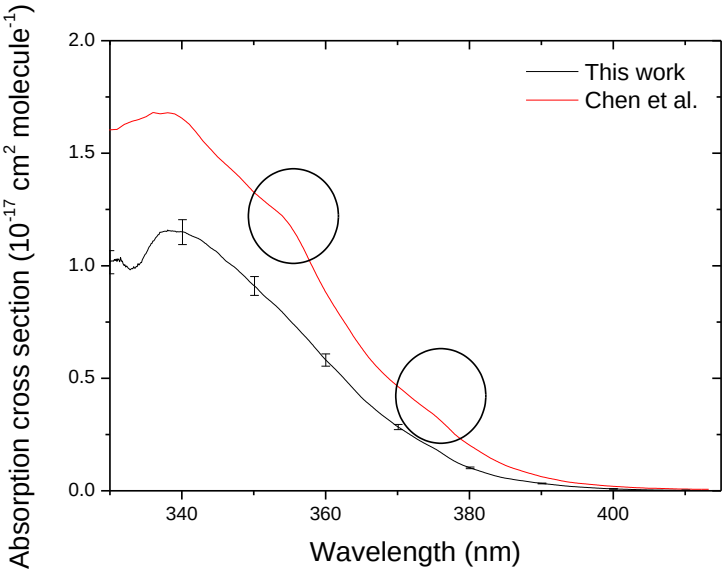

Figure 3.14 Comparison of the gas phase absorption cross section measurements of 2-NP from this work and from Chen et al. (42).

3.5. Acetaldehyde

Acetaldehyde, also known as ethanal, is one of the simplest aldehyde compounds. Measurements at urban sites have found that acetaldehyde accounts for almost one fifth (18-21 %) of the detected carbonyls in the atmosphere (49). Their prevalence in the atmosphere is important for several reasons, including playing a significant role in the formation of photochemical smog and other adverse health effects (50). The impact of acetaldehyde on health ranges from the relatively mild, such as eye irritation, to upper respiratory system problems and other toxic and carcinogenic effects (49; 51; 52). Acetaldehyde is an important precursor for peroxyacetyl nitrate, PAN, accounting for 44 % of its global production (53). PAN is a pollutant of concern owing to its mutagenic activity (52).

Acetaldehyde is produced in the atmosphere through the oxidation of NO_x and VOCs (18). One of the main direct sources is from vehicle emissions (51). Observations have been made in a number of cities. In Mexico City, the maximum mixing ratio of acetaldehyde was found at 8 am, with a daily average mixing ratio of 15 ppbv (54). Much higher acetaldehyde levels were seen in Sao Paulo, Rio de Janeiro and Salvador in Brazil. Levels of up to 35 ppbv in outdoor areas and up to high levels of 240 ppbv in highway tunnels have been observed. These high mixing ratios have been attributed to the popularity of ethanol fuelled vehicles in the Brazil (55). Ambient measurements in six locations in Southern California were taken for 24 hour periods over the course of a year-long campaign. The atmospheric mixing ratio of acetaldehyde was found to vary seasonally with an average of 2.9-4.8 ppbv, depending on location (56). These baseline studies were undertaken because of the increase in popularity of alcohols as fuels. As shown by Grosjean et al. increased alcohol fuels lead to increased formaldehyde and acetaldehyde production through secondary reactions of ethanol combustion emissions (56). The ambient levels of carbonyls in Los Angeles have been investigated in other studies (50). These measurements were taken in a number of different conditions from moderate levels of pollution to an extreme smog event. Levels of ≤ 35 ppbv were found with a large diurnal variation (50). While high levels of acetaldehyde have been observed

in California and Brazil, a study in Hong Kong found that over a 24 hour period the average mixing ratio was only 4.3 ppbv (49). Measurements in Atlanta, Georgia found that aldehydes are a crucial component in the study of photochemical pollution as they are a source of free radicals (57).

The photochemical rate of acetaldehyde can be calculated as described in equation 1.5. In order to determine this value an accurate absorption cross section value is needed. The determination of a broad spectral cross section can allow the determination of removal of acetaldehyde from the atmosphere. It is also used as a Criegee intermediate and OH radical scavenger in chamber experiments and the absorption cross section could be used to help monitor its mixing ratio during those experiments (58-60).

3.5.1. Results

Acetaldehyde has two prominent absorption peaks. One is centred at 180 nm, due to the π to π* transition, and the other is centred at 290 nm, due to the n to π*transition. The origin of the peak at 290 nm is due to the transition of the non bonding lone pair of electrons on the oxygen in the molecule to the carbonyl group. The n energy level has a higher level than π so the transition from n to π* occurs with lower energy at a longer wavelength. The tail end of the absorption peak occurs towards the short wavelength limit of the IBBCEAS spectral range.

Acetaldehyde was used as an OH scavenger during SOA formation experiments. It was added in large excess, with mixing ratios of 20 and 28 ppmv. The general shape of the cross section spectrum shown in Figure 3.15 is consistent in both shape and magnitude for the two measurements. For the 20 ppmv measurement the absorption drops below zero above 340 nm due changes in I_0 or mirror reflectivity during the experiment. Several vibronic structures are present in the spectra, with peaks separated by between 100 and 161 cm^{-1}.

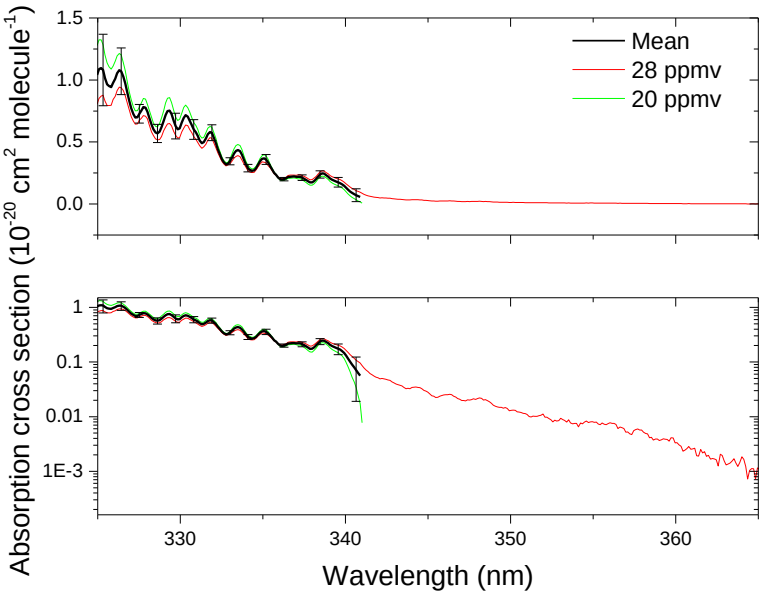

Figure 3.15 The absorption cross section spectra of ethanal measured for mixing ratios of 28 ppmv (red) and 20 ppmv (green). The mean of the measurements is shown in black. There is good agreement between the two measurements below 340 nm, while at longer wavelengths the 20 ppmv measurement drops below zero.

A number of measurements for the absorption cross section have been reported (61). These have been compared to the cross section determined in this work with the IBBCEAS/chamber combination. There is good agreement between the cross sections as determined with the IBBCEAS and those previously reported, Figure 3.16. The spectral shape and intensity match well with the Schneider-Moortgat group (reported to a resolution of 0.08 nm) (62). There is also a high level of agreement for the peak position with the measurements from Libuda (1 nm resolution), while their intensity is higher than our own. The Meyrahn et al., Martinez et al. and Mc Millan et al. measurements (1.9, 0.5 and N/A nm resolution) all show intensities similar to ours, but spectral structures are much less noticeable and peak positions cannot be compared (63-65). The high resolution, low pressure (0.038-0.090 Torr) measurements over 113 – 413 nm made by Limao-Vieira using synchrotron radiation diverge from other measurements (66). Although there is broad agreement with the other measurements, much of the finer structure is not as apparent in their spectra.

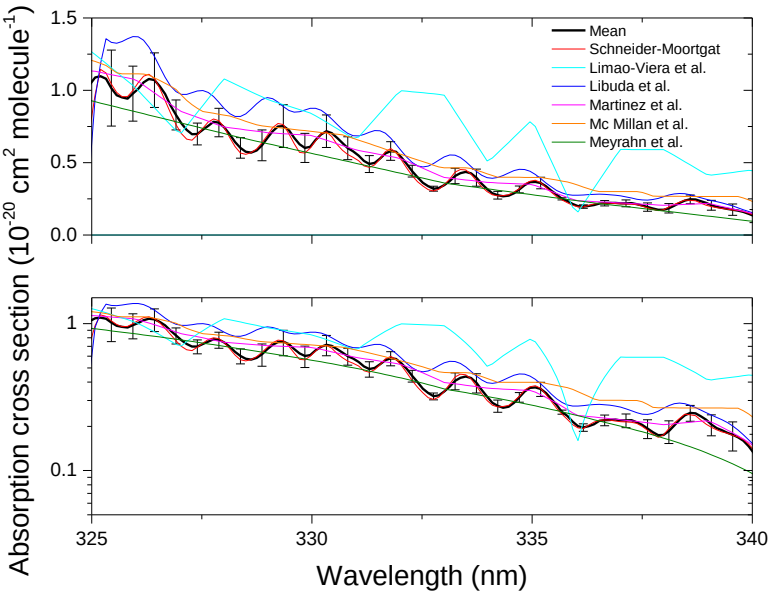

Figure 3.16 Comparison of previously reported absorption cross sections of acetaldehyde with that determined in this work. Our results are broadly consistent in magnitude with all these spectra, and show the same spectral structure as a number of papers (61; 63-67).

3.6. Acenaphthylene

Acenaphthylene is a PAH consisting of two fused benzene rings with a further alkene bridge, Figure 3.17. The structure has a large degree of electron delocalisation due to the conjugation in the system, which extends the absorption of the π to π^* band to longer wavelengths. Acenaphthylene is one of the 126 PAHs on the US EPA priority pollutant list (68). Phototoxicity, the result of light interactions with compounds causing toxic products, has been associated with PAHs. As with all PAHs, acenaphthylene has multiple emission sources. Burning of agricultural waste has been found to emit a large number of low molecular weight PAHs, of which acenaphthylene was one of the most prominent (69). It is also been found in liquid fuel, domestic waste, and landfill burning emissions (70). Acenaphthylene was amongst a large number of PAHs found in vehicle emissions (71). Numerous studies have found that acenaphthylene is the 3rd most prevalent PAH in cigarette emissions (72; 73). In areas where large numbers of smokers congregate, the concentrations of this compound and other PAHs like it would quickly increase. Overall concentration of PAHs was found to be 4725 ng $cigarette^{-1}$

and 557 ng cigarette^{-1} for acenaphthylene (74). As well as being present in cigarette smoke, there is also a significant presence of acenaphthylene in coal tar (75). The phototoxicity of a molecule is affected by its ability to absorb light. Measuring the absorption cross section of acetaldehyde allows an assessment of its phototoxicity to be made (68).

3.6.1. Results

There were two different purities of acenaphthylene used for the absorption cross section measurements below. One was a mixture of 75 % acenaphthylene and 25 % acenaphthene, the other was ≥ 99 % acenaphthylene (Table 3.2). Acenaphthene, Figure 3.17, has a similar structure as that of acenaphthylene, but its lack of a bridging double bond reduces π-conjugation in the molecule. Consequently, acenaphthene absorbs at much shorter wavelengths than acenaphthylene and not in the range of the IBBCEAS instrument. As a result, the presence of acenaphthene should not affect the measured absorption spectrum. For the sample of 75 % purity, the rate of introduction of acenaphthylene and acenaphthene into the chamber was assumed to be the same based on the nearly identical boiling points of the two compounds (280 and 279°C, respectively) and their similar chemical structures. The compound was added to the chamber using the impinger in the same manner as described previously. For the lower purity sample, it was assumed that the mass of pure acenaphthylene added would be 75 % of the total mass added.

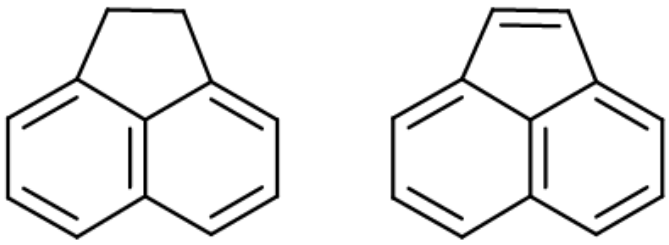

Figure 3.17 Chemical structure for acenaphthene (left) and acenaphthylene (right).

Table 3.2 Experimental details for acenaphthylene absorption cross section measurement.

Number	Date	Mixing ratio (ppbv)	Purity
1	23/10/14	121	75 %
2	23/04/15	308	≥ 99 %
3	14/05/15	82	≥ 99 %

The absorption cross sections measured in the three experiments are shown in Figure 3.18. After controlling for the lower purity of one of the samples of acenaphthylene, there was close agreement between the three measurements of the different mixing ratios. The absorption spectrum has three prominent peaks in the spectral range of the IBBCEAS system. The peak maxima were at 327.2 nm (26,867 cm^{-1}), 332.6 nm (30,066 cm^{-1}) and 338.8 nm (29,516 cm^{-1}) and had corresponding absorption cross sections of 1.94 x 10^{-17}, 1.63 x 10^{-17}, and 2.46 x 10^{-18} cm^2 $molecule^{-1}$ respectively. In addition, a very weak peak is seen at 345 nm (28,986 cm^{-1}). The separation between this peak and the one centred at 338.83 nm matches the 530 cm^{-1} separation of other peaks, suggesting that it is a real vibronic absorption feature and not an experimental artefact. The vibrational progression therefore appears to include all these absorption bands. The magnitudes of the 327 nm and 333 nm absorption peaks are similar, but a factor of six more intense than the peak at 339 nm. This suggests that the latter does not form part of the same progression. If this is the case, then the band origin occurs at 333 nm. The weak peak at 339 nm, and the very weak peak at 345 nm (Figure 3.19) therefore likely to be transitions from the v = 1 and v = 2 excited vibrational levels in the ground electronic state. With energy level differences of about 530 cm^{-1}, the population of these vibrational levels would be about 6 % (v = 1) and about 0.4 % (v = 2) in the ground electronic state.

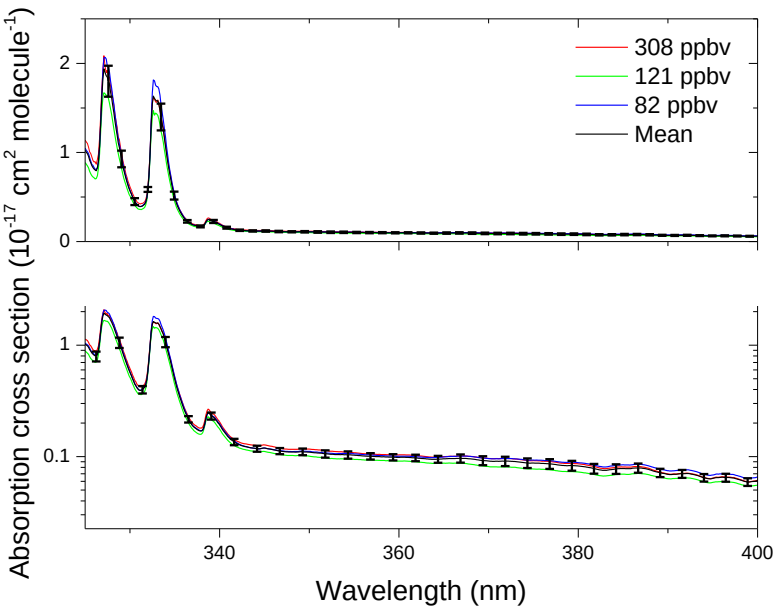

Figure 3.18 Absorption cross section of acenaphthylene. The three obvious peaks are separated by 530 cm^{-1}.

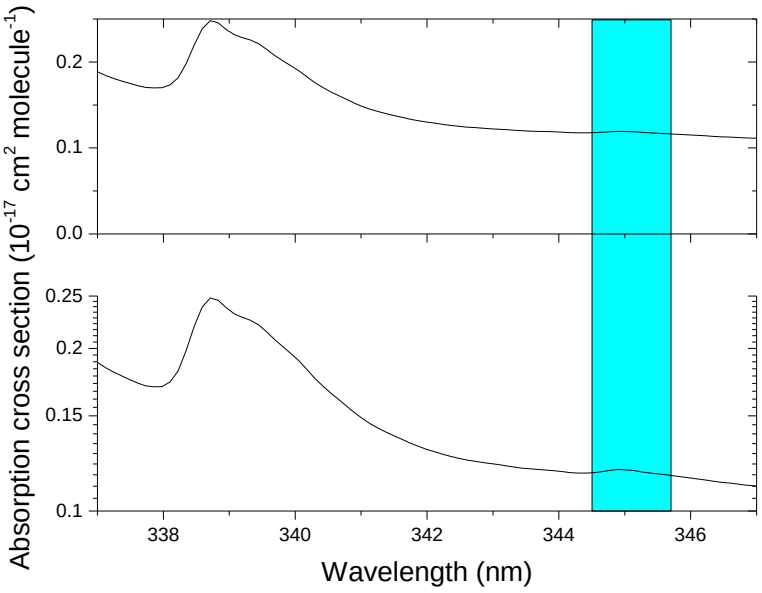

Figure 3.19 An expanded view of Figure 3.19 to highlight a very weak absorption peak at 345 nm.

A solution phase measurement was made with the 99 % pure acenaphthylene dissolved in hexane (Figure 3.21). A linear relationship was again observed between absorbance and concentration (Figure 3.20). Similar peaks were present in the solution phase as in the gas phase spectrum, with evident broadening of the peaks caused by the solvent. There is spectral shift of about 7 nm to longer wavelengths

in the hexane solution (Figure 3.21). The peak that is centred at 339.2 nm has a much larger intensity in the solution phase than the gas phase, and is likely to correspond to the band origin, while vibrationally excited levels in the solution would give rise to the shoulder around 345 nm. Thus, taking the spectral shift into account, the features of the gas and solution phase spectra display the same, broad pattern.

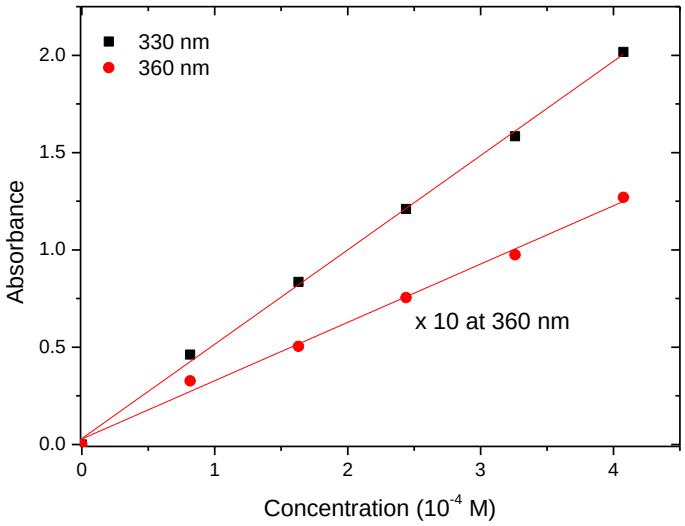

Figure 3.20 Solution phase absorbance of acenaphthylene as a function of concentration at two wavelengths, 330 nm and 360 nm. The respective values of r^2 are 0.999 and 0.997.

To our knowledge no previous acenaphthylene gas phase absorption cross section has been reported. The closest comparison that can be made is to a paper which gives the shape of the absorption in a cyclohexane solution. While no values for the intensity are given, three peaks were reported at 325.8, 331.5 and 337.3 nm. Each peak is separated by 518-530 cm^{-1} (76). These results are therefore consistent with our spectra.

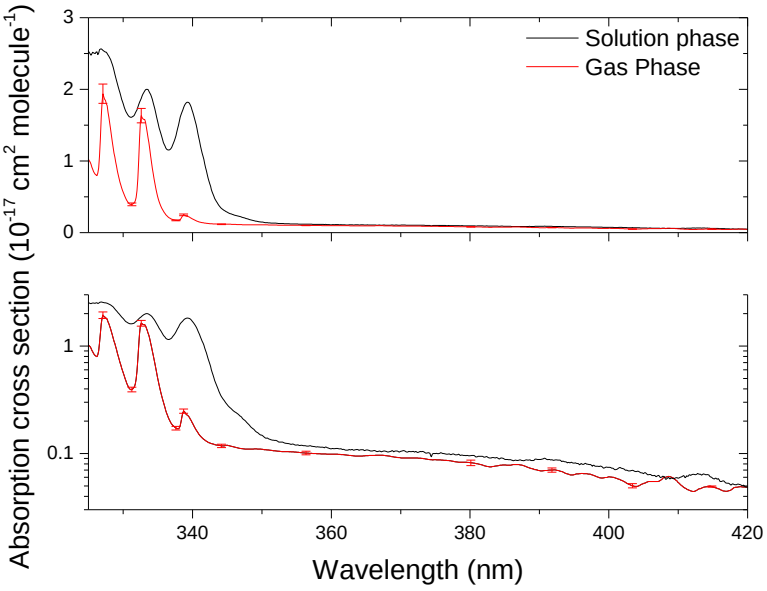

Figure 3.21 Comparison of the gas phase and solution phase absorption cross sections.

3.7. Water

Water vapour is the most important greenhouse gas in the earth's atmosphere and it is a major absorber of solar radiation (77). The details of its impact are still partially unknown. It has been proposed that as much as 25-30 % of the difference between theoretical and experimental solar radiation absorption in the near UV may be due to water vapour (78; 79). We can be confident that the extinction seen is almost exclusively due to absorption because water vapour scattering has a small effect under atmospheric conditions (80). While water vapour is present throughout the atmosphere, its concentration varies considerable depending on location, season, and altitude. It can range from trace levels to almost 4 % of the composition of the atmosphere. It is responsible for the removal of significant incoming solar radiation through absorption. This coupled with the fact that it is an extremely important absorber of out-going thermal radiation make it particularly important to fully and accurately characterise its full absorption spectrum (79). A recent study by Du et al. used CRDS to directly measure absorption from the ground vibrational state of the water monomer at short wavelengths, 290-350 nm (78). The measurements are in the near-UV region from 290 to 350 nm with a 5 nm interval, and seem to indicate that water absorption increased strongly below 335 nm. This

result is consistent with the same group's study on the absorption of adsorbed water on fused silica (81). However, their result is surprising because theoretical calculations suggest that water absorption should get weaker in the near-UV. As the IBBCEAS allows for continuous measurements over a broad spectral range, the aim of this experiment was to test for the presence of any absorption caused by water, to compare it to the values reported in the literature, and to extend the spectrum to longer wavelengths (> 350 nm).

Very recently, the long light paths through the atmosphere of long-path DOAS and MAX-DOAS measurements have been exploited to measure water absorption in the atmosphere down to 330 nm (82). These measurements reported an upper limit for the differential absorption cross section of 3×10^{-27} cm^2 $molecule^{-1}$ (at 0.45 nm resolution) and pointed to the need for further work on the near-UV water absorption spectrum. Integrating cavity measurements have reported very low levels of absorption in the blue spectra region with a further decrease towards shorter wavelengths (83). More importantly, theoretical calculations indicate that the near-UV absorption of the monomer is both weak and generally decreases further into the ultraviolet.

3.7.1. Results

The relative humidity (RH) of the chamber was raised to 80 % prior to the measurements using the method described in Chapter 2. To make multiple measurements over the course of a single experiment, the concentration of water was lowered a number of times by flushing in short bursts with dry air. A constant air flow was maintained across the dielectric mirrors to prevent contamination of mirror surfaces through deposition of particles or adsorption of gases. This air flow is usually connected to the same inlet line as the chamber purge air, but because the flow rate would be greatly reduced during flushing, for these experiments, nitrogen from a gas cylinder was used for the purge gas. By flushing the chamber, as shown in Figure 3.22, several measurements of the water absorption could be made during an experiment. Each change in the relative humidity corresponds to

approximately a 20 % drop, or to changes in the water monomer concentration of around 1 × 10^{17} cm^{-3}. When the absorption for each step was determined, a number of narrow peaks were found. These were located at 341.6, 354.1, 368.2 and 384.5 nm. These peaks arise from the formation of nitrous acid, HONO. HONO formation in atmospheric chambers is well known and occurs via reaction of adsorbed water and nitrogen oxides on chamber surfaces (84).

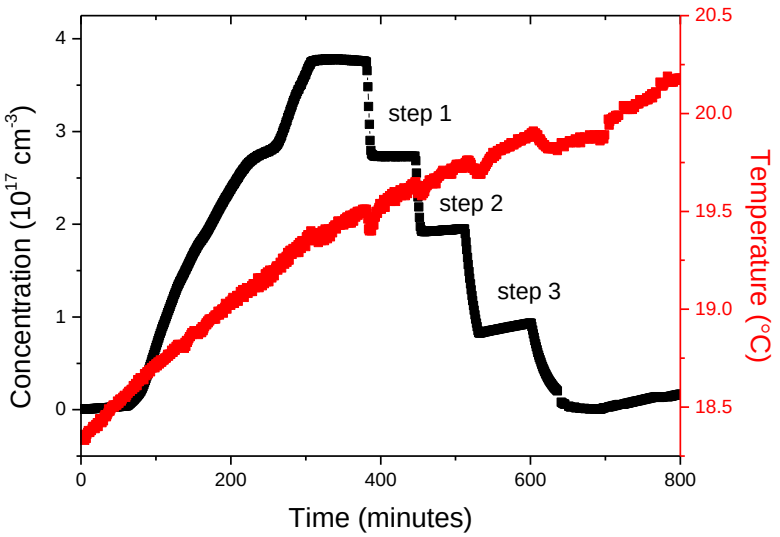

Figure 3.22 Time profile of the concentration of water monomer (black) and temperature in the chamber (red). The humidity was reduced in several steps by flushing the chamber.

Figure 3.23 shows the absorption calculated for the three step changes in the experiment. There is no structure that is consistent for the three step changes. The shape of the mirror reflectivity is seen in the Step 1 absorption. There are a number of narrow peaks visible that are associated with HONO absorption (85). This is in stark comparison with the values reported by Du et al. which show a strong absorption in this region Figure 3.24.

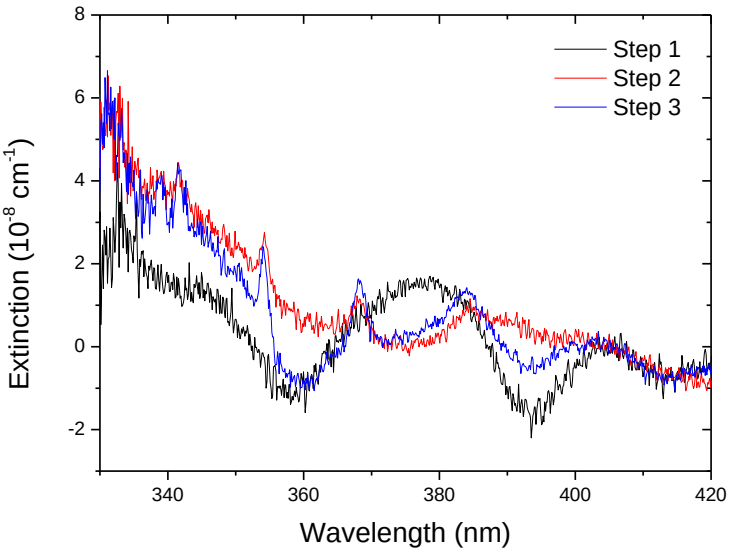

Figure 3.23 The absorption spectra for the three step changes shown in Figure 3.22. There are no consistent absorptionfeatures present except for the narrow HONO peaks.

The magnitude of the absorption reported by the Du et al. group should be visible in our measurement region(78). An absorption cross section was determined for the Step 1 extinction from Figure 3.23. The values this gave were in the region of 1 x 10^{-25} cm^2 $molecule^{-1}$. This is an order of magnitude lower than the measurements reported by Du et al. However, the only structure that is visible from the IBBCEAS measurements is some structure from the mirror reflectivity. The discrepancy between the Du et al. measurements and our results may be attributable to an artefact arising from water vapour coming into contact with the cavity mirrors in their CRDS vacuum cell. The same authors observed successive water uptake on cavity mirrors even at low water pressures in another study (81). Such water adsorption on the mirrors would alter the mirror reflectivity and hence the ring-down times in the spectrometer, which would be interpreted as an absorption. A similar effect has previously been observed by our group involving the sensitivity of optical cavity spectrometer performance to water uptake on mirrors in the deep-UV (86). If the assumption is true, it implies that the absorption registered by the Du et al. group may be incorrect because absorption measurements at all wavelengths would be affected by water uptake on the

mirrors. Our IBBCEAS measurements, which we have published, can be taken as an upper limit for the absorption cross section for water (87).The values that are reported here do not support the values reported by Du et al. and are generally consistent with the theoretical absorption cross section levels reported by Lampel et al. (82).

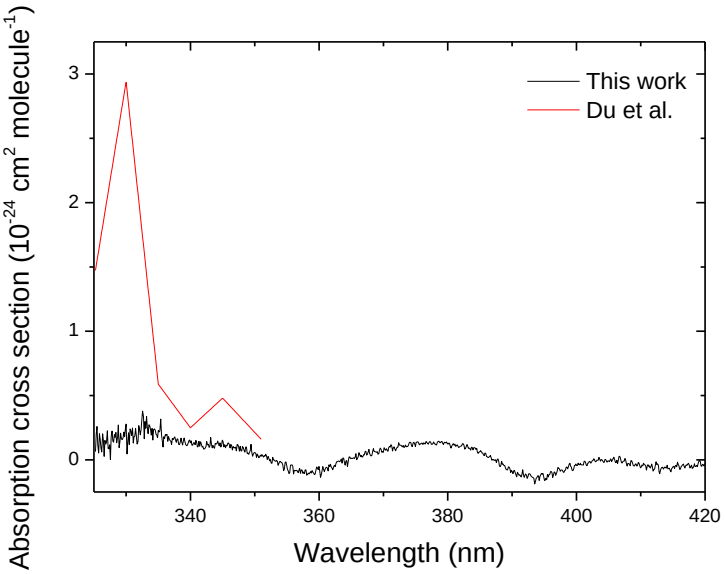

Figure 3.24 Absorption cross section spectrum of water reported by Du et al. and absorption cross section determined by the Step 1 extinction from Figure 3.23. As well as a general absorption, there is a peak present at 330 nm that is not seen in our measurements.

3.8. Conclusions

The experiments presented in this chapter illustrate the use of IBBCEAS in conjunction with a simulation chamber to measure the absorption cross section for several compounds in the gas phase that are otherwise difficult to determine experimentally. This ranges from the broad absorption of 2-NP to the structured, weakly absorbing acetaldehyde. Some of these compounds have no reported gas phase cross sections, 1-NN and acenaphthylene, while others have very limited measurements, 2-NP. One of the reasons for the lack of measurements is the low vapour pressure of these compounds, Table 3.1. The difficulty of adding 1-NN to the chamber can be attributed to its low vapour pressure. The vapour pressure of 1-NN

is about 6 orders of magnitude lower than that of acetaldehyde, making it more difficult not only to add the compound to the chamber but also to keep the compound in the gas phase in the chamber. This is reflected in the large uncertainties associated with the 1-NN cross section as shown in Figure 3.6. The compounds needed to be heated with a heat gun prior to addition. This works well for compounds with relatively high vapour pressures, but with compounds such as 1-NN that need to be heated for long periods of time, there is some risk of thermal decomposition of the compound. A more controllable heating process could help with this. Another avenue that should be looked at is adding the compound to the chamber as a solution, for instance, as droplets in a solvent. This could allow the consistent addition of very low vapour pressure compounds.

The compounds used in these experiments were not purified after they were received from their suppliers. All compounds were purchased at the highest quality available at the time. However, for weakly absorbing species, an impurity that was highly absorbing could influence the measured absorption cross section. In our opinion, this does not seem likely in any of the cross sections shown in this chapter. There are no errant or unexpected peaks. However, in future the inclusion of an additional purification step to any compounds that are being used would allay any doubt about their purity. The purity of biacetyl and methyl vinyl ketone was checked with a proton NMR; these were found to be at least 97-98 % pure. The IBBCEAS measurement of absorption cross section has already been validated for benzaldehyde (Chapter 2). The short-wavelength absorption of water was also studied. Water is such a prominent atmospheric constituent that any absorption by it could have a significant radiative or photochemical effect. However, we were not able to confirm any absorption from water in the UV/Vis region our measurements. Instead, we have reported new upper limits for the water absorption cross section in this region, and call into question the previously reported spectrum.

References

1. Reichardt C. 1988. *Solvents and Solvent Effects in Organic Chemistry*. Federal Republic of Germany
2. Homocianu M. 2011. Solvent effects on the electronic absorption and fluorescence spectra. *Journal of Advanced Research in Physics* 2
3. Rusu E, Dorohoi D-O, Airinei A. 2008. Solvatochromic effects in the absorption spectra of some azobenzene compounds. *Journal of Molecular Structure* 887:216-9
4. Eisenreich SJ, Looney BB, Thornton JD. 1981. Airborne organic contaminants in the Great Lakes ecosystem. *Environmental Science & Technology* 15:30-8
5. Sonnefeld WJ, Zoller WH, May WE. 1983. Dynamic coupled-column liquid-chromatographic determination of ambient-temperature vapor pressures of polynuclear aromatic hydrocarbons. *Analytical Chemistry* 55:275-80
6. Goldfarb JL, Suuberg EM. 2008. Vapor pressures and enthalpies of sublimation of ten polycyclic aromatic hydrocarbons determined via the Knudsen effusion method. *Journal of Chemical & Engineering Data* 53:670-6
7. Odabasi M, Cetin E, Sofuoglu A. 2006. Determination of octanol–air partition coefficients and supercooled liquid vapor pressures of PAHs as a function of temperature: application to gas–particle partitioning in an urban atmosphere. *Atmospheric Environment* 40:6615-25
8. Schauer JJ, Kleeman MJ, Cass GR, Simoneit BR. 1999. Measurement of emissions from air pollution sources. 2. C1 through C30 organic compounds from medium duty diesel trucks. *Environmental science & technology* 33:1578-87
9. Veres PR, Faber P, Drewnick F, Lelieveld J, Williams J. 2013. Anthropogenic sources of VOC in a football stadium: Assessing human emissions in the atmosphere. *Atmospheric Environment* 77:1052-9
10. Atkinson R. 1990. Gas-phase tropospheric chemistry of organic compounds: a review. *Atmospheric Environment. Part A. General Topics* 24:1-41
11. Bandow H, Washida N. 1985. Ring-cleavage Reactions of Aromatic Hydrocarbons Studied by FT–IR Spectroscopy. II. Photooxidation of o-, m-, and p-Xylenes in the NO_x–Air System. *Bulletin of the Chemical Society of Japan* 58:2541-8
12. Plum CN, Sanhueza E, Atkinson R, Carter WP, Pitts JN. 1983. Hydroxyl radical rate constants and photolysis rates of alpha-dicarbonyls. *Environmental science & technology* 17:479-84
13. Blacet F, Bell W. 1953. The mechanism of biacetyl photolysis. *Discussions of the Faraday Society* 14:70-6
14. Calvert J, Pitts J. 1966. jr., Photochemistry. *Wiley, New York* 8:99
15. Horowitz A, Meller R, Moortgat GK. 2001. The UV–VIS absorption cross sections of the α-dicarbonyl compounds: pyruvic acid, biacetyl and glyoxal. *Journal of Photochemistry and Photobiology A: Chemistry* 146:19-27
16. Voigt S, Orphal J, Burrows JP. 2002. The temperature and pressure dependence of the absorption cross-sections of NO_2 in the 250–800 nm region measured by Fourier-transform spectroscopy. *Journal of Photochemistry and Photobiology A: Chemistry* 149:1-7
17. Dimashki M, Harrad S, Harrison RM. 2000. Measurements of nitro-PAH in the atmospheres of two cities. *Atmospheric Environment* 34:2459-69
18. Finlayson-Pitts BJ, Pitts JN. 1997. Tropospheric Air Pollution: Ozone, Airborne Toxics, Polycyclic Aromatic Hydrocarbons, and Particles. *Science* 276:1045-51
19. Albinet A, Leoz-Garziandia E, Budzinski H, Villenave E. 2007. Polycyclic aromatic hydrocarbons (PAHs), nitrated PAHs and oxygenated PAHs in ambient air of the

Marseilles area (South of France): Concentrations and sources. *Science of The Total Environment* 384:280-92
20. Tokiwa H, Ohnishi Y, Rosenkranz HS. 1986. Mutagenicity and carcinogenicity of nitroarenes and their sources in the environment. *CRC Critical Reviews in Toxicology* 17:23-58
21. Atkinson R, Arey J. 1994. Atmospheric chemistry of gas-phase polycyclic aromatic hydrocarbons: formation of atmospheric mutagens. *Environmental Health Perspectives* 102:117
22. Ames BN, Durston WE, Yamasaki E, Lee FD. 1973. Carcinogens are mutagens: a simple test system combining liver homogenates for activation and bacteria for detection. *Proceedings of the National Academy of Sciences* 70:2281-5
23. Øvrevik J, Arlt V, Øya E, Nagy E, Mollerup S, Phillips D, Låg M, Holme J. 2010. Differential effects of nitro-PAHs and amino-PAHs on cytokine and chemokine responses in human bronchial epithelial BEAS-2B cells. *Toxicology and applied pharmacology* 242:270-80
24. Verschoyle R, Carthew P, Wolf C, Dinsdale D. 1993. 1-Nitronaphthalene toxicity in rat lung and liver: effects of inhibiting and inducing cytochrome P450 activity. *Toxicology and applied pharmacology* 122:208-13
25. Humans IWGotEoCRt. 2008. IARC monographs on the evaluation of carcinogenic risks to humans. Volume 97. 1, 3-butadiene, ethylene oxide and vinyl halides (vinyl fluoride, vinyl chloride and vinyl bromide). *IARC monographs on the evaluation of carcinogenic risks to humans/World Health Organization, International Agency for Research on Cancer* 97:3
26. Ciccioli P, Cecinato A, Brancaleoni E, Frattoni M, Zacchei P, Miguel AH, Vasconcellos P. 1996. Formation and transport of 2-nitrofluoranthene and 2-nitropyrene of photochemical origin in the troposphere. *Journal of Geophysical Research: Atmospheres (1984–2012)* 101:19567-81
27. Nielsen T, Ramdahl T, Bjørseth A. 1983. The fate of airborne polycyclic organic matter. *Environmental Health Perspectives* 47:103
28. Wing CY, Fine DH, Chiu KS, Biemann K. 1984. Determination of nitrated polycyclic aromatic hydrocarbons in diesel particulates by gas chromatography with chemiluminescent detection. *Analytical chemistry* 56:1158-62
29. Gupta P, Harger WP, Arey J. 1996. The contribution of nitro-and methylnitronaphthalenes to the vapor-phase mutagenicity of ambient air samples. *Atmospheric Environment* 30:3157-66
30. Feilberg A, Kamens R, Strommen M, Nielsen T. 1999. Modeling the formation, decay, and partitioning of semivolatile nitro-polycyclic aromatic hydrocarbons (nitronaphthalenes) in the atmosphere. *Atmospheric Environment* 33:1231-43
31. Zugazagoitia JS, Almora-Díaz CX, Peon J. 2008. Ultrafast intersystem crossing in 1-nitronaphthalene. An experimental and computational study. *The Journal of Physical Chemistry A* 112:358-65
32. Nojima K, Fukaya K, Fukui S, Kanno S. 1975. The formation of nitrophenols and nitrobenzene by the photochemical reaction of benzene in the presence of nitrogen monoxide. *Chemosphere* 2:77-82
33. Harrison MA, Barra S, Borghesi D, Vione D, Arsene C, Olariu RI. 2005. Nitrated phenols in the atmosphere: a review. *Atmospheric Environment* 39:231-48
34. Hinkel M, Reischl A, Schramm K-W, Trautner F, Reissinger M, Hutzinger O. 1989. Concentration levels of nitrated phenols in conifer needles. *Chemosphere* 18:2433-9

35. Natangelo M, Mangiapan S, Bagnati R, Benfenati E, Fanelli R. 1999. Increased concentrations of nitrophenols in leaves from a damaged forestal site. *Chemosphere* 38:1495-503
36. Nojima K, Kawaguchi A, Ohya T, Kanno S, Hirobe M. 1983. Studies on Photochemical Reaction of Air Pollutants. X. Identification of Nitrophenols in Suspended Particulates. *CHEMICAL & PHARMACEUTICAL BULLETIN* 31:1047-51
37. Atkinson R, Aschmann SM, Arey J. 1992. Reactions of hydroxyl and nitrogen trioxide radicals with phenol, cresols, and 2-nitrophenol at 296+-0.2 K. *Environmental science & technology* 26:1397-403
38. Bolzacchini E, Bruschi M, Hjorth J, Meinardi S, Orlandi M, Rindone B, Rosenbohm E. 2001. Gas-phase reaction of phenol with NO_3. *Environmental science & technology* 35:1791-7
39. Leuenberger C, Ligocki MP, Pankow JF. 1985. Trace organic compounds in rain. 4. Identities, concentrations, and scavenging mechanisms for phenols in urban air and rain. *Environmental science & technology* 19:1053-8
40. Leuenberger C, Czuczwa J, Tremp J, Giger W. 1988. Nitrated phenols in rain: atmospheric occurrence of phytotoxic pollutants. *Chemosphere* 17:511-5
41. Lüttke J, Levsen K. 1997. Phase partitioning of phenol and nitrophenols in clouds. *Atmospheric Environment* 31:2649-55
42. Chen J, Wenger JC, Venables DS. 2011. Near-ultraviolet absorption cross sections of nitrophenols and their potential influence on tropospheric oxidation capacity. *The Journal of Physical Chemistry A* 115:12235-42
43. Bejan I, El Aal YA, Barnes I, Benter T, Bohn B, Wiesen P, Kleffmann J. 2006. The photolysis of ortho-nitrophenols: a new gas phase source of HONO. *Physical Chemistry Chemical Physics* 8:2028-35
44. Jacobson MZ. 1999. Isolating nitrated and aromatic aerosols and nitrated aromatic gases as sources of ultraviolet light absorption. *Journal of Geophysical Research: Atmospheres* 104:3527-42
45. Chen B, Yang C, Goh NK. 2005. Direct photolysis of nitroaromatic compounds in aqueous solutions. *Journal of Environmental Sciences* 17:598-604
46. Alif A, Pilichowski J-F, Boule P. 1991. Photochemistry and environment XIII: Phototransformation of 2-nitrophenol in aqueous solution. *Journal of Photochemistry and Photobiology A: Chemistry* 59:209-19
47. Kleffmann J. 2007. Daytime sources of nitrous acid (HONO) in the atmospheric boundary layer. *ChemPhysChem* 8:1137-44
48. Molina L, Molina M. 1986. Absolute absorption cross sections of ozone in the 185-to 350-nm wavelength range. *Journal of Geophysical Research: Atmospheres* 91:14501-8
49. Sin DW, Wong Y-C, Louie PK. 2001. Trends of ambient carbonyl compounds in the urban environment of Hong Kong. *Atmospheric Environment* 35:5961-9
50. Grosjean D. 1982. Formaldehyde and other carbonyls in Los Angeles ambient air. *Environmental science & technology* 16:254-62
51. Stupfel M. 1976. Recent advances in investigations of toxicity of automotive exhaust. *Environmental Health Perspectives* 17:253
52. Shepson PB, Kleindienst TE, Edney EO, Nero CM, Cupitt LT, Claxton LD. 1986. Acetaldehyde: the mutagenic activity of its photooxidation products. *Environmental science & technology* 20:1008-13
53. Fischer E, Jacob DJ, Yantosca RM, Sulprizio MP, Millet D, Mao J, Paulot F, Singh H, Roiger A, Ries L. 2014. Atmospheric peroxyacetyl nitrate (PAN): a global budget and source attribution. *Atmospheric Chemistry and Physics* 14:2679-98

54. Baez A, Belmont R, Padilla H. 1995. Measurements of formaldehyde and acetaldehyde in the atmosphere of Mexico City. *Environmental Pollution* 89:163-7
55. Grosjean D, Miguel AH, Tavares TM. 1990. Urban air pollution in Brazil: acetaldehyde and other carbonyls. *Atmospheric Environment. Part B. Urban Atmosphere* 24:101-6
56. Grosjean D. 1991. Ambient levels of formaldehyde, acetaldehyde and formic acid in southern California: results of a one-year baseline study. *Environmental science & technology* 25:710-5
57. Grosjean E, Williams EL, Grosjean D. 1993. Ambient levels of formaldehyde and acetaldehyde in Atlanta, Georgia. *Air & Waste* 43:469-74
58. Docherty KS, Ziemann PJ. 2003. Effects of stabilized Criegee intermediate and OH radical scavengers on aerosol formation from reactions of β-pinene with O_3. *Aerosol Science & Technology* 37:877-91
59. Taatjes CA, Welz O, Eskola AJ, Savee JD, Osborn DL, Lee EP, Dyke JM, Mok DW, Shallcross DE, Percival CJ. 2012. Direct measurement of Criegee intermediate (CH_2OO) reactions with acetone, acetaldehyde, and hexafluoroacetone. *Physical Chemistry Chemical Physics* 14:10391-400
60. Johnson D, Lewin AG, Marston G. 2001. The effect of Criegee-intermediate scavengers on the OH yield from the reaction of ozone with 2-methylbut-2-ene. *The Journal of Physical Chemistry A* 105:2933-5
61. Moortgat WSaGK. 1989. UV/VIS Spectra of Atmospheric Constituents, Version 1. ed. RR Personal communication to E.-P. Röth, G. Moortgat, R. Meller, and W. Schneider
62. 2016. *The MPI-Mainz UV/VIS Spectral Atlas of Gaseous Molecules of Atmospheric Interest*. http://satellite.mpic.de/spectral_atlas
63. Meyrahn H. 1984. *Bildungswege und Analytik des Peroxyacetylnitrates (PAN) in der Atmosphäre*
64. Martinez RD, Buitrago AA, Howell NW, Hearn CH, Joens JA. 1992. The near UV absorption spectra of several aliphatic aldehydes and ketones at 300 K. *Atmospheric Environment. Part A. General Topics* 26:785-92
65. Calvert JG, Pitts, J. N. 1966. CALVERT,JG - PHOTOCHEMISTRY. *Journal De Chimie Physique* 63:368
66. Limao-Vieira P, Eden S, Mason N, Hoffmann S. 2003. Electronic state spectroscopy of acetaldehyde, CH_3CHO, by high-resolution VUV photo-absorption. *Chemical physics letters* 376:737-47
67. Libuda HG. 1992. *Spektroskopische und kinetische Untersuchungen an halogenierten Carbonylverbindungen von atmosphärischem Interesse*. Univ. Wuppertal, Germany
68. Yan J, Wang L, Fu PP, Yu H. 2004. Photomutagenicity of 16 polycyclic aromatic hydrocarbons from the US EPA priority pollutant list. *Mutation Research/Genetic Toxicology and Environmental Mutagenesis* 557:99-108
69. Kakareka SV, Kukharchyk TI. 2003. PAH emission from the open burning of agricultural debris. *Science of the total environment* 308:257-61
70. Lemieux PM, Lutes CC, Santoianni DA. 2004. Emissions of organic air toxics from open burning: a comprehensive review. *Progress in energy and combustion science* 30:1-32
71. de Abrantes R, de Assuncao JV, Pesquero CR, Bruns RE, Nóbrega RP. 2009. Emission of polycyclic aromatic hydrocarbons from gasohol and ethanol vehicles. *Atmospheric Environment* 43:648-54
72. Neurath GB. 1972. *The Chemistry of Tobacco and Tobacco Smoke:Recent advances in knowledge of the chemical composition of tobacco smoke*. pp 77-97. Springer

73. Bolte G, Heitmann D, Kiranoglu M, Schierl R, Diemer J, Koerner W, Fromme H. 2008. Exposure to environmental tobacco smoke in German restaurants, pubs and discotheques. *Journal of Exposure Science and Environmental Epidemiology* 18:262-71
74. Lu H, Zhu L. 2007. Pollution patterns of polycyclic aromatic hydrocarbons in tobacco smoke. *Journal of hazardous materials* 139:193-8
75. Wise SA, Benner BA, Byrd GD, Chesler SN, Rebbert RE, Schantz MM. 1988. Determination of polycyclic aromatic hydrocarbons in a coal tar standard reference material. *Analytical chemistry* 60:887-94
76. Banisaukas J, Szczepanski J, Eyler J, Vala M, Hirata S, Head-Gordon M, Oomens J, Meijer G, von Helden G. 2003. Vibrational and Electronic Spectroscopy of Acenaphthylene and Its Cation. *The Journal of Physical Chemistry A* 107:782-93
77. Houghton JT, Ding Y, Griggs DJ, Noguer M, van der Linden PJ, Dai X, Maskell K, Johnson C. 2001. Climate change 2001: the scientific basis.
78. Du J, Huang L, Min Q, Zhu L. 2013. The influence of water vapor absorption in the 290–350 nm region on solar radiance: Laboratory studies and model simulation. *Geophysical Research Letters* 40:4788-92
79. Ramanathan V, Vogelmann AM. 1997. Greenhouse effect, atmospheric solar absorption and the Earth's radiation budget: From the Arrhenius-Langley era to the 1990s. *Ambio*:38-46
80. Sutton JA, Driscoll JF. 2004. Rayleigh scattering cross sections of combustion species at 266, 355, and 532 nm for thermometry applications. *Optics letters* 29:2620-2
81. Du J, Huang L, Zhu L. 2013. Absorption Cross Sections of Surface-Adsorbed H_2O in the 295–370 nm Region and Heterogeneous Nucleation of H_2O on Fused Silica Surfaces. *The Journal of Physical Chemistry A* 117:8907-14
82. Lampel J, Pöhler D, Tschritter J, Frieß U, Platt U. 2015. On the relative absorption strengths of water vapour in the blue wavelength range. *Atmospheric Measurement Techniques* 8:4329-46
83. Pope RM, Fry ES. 1997. Absorption spectrum (380–700 nm) of pure water. II. Integrating cavity measurements. *Appl. Opt.* 36:8710-23
84. Carter WP, Cocker DR, Fitz DR, Malkina IL, Bumiller K, Sauer CG, Pisano JT, Bufalino C, Song C. 2005. A new environmental chamber for evaluation of gas-phase chemical mechanisms and secondary aerosol formation. *Atmospheric Environment* 39:7768-88
85. Bongartz A, Kames J, Welter F, Schurath U. 1991. Near-UV absorption cross sections and trans/cis equilibrium of nitrous acid. *The Journal of Physical Chemistry* 95:1076-82
86. Darby SB, Smith PD, Venables DS. 2012. Cavity-enhanced absorption using an atomic line source: application to deep-UV measurements. *Analyst* 137:2318-21
87. Wilson EM, Wenger JC, Venables DS. 2016. Upper limits for absorption by water vapor in the near-UV. *Journal of Quantitative Spectroscopy and Radiative Transfer* 170:194-9

4. Optical Properties of Secondary Organic Aerosol formed by Ozonolysis of α-pinene

4.1. Introduction

Volatile organic compounds are prevalent in the troposphere. Their relatively high vapour pressure ensures that they evaporate or sublime to the gas phase. An estimate of 1150 TgC per year are reported to be emitted into the atmosphere (1). This is composed of a range of compounds including isoprene (44 %), reactive or non-reactive VOCs (45 %), and monoterpenes (11 %) (2; 3). Monoterpenes have the molecular formula of $C_{10}H_{16}$ and consist of cyclic or linear alkenes. One of the most common monoterpenes is α-pinene, which contains a four membered ring and has an endocyclic double bond, Figure 4.1 (4).

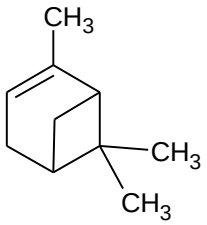

Figure 4.1 Structure of α-pinene.

α-pinene is a biogenic VOC that is released from forests all over the world. It gets its name from one of its primary emission sources, pine trees (5). The yearly emission

for α-pinene into the environment has been measured as up to 50 TgC per year, which is equivalent to annual emissions of all anthropogenic hydrocarbons (6; 7). Although exposure to α-pinene can result in skin or mucous membrane irritation, allergic contact dermatitis or chronic lung function impairment, the direct health effects play a relatively small part in α-pinene's global impact (8-11). Rather, the products of α-pinene oxidation result in secondary organic aerosol (SOA) formation that has significant climate and health effects.

The formation of SOA from monoterpenes has been widely studied (12-17). Oxidation of monoterpenes accounts for a large proportion of their particle formation events (18-20). Particular attention has been paid to both α- and β-pinene as they contribute significantly to monoterpene emissions (21-23).

The three main routes for α-pinene oxidation are reaction with OH, NO_3, or ozone (24). The OH and NO_3 radicals are important atmospheric oxidising agents. They are responsible for most day and night time oxidation of VOCs respectively. Their initial oxidation products include carbonyls, carboxylic acids, alcohols and organic nitrates (18; 20; 25-29). Reactions with ozone are an important loss process for alkenes in the atmosphere, and ozone is responsible for up to 80 % of the atmospheric losses of α-pinene (3; 30-32).

The general mechanism of ozonolysis of α-pinene is well-known. Ozone attacks across the unsaturated double bond on the ring of the α-pinene to produce a primary ozonide. This ozonide decomposes to form an excited criegee intermediate, that is, a carbonyl oxide with two charged centres (33). These criegee intermediates are then either collisionally stabilised or decompose to form OH (34). Any OH formed is then an additional oxidising species present in the system and can influence the reaction in two ways. Firstly, OH can react with α-pinene directly. This reaction is faster than the ozone reaction and can form different products (30). Secondly, the OH radical can also age the SOA particles and interact with the oxidation products (35-37). The initial steps and oxidation products in the ozonolysis of α-pinene are shown in Figure 4.2 (38). Multiple generations of oxidation and species production continue the oxidation process beyond the

species shown in Figure 4.2. Even though the α-pinene/ozone system has been intensively studied, the full reaction scheme is complex and not fully understood. As these species are progressively oxidised, the vapour pressures of their products tend to decrease, which results in the formation of SOA through the partitioning between the gas and particle phase (39; 40).

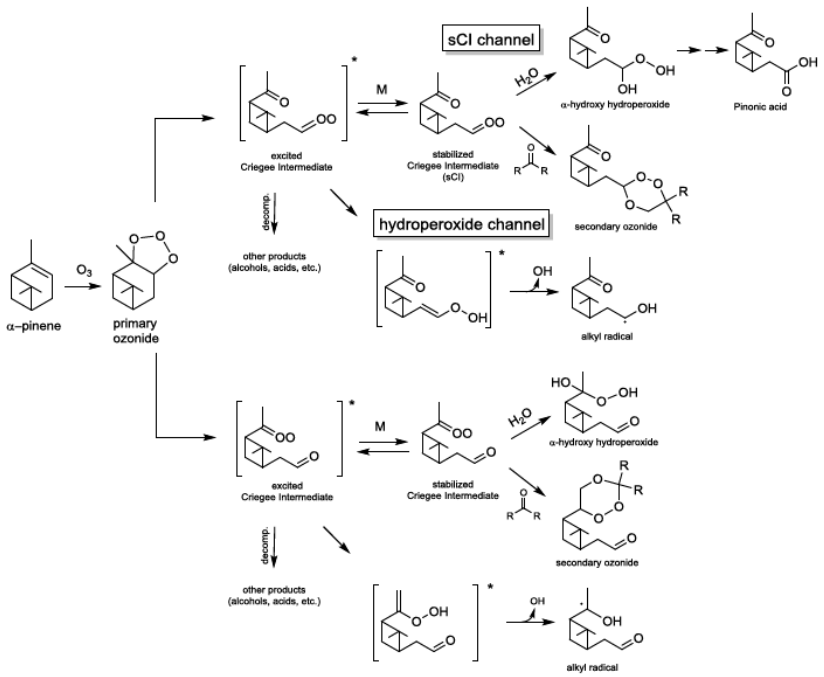

Figure 4.2 Reaction pathway for the ozonolysis of α-pinene. Reproduced from Kristensen et al. (38).

The mass yield of α-pinene SOA from ozonolysis depends on a number of factors including hydrocarbon concentration, relative humidity, availability of OH, and temperature (41-45). Ozonolysis of α-pinene is efficient in SOA formation with reported yields of up to 0.67 (46). The reaction pathways can be modified by the addition of compounds to the α-pinene/ozone system. For example, cyclohexane can be used to remove the OH radical, while water vapour is an important criegee intermediate scavenger in the ambient atmosphere (35; 37).

The focus of this chapter is on the optical properties of α-pinene SOA. The interaction between light and biogenic SOA particles was first reported by Went in

1960 (47). Went noticed a recurring blue haze present over large forested areas. There have been a number of field studies that have reported similar haze affects. These events occur widely, and have been observed, inter alia, in Canada, Finland, Portugal, and Australia (16; 48-50). The organic aerosols that are responsible for this haze also comprise a large fraction of the fine particulates in the atmosphere (39). The effects of different atmospheric species on the radiative balance, and the uncertainties associated with aerosols in particular, was discussed in Chapter 1 (51). To address these uncertainties, the optical properties of aerosols need to be characterised.

The formation, composition, and optical properties of secondary organic aerosols have received a great deal of interest in the last few years and have been the subject of several reviews (52-55). SOA contributes 70-90 % of the aerosol mass loading in the lower troposphere (56-58). As a result it is necessary to know the impact these species have on the climate and one way to do this is through the study of their optical properties. The refractive indices of a number of SOA particles formed from prominent VOCs have been studied. These include SOA as a result of toluene photooxidation, toluene oxidation, limonene photooxidation, guaiacol OH oxidation, β-pinene NO_3 oxidation, and α-pinene ozonolysis (59-67). A comprehensive list of these studies have been reported in a recent review article by Moise et al. (53).

One of the fundamental properties of substances used to determine their optical properties is the complex refractive index (Chapter 1). The complex refractive index (CRI) of SOA varies over a wide range of values (1.35 to 1.60), making their contribution to radiative forcing extremely dependent on particle type (53). Moreover, a significant spectral dependence has also been reported for these types of particles at shorter wavelengths (62; 63). There have been a number of studies of the optical properties of SOA formed by the ozonolysis of α-pinene. Kim et al. used a nephelometer to determine the RI value of these particles at 670 nm (68). An OH scavenger was added and the aerosol mass concentration was varied. Neither condition was determined to affect the RI values. Nakayama et al. used a nephelometer for scattering measurements and a CRDS system for extinction

measurements in their optical property study of α-pinene/ozonolysis SOA (63). They found that there was no light absorption due to the SOA particles at the two wavelengths of their instruments, 355 and 532 nm. The LACIS (Leipzig Aerosol Cloud Interaction Simulator) optical particle spectrometer (OPS) was used to determine a RI value of 1.45 for α-pinene/ozonolysis SOA. LACIS is a laminar flow tube connected to a white-light optical particle spectrometer. The RI value was not determined directly: the OPS measures the amount of scattered light, which depends on the RI at a given mobility diameter. Measurements were taken for succinic acid (RI = 1.41) and ammonium sulphate (RI = 1.53), while the RI of α-pinene/ozone SOA of 1.45 fell between these values. Lambe et al. used a real time CRD photoacoustic spectrometry measurements at 405 and 532 nm to study the influence of oxidation level on RI values (61). They found that the real part of the RI decreased with increasing oxidation level. The effect of the aging of α-pinene/ozone SOA with ammonia on the RI values was studied by Flores et al. using a system very similar to an IBBCEAS which they called Broadband Cavity-Enhanced Spectroscopy (BBCES), with a measurement range of 360 to 420 nm (64). They found the average RI value increased from 1.50 to 1.57 when the particles were aged by exposure to ammonia over a 15 hour period. This could have important real world implications as particles are aged over time.

The aim of this chapter is to investigate the optical properties of the α-pinene/ozone SOA system in the near-UV and blue spectral regions. In particular, the work will focus on how the SOA mass yield, extinction, Angstrom exponent (AE) and refractive index evolve over time under different reaction conditions. The influence of the reactant concentration, presence of an OH scavenger, and relative humidity on the optical properties of SOA is studied, and our findings are compared to the results of other studies in the literature.

4.2. Experimental Methods

Reaction procedure and conditions

Several experimental parameters were varied to investigate the effect on the optical properties, including (a) the reactant concentrations, (b) the effect of cyclohexane, an OH scavenger, and (c) the influence of water vapour (including as a criegee scavenger), on the α-pinene/ozone SOA system. The different experimental conditions are outlined in Table 4.1.

Table 4.1 List of experiments for the α-pinene ozonolysis system.

Experiment number	Date	α-pinene mixing ratio (ppbv)	Ozone mixing ratio (ppbv)	Conditions
1	24/04/15	300	300	Reference experiment
2	30/04/15	400	400	Higher concentration
3	05/05/15	300	300	Cyclohexane
4	12/05/15	600	600	Highest concentration
5	22/05/15	300	300	70 % relative humidity

These experiments were performed in conjunction with Sakthivel Kartigueyane, a master's student visiting from Laboratoire Interuniversitaire des Systèmes Atmosphériques (LISA) in Paris. α-pinene and cyclohexane were added to the chamber via the impinger as described in Chapter 3 and water vapour was added as previously described. Experiments followed the same initial procedure as in Chapter 2. To promote homogeneous mixing of the sample in the chamber, the fans in the chamber were turned on before and left on for 10 minutes after the addition of reactants to the chamber. The compounds were added in the following order: first, any compounds that would change the reaction pathway were added (i.e. water vapour or OH scavenger), approximately 20 minutes later, α-pinene was added, a further 20 minutes were allowed for mixing and to establish a spectroscopic baseline, and then ozone was added.

Introduction of ozone

Accurate control of the initial ozone concentration was necessary. Ozone concentrations in the chamber were monitored with a Thermo ozone monitor. However, the initial concentration of ozone could not be monitored directly because mixing in the chamber was not instantaneous and the ozone would immediately begin to react with the α-pinene. Instead, a calibration curve was determined of ozone concentration against the ozone generation time (Figure 4.3). Pure O_2 flowed into the generator at a fixed flow rate of 2 L min^{-1} and an electrical discharge converted a portion of the oxygen to ozone. Ozone was added to the chamber four times. The ozone generator produced a constant concentration of ozone at a given flow rate. The r^2 fit value of the calibration curve was 0.996, showing that the addition time could be used to accurately add the desired concentration of ozone to the chamber.

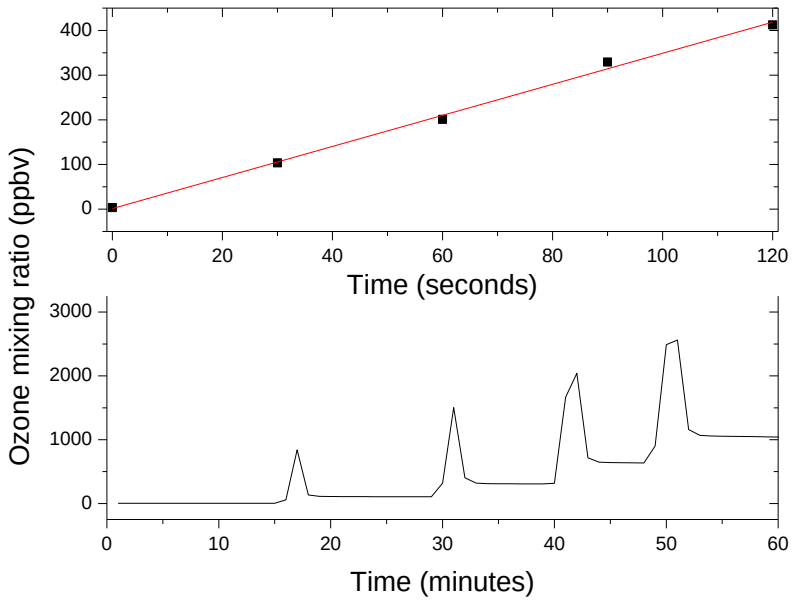

Figure 4.3 Top: the dependence of stable ozone concentration on the duration that ozone was added. Bottom: the time profile of multiple additions of ozone into the chamber. The large peaks are a result of the close proximity of the sampling point to the injection port.

Gas phase absorption

The IBBCEAS measures the extinction caused by both gas and particle species in the chamber and cannot differentiate between scattering and absorption. For the

α-pinene/ozone system, primary reactants do not absorb in the spectral range of the IBBCEAS system. The absorption of α-pinene is negligible above 250 nm (69). This simplifies analysis of the resulting SOA extinction data as there is no α-pinene absorption structure present in the region of interest. Ozone has a structured absorption spectrum below about 340 nm, but its absorption cross section is small in this region and its contribution to the overall extinction is not significant at the concentrations used in these experiments.

Particle size distributions

The SMPS measures the electrical mobility of particles and by doing this is able to produce a size distribution. By using an assumed density of the particles we can estimate the mass of the particles formed in the chamber. SOA densities range from 1.07 to 1.69 μg m^{-3} (70). A density of 1.2 g cm^{-3} for α-pinene SOA has been widely reported and used (68; 71; 72). The density of SOA can change over the course of an experiment as gas phase species with differing molar masses condense onto the surface of existing particles. However, various studies have reported differing aging effects on density. In experiments with mass concentrations similar to ours, the density was found to be constant, although higher densities have also been reported in some circumstances and high mass loads are known to cause a decrease in density (70; 73). In this study, we use a constant particle density of 1.2 g cm^{-3} in order to be able to compare results. In Figure 4.4 the change in particle number and mass concentration is shown over time. The ozone was added to the system at time = 0 min and is followed by instant and rapid formation of particles, as expected (45). The time resolution of the SMPS is three minutes per scan. As particle formation occurs rapidly, some of the initial phase of the reaction may be missed by the SMPS measurements.

The size distribution evolves during each SOA experiment, as shown in Figure 4.5. Particle size increases as smaller particles coagulate with one another and explains the observed decrease in the number concentration of particles. The median particle diameter (MPD) is a commonly used metric for describing particle size, although it must be remembered that this number is only representative of a distribution of sizes (74) (Figure 4.5).

Sometimes instabilities were seen in the SMPS and other measurements. For example, there is a series of rapid changes to the mass and number plots after 68 minutes in Figure 4.5. The same instability is seen in the ozone concentration and to a lesser extent in the IBBCEAS extinction data, Figure 4.6. There is no obvious reason for these changes. There were no reported electrical faults in any of the systems and no additional changes were made to the experimental system. A possible explanation for this is that the fans in the chamber were turned on at this point, but not recorded. This could cause agitation of the particles in the chamber which could change local concentrations, especially near the sampling ports for the SMPS and ozone monitor. This may be why the effects are not as pronounced in the IBBCEAS measurements, which takes its measurements across the entire length of the chamber and would be less effected by variation of local concentrations in the chamber. Where such instabilities occur in individual experiments, the analysis only extends up to the point when the instabilities are evident.

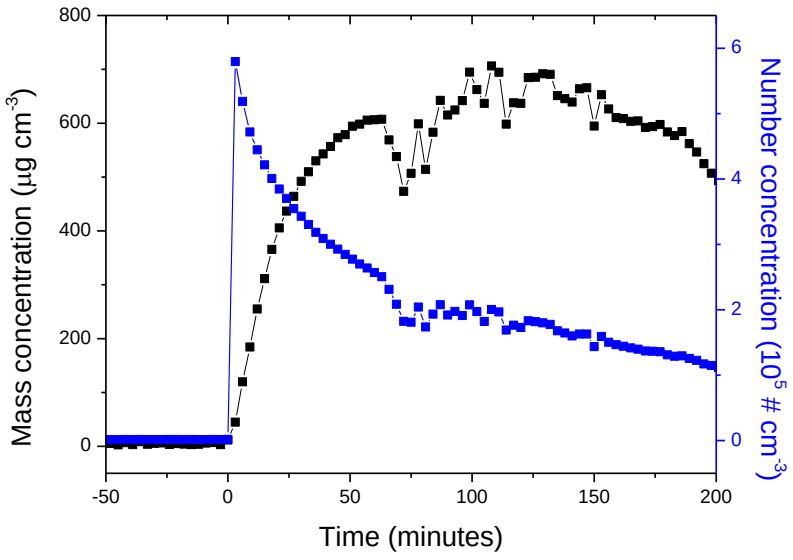

Figure 4.4 The time profile of the mass concentration and particle concentration during an α-pinene ozonolysis (Experiment 1). Ozone is added to the system at 0 minutes.

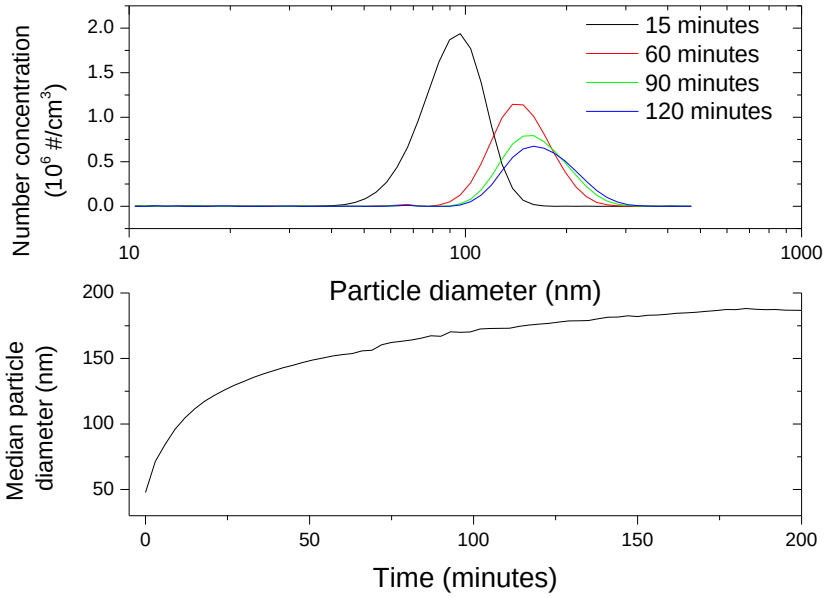

Figure 4.5 Top: the size distribution at selected times over the course of the experiment. Bottom: the temporal profile of the MPD. The size increases rapidly over the first 20 minutes of the reaction.

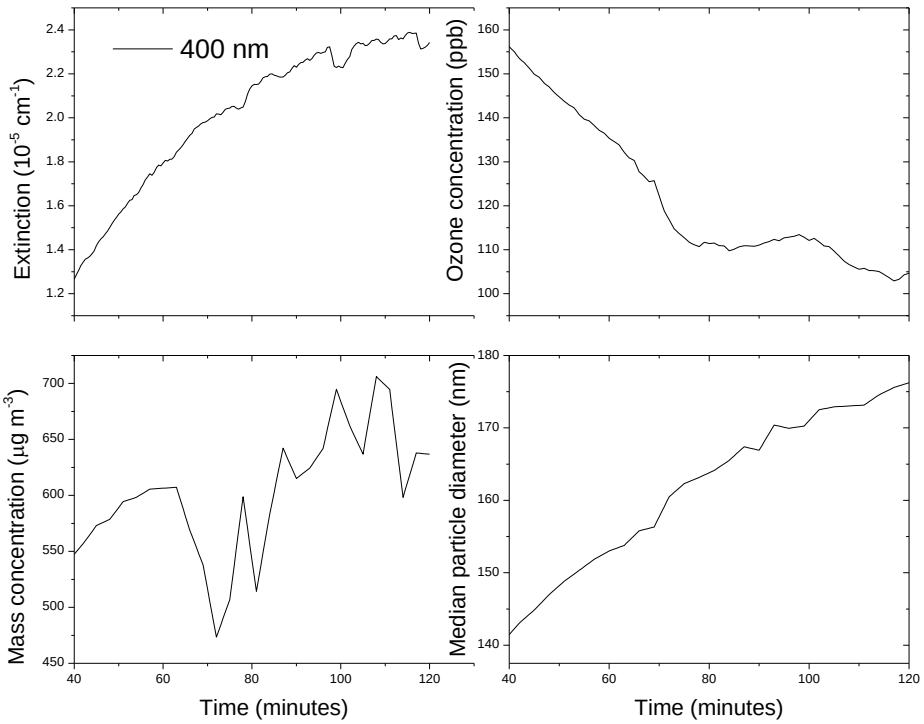

Figure 4.6 Temporal profiles of extinction, ozone concentration, mass concentration and particle diameter during the instability event.

Refractive index

The SMPS was used in conjunction with the IBBCEAS extinction measurements to determine the SOA RI. To do so, the measured extinction was compared to the extinction calculated by using Mie theory. Mie theory uses the number distribution from the SMPS and an assumed RI. Although other models for the physical structure of the particles exist, we assume homogeneous spheres for the Mie calculations in common with most studies. The RI was identified as that value that produced the minimum difference between the calculated and measured extinction values. The continuous spectral range of the IBBCEAS allows us to monitor the RI values over both time and a wide spectral range. This is in contrast to most previous measurements that took place either at longer wavelengths, a small number of discrete wavelengths, or both, Table 4.2.

Table 4.2 Reported RI values for α-pinene/ozonolysis SOA.

Refractive index	Wavelength (nm)	Reference
1.44	>350	Schnaiter et al. (75)
1.45	visible	Wex et al. (76)
1.458	355	Nakayama et al. (77)
1.411	532	Nakayama et al. (63)
1.4-1.53	670	Kim et al.(68)
1.45-1.51	405	Lambe et al. (78)
1.5	360-420	Flores et al.(79)
1.49	532	Redmond and Thompson (67)

Using a representative literature value of 1.45 for the RI, the Mie extinction was calculated for the particles formed from 300 ppbv of α-pinene and 300 ppbv of ozone after 60 minutes. Figure 4.7shows the comparison between the IBBCEAS extinction and the Mie based extinction. It is apparent that there is a large difference between the experimental and calculated spectra. When the Mie calculations were used to retrieve the RI from the experimental measurements, the best fit diverged widely from the literature consensus, giving a RI value of 1.7. This

value was far outside any reported values for the RI for this SOA in this or any other wavelength region. The following section considers possible causes for this discrepancy and solutions to treat the data in a reasonable fashion.

There are three plausible explanations for the observed discrepancy between the calculated and measured extinctions. These are: (1) inaccuracies in the extinction measurement, (2) an incorrect algorithm for the Mie calculations, or (3) inaccuracies in the SMPS measurements used in the calculations. Each possibility will be examined in turn.

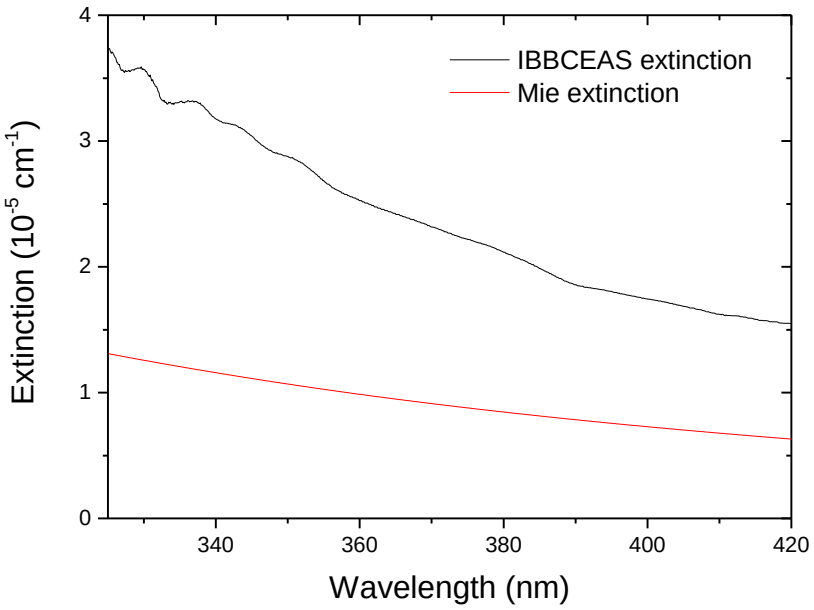

Figure 4.7 Comparison between the experimental extinction spectrum and that calculated from Mie theory using a RI value of 1.45. The large difference between the calculated and measured extinction is discussed in the text.

The first possibility is that the IBBCEAS measurements were inaccurate. The IBBCEAS data could be inaccurate in terms of their wavelength or the extinction values. The wavelength was considered not to be a large source of uncertainty as its calibration is a standard procedure and uncertainties in wavelength are very small. The measured IBBCEAS extinction depends on the reflectivity of the mirrors

Equation 2.3**,** which must be calibrated for quantitative measurements. Mechanical instabilities could misalign the optical system or alter the effective mirror reflectivity. Alternatively, the calibration of the mirror reflectivities could be inaccurate. To ensure measurement quality, a daily mirror reflectivity calibration was performed to account for any long-term changes in the reflectivity. The mirror reflectivity was found to be reasonably stable from one calibration to another, suggesting that neither the calibration procedure nor temporal changes in cavity alignment were the cause of the discrepancy. Moreover, the accuracy of the IBBCEAS extinction measurements was good, as seen from a comparison of the measured absorption cross sections against those reported in the literature. In general, the IBBCEAS results agree with published absorption cross sections to within 7 % percent. Examples include the absorption cross sections of benzaldehyde Figure 2.18 and acetaldehyde (Figure 4.8). In the latter case, we note that acetaldehyde was used during aerosol experiments as an OH scavenger; as such, it was determined using the same mirror reflectivity calibration values as the aerosol. These cross sections were determined using the same technique used to measure the aerosol extinction.

Considering the agreement to within a few percent between our results and the literature reported spectra, and that the mirror reflectivity was calibrated daily to ensure against longer term drifts, inaccuracies in the IBBCEAS measurements can be excluded as the source of the observed discrepancy.

Another possible source of error was the code used to calculate the extinction based on Mie theory. The Mie theory code, as with most Mie theory algorithms, made a number of assumptions about the particles: that they were spherical, homogenous and internally mixed. This is generally true for particles in the accumulation mode (80). The code was developed for this project and was validated against a code that had been used previously during similar IBBCEAS measurements of aerosol optical properties. The code was applied during a campaign in the SAPHIR chamber in Jülich in Germany in which ammonium sulphate was used as a model aerosol (81). The CRI of ammonium sulphate is well known (e.g., $1.52 + 1 \times 10^{-7}$ i at 680 nm (82)). Using this CRI value and size

distribution measurements from an SMPS, the extinction coefficient calculated with the code was in reasonable agreement with extinction measurements by an IBBCEAS and other instruments. These considerations therefore indicate that the Mie calculation code was likely free of errors.

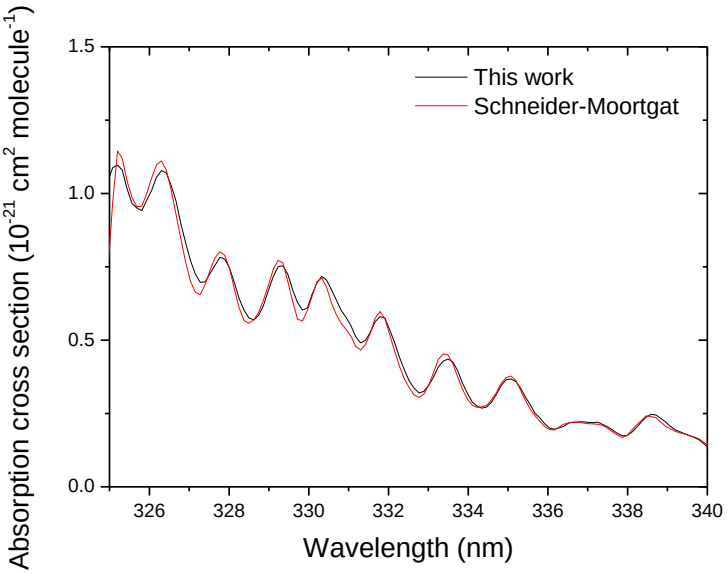

Figure 4.8 Comparison of the acetaldehyde absorption cross section spectra from this work and from Schneider and Moortgat (83).

The third likely source of the discrepancy lies in the accuracy of the SMPS measurements used in the Mie calculations. The SMPS model used, TSI 3034, is stated for use under both low and high particle concentrations up to a concentration of 2.4 x 10^6 particles cm^{-3}. The highest particle concentration in our experiments was 3.7 x 10^5 particles cm^{-3} and within the normal operating range of the instrument. However, the SMPS had not been calibrated for a number of years, neither in terms of its sizing nor in terms of its counting accuracy. It had also not been compared against other similar instruments. Although particles could be lost to the tubing connecting the SMPS to the chamber and internally within the SMPS, this is considered unlikely because the sample inlet tubing was the standard antistatic tubing used for particles sampling with specific properties to minimise

such losses. The mechanism for size selecting the particles in the SMPS for counting could also result in inaccurate size distribution measurements. Particles are sized according to their electrical mobility assuming a charge of + 1. However, up to 10 % of particles above 200 nm may carry double charges. This would shift the apparent distribution to smaller sizes that interact much less strongly with light. Nevertheless, the effect of multiply-charged particles is well known and the sample distribution is corrected automatically by the SMPS software. This, too, is an unlikely cause of the discrepancy.

Other possible sources of uncertainty are that the SMPS could be inaccurate in its sizing measurement, or in the counting accuracy of the condensation particle counter (CPC) unit. The likelihood of these measurements contributing to our SMPS results were discussed with experienced SMPS users at the Leibniz Institute for Tropospheric Research. Particle sizing was regarded as relatively robust and an unlikely source of a large deviation as seen in our Mie-observation discrepancy. On the other hand, they did consider it likely that the CPC unit and particle counter could explain the large difference. This is particularly true for using SMPS instrumentation in relatively dirty environments, as in our atmospheric simulation chamber studies. Under circumstances where the SMPS could get relatively dirty, there could be significant undercounting of particles. As this explanation is both consistent with the technical experience of other SMPS users, and is the only reasonable remaining explanation for the discrepancy, we consider that undercounting the number of particles in each size bin by the SMPS led to subsequent underestimation of the extinction in Mie calculations.

This discrepancy between the IBBCEAS measured and Mie calculated extinctions has been noted previously in our chamber-IBBCEAS system. Previously, the extinction of ammonium sulphate was measured in the CRAC chamber using the IBBCEAS and the extinction was calculated using the same code as here (84). The discrepancy between the data in the work by Isaac et al. was handled by scaling the calculated Mie extinction spectra to match the experimental spectra. Doing so is equivalent to scaling the magnitude of the number distribution by the same factor. The Mie extinction calculations were scaled by a factor of 2.69 to match the

experimental extinction. This factor was used in subsequent measurements to correct the calculated extinction. The assumptions in this approach are that (a) the same factor applies across the size distribution, (b) the factor is relatively stable in time and (c) all sizes are affected equally. Although it was not possible to test these assumptions directly, the following sections show that the resulting RI for α-pinene SOA, a system that has been studied by numerous groups, is broadly in line with the reported literature values for the RI (63; 67; 68; 75-78; 85). We therefore consider this to be a sufficiently reliable approach to studying the aerosol optical properties.

4.3. SOA evaluation and extinction

The experiment for the oxidation of 300 ppbv of α-pinene with 300 ppbv of ozone will be referred to as the 'reference' experiment for the remainder of this chapter. Every other experiment will be compared to this to see how varying the experimental conditions affect the physical and optical properties.

Particles formed almost instantaneously once the ozone was added. This is seen in the rapid increase in extinction measured by IBBCEAS, and also by the sharp change in the particle mass concentration, Figure 4.4. The extinction of the evolving α-pinene SOA is shown in Figure 4.9 and increased over time, following the increase in concentration, particularly of larger particles.

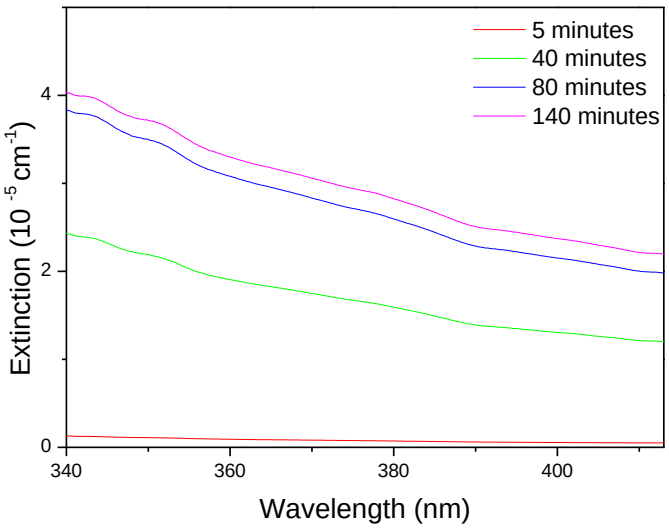

Figure 4.9 The change in sample extinction spectra following the addition of ozone to α-pinene in the chamber. The time refers to minutes after ozone was added.

4.3.1. Particle absorption

The spectral shape of the extinction shown in Figure 4.9 is typical of purely scattering particles and increases monotonically to short wavelengths. SOA from α-pinene ozonolysis is widely reported as being purely scattering in the spectral region of interest here (63; 73; 75; 86). A UV/Vis spectrometer was used to analyse the particles and to confirm their non-absorbing nature. Particles were collected onto a filter for 30 minutes, as described in Chapter 2.

Previous α-pinene SOA filter samples have been extracted into either water or methanol (25; 41). As there was no consistently used solvent, both solvents were tested here. The filter was cut in half; one half was extracted into methanol and the other half into water. Each filter was added to 10 ml of the solvent in a sample vial, which were capped and sonicated for 5 minutes each. The filter was then removed. During the sonication process, small pieces of the filter became suspended in the solution. These were removed by passing the solution through a 0.45 PTFE filter. This is a typical method used to extract particles into solution (87-90). Each sample was run through a Thermo Scientific Evolution 60 UV/Vis spectrometer as described

in Chapter 3. Updyke et al. measured the effects of ammonia aging of SOA species from biogenic and anthropogenic sources. They extracted particles from filters in the same manner as that undertaken in this work, i.e. placed filter in solvent, sonicated and pass solution through syringe filter (88). This solution was used to measure pure absorbance in a dual-beam spectrometer. The particles collected onto the surface of the filters are dissolved into solution. This ensures that there are no scattering effects associated with the UV/Vis spectrometer measurements (89). This type of UV/Vis spectrometer measurements have also been recorded by Nguyen et al. when determining the formation of nitrogen and sulfur containing absorbing particles (91). They did not report any scattering effects in their measurements. This enabled us to use the UV/Vis spectrometer to measure the absorption due to the SOA particles.

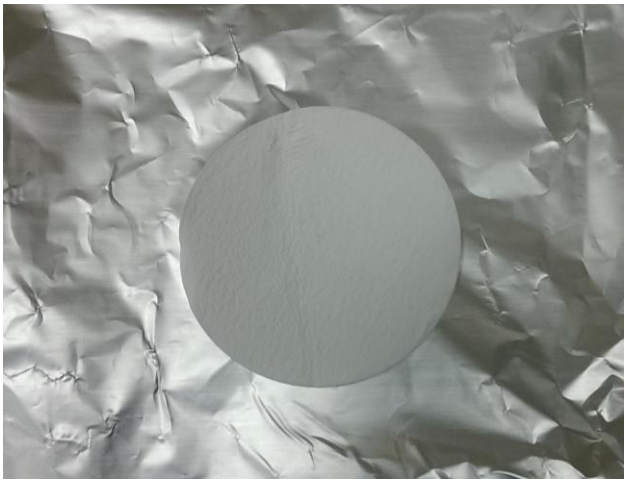

Figure 4.10 Filter after SOA was impacted on it for 30 minutes. Note, there is no presence of any visible SOA, indicating their non-absorbing nature in the visible region.

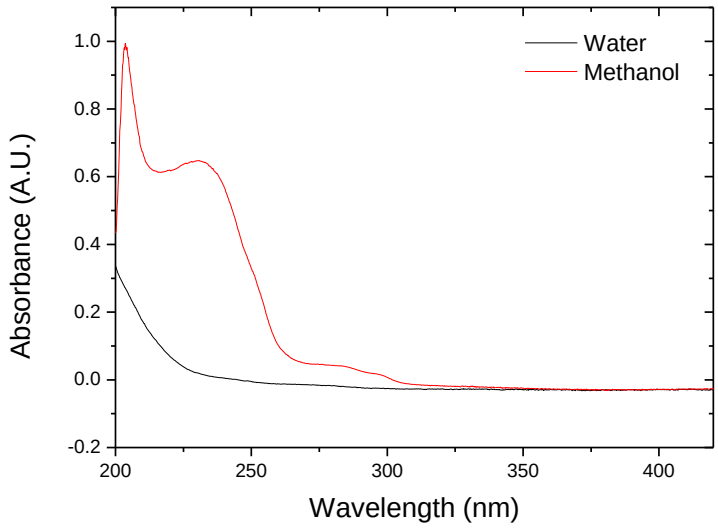

Figure 4.11 Absorbance spectrum of the α-pinene ozonolysis SOA after extraction into either water or methanol. The spectra indicate that there is no appreciable absorbance above 300 nm.

Figure 4.11 shows the absorbance of the SOA particles. Above the lower limit of our spectrometer's spectral range (325 nm), the absorption is minimal. This indicates the non-absorbing nature of the SOA particles formed in the reaction between ozone and α-pinene. At deep-UV wavelengths (below 300 nm), there is increased absorbance in the sample extracted into methanol. There have been instances of methanol forming new products when reacting with aerosol species but this does not affect our conclusions about the non-absorbing nature of the SOA above about 300 nm (92). Based on our measurements as well as other literature reports, we conclude that the particles are purely scattering in the near-UV and visible spectral regions.

As all the extinction caused by α-pinene ozonolysis SOA is purely scattering between 320 and 420 nm, we can already describe one of the fundamental optical properties, the single scattering albedo (SSA). The SSA is the ratio of the scattering to the extinction:

$$\omega_0 = \frac{\sigma_s}{\sigma_s + \sigma_a} \qquad (4.1)$$

where σ_s is the scattering coefficient, σ_a is the absorption coefficient and $\omega_0$is the SSA. As the particles are purely scattering, the SSA is 1 in our region of interest. This indicates that these particles will tend to have a negative radiative forcing effect and therefore contribute to a cooling effect on climate.

4.3.2. Optical properties

Angstrom exponent

An empirical formula to describe the approximate spectral dependence of extinction caused by aerosols was first proposed in 1929 (93):

$$\mathrm{AOD}_\lambda = \beta\lambda^{-\alpha} \quad \textbf{(4.2)}$$

where AOD_λ is the aerosol optical depth at a given wavelength $\boldsymbol{\lambda}$, β is the Angstrom turbidity coefficient which equal AOD at $\boldsymbol{\lambda}$ = 1 µm and α is the Angstrom exponent. This allows the calculation of an approximate AOD at any wavelength. The extinction at any point, assuming it is purely scattering, can also be determined in this manner by substituting the extinction coefficient, $\boldsymbol{\varepsilon}$, in place of the AOD (94). The AE is commonly calculated by applying Equation 4.2 at two different wavelengths:

$$\propto = -\frac{\ln\frac{\varepsilon\lambda\,1}{\varepsilon\lambda\,2}}{\ln\frac{\lambda\,1}{\lambda\,2}} \quad \textbf{(4.3)}$$

where, $\boldsymbol{\varepsilon_{\lambda 1}}$ is the extinction at wavelength 1, $\boldsymbol{\varepsilon_{\lambda 2}}$ is the extinction at wavelength 2 and, $\boldsymbol{\lambda_1}$ and $\boldsymbol{\lambda_2}$ are wavelengths 1 and 2 respectively. The IBBCEAS measurement of extinctions over a broad wavelength region gives a wide range of values for the extinction. Calculating the slope of a double natural log plot of extinction against wavelength, over the full wavelength range, gives α. This linear relationship remains true for unimodal systems, such as the single particle source in this chamber experiment. In bimodal or multimodal samples, such as those found in real world environments, the relationship deviates from linearity due to multiple particle sources. In such instances a second order polynomial fit is applied to find a more accurate value for AE (95). The extinction data at 60 minutes was used to first determine the AE. The double natural log plot of extinction against wavelength was

graphed and the slope was determined for the range of 340 to 420 nm. The AE value is the negative of the slope, Figure 4.12. The value of the (negative) slope is 3.55 with an r^2 of 0.993. The AE was calculated throughout the entire course of the experiment to monitor the change in AE value as a function of time, Figure 4.12. The AE starts off with an extremely high value of 6.5 and decreases throughout the experiment. It falls to 3.7 within 30 minutes and gradually decreases to 3.1 over the next 110 minutes.

As well as being used to estimate extinction values at a given wavelength, AE has also been used as a qualitative indicator of particle size. In 1955 a relationship was proposed by Junge that relates particle size and the AE(96):

$$\frac{dN}{d(\ln r)} = c.\, r^{-\upsilon} \qquad \textbf{(4.4)}$$

Here *dN* is the number concentration of particles with radii between r and r+dr, *c* and *υ* are fitting parameters and *r* is the particle radius. In 1983, Tomasi et al. showed that the relationship between the AE and the parameter υ was $\alpha \approx \upsilon + 2$ for particles in the size range of 100 nm to 1 μm (97). This relationship has been used numerous times to estimate particle size distribution (98-101). In Brazil, the AE and MPD were measured for smoke particles. The AE was calculated from the AOD values as determined by the AERONET Sun Photometer between 338 and 437 nm. A Passive Cavity Aerosol Spectrometer Probe was used to measure the particle sizes (94). A good correlation was found between the AE and MPD values.

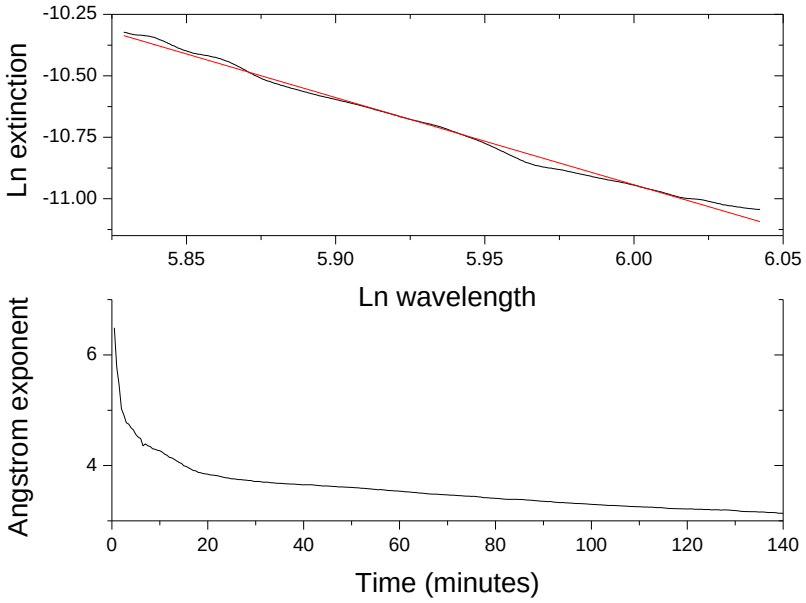

Figure 4.12 Top: the linear fit of the double natural log plot of extinction and wavelength after 60 minutes. Bottom: the change in AE over time.

Large AE values are associated with small particles and vice versa. Values of $\alpha \leq 1$ typically indicate coarse particles, with radii ≥ 500 nm, whereas $\alpha \geq 2$ are typical of fine mode particles with radii ≤ 500 nm (101). The values in our experiments are initially very high (< 6) and then decrease to a steady level of ca. 3 after 30 minutes. This is consistent with an initial period of very small particles (< 100 nm) which increase rapidly in size, followed by a levelling off of particle growth. The MPD, Figure 4.4, follows the trend indicated by the AE measurements, i.e. small particles initially, rapid particle growth within the first 20 minutes, and then much slower particle growth over the next 110 minutes.

The AE was plotted against the MPD to investigate the correlation between these values. The slope for the entire 140 minutes experiment was obtained and is shown in Figure 4.13. A high r^2 value was found in this plot, 0.9324, demonstrating a reasonable correlation between AE and MPD. Nevertheless, there is a large deviation for approximately the first 30 points in the graph; that corresponds to the first 15 minutes of the experiment. This is a period of very rapid particle formation and growth, Figure 4.5. Once the initial 15 minutes of the experiment were removed, the r^2 increased to 0.984. This deviation from the generally linear

AE/MPD relationship in the first 15 minutes may arise because the size distribution changes faster than the SMPS time resolution. The SMPS measures particle sizes sequentially from smallest to largest over a three minutes period. In contrast, the IBBCEAS measurements integrate the whole intensity spectrum over a shorter time period of 30 s. The three minute time period needed to record one scan with the SMPS would not accurately capture a size distribution that is evolving rapidly. This gives an indication of potential issues with the SMPS measurements in the initial particle formation period. As the determination of the RI depends in part on the SMPS measurements it was decided to only determine the RI values from 15 minutes after initiating ozonolysis.

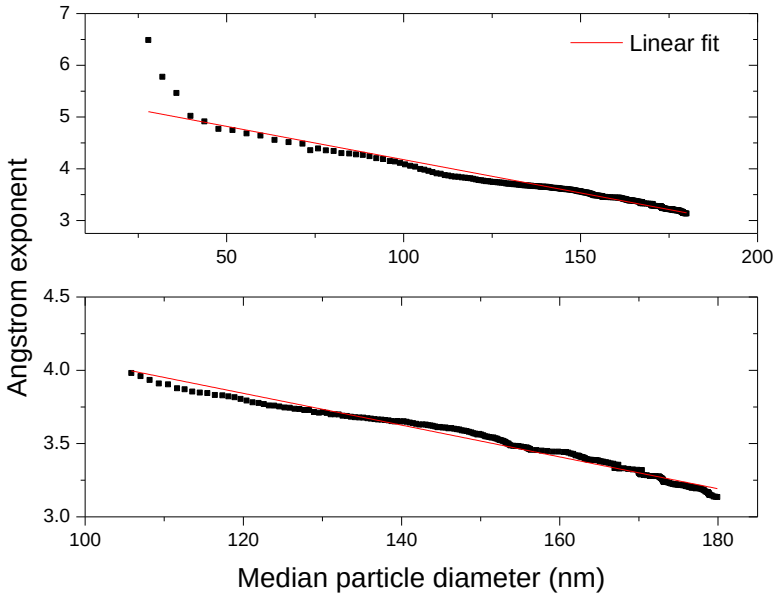

Figure 4.13 Top figure shows plot of AE and MPD for the full, 140 minute, reference experiment. The bottom figure shows AE after 20 minutes.

There are a number of wobbles present in the AE against MPD plot, Figure 4.13. Possible reasons for these features include skewed size distributions or errors in the AE values arising from extinction errors or SMPS data. If the SMPS distribution was skewed then the MPD may not be a true reflection of the dominant particle size. The number distribution profile at a number of times is shown in Figure 4.5. The

particles grow in size and the spread of the distribution increases with time. Even with the increase in the distribution width, the distribution has the same level of skewness throughout the course of the experiment. Skewness is the measure of asymmetry present in a distribution. The skewness for a number of the measured distributions were determined, Figure 4.14, and found to be between 0.5 and 1 during the experiment. Skewness values between -2 and 2 are considered not to be skewed (102). As the distribution did not become appreciably skewed during the course of the experiment the MPD should reflect the most dominant particle size and would not be the issue causing the wobbles.

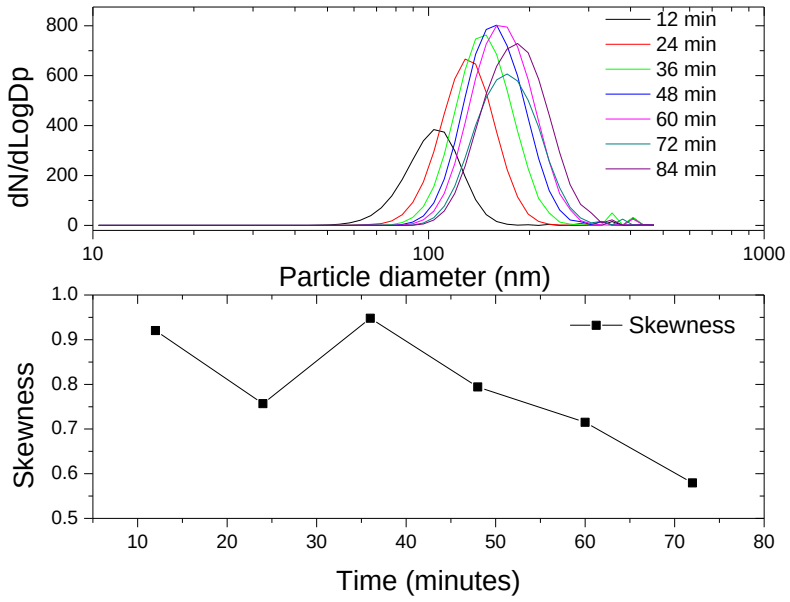

Figure 4.14 Top figure displays a number of size distributions for the particles a number of minutes after particle formation. The bottom figure is the level of skewness for the distributions.

There is some instability in the extinction, particle number and particle diameter after 68 minutes which has previously been discussed, Figure 4.7. As the extinction values and the MPD are affected by these instabilities it is likely that this is a factor in the presence of these wobbles.

Refractive index

RI values change as a function of wavelength, Figure 4.15 (77; 103). The RI values presented here cover a continuous spectral region, 340-420 nm, which is in contrast

to most previous RI determinations, which have been measured at one wavelength or a few discrete wavelengths, Table 4.2. Some of these other measurements were made with a nephelometer which can have up to 7 specific wavelengths of measurement, and are mostly outside of the near-UV wavelength region (63). Our results show that the RI increases towards shorter wavelengths, as expected (77). The shape of the RI values is not smooth, however; there is also spectral structure present that is likely an artefact of the optical system. A quadratic fit was found to give a good fit to overall spectral shape of the RI spectrum and was applied to the RI data to remove this structure and better show the trend in RI with wavelength. A quadratic progression of the RI values has also been used to describe the increase of RI for water from 280-420 nm (104).

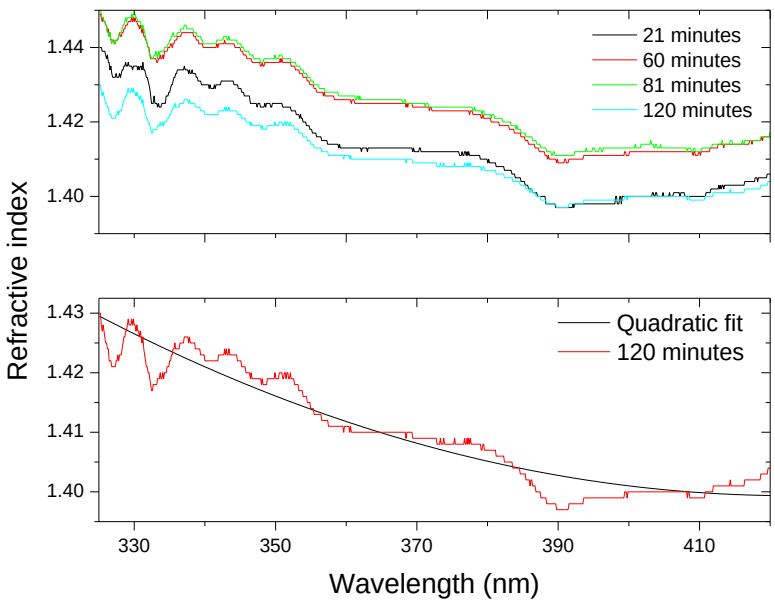

Figure 4.15 Top: RI spectra at different times for the reference experiment. Bottom: Illustration of a quadratic line through the experimentally-derived RI values at 120 minutes.

The residual structures bear strong similarities to the mirror reflectivity spectrum, Figure 4.16, peaks and troughs occur at similar wavelengths, especially around 380 nm. While the positions of these structures are not a perfect match, the overall trends of the residual suggests that the structure present in the RI spectrum is due

to small contributions of the mirror reflectivity structure present in the IBBCEAS extinction.

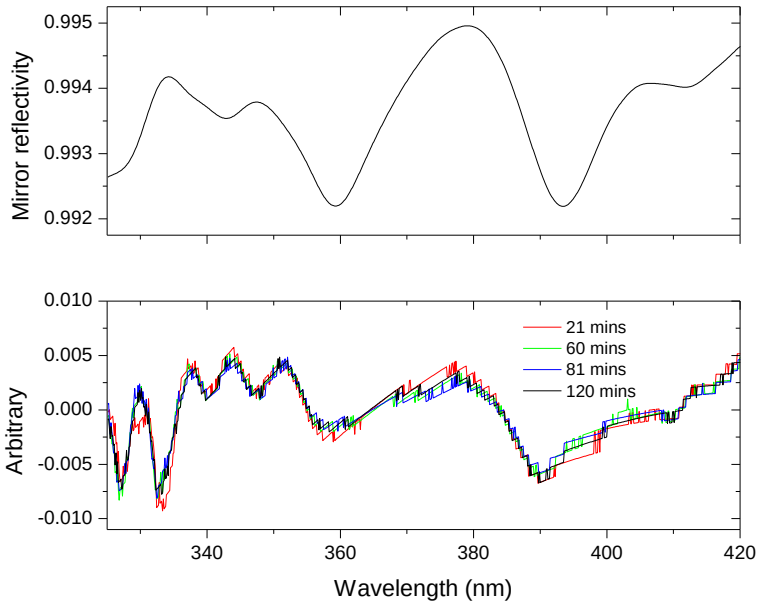

Figure 4.16 Top: IBBCEAS mirror reflectivity spectrum. Bottom: Residual RI spectral structure at 21, 60, 81 and 120 minutes after subtracting the quadratic fit from the experimental values.

The residual structure is present to the same degree in all four RI measurements. The effects are small and are easily removed.

With the residual structures removed, we are able to better show changes in RI values for the range of 325-420 nm, Figure 4.17. The shape of the spectral dependence of RI is nearly identical at 60, 81 and 120 minutes, but different for 21 minutes. The shape difference could imply that either the size distribution is still evolving too quickly at this time for the SMPS measurements or that the larger number of smaller particles affects the RI values at shorter wavelengths. The differences in the values for the 81 and 120 minute RI stem from the instability of the SMPS data after 68 minutes Figure 4.6. Prior to the instability, the mass concentration had stopped increasing. Assuming there would not have been any increase or decrease in mass concentration and number distribution, at 81 minutes the values are the same as if there was no instability. The SMPS data at 60 minutes agree very closely with the values at 81 minutes, Figure 4.17.

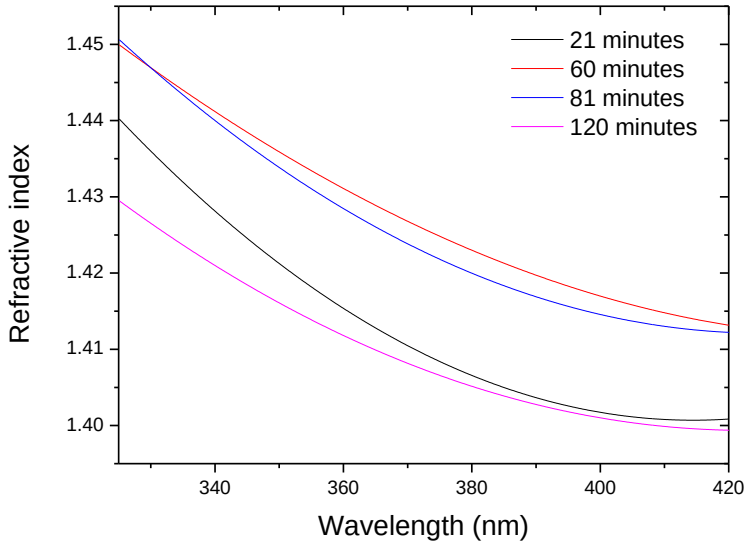

Figure 4.17 Quadratic fit to the four RI plots shown in Figure 4.15.

There is a reasonable agreement between the RI values at 60 and 81 minutes. These results were compared with literature results for this time period, Table 4.3. As most of these results are only at singular wavelengths our results can only be directly compared at these wavelengths.

The values determined here are broadly similar to reported data but tend to be slightly lower. This may be due to the assumption that was made as to the SMPS correction factor. The values from the Schnaiter et al. paper were determined by comparing the extinction as measured by a nephelometer at three wavelengths, 450, 550 and 700 nm, and the theoretical extinction determined through the use of Mie theory. The RI was first estimated by comparing the α-pinene SOA to similar species, pinic acid diethyl ester, cyclopropanedicarboxylic acid diethyl ester and octanedioic acid diethyl ester. The theoretical extinction was then matched to the measured nephelometer data to determine the RI. As the nephelometer only records at a limited number of wavelengths Schnaiter et al. could not account for the wavelength dependence of RI. As the RI values increase towards shorter wavelengths, their RI values found using nephelometer measurements at 450, 550 and 700 nm may be too low. The Flores paper is the only paper that has highly

sensitive measurements over a spectral range similar to ours although they only reported an average RI. It should be noted that the values determined by Lambe et al. have a large range of values at one wavelength. They found that the RI varied with a change in the O/C ratio of the particles. The lower the O/C ratio the higher the RI, 1.45 was at high O/C and 1.51 was at low O/C ratio. They determined the RI values for a number of hydrocarbons and found the changes to be precursor specific. For α-pinene they determined the Δ (n) / Δ (O/C) was -0.11.

Table 4.3 Comparison of RI values calculated for the reference experiment with literature values

	Literature		**This work**	
Wavelength (nm)	**Values**	**Reference**	**Wavelength (nm)**	**Values**
>350	1.44	Schnaiter et al. (75)	350	1.433
355	1.458	Nakayama et al. (77)	355	1.431
405	1.45-1.51	Lambe et al. (78)	405	1.413
360-415	Average value over range is 1.5	Flores et al. (79)	360	1.427
			370	1.422
			380	1.419
			390	1.416
			400	1.414
			410	1.412
			415	1.412

4.4. Concentration Effects

In the reference experiment, 300 ppbv of α-pinene reacted with 300 ppbv of ozone. In the following experiments, the starting concentrations of the α-pinene and ozone

were both elevated to 400 ppbv and 600 ppbv of each species. This allowed the influence of concentration on the formation and optical properties of α-pinene/ozonolysis SOA to be tested. The results were then compared to the reference experiment.

The maximum mass concentration of the SOA increased strongly as the concentration of the starting material increased, Figure 4.18. This is expected as higher precursor concentrations result in more low volatility products that can condense onto existing aerosols. There is also an increase in SOA mass yield (ϒ), Figure 4.18, which is defined as follows:

$$\Upsilon = \frac{\Delta[\mathrm{SOA}]}{\Delta[\alpha\text{−pinene}]} \qquad \textbf{(4.5)}$$

where *Δ[SOA]* is the change in SOA mass concentration between the beginning and end of the reaction and *Δ[α-pinene]* is the change in α-pinene during the same time. The mass concentration of the SOA was monitored continuously throughout the experiment whereas the α-pinene concentration was not directly monitored. There have been a number of experiments that have reported the loss of α-pinene due to reaction with ozone. Lambe et al. found that 90 % of α-pinene was used after 45 minutes (61). Another experiment states that after 1 hour the particle mass is at a maximum and that α-pinene is at 15 % of its original concentration (40). We use this assumed concentration (15 % of the original level remaining after one hour) to determine the yield of the experiments. Oxidation of α-pinene is fast and largely complete within 1 hour, whereas the loss rate of particles to walls is modest. Accordingly, and in common with other studies, the SMPS data was not corrected for wall losses (36; 43).

The SOA mass yield increases with increasing precursor concentrations, as seen in previous studies (43). The aerosol yield of the oxidation of α-pinene has been studied extensively, and an increase in yield with precursor concentration has been repeatedly shown for both general SOA systems and for α-pinene/ozone SOA (40; 43; 44; 105-107). This increase in yield, Figure 4.18, arises because the increased particle surface area promotes greater condensation of lower volatility species from the gas phase.

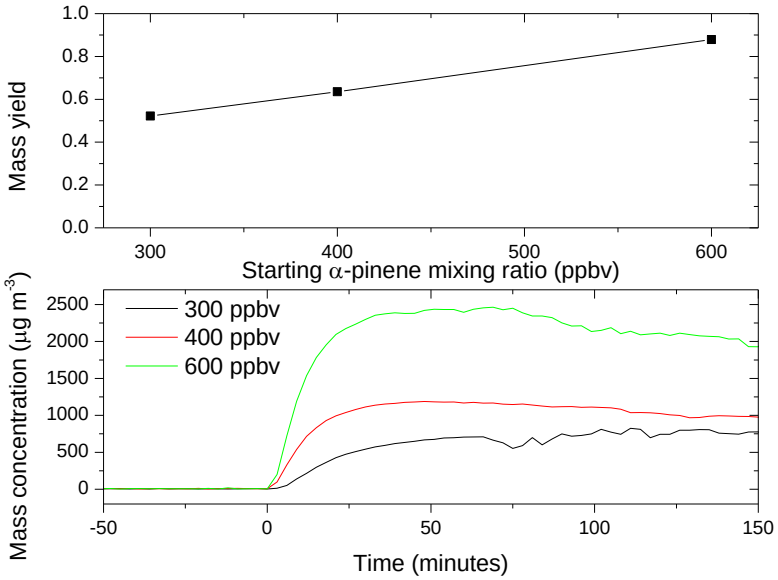

Figure 4.18 Top: SOA mass yield for different precursor mixing ratios of α-pinene. Bottom: Time profile of the SOA mass concentration at three different precursor concentrations. The ratio of α-pinene and ozone was always 1:1. The rate and extent of SOA formation increases at higher mixing ratios.

The yield for the 300 ppbv starting mixing ratio is consistent with values for experiments with similar mass concentration. It has also been shown that higher mass concentration lead to increasingly high yields, such as those seen here (68).

The extinction of the particles also increases with increased concentration, as expected for the high mass concentrations and larger particles. The extinctions spectra 20 minutes after the introduction of ozone are shown in Figure 4.19. Large differences in extinction spectra are seen between the experiments. As previously observed, the extinction increases towards shorter wavelengths in keeping with the non-absorbing, purely scattering nature of the particles. Some residual structure from the mirror reflectivity is present in the extinction spectra, but does not affect the overall conclusions that can be drawn from the data.

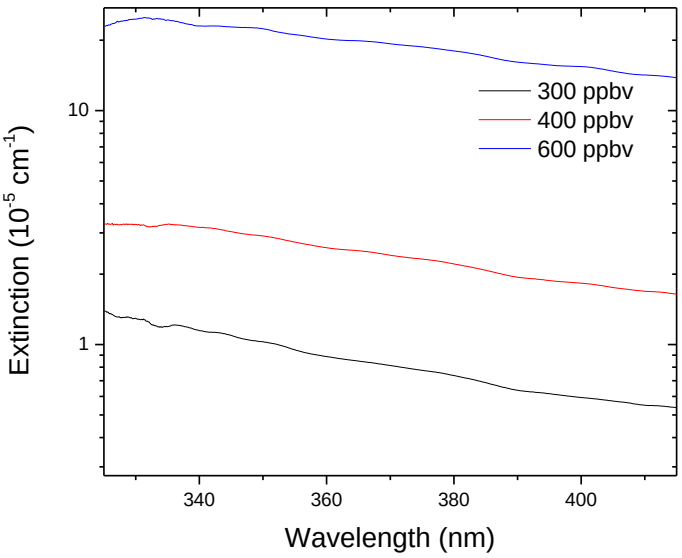

Figure 4.19 Extinction spectra for the 300, 400 and 600 ppbv α-pinene/ozonolysis experiments after 20 minutes.

The slopes of the extinction spectra decrease with increased starting mixing ratio, Figure 4.19. This leads to a smaller AE value at higher precursor mixing ratios. The mixing ratio experiments show the same trend in both AE and MPD as seen previously, although there is some divergence in the AE time profiles at early times. For example, in the 600 ppbv experiment the AE values remain constant from 5 to 15 minutes, Figure 4.20. There is no clear reason for this behaviour or why it is present here and not in the other experiments. The fans in the chamber were turned off within this period for all experiments. The fans could influence the particle size distribution, for example, by forcing larger particles to the walls, or by the effect of turbulence on the rates of coagulation of particles. Such changes in the size distribution would influence the extinction spectra of the particles and hence the AE. It is possible that the high mass concentration, high number distribution and large particle at this early time in the 600 ppbv experiment may be the reason that this shape change only appears here and not in the other experiments.

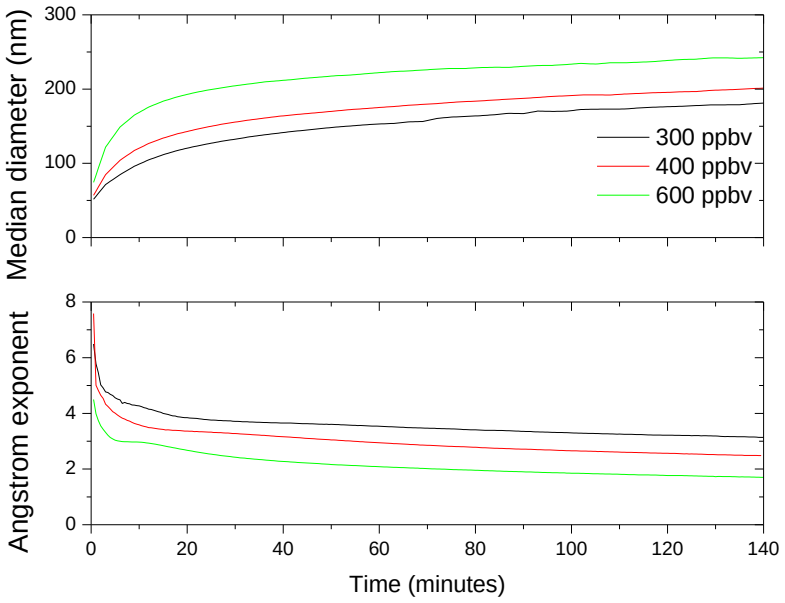

Figure 4.20 Comparison between the time profile of MPD and α for experiments with three different precursor mixing ratios.

When AE was plotted against the MPD for the reference experiment, Figure 4.13, the relationship between them was weakest during the first 15 minutes. For the 400 and 600 ppbv experiments there were similar periods of rapid initial particle growth, Figure 4.20. After this early period was removed from the AE vs. MPD plots for these two experiments. The AE varied linearly with MPD. The linear fits are quite good, with goodness of fit values of 0.984, 0.992 and 0.996 for the 300, 400 and 600 ppbv experiments respectively. The goodness of fit for the points increases as the mixing ratio of precursor increases.

In Table 4.4 a series of AE are compared to particles of the same MPD from the different experiments. Despite having the same MPD, the AE varies significantly for different experimental conditions. For example an AE value of 3.5 corresponds to both 126.7 nm, for the 400 ppbv experiment, and 148.8 nm for the 300 ppbv experiment. This could be a result of the different number distribution widths, since the MPD does not fully characterise the distribution. In order words, although the MPD may be the same for different experiments, the particle size distribution could have varying distribution widths with a wider spread of smaller and larger particles

at these times. However, the table shows several values with similar distributions, as indicated by the MPD and the distribution width. In these cases with similar physical properties, the observed differences in the AE could reflect different chemical compositions and thus differences in RI between the different reactions conditions.

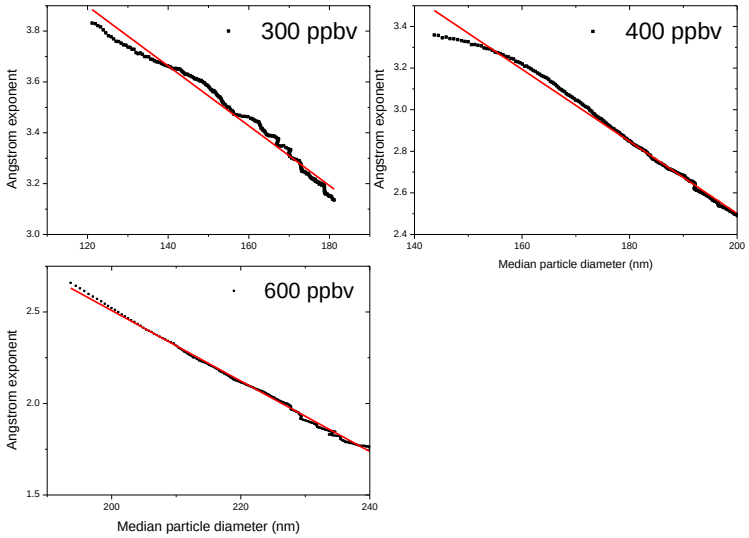

Figure 4.21 AE and MPD plot for the three concentration experiments after the initial period of rapid particle growth was removed from the graph.

Table 4.4 Comparison of AE values and their corresponding particle diameter at similar MPD. Also included is the FWHM to represent the particle number distribution width.

Starting mixing ratio (ppbv)	Angstrom Exponent	Median Particle Diameter (nm)	Distribution width at FWHM (nm)
300	3.829	121.9	52
400	3.557	126.7	47
600	3.319	121.7	60
300	3.598	148.8	65
400	3.342	148.8	57
600	3.000	148.8	62
300	3.145	180.4	93
400	2.851	180.5	85
600	2.641	183.7	71

Refractive index

The RI spectra for α-pinene SOA was reported for our reference experiment in Figure 4.17. However, a direct comparison with the experiments at 400 and 600 ppbv is probably not meaningful because the RI depends on the progress of the reaction. RI values change with aging and can depend on the rate of reaction, and specifically on the production of OH radicals. For example, the different RI values after 21 minutes for the three mixing ratio experiments are shown in Figure 4.22.

The RI values increase at higher precursor mixing ratios at this early reaction time, as does the MPD. A similar increase in the RI of SOA from α-pinene ozonolysis with higher mass concentrations has been observed before (68). The RI values for each of the three mixing ratio experiments increases as a function of time. The temporal change in the RI at 410 nm is shown in Figure 4.23 for the three experiments. Several factors may contribute to this effect. It is known that there is a link between larger dry aerosol particles and a larger real part of the RI (108; 109). A decrease in the imaginary part of the RI was also found, but this does not interest us here as the SOA particles are considered to be purely scattering. In addition, oxidative aging affects the density of the particles and chemical speciation (63; 110; 111). This

aging can occur in both the gas and particle phases, and the relatively lengthy reaction time allows significant aging to occur in our experiments. Particles age due to their interaction with, amongst other things, the OH radical, which is released during the ozonolysis of α-pinene. OH is the dominant atmospheric oxidant and has been found to increase the concentration of first generation SOAs (112). OH can then react with volatile species, to form lower volatility compounds and alter the composition of the particles (113). The change in the composition of the particles can also influence their optical properties. The particles are non-absorbing, as our dissolved filter samples indicate. This has also been shown during prolonged (29.5 hour) aging of this type of SOA in the SAPHIR chamber in Jülich, Germany (85).

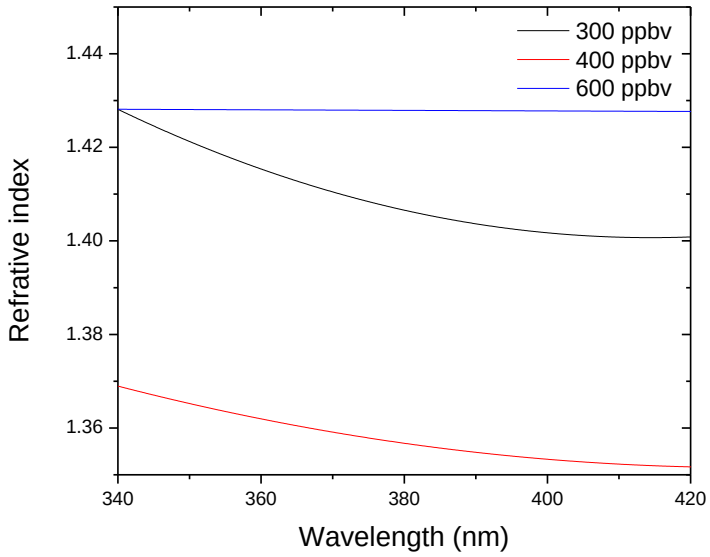

Figure 4.22 The spectral dependence of the RI values for the three mixing ratio experiments after 21 min of reaction. Curves show the best quadratic fits to the experimental data, and not the experimental data itself.

The CRI of SOA has been reported to change during particle ageing (79; 85). In a study that looked at the aging effects of SOA from α-pinene ozonolysis with ammonia, the average values of the real component of the RI rose from 1.50 to 1.57 after a 15 hour exposure to ammonium. It has been shown that oxidation

reactions between OH radicals and semivolatile organic compounds occur as a result of the α-pinene/ozone reaction. The formation of these new particles change the composition of the SOA in the chamber over time (113). It is believed that this aging affect is responsible for the increase of RI over time. This increase in the RI values with OH aging has be attributed to the increased oxidation of the SOA (85). As OH is formed during the ozonolysis of α-pinene, there is a good indication that these particles undergo oxidative aging by reacting with this species. To investigate the possible effects of OH radical on the SOA particles, cyclohexane (an OH scavenger) was added in excess in the experiment described in the next section.

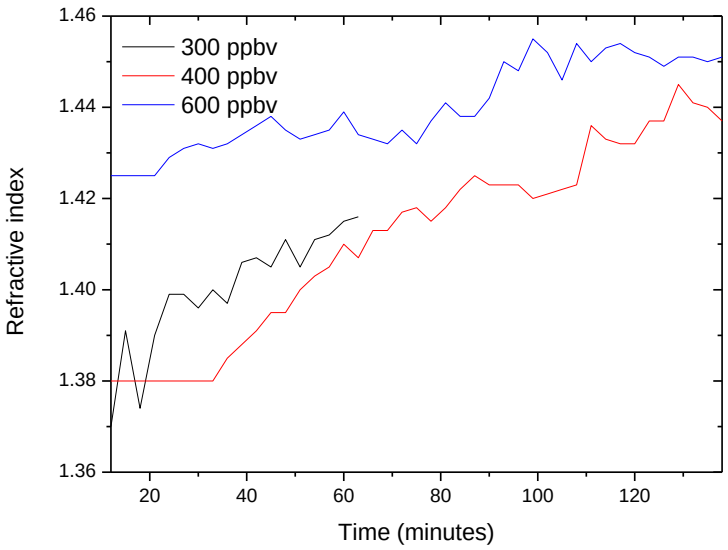

Figure 4.23 Temporal change in RI at 410 nm. Values after 63 minutes for the 300 ppbv experiment were removed for the reasons given in Section 4.2.

4.5. The role of OH reactions

The reaction pathway for the ozonolysis of α-pinene was discussed at the start of this chapter. In the initial phase of the reaction, criegee intermediates are formed when ozone reacts across a double bond. Criegee intermediates are short-lived carbonyl oxides with two charged centres which can go on to form the OH radical. Both OH radicals and criegee intermediates are highly reactive species and can strongly influence the physical, chemical and optical properties of SOA. Once OH is

formed during the reaction it reacts with α-pinene and its ozonolysis products at a much faster rate than ozone. Studies have found that at 298 K α-pinene reacts with ozone with a rate constant of 1.07 x 10^{-16} cm^3 $molecule^{-1}$ s^{-1} and with the OH radical with a rate constant of 5.38 x $10^{-11}cm^3$ $molecule^{-1}$ s^{-1} (114; 115). For this reason, once OH is formed, it becomes the most oxidising species in the system.

To investigate the influence of these species on the production and optical properties of SOA, a scavenger species was added to the chamber prior to the addition of ozone or α-pinene. Common OH radical scavengers include alcohols, aldehydes or cyclohexane (37). In our experiments, cyclohexane was used as a scavenger and was in large excess (20ppmv). This mixing ratio was 160 times higher than that of α-pinene, while its respective rate coefficient for reaction with OH was 7 times smaller than that for α-pinene (116). Therefore, the excess if cyclohexane ensures that almost all OH would be removed by the scavenger and not by α-pinene or its products.

In our experiments, most but not all ozone is consumed during the reaction. The comparative losses in ozone in the first 20 minutes of the reaction show that ozone dominates oxidation in the early stages of both experiments Figure 4.24. After this time the ozone mixing ratios diverge. Less ozone is consumed in the absence of any scavenger, because of preferential reaction of the OH radical with the double bond consumes these primary reaction sites for ozone. In some cases, up to 50 % of the α-pinene has been measured as reacting with OH instead of ozone (36).

The mass concentration, maximum number of particles and mass yield is lower when the OH scavenger is present in our chamber experiments, Table 4.5. The drop in yield is consistent with cyclohexane experiments with similar mass concentrations (117). OH radicals have been reported to react with volatile species to form lower volatility species capable of forming SOA (113). The drop in maximum number concentration, which occurs for each experiment within three minutes of the introduction of the ozone, is more unusual. Based on the time profile of ozone, Figure 4.24, it was assumed that ozonolysis was the major factor in particle formation within the first 20 minutes. However, OH radical chemistry increases the

maximum number of particles formed within the first three minutes. OH radicals have been found to increase the concentration of first generation SOA species which suggests that even in the initial stages of the reaction there is still OH radical chemistry taking place (112). Both the maximum MPD and the size distribution in the reference and cyclohexane experiments were similar.

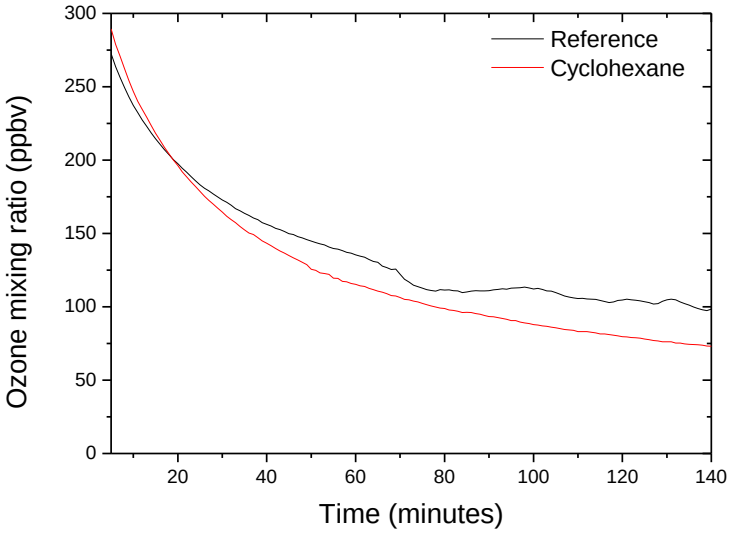

Figure 4.24 Temporal change in ozone concentration for the reference and scavenger experiments.

Table 4.5 Comparison of physical properties for α-pinene ozonolysis with cyclohexane and reference experiment.

	Reference	**Cyclohexane**
Maximum mass concentration (μg m^{-3})	732	545
Aerosol Yield	0.52	0.39
Maximum number concentration (10^5 # cm^{-3})	5.78	3.03
Maximum median diameter (nm)	181	183

Multiple studies have shown that the addition of OH scavengers to the system has an inconsistent effect on the SOA yield. Docherty et al. and Jenkin reported that scavengers had no affect on the yield, while Iinuma et al. reported an increase in yield (118-120). In general, higher volatility products are formed via OH/scavenger reactions and do not condense as readily to the particle phase (36). Several reasons have been given for the observed inconsistency in SOA yield. The position of the double bond in the molecule and the impact on the HO_2:RO_2 ratio in the reaction have both been cited as possible causes (37). Typically HO_2 and RO_2 radicals are formed as a result of the OH radical/scavenger interaction. Scavengers that produce a higher amount of HO_2 radicals tend to have higher SOA yields. Traditional scavengers that have been used include carbon monoxide, 1 or 2-butanol and cyclohexane (37). These scavengers affect the HO_2:RO_2 balance differently: CO produces the most HO_2, 1-and 2-butanol the next largest amount and cyclohexane the least. As the ambient environment tends to have a high HO_2 to RO_2 ratio, CO is the preferred scavenger for simulating real world conditions. However, in large simulation chambers, such as the one used in our experiments, the high levels of CO needed would pose a safety hazard. In contrast to CO, cyclohexane increases RO_2 radical concentrations owing to the exclusive production of the cyclohexylperoxy radical (118). It should be noted that the products of OH radicals and cyclohexane have no direct effect on the SOA mass concentration. Some studies have shown that the use of cyclohexane reduces the yield. This effect on yield depends on the mass loading: no effects were observed at low concentrations typical of the atmosphere, but at higher mass concentrations there was a decrease in yield (45). The mass concentrations in our experiments are similar to those that saw drops in yield.

Particle size differences are reflected in the different AE values in the presence and absence of a scavenger. The MPD is larger in the scavenger experiment than the reference experiment for the first 100 minutes. This is reflected in a lower AE value for the scavenger experiment in this time period. After this the MPD and AE values are nearly identical in the two experiments, Figure 4.25. The particles formed for

both the reference and cyclohexane have similarly sized particles at this time, although the mass concentration is lower.

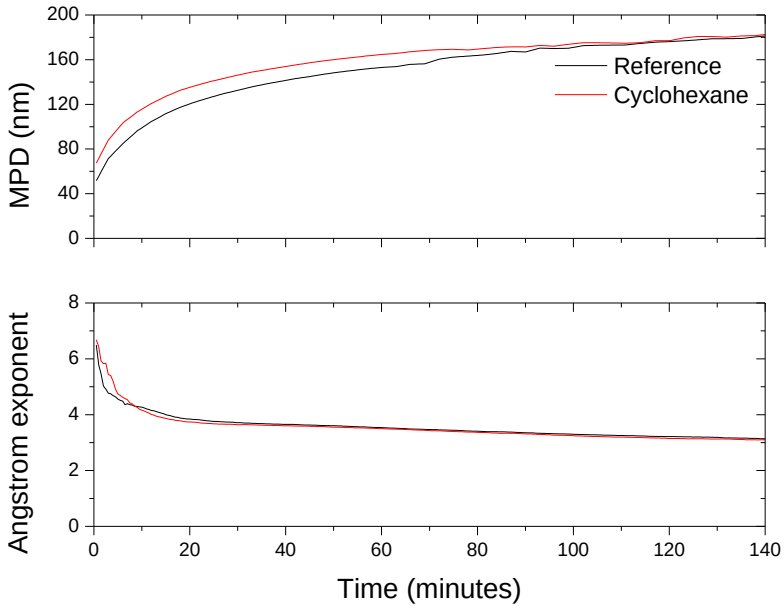

Figure 4.25 Temporal trends in the particle diameter (top) and Angstrom exponent (bottom) in the reference and cyclohexane experiments.

The extinction spectra after 120 minutes for the reference and cyclohexane experiments are shown in Figure 4.26. The particle sizes in both experiments are similar at this time, Figure 4.25. As stated, the presence of the OH scavenger reduces the number and mass concentration. However even with few particles present in the cyclohexane experiment, the measured extinction is between 14 (340 nm) and 18 % (415 nm) higher than the reference experiment. This higher extinction likely results from different chemical composition of the particles as a result of the removal of OH radicals. Using the Master Chemical Mechanism, Jenkin determined a number of potential chemical species as a result of the α-pinene/ozone reactions in the presence and absence of an excess of cyclohexane (118). The Jenkin's study showed that there would be a decrease in the levels of pinonaldehyde and acetone and an increase in pinonic acid, pinalic-3-acid, pinic acid, 10-hydroxypinonic acid and formaldehyde. The decrease in pinonaldehyde is a possible reason for the drop in SOA mass concentration. Pinonaldehyde has a low

vapour pressure (0.0315 mmHg), which could lead to SOA formation (121). As well as being predicted to be a major product of the α-pinene/ozone reaction, it is also one of the main components of the SOA formed (122). The increase in pinonic acid, pinalic-3-acid, pinic acid, 10-hydroxypinonic acid and formaldehyde may cause the increase in scattering although we could not find any evidence to support this.

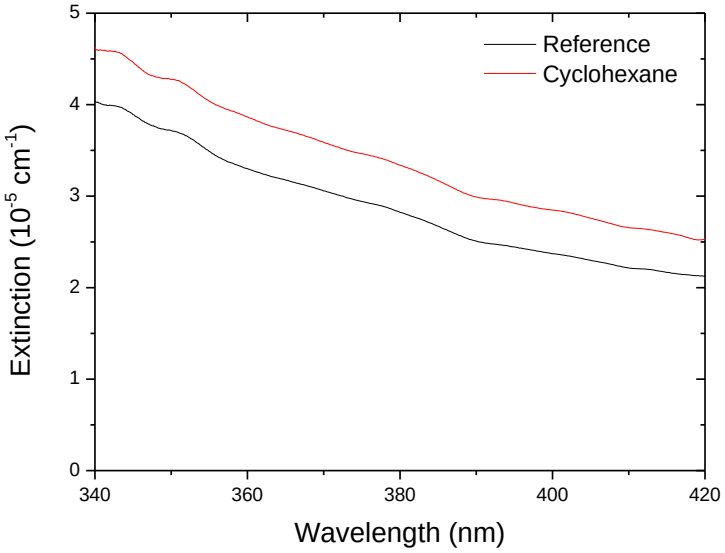

Figure 4.26 Extinction spectra 120 minutes after ozone addition to the chamber, showing the effects of OH scavenger (cyclohexane) compared to the reference experiment.

The affects of these scavengers on the optical properties of the SOA are evident in the refractive index values. The RI values are larger by 0.02 on average at every wavelength, Figure 4.27. The size of the particles with and without the addition of cyclohexane are similar, Figure 4.25, so any differences in the RI likely arise from different chemical composition of the particles. Lambe et al. have reported the effect of oxidation on the RI (78). They stated that oxidative effects change the RI or SOA by varying the mean molecular mass, the density as well as the polarizability of the particles. They found that the RI values decreased as the O/C ratio of the species increased. While we did not monitor the ratio of O/C in our experiments, the presence of an OH scavenger removes an important oxidation pathway. This

could reduce the overall O/C ratio in the system. Our findings, of increasing RI values in the presence of cyclohexane, differ from those of Kim et al. They used a polar nephelometer to determine the refractive index values of SOA from α-pinene ozonolysis with and without cyclohexane at 670 nm (68). Within the resolution of their measurements, they found that the scavenger made no difference to the SOA refractive index. However, their stated uncertainty of ± 0.03 may have been too large to determine the 0.02 difference in refractive index that we report here. Moreover, the influence of scavengers on the SOA refractive index at 670 nm may differ from that below 420 nm.

It was previously stated that oxidative aging caused by reactions with OH increase the RI values with time (112). However, even with the OH radicals removed from the system the RI increased throughout the course of the experiment. Not much attention has been given to the potential oxidative aging effects of ozone. A study by Kourtchev et al. collected filter samples in an experiment that looked at the potential aging of the SOA formed by the ozonolysis of α-pinene. The molecular composition of these SOA particles was investigated through the use of ultra high resolution mass spectroscopy (54). They found no difference in the molecular composition of the SOA after long term exposure to excess ozone. A different study that looked at the aging effects ozone on the SOA formed from α-pinene oxidation, was performed by Denjean et al. in 2015 (123). They did not measure any change in the CRI when the SOA was aged with exposure to excess ozone. Their measurements had an uncertainty of ± 0.03, so the smaller changes in RI that we observe here would not be apparent. It is still unclear by what means the RI values of the particles increase over time in the absence of OH aging.

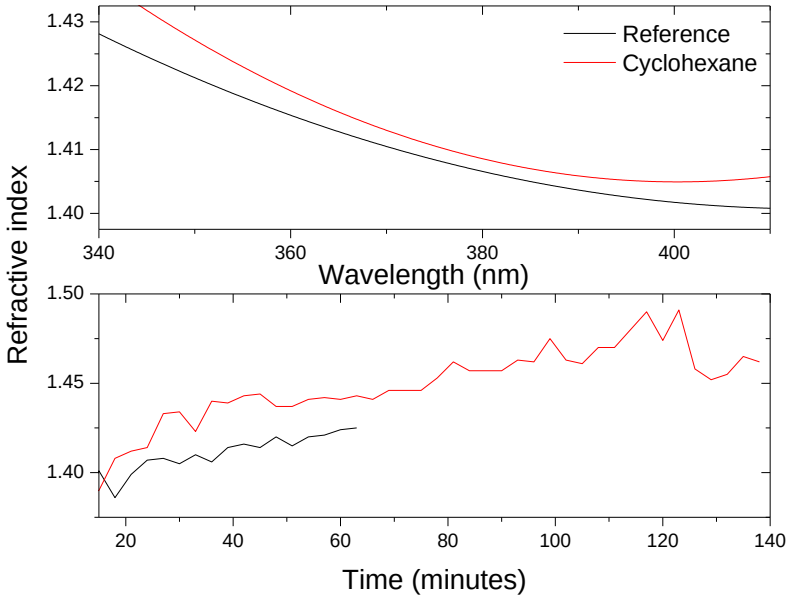

Figure 4.27 Refractive index spectra (after 21 minutes) and time profile of the refractive index at 340 nm for the reference experiment and that with cyclohexane as an OH scavenger.

4.6. Relative Humidity Effects

Relative humidity (RH) is an important variable that can influence the production and properties of aerosol. Whereas chamber experiments are often performed under extremely dry (RH < 5 %) conditions, the RH in the lower troposphere is typically much higher. To test for the effects of high RH on the formation of SOA, water vapour was added to the chamber prior to the ozonolysis of α-pinene. The RH in the chamber was raised to 70 %, compared to the majority of the experiments discussed in this work where the RH was below 0.5 %.

Differences in how the RH affects the particle size and mass concentrations are summarised in Table 4.6. Humidifying the sample air results in a large increase in the number of particles, but roughly equivalent mass concentration and mass yield, with a decrease observed in the median size of the particles. As the smaller particle size occurred concurrently with an equivalent mass concentration and yield, the

particles must necessarily be significantly more abundant if the density is similar. This is what is seen in Table 4.6.

Table 4.6 Physical particle properties in the reference (RH ca. 0.3 %) and high RH reaction environments. The maximum number concentration occurs near the start of the experiment, while the other values are reported for the end of the experiment.

	Mass concentration (μgm^{-3})	**Mass yield**	**Maximum number concentration (10^5# cm^{-3})**	**Median particle diameter (nm)**
Reference	732	0.52	5.78	180
High RH (70 %)	747	0.53	11.37	165

A number of studies have investigated the influence of RH on particle formation in the α-pinene/ozone SOA system. Li et al. studied the gas-particle partitioning for organic peroxides during the α-pinene ozonolysis process and found no change in the mass concentration or yield for SOA formed at 0 % or 60 % RH (124). This is consistent with our observations. Their measured mass yield was also comparable (0.41 for 275 ppbv of α-pinene) with our yield (0.52 for 300 ppbv of α-pinene). Another study of the refractive index of oxidised α and β-pinene and toluene saw similar physical changes as in our experiments. That is, for a 20 % increase in RH Kim et al. saw a large increase in number density, a decrease in particle size, and a slight increase in mass concentration (68). However, there are other conflicting reports on the effect of high RH on α-pinene SOA formation.

The effects of relative humidity changes on SOA formation have been studied for other SOA systems. Cocker et al. investigated the effect of 50 % RH on the formation of SOA from m-xylene and 1,3,5-trimethylbenzene photooxidation and found the effect negligible (125). The SOA yield was found to increase for the photolysis of p-xylene in RH levels of 5 to 75 %, which they attributed to increased levels of HONO (125). High RH levels were also found to increase SOA formation for both toluene and xylene (126; 127). So, within general SOA formation experiments, humidity has no consistent effect on the SOA yield. The specific effects of RH on the α-pinene/ozone SOA system also have a thorough history of investigation. Jonsson et al. studied the effects of RH on particle formation for a series of monoterpenes,

including limonene, Δ-3-carene, and α-pinene (128). Ozone was used as the oxidising species in all three cases. In each case CI were also formed during the ozonolysis. Increased levels of water vapour were added to the system to measure its effect on particle formation. For α-pinene, and all of the other monoterpenes studied, increasing RH increased the number of particles, mass concentration, and particle size (128). While an increase in mass concentration at higher RH has been observed, the response of the particle number concentration is inconsistent, and may increase, decrease, or remain unchanged (35; 125; 128-130). It has been reported that during particle formation events, organic compounds can partition into the aqueous phase, which provides other possible oxidation routes that could lead to the formation of low volatility products (131). This may be a possible explanation for the increase in particle number concentration in our experiment. A number of compound types have been singled out as being especially important as aqSOA precursors, including aldehydes, acetone and monocarboxylic acids (132). Some species of these types occur in our system, including pinonaldehyde, pinonic acid and acetone, and could be the reason for the increased number of particles.

High RH increased the SOA extinction especially in the initial particle formation period, Figure 4.28 and Figure 4.29. Extinction in the first 20 minutes was up to 60 % larger across all wavelengths under humid conditions. This difference decreased to ca. 20 % after 80 minutes. The maximum mass concentration for the two experiments was similar, although the mass concentration increased more rapidly at high RH. This led to a higher mass concentration in the chamber in the initial 90 minutes of the experiment. The larger number of particles would also cause an increase in the measured extinction. However, this does not explain why the extinction remains higher at the end of the high RH experiment compared to the reference experiment, because the mass and number concentrations are approximately the same at this point. Coupled with the smaller MPD suggests that the chemical composition of the SOA changes as a result of high levels of water.

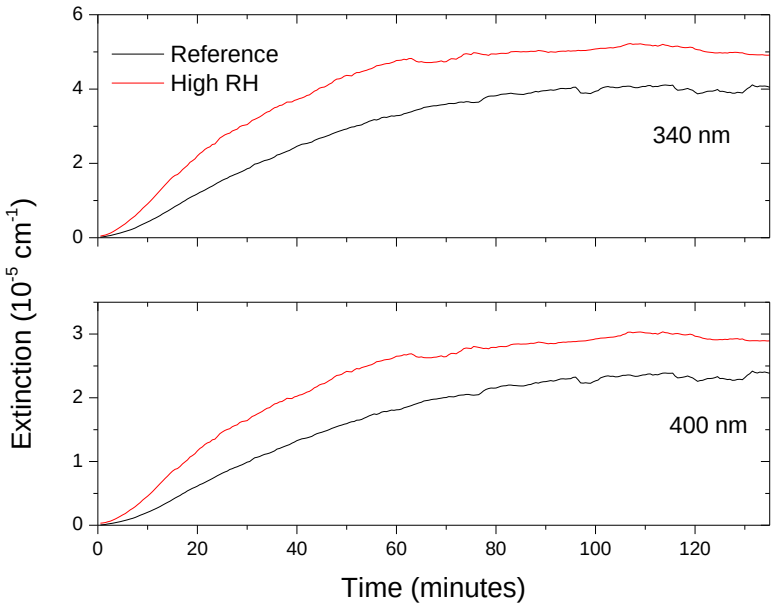

Figure 4.28 Temporal comparison of the extinction for the reference (black) and high RH (red) at 340 nm (top) and 400 nm (bottom).

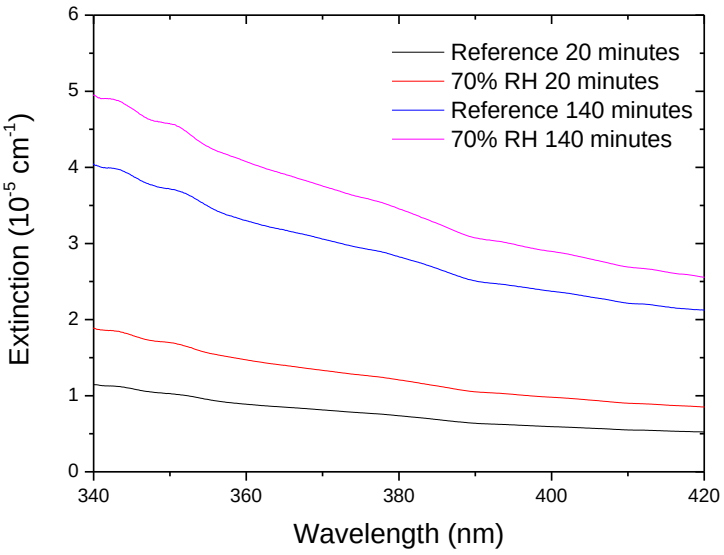

Figure 4.29 Extinction spectra for low and high RH experiments. The extinction spectra are consistently higher during high RH experiments.

The time profile of the MPD and AE is shown in Figure 4.30. The smaller median diameter under humid conditions in Table 4.6 is consistent with the higher angstrom exponents at the end of the experiments, Figure 4.30. Under humid conditions, however, the Angstrom Exponent of newly formed SOA behaves

surprisingly differently to that under dry conditions. In the early stages of SOA formation (< 5 min), the AE is initially small but increases sharply, instead of decreasing monotonically from high initial values, as in other experiments. This suggests that there could be initial formation of relatively large particles, given that AE values of 2 are typical of particles with radii above 500 nm. Although the MPD of the particles increases from small to larger particles with time, the upper sizing limit of the SMPS was 487 nm (diameter), and very large particles could be missed. However, there is also no indication that any large particles were formed in the initial phase of particle formation. Indeed, the particles grew from small to large much in the same way as in the other α-pinene ozonolysis experiments.

A study was undertaken that compared SOA size distribution in a dry smog chamber to measurements in Los Angeles of sulphate particles. Hering et al. found that the smog chamber data had a mass median diameter at 200 nm, which they attributed to the condensation mode. However, in the field measurement a mass median diameter of 700 nm was found which was attributed to the droplet mode (133). This finding is consistent with the hypothesis that high water vapour could promote the formation of a few, very large particles, which would explain our low AE values as well as why the SMPS did not show an unusual particle size distribution at an early stage of the reaction. If the water surrounding the particles then evaporated, the SOA would remain but not the large particle size.

These differences in the extinction and particle size distribution suggest that high humidity could alter the refractive index of α-pinene SOA. RI spectra were calculated based on the measured size distributions, Figure 4.31. The high RH experiment near the start of the experiment has an unusually large increase (0.133 at 410 nm to 0.14 at 340 nm) in RI compared to the reference experiment. The RI remained higher in the high RH experiment than in the reference experiment (+ 0.104 at 410 nm to + 0.119 at 340 nm at the end of the experiment). The retrieved refractive index of high RH experiments varied somewhat erratically over time and no overall temporal trend in the refractive index was evident, Figure 4.32. In contrast, the refractive index increased with aging under dry conditions and could indicate that the SOA aged differently under humid conditions.

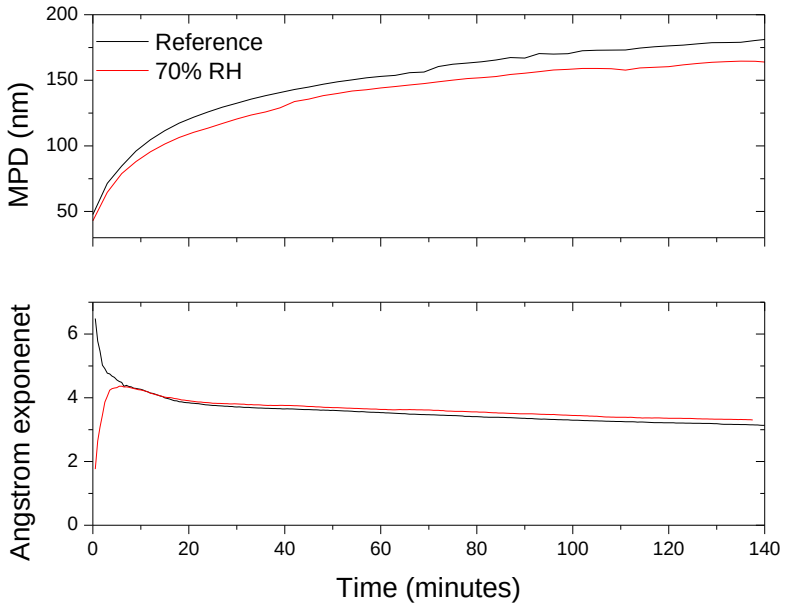

Figure 4.30 Top: Temporal trend for the MPD for the reference (black) and high RH (red) experiments. Bottom: AE values for the reference and high RH experiments over the same time.

The presence of water in the chamber would lead to the uptake of water onto the particles. Exposing aerosols to high humidity can also change their chemical composition, and physical and optical properties. Water acts as a criegee intermediate scavenger during the experiment as it reacts with CI (128; 134). This in turn has been suggested to affect the formation of low volatility products and thereby to alter the mass yield of SOA. The removal of the CI would also impact the formation of OH radicals in the system. A number of studies have focused on the optical properties of purely scattering aerosols due to changes of RH (135-137), as well as the effect of high RH on the aerosol extinction of absorbing species (138). We have also seen how the presence of water can cause an increase in the formation of low volatility species.

There is little consensus on the effect that increased RH has on the composition of the SOA particles. Pinonaldehyde is one of the major carbonyl products formed during the ozonolysis of α-pinene, but even so, there is no agreement as to whether it increases, decreases, or is unaffected by an increase in RH (139-141). One of the main additional products formed during the high RH reaction is 10 carbon multi

functional acid (128). This has been linked to the increase in SOA formation. A change in the HO_2:RO_2 balance may be involved with the formation pathway. The concentration of water has been shown to increase the self reaction of HO_2 (128; 142; 143). This would change the balance between HO_2 and RO_2. This same change in that balance was seen when the OH radical was removed. During that experiment there was an increase in the RI values, Figure 4.27. The change in this balance could be one of the reasons that there is once again an increase in the RI values.

As discussed, the presence of water vapour in the system changes the products formed. The change in the composition of the particles can have a major impact on the optical properties of those particles. Water is a CI scavenger and due to the high concentration of water vapour in the ambient atmosphere, it will dominate the reactions with the CI (35). This will change the reaction pathway. The IBBCEAS system measured higher extinctions in the high RH experiments than the low RH. A similar increase in the RI values with increased levels of RH were found in two photooxidation of α-pinene in the presence of NO_x studies (1.458 to 1.51) (77; 144).

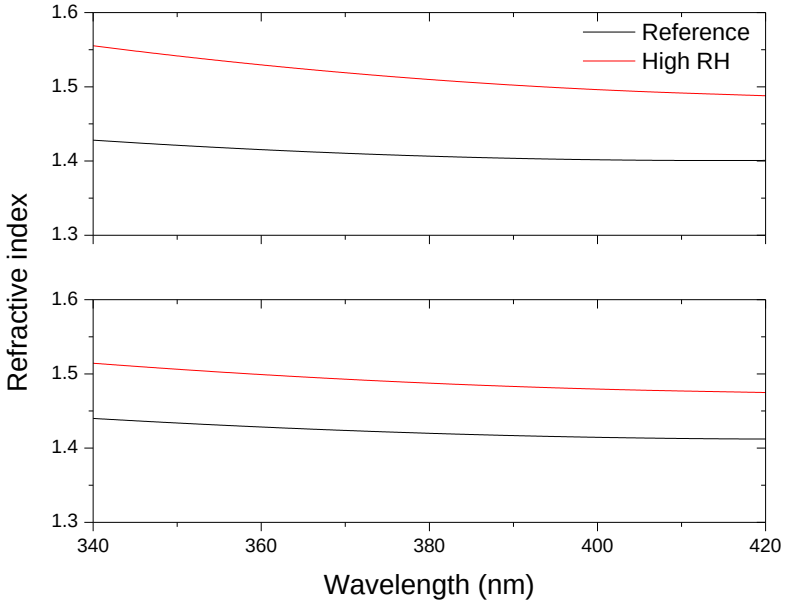

Figure 4.31 Spectral dependence of RI values at low and high RH values after 21 minutes (top) and 81 minutes (bottom).

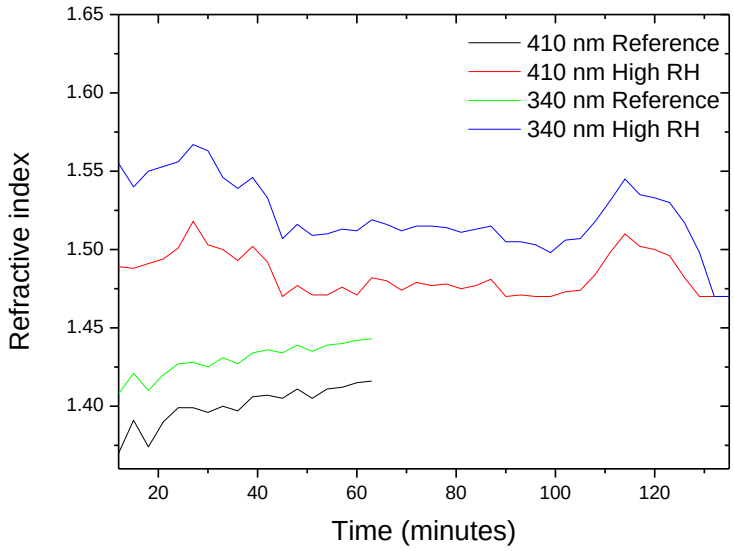

Figure 4.32 Temporal profile of refractive index values for high and low RH experiments at 340 nm and 410 nm. Data for low RH was removed after 63 minutes due to instabilities in the SMPS measurements.

Although it was not possible to provide a mechanism explaining why the RI values increased with RH, it is likely that this difference reflects a change in the reaction pathway and the products formed during the ozonolysis of α-pinene. This could result from increased concentrations of RO_2 radicals, which were present in a previous experiment that also had higher RI values, Figure 4.27. Water has been reported as being one of the largest secondary pathways for CI in the atmosphere due to its abundance (145).

4.7. Atmospheric implications

Chemical, physical or optical differences in SOA can impact on the environment in which they are located. We have seen that changing the size of particles affects not only their scattering properties but also their refractive index values. This can also be said of the changes in chemical properties. Studies have shown that a change in the refractive index value from 1.4 to 1.5 results in a decrease in radiative forcing by 12-19 % in non-absorbing aerosols such as the SOA shown in this work (68; 146;

147). The values listed in Table 4.2 gives RI values ranging from 1.45 to 1.51 in our region of interest. This spread of values is relevant to ozonolysis reactions at low RH. When the conditions of the experiment were changed, high RH or scavengers, there was a change in the RI values. Again these differences in the RI values relate to different reaction conditions and can affect the radiative forcing properties of the SOA. The values for the high RH are approximately 0.1 higher than in the reference experiment. Due to the abundance of water vapour in the atmosphere, this could be an important reaction pathway for the ozonolysis of α-pinene and would impact the radiative forcing effects of the SOA.

4.8. Conclusions

The optical properties of SOA particle formation from the ozonolysis of α-pinene under a number of different conditions were examined. Due to the increased availability of SOA particles for low volatility gases to condense on, it was demonstrated that by increasing the amount of starting material there was a corresponding increase in the mass yield. Changes in the reaction pathway of the ozonolysis through the use of scavengers caused the overall yield to decrease. The optical properties of these SOA particles were studied. Filter extracts showed that the particles were non-absorbing in our region of interest. Using the IBBCEAS the spectral dependence has been shown for the RI values of these compounds in our wavelength region. Values for RI were determined to range from 1.45 (at 340 nm) to 1.42 (at 410 nm) 81 minutes after the initial particle formation. Our measurements differ from most previously reported RI values which are typically at single wavelengths. By measuring the RI values over a broad spectral range, a better sense of the radiative forcing effects of these types of particles can be achieved, along with the angstrom exponent in the near-UV. Lastly, the size distribution, aging and composition of the SOA particles have been shown to affect their optical properties. The aging of the SOA increases as a function of time in the presence of OH. At high RH, the RI increases by a sufficiently large amount that it would have a major impact on the radiative forcing affect of the SOA. As the values

for the RI changed with each of these conditions, the composition and size of these particles need to be taken into account in any modelling study or climate impact calculation in order to obtain a more accurate understanding of the impact.

References

1. Pathak R, Presto A, Lane T, Stanier C, Donahue N, Pandis S. 2007. Ozonolysis of α-pinene: parameterization of secondary organic aerosol mass fraction. *Atmospheric Chemistry and Physics* 7:3811-21
2. Guenther A, Hewitt CN, Erickson D, Fall R, Geron C, Graedel T, Harley P, Klinger L, Lerdau M, McKay W. 1995. A global model of natural volatile organic compound emissions. *Journal of Geophysical Research: Atmospheres* 100:8873-92
3. Griffin RJ, Cocker III DR, Seinfeld JH, Dabdub D. 1999. Estimate of global atmospheric organic aerosol from oxidation of biogenic hydrocarbons. *Geophysical research letters* 26:2721-4
4. Paulson SE, Chung M, Sen AD, Orzechowska G. 1998. Measurement of OH radical formation from the reaction of ozone with several biogenic alkenes. *Journal of Geophysical Research: Atmospheres* 103:25533-9
5. Arnts RR, Petersen WB, Seila RL, Gay BW. 1982. Estimates of α-pinene emissions from a loblolly pine forest using an atmospheric diffusion model. *Atmospheric Environment (1967)* 16:2127-37
6. Isaksen IS, Hov Ø. 1987. Calculation of trends in the tropospheric concentration of O_3, OH, CO, CH_4 and NO_x. *Tellus B* 39:271-85
7. Guenther CC. 2006. Estimates of global terrestrial isoprene emissions using MEGAN (Model of Emissions of Gases and Aerosols from Nature). Atmospheric Chemistry and Physics
8. Dooms-Goossens A, Deoreef H, Holvoet C, Maertens M. 1977. Turpentine-induced hypersensitivity to peppermint oil. *Contact Dermatitis* 3:304-8
9. Brun R. 1975. Epidemiology of contact dermatitis in Geneva (1000 cases). *Contact Dermatitis* 1:214-7
10. Hedenstierna G, Alexandersson R, Wimander K, Rosen G. 1983. Exposure to terpenes: effects on pulmonary function. *International archives of occupational and environmental health* 51:191-8
11. Parmeggiani L. 1983. *Encyclopaedia of occupational health and safety. Third (revised) edition. Vol. 1 AK; Vol. 2 LZ*. International labour office
12. Northcross AL, Jang M. 2007. Heterogeneous SOA yield from ozonolysis of monoterpenes in the presence of inorganic acid. *Atmospheric Environment* 41:1483-93
13. Hu D, Bian Q, Li TW, Lau AK, Yu JZ. 2008. Contributions of isoprene, monoterpenes, β-caryophyllene, and toluene to secondary organic aerosols in Hong Kong during the summer of 2006. *Journal of Geophysical Research: Atmospheres* 113
14. Seinfeld JH, Erdakos GB, Asher WE, Pankow JF. 2001. Modeling the formation of secondary organic aerosol (SOA). 2. The predicted effects of relative humidity on aerosol formation in the α-pinene-, β-pinene-, sabinene-, Δ3-carene-, and cyclohexene-ozone systems. *Environmental science & technology* 35:1806-17
15. Ng N, Chhabra P, Chan A, Surratt J, Kroll J, Kwan A, McCabe D, Wennberg P, Sorooshian A, Murphy S. 2007. Effect of NO_x level on secondary organic aerosol (SOA) formation from the photooxidation of terpenes. *Atmospheric Chemistry and Physics* 7:5159-74
16. Spittler M, Barnes I, Bejan I, Brockmann K, Benter T, Wirtz K. 2006. Reactions of NO_3 radicals with limonene and α-pinene: Product and SOA formation. *Atmospheric Environment* 40:116-27

17. Sakulyanontvittaya T, Guenther A, Helmig D, Milford J, Wiedinmyer C. 2008. Secondary organic aerosol from sesquiterpene and monoterpene emissions in the United States. *Environmental science & technology* 42:8784-90
18. Yu J, Cocker III DR, Griffin RJ, Flagan RC, Seinfeld JH. 1999. Gas-phase ozone oxidation of monoterpenes: Gaseous and particulate products. *Journal of Atmospheric Chemistry* 34:207-58
19. Yu J, Griffin RJ, Cocker DR, Flagan RC, Seinfeld JH, Blanchard P. 1999. Observation of gaseous and particulate products of monoterpene oxidation in forest atmospheres. *Geophysical Research Letters* 26:1145-8
20. Larsen BR, Di Bella D, Glasius M, Winterhalter R, Jensen NR, Hjorth J. 2001. Gas-phase OH oxidation of monoterpenes: Gaseous and particulate products. *Journal of Atmospheric Chemistry* 38:231-76
21. Guenther A, Zimmerman P, Wildermuth M. 1994. Natural volatile organic compound emission rate estimates for US woodland landscapes. *Atmospheric Environment* 28:1197-210
22. Geron C, Rasmussen R, R. Arnts R, Guenther A. 2000. A review and synthesis of monoterpene speciation from forests in the United States. *Atmospheric Environment* 34:1761-81
23. Fuentes JD, Lerdau M, Atkinson R, Baldocchi D, Bottenheim JW, Ciccioli P, Lamb B, Geron C, Gu L, Guenther A, Sharkey TD, Stockwell W. 2000. Biogenic Hydrocarbons in the Atmospheric Boundary Layer: A Review.
24. Atkinson R. 1995. Gas phase tropospheric chemistry of organic compounds. *Issues in environmental science and technology* 4:65-90
25. Camredon M, Hamilton J, Alam M, Wyche K, Carr T, White I, Monks P, Rickard A, Bloss W. 2010. Distribution of gaseous and particulate organic composition during dark α-pinene ozonolysis. *Atmospheric Chemistry and Physics* 10:2893-917
26. Glasius M, Lahaniati M, Calogirou A, Di Bella D, Jensen NR, Hjorth J, Kotzias D, Larsen BR. 2000. Carboxylic acids in secondary aerosols from oxidation of cyclic monoterpenes by ozone. *Environmental Science & Technology* 34:1001-10
27. Hallquist M, Wenger J, Baltensperger U, Rudich Y, Simpson D, Claeys M, Dommen J, Donahue N, George C, Goldstein A. 2009. The formation, properties and impact of secondary organic aerosol: current and emerging issues. *Atmospheric Chemistry and Physics* 9:5155-236
28. Perraud V, Bruns EA, Ezell MJ, Johnson SN, Greaves J, Finlayson-Pitts BJ. 2010. Identification of organic nitrates in the NO3 radical initiated oxidation of α-pinene by atmospheric pressure chemical ionization mass spectrometry. *Environmental science & technology* 44:5887-93
29. Warneke C, De Gouw J, Goldan P, Kuster W, Williams E, Lerner B, Jakoubek R, Brown S, Stark H, Aldener M. 2004. Comparison of daytime and nighttime oxidation of biogenic and anthropogenic VOCs along the New England coast in summer during New England Air Quality Study 2002. *Journal of Geophysical Research: Atmospheres* 109
30. Atkinson R. 1997. Gas-phase tropospheric chemistry of volatile organic compounds: 1. Alkanes and alkenes. *Journal of Physical and Chemical Reference Data* 26:215-90
31. Calvert JG, Atkinson R, Becker KH, Kamens RM, Seinfeld JH, Wallington TH, Yarwood G. 2002. *The mechanisms of atmospheric oxidation of the aromatic hydrocarbons*. Oxford University Press
32. Atkinson R. 2000. Atmospheric chemistry of VOCs and NO_x. *Atmospheric environment* 34:2063-101
33. Criegee R, Wenner G. 1949. Die Ozonisierung des 9,10-Oktalins. *Justus Liebigs Annalen der Chemie* 564:9-15

34. Atkinson R, Aschmann SM, Arey J, Shorees B. 1992. Formation of OH radicals in the gas phase reactions of O3 with a series of terpenes. *Journal of Geophysical Research: Atmospheres* 97:6065-73
35. Bonn B, Moorgat G. 2002. New particle formation during α-and β-pinene oxidation by O_3, OH and NO_3, and the influence of water vapour: particle size distribution studies. *Atmospheric Chemistry and Physics* 2:183-96
36. Henry KM, Donahue NM. 2011. Effect of the OH radical scavenger hydrogen peroxide on secondary organic aerosol formation from α-pinene ozonolysis. *Aerosol Science and Technology* 45:696-700
37. Keywood M, Kroll J, Varutbangkul V, Bahreini R, Flagan R, Seinfeld J. 2004. Secondary organic aerosol formation from cyclohexene ozonolysis: Effect of OH scavenger and the role of radical chemistry. *Environmental science & technology* 38:3343-50
38. Kristensen K, Cui T, Zhang H, Gold A, Glasius M, Surratt JD. 2014. Dimers in α-pinene secondary organic aerosol: effect of hydroxyl radical, ozone, relative humidity and aerosol acidity. *Atmospheric Chemistry and Physics* 14:4201-18
39. Jimenez J, Canagaratna M, Donahue N, Prevot A, Zhang Q, Kroll JH, DeCarlo PF, Allan JD, Coe H, Ng N. 2009. Evolution of organic aerosols in the atmosphere. *Science* 326:1525-9
40. Odum JR, Hoffmann T, Bowman F, Collins D, Flagan RC, Seinfeld JH. 1996. Gas/Particle Partitioning and Secondary Organic Aerosol Yields. *Environmental Science & Technology* 30:2580-5
41. Eddingsaas N, Loza C, Yee L, Chan M, Schilling K, Chhabra P, Seinfeld J, Wennberg P. 2012. α-pinene photooxidation under controlled chemical conditions–Part 2: SOA yield and composition in low-and high-NO_x environments. *Atmospheric Chemistry and Physics* 12:7413-27
42. Healy RM, Temime B, Kuprovskyte K, Wenger JC. 2009. Effect of relative humidity on gas/particle partitioning and aerosol mass yield in the photooxidation of p-xylene. *Environmental science & technology* 43:1884-9
43. Henry KM, Lohaus T, Donahue NM. 2012. Organic aerosol yields from α-pinene oxidation: bridging the gap between first-generation yields and aging chemistry. *Environmental science & technology* 46:12347-54
44. Pathak RK, Stanier CO, Donahue NM, Pandis SN. 2007. Ozonolysis of α-pinene at atmospherically relevant concentrations: Temperature dependence of aerosol mass fractions (yields). *Journal of Geophysical Research: Atmospheres* 112
45. Shilling J, Chen Q, King S, Rosenoern T, Kroll J, Worsnop D, McKinney K, Martin S. 2008. Particle mass yield in secondary organic aerosol formed by the dark ozonolysis of α-pinene. *Atmospheric Chemistry and Physics* 8:2073-88
46. Hoffmann T, Odum JR, Bowman F, Collins D, Klockow D, Flagan RC, Seinfeld JH. 1997. Formation of organic aerosols from the oxidation of biogenic hydrocarbons. *Journal of Atmospheric Chemistry* 26:189-222
47. Went FW. 1960. Blue Hazes in the Atmosphere. *Nature* 187:641-3
48. Leaitch W, Bottenheim J, Biesenthal T, Li SM, Liu P, Asalian K, Dryfhout-Clark H, Hopper F, Brechtel F. 1999. A case study of gas-to-particle conversion in an eastern Canadian forest. *Journal of Geophysical Research: Atmospheres* 104:8095-111
49. Mäkelä J, Aalto P, Jokinen V, Pohja T, Nissinen A, Palmroth S, Markkanen T, Seitsonen K, Lihavainen H, Kulmala M. 1997. Observations of ultrafine aerosol particle formation and growth in boreal forest. *Geophysical Research Letters* 24:1219-22
50. Kavouras IG, Mihalopoulos N, Stephanou EG. 1998. Formation of atmospheric particles from organic acids produced by forests. *Nature* 395:683-6

51. Change IC. 2013. The physical science basis. Contribution of working group I to the fifth assessment report of the intergovernmental panel on climate change. *K., Tignor, M., Allen, SK, Boschung, J., Nauels, A., Xia, Y., Bex, V., Midgley, PM, Eds*:1535
52. McMurry PH. 2000. A review of atmospheric aerosol measurements. *Atmospheric Environment* 34:1959-99
53. Moise T, Flores JM, Rudich Y. 2015. Optical properties of secondary organic aerosols and their changes by chemical processes. *Chemical reviews* 115:4400-39
54. Kourtchev I, Doussin J, Giorio C, Mahon B, Wilson E, Maurin N, Pangui E, Venables D, Wenger J, Kalberer M. 2015. Molecular composition of aged secondary organic aerosol generated from a mixture of biogenic volatile compounds using ultrahigh resolution mass spectrometry. *Atmos. Chem. Phys. Discuss* 15:535
55. Kourtchev I, Doussin J-F, Giorio C, Mahon B, Wilson EM, Maurin N, Pangui E, Venables DS, Wenger JC, Kalberer M. 2015. Molecular composition of fresh and aged secondary organic aerosol from a mixture of biogenic volatile compounds: a high-resolution mass spectrometry study. *Atmospheric Chemistry and Physics* 15:5683-95
56. Pye HO, Seinfeld JH. 2010. A global perspective on aerosol from low-volatility organic compounds. *Atmospheric Chemistry and Physics* 10:4377-401
57. Spracklen D, Jimenez J, Carslaw K, Worsnop D, Evans M, Mann G, Zhang Q, Canagaratna M, Allan J, Coe H. 2011. Aerosol mass spectrometer constraint on the global secondary organic aerosol budget. *Atmospheric Chemistry and Physics* 11:12109-36
58. Heald C, Kroll J, Jimenez J, Docherty K, DeCarlo P, Aiken A, Chen Q, Martin S, Farmer D, Artaxo P. 2010. A simplified description of the evolution of organic aerosol composition in the atmosphere. *Geophysical Research Letters* 37
59. Liu P, Zhang Y, Martin ST. 2013. Complex refractive indices of thin films of secondary organic materials by spectroscopic ellipsometry from 220 to 1200 nm. *Environmental science & technology* 47:13594-601
60. Kim H, Paulson SE. 2013. Real refractive indices and volatility of secondary organic aerosol generated from photooxidation and ozonolysis of limonene, α-pinene and toluene. *Atmospheric Chemistry and Physics* 13:7711-23
61. Lambe AT, Cappa CD, Massoli P, Onasch TB, Forestieri SD, Martin AT, Cummings MJ, Croasdale DR, Brune WH, Worsnop DR. 2013. Relationship between oxidation level and optical properties of secondary organic aerosol. *Environmental science & technology* 47:6349-57
62. Nakayama T, Sato K, Matsumi Y, Imamura T, Yamazaki A, Uchiyama A. 2013. Wavelength and NO_x dependent complex refractive index of SOAs generated from the photooxidation of toluene. *Atmospheric Chemistry and Physics* 13:531-45
63. Nakayama T, Matsumi Y, Sato K, Imamura T, Yamazaki A, Uchiyama A. 2010. Laboratory studies on optical properties of secondary organic aerosols generated during the photooxidation of toluene and the ozonolysis of α-pinene. *Journal of Geophysical Research: Atmospheres* 115
64. Flores JM, Washenfelder R, Adler G, Lee H, Segev L, Laskin J, Laskin A, Nizkorodov S, Brown S, Rudich Y. 2014. Complex refractive indices in the near-ultraviolet spectral region of biogenic secondary organic aerosol aged with ammonia. *Physical Chemistry Chemical Physics* 16:10629-42
65. Varma RM, Ball SM, Brauers T, Dorn H, Heitmann U, Jones R, Platt U, Pöhler D, Ruth AA, Shillings A. 2013. Light extinction by secondary organic aerosol: an intercomparison of three broadband cavity spectrometers. *Atmospheric Measurement Techniques* 6 3115-30

66. Kim H, Barkey B, Paulson SE. 2012. Real refractive indices and formation yields of secondary organic aerosol generated from photooxidation of limonene and α-pinene: the effect of the HC/NO_x Ratio. *The Journal of Physical Chemistry A* 116:6059-67
67. Redmond H, Thompson JE. 2011. Evaluation of a quantitative structure–property relationship (QSPR) for predicting mid-visible refractive index of secondary organic aerosol (SOA). *Physical Chemistry Chemical Physics* 13:6872-82
68. Kim H, Barkey B, Paulson SE. 2010. Real refractive indices of α-and β-pinene and toluene secondary organic aerosols generated from ozonolysis and photo-oxidation. *Journal of Geophysical Research: Atmospheres* 115
69. Kubala D, Drage E, Al-Faydhi A, Kočíšek J, Papp P, Matejčík V, Mach P, Urban J, Limao-Vieira P, Hoffmann SV. 2009. Electron impact ionisation and UV absorption study of α-and β-pinene. *International Journal of Mass Spectrometry* 280:169-73
70. Chen X, Hopke P. 2009. Secondary organic aerosol from α-pinene ozonolysis in dynamic chamber system. *Indoor Air* 19:335-45
71. Zelenyuk A, Yang J, Song C, Zaveri RA, Imre D. 2008. A new real-time method for determining particles' sphericity and density: application to secondary organic aerosol formed by ozonolysis of α-pinene. *Environmental science & technology* 42:8033-8
72. Malloy QG, Nakao S, Qi L, Austin R, Stothers C, Hagino H, Cocker III DR. 2009. Real-time aerosol density determination utilizing a modified scanning mobility particle sizer—aerosol particle mass analyzer system. *Aerosol Science and Technology* 43:673-8
73. Denjean C, Formenti P, Picquet-Varrault B, Pangui E, Zapf P, Katrib Y, Giorio C, Tapparo A, Monod A, Temime-Roussel B. 2015. Relating hygroscopicity and optical properties to chemical composition and structure of secondary organic aerosol particles generated from the ozonolysis of α-pinene. *Atmospheric Chemistry and Physics* 15:3339-58
74. Scientific H. 2012. A guidebook to particle size analysis. *Horiba Instruments, Inc*:1-29
75. Schnaiter M, Horvath H, Möhler O, Naumann K-H, Saathoff H, Schöck O. 2003. UV-VIS-NIR spectral optical properties of soot and soot-containing aerosols. *Journal of Aerosol Science* 34:1421-44
76. Wex H, Petters M, Carrico C, Hallbauer E, Massling A, McMeeking G, Poulain L, Wu Z, Kreidenweis S, Stratmann F. 2009. Towards closing the gap between hygroscopic growth and activation for secondary organic aerosol: Part 1–Evidence from measurements. *Atmospheric Chemistry and Physics* 9:3987-97
77. Nakayama T, Sato K, Matsumi Y, Imamura T, Yamazaki A, Uchiyama A. 2012. Wavelength dependence of refractive index of secondary organic aerosols generated during the ozonolysis and photooxidation of α-pinene. *Sola* 8:119-23
78. Lambe AT, Cappa CD, Massoli P, Onasch TB, Forestieri SD, Martin AT, Cummings MJ, Croasdale DR, Brune WH, Worsnop DR, Davidovits P. 2013. Relationship between Oxidation Level and Optical Properties of Secondary Organic Aerosol. *Environmental Science & Technology* 47:6349-57
79. Flores JM, Washenfelder RA, Adler G, Lee HJ, Segev L, Laskin J, Laskin A, Nizkorodov SA, Brown SS, Rudich Y. 2014. Complex refractive indices in the near-ultraviolet spectral region of biogenic secondary organic aerosol aged with ammonia. *Physical Chemistry Chemical Physics* 16:10629-42
80. Guyon P, Boucher O, Graham B, Beck J, Mayol-Bracero OL, Roberts GC, Maenhaut W, Artaxo P, Andreae MO. 2003. Refractive index of aerosol particles over the

Amazon tropical forest during LBA-EUSTACH 1999. *Journal of Aerosol Science* 34:883-907

81. Varma R, Ball S, Brauers T, Dorn H, Heitmann U, Jones R, Platt U, Pöhler D, Ruth AA, Shillings A. 2013. Light extinction by secondary organic aerosol: an intercomparison of three broadband cavity spectrometers.
82. Toon OB, Pollack JB, Khare BN. 1976. The optical constants of several atmospheric aerosol species: Ammonium sulfate, aluminum oxide, and sodium chloride. *Journal of Geophysical Research* 81:5733-48
83. Moortgat WSaGK. 1989. UV/VIS Spectra of Atmospheric Constituents, Version 1. ed. RR Personal communication to E.-P. Röth, G. Moortgat, R. Meller, and W. Schneider
84. Isaac S, Wilson E, Chandran S, Anin P, Venables DS, Wenger JC, Varma R. Integrating Nephelometer to Measure Scattering Coefficient of Atmospheric Aerosols. *Submitted*
85. Flores J, Zhao D, Segev L, Schlag P, Kiendler-Scharr A, Fuchs H, Watne Å, Bluvshtein N, Mentel TF, Hallquist M. 2014. Evolution of the complex refractive index in the near UV spectral region in ageing secondary organic aerosol. *Atmos Chem Phys Discus* 14:4149-87
86. Ma L, Thompson JE. 2012. Optical properties of dispersed aerosols in the near ultraviolet (355 nm): measurement approach and initial data. *Analytical chemistry* 84:5611-7
87. Limbeck A, Kulmala M, Puxbaum H. 2003. Secondary organic aerosol formation in the atmosphere via heterogeneous reaction of gaseous isoprene on acidic particles. *Geophysical Research Letters* 30
88. Updyke KM, Nguyen TB, Nizkorodov SA. 2012. Formation of brown carbon via reactions of ammonia with secondary organic aerosols from biogenic and anthropogenic precursors. *Atmospheric environment* 63:22-31
89. Zhang X, Lin Y-H, Surratt JD, Zotter P, Prévôt ASH, Weber RJ. 2011. Light-absorbing soluble organic aerosol in Los Angeles and Atlanta: A contrast in secondary organic aerosol. *Geophysical Research Letters* 38:n/a-n/a
90. Mitchell BG, Kahru M, Wieland J, Stramska M, Mueller J. 2002. Determination of spectral absorption coefficients of particles, dissolved material and phytoplankton for discrete water samples. *Ocean optics protocols for satellite ocean color sensor validation, Revision* 3:231-57
91. Nguyen TB, Lee PB, Updyke KM, Bones DL, Laskin J, Laskin A, Nizkorodov SA. 2012. Formation of nitrogen-and sulfur-containing light-absorbing compounds accelerated by evaporation of water from secondary organic aerosols. *Journal of Geophysical Research: Atmospheres* 117
92. Bateman AP, Walser ML, Desyaterik Y, Laskin J, Laskin A, Nizkorodov SA. 2008. The Effect of Solvent on the Analysis of Secondary Organic Aerosol Using Electrospray Ionization Mass Spectrometry. *Environmental Science & Technology* 42:7341-6
93. Ångström A. 1929. On the atmospheric transmission of sun radiation and on dust in the air. *Geografiska Annaler* 11:156-66
94. Reid JS, Eck TF, Christopher SA, Hobbs PV, Holben B. 1999. Use of the Ångstrom exponent to estimate the variability of optical and physical properties of aging smoke particles in Brazil. *Journal of Geophysical Research: Atmospheres* 104:27473-89
95. Soni K, Singh S, Bano T, Tanwar R, Nath S. 2011. Wavelength dependence of the aerosol Angstrom exponent and its implications over Delhi, India. *Aerosol Science and Technology* 45:1488-98

96. Junge C. 1955. The size distribution and aging of natural aerosols as determined from electrical and optical data on the atmosphere. *Journal of Meteorology* 12:13-25
97. Tomasi C, Caroli E, Vitale V. 1983. Study of the relationship between Ångström's wavelength exponent and Junge particle size distribution exponent. *Journal of climate and applied meteorology* 22:1707-16
98. Eck T, Holben B, Ward D, Dubovik O, Reid J, Smirnov A, Mukelabai M, Hsu N, O'neill N, Slutsker I. 2001. Characterization of the optical properties of biomass burning aerosols in Zambia during the 1997 ZIBBEE field campaign. *Journal of Geophysical Research: Atmospheres* 106:3425-48
99. O'Neill N, Eck T, Holben B, Smirnov A, Dubovik O, Royer A. 2001. Bimodal size distribution influences on the variation of Angstrom derivatives in spectral and optical depth space. *Journal of Geophysical Research: Atmospheres* 106:9787-806
100. Singh S, Singh B, Gera B, Srivastava MK, Dutta H, Garg S, Singh R. 2006. A study of aerosol optical depth in the central Indian region (17.3–8.6° N) during ISRO-GBP field campaign. *Atmospheric Environment* 40:6494-503
101. Schuster GL, Dubovik O, Holben BN. 2006. Angstrom exponent and bimodal aerosol size distributions. *Journal of Geophysical Research: Atmospheres* 111
102. Trochim WM, Donnelly JP. 2001. Research methods knowledge base.
103. Chang H, Charalampopoulos T. Determination of the wavelength dependence of refractive indices of flame soot. *Proc. Proceedings of the Royal Society of London A: Mathematical, Physical and Engineering Sciences*, *1990*, 430:577-91: The Royal Society
104. Segelstein DJ. 1981. *The complex refractive index of water*. University of Missouri--Kansas City
105. Presto AA, Huff Hartz KE, Donahue NM. 2005. Secondary organic aerosol production from terpene ozonolysis. 1. Effect of UV radiation. *Environmental science & technology* 39:7036-45
106. Presto AA, Huff Hartz KE, Donahue NM. 2005. Secondary organic aerosol production from terpene ozonolysis. 2. Effect of NO_x concentration. *Environmental Science & Technology* 39:7046-54
107. Presto AA, Donahue NM. 2006. Investigation of α-Pinene + Ozone Secondary Organic Aerosol Formation at Low Total Aerosol Mass. *Environmental Science & Technology* 40:3536-43
108. Benkő D, Molnar A, Imre K. 2009. Study on the size dependence of complex refractive index of atmospheric aerosol particles over Central Europe. *Quarterly Journal of the Hungarian Meteorological Service* 113:157-75
109. Ebert M, Weinbruch S, Hoffmann P, Ortner HM. 2004. The chemical composition and complex refractive index of rural and urban influenced aerosols determined by individual particle analysis. *Atmospheric Environment* 38:6531-45
110. Liu Y, Daum PH. 2008. Relationship of refractive index to mass density and self-consistency of mixing rules for multicomponent mixtures like ambient aerosols. *Journal of Aerosol Science* 39:974-86
111. Cappa CD, Che DL, Kessler SH, Kroll JH, Wilson KR. 2011. Variations in organic aerosol optical and hygroscopic properties upon heterogeneous OH oxidation. *Journal of Geophysical Research: Atmospheres* 116
112. Donahue NM, Henry KM, Mentel TF, Kiendler-Scharr A, Spindler C, Bohn B, Brauers T, Dorn HP, Fuchs H, Tillmann R. 2012. Aging of biogenic secondary organic aerosol via gas-phase OH radical reactions. *Proceedings of the National Academy of Sciences* 109:13503-8

113. Salo K, Hallquist M, Jonsson ÅM, Saathoff H, Naumann K-H, Spindler C, Tillmann R, Fuchs H, Bohn B, Rubach F. 2011. Volatility of secondary organic aerosol during OH radical induced ageing. *Atmospheric Chemistry and Physics* 11:11055-67
114. Stewart DJ, Almabrok S, Lockhart J, Mohamed O, Nutt D, Pfrang C, Marston G. 2013. The kinetics of the gas-phase reactions of selected monoterpenes and cyclo-alkenes with ozone and the NO 3 radical. *Atmospheric Environment* 70:227-35
115. Renbaum-Wolff L, Smith GD. 2012. "Virtual Injector" Flow Tube Method for Measuring Relative Rates Kinetics of Gas-Phase and Aerosol Species. *The Journal of Physical Chemistry A* 116:6664-74
116. Atkinson R. 2003. Kinetics of the gas-phase reactions of OH radicals with alkanes and cycloalkanes. *Atmospheric Chemistry and Physics* 3:2233-307
117. Saathoff H, Naumann K-H, Möhler O, Jonsson ÅM, Hallquist M, Kiendler-Scharr A, Mentel TF, Tillmann R, Schurath U. 2009. Temperature dependence of yields of secondary organic aerosols from the ozonolysis of α-pinene and limonene. *Atmospheric Chemistry and Physics* 9:1551-77
118. Jenkin M. 2004. Modelling the formation and composition of secondary organic aerosol from α-and β-pinene ozonolysis using MCM v3. *Atmospheric Chemistry and Physics* 4:1741-57
119. Iinuma Y, Böge O, Miao Y, Sierau B, Gnauk T, Herrmann H. 2005. Laboratory studies on secondary organic aerosol formation from terpenes. *Faraday discussions* 130:279-94
120. Docherty KS, Ziemann PJ. 2003. Effects of stabilized Criegee intermediate and OH radical scavengers on aerosol formation from reactions of β-pinene with O_3. *Aerosol Science & Technology* 37:877-91
121. Bilde M, Pandis SN. 2001. Evaporation rates and vapor pressures of individual aerosol species formed in the atmospheric oxidation of α-and β-pinene. *Environmental science & technology* 35:3344-9
122. Jang M, Kamens RM. 1999. Newly characterized products and composition of secondary aerosols from the reaction of α-pinene with ozone. *Atmospheric Environment* 33:459-74
123. Denjean C, Formenti P, Picquet-Varrault B, Camredon M, Pangui E, Zapf P, Katrib Y, Giorio C, Tapparo A, Temime-Roussel B. 2015. Aging of secondary organic aerosol generated from the ozonolysis of α-pinene: effects of ozone, light and temperature. *Atmospheric Chemistry and Physics* 15:883-97
124. Li H, Chen Z, Huang L, Huang D. 2016. Organic peroxides' gas-particle partitioning and rapid heterogeneous decomposition on secondary organic aerosol. *Atmospheric Chemistry and Physics* 16:1837-48
125. Cocker Iii DR, Mader BT, Kalberer M, Flagan RC, Seinfeld JH. 2001. The effect of water on gas–particle partitioning of secondary organic aerosol: II. m-xylene and 1, 3, 5-trimethylbenzene photooxidation systems. *Atmospheric Environment* 35:6073-85
126. Kamens RM, Zhang H, Chen EH, Zhou Y, Parikh HM, Wilson RL, Galloway KE, Rosen EP. 2011. Secondary organic aerosol formation from toluene in an atmospheric hydrocarbon mixture: water and particle seed effects. *Atmospheric Environment* 45:2324-34
127. Zhou Y, Zhang H, Parikh HM, Chen EH, Rattanavaraha W, Rosen EP, Wang W, Kamens RM. 2011. Secondary organic aerosol formation from xylenes and mixtures of toluene and xylenes in an atmospheric urban hydrocarbon mixture: Water and particle seed effects (II). *Atmospheric environment* 45:3882-90

128. Jonsson ÅM, Hallquist M, Ljungström E. 2006. Impact of humidity on the ozone initiated oxidation of limonene, Δ3-carene, and α-pinene. *Environmental science & technology* 40:188-94
129. Bonn B, Schuster G, Moortgat GK. 2002. Influence of water vapor on the process of new particle formation during monoterpene ozonolysis. *The Journal of Physical Chemistry A* 106:2869-81
130. Cocker Iii DR, Clegg SL, Flagan RC, Seinfeld JH. 2001. The effect of water on gas–particle partitioning of secondary organic aerosol. Part I: α-pinene/ozone system. *Atmospheric Environment* 35:6049-72
131. Sullivan A, Hodas N, Turpin B, Skog K, Keutsch F, Gilardoni S, Paglione M, Rinaldi M, Decesari S, Facchini M. 2015. Evidence for ambient dark aqueous SOA formation in the Po Valley, Italy. *Atmospheric Chemistry and Physics Discussions* 15:35485-521
132. Blando JD, Turpin BJ. 2000. Secondary organic aerosol formation in cloud and fog droplets: a literature evaluation of plausibility. *Atmospheric Environment* 34:1623-32
133. Hering SV, Friedlander S. 1982. Origins of aerosol sulfur size distributions in the Los Angeles basin. *Atmospheric Environment (1967)* 16:2647-56
134. Ziemann PJ. 2002. Evidence for low-volatility diacyl peroxides as a nucleating agent and major component of aerosol formed from reactions of O3 with cyclohexene and homologous compounds. *The Journal of Physical Chemistry A* 106:4390-402
135. Baynard T, Garland R, Ravishankara A, Tolbert M, Lovejoy E. 2006. Key factors influencing the relative humidity dependence of aerosol light scattering. *Geophysical research letters* 33
136. Fierz-Schmidhauser R, Zieger P, Wehrle G, Jefferson A, Ogren JA, Baltensperger U, Weingartner E. 2010. Measurement of relative humidity dependent light scattering of aerosols. *Atmospheric Measurement Techniques* 3:39-50
137. Garland RM, Ravishankara AR, Lovejoy ER, Tolbert MA, Baynard T. 2007. Parameterization for the relative humidity dependence of light extinction: Organic-ammonium sulfate aerosol. *Journal of Geophysical Research: Atmospheres* 112:D19303
138. Michel Flores J, Bar-Or R, Bluvshtein N, Abo-Riziq A, Kostinski A, Borrmann S, Koren I, Rudich Y. 2012. Absorbing aerosols at high relative humidity: linking hygroscopic growth to optical properties. *Atmospheric Chemistry and Physics* 12:5511-21
139. Warscheid B, Hoffmann T. 2001. On-line measurements of α-pinene ozonolysis products using an atmospheric pressure chemical ionisation ion-trap mass spectrometer. *Atmospheric Environment* 35:2927-40
140. Baker J, Aschmann SM, Arey J, Atkinson R. 2002. Reactions of stabilized criegee intermediates from the gas-phase reactions of O_3 with selected alkenes. *International journal of chemical kinetics* 34:73-85
141. Berndt T, Böge O, Stratmann F. 2003. Gas-phase ozonolysis of α-pinene: gaseous products and particle formation. *Atmospheric Environment* 37:3933-45
142. Kanno N, Tonokura K, Tezaki A, Koshi M. 2005. Water dependence of the HO_2 self reaction: Kinetics of the HO_2-H_2O complex. *The Journal of Physical Chemistry A* 109:3153-8
143. Reichert L, Hernández A, Stöbener D, Burkert J, Burrows J. 2003. Investigation of the effect of water complexes in the determination of peroxy radical ambient concentrations: Implications for the atmosphere. *Journal of Geophysical Research: Atmospheres* 108
144. Yu Y, Ezell MJ, Zelenyuk A, Imre D, Alexander L, Ortega J, D'Anna B, Harmon CW, Johnson SN, Finlayson-Pitts BJ. 2008. Photooxidation of α-pinene at high relative

humidity in the presence of increasing concentrations of NOx. *Atmospheric environment* 42:5044-60

145. Ryzhkov AB, Ariya PA. 2004. A theoretical study of the reactions of parent and substituted Criegee intermediates with water and the water dimer. *Physical Chemistry Chemical Physics* 6:5042-50

146. Marshall SF, Covert DS, Charlson RJ. 1995. Relationship between asymmetry parameter and hemispheric backscatter ratio: implications for climate forcing by aerosols. *Appl. Opt.* 34:6306-11

147. Andrews E, Sheridan PJ, Fiebig M, McComiskey A, Ogren JA, Arnott P, Covert D, Elleman R, Gasparini R, Collins D. 2006. Comparison of methods for deriving aerosol asymmetry parameter. *Journal of Geophysical Research: Atmospheres* 111

5. Physical and Optical Properties of Secondary Organic Aerosol formed by the Photolysis of 2-Nitrophenol

5.1. Introduction

The potential importance of nitrated and aromatic aerosol species on light absorption was first suggested by Jacobson in 1999 (1). His proposal originated from observations that UV light levels in the boundary layer in Los Angeles were significantly lower than those above the boundary layer. This difference could not be accounted for by known scattering or absorbing sources, but the UV solar irradiance was observed to decrease as aerosol concentrations increased. Moreover, there was an associated increase in the presence of nitrated or aromatic aerosol species as the UV irradiance decreased (1). Jacobson suggested that nitrated aromatic compounds could be responsible for this effect because they absorb strongly in the near-UV region (1). The measured UV irradiance reduction was compared to theoretical calculations of the UV irradiance reduction potential for several species. Nitrocresol was chosen as representative of nitroaromatic species: it has a low vapour pressure which results in either self-condensation or condensation onto the surface of existing aerosols. The influence of the nitrated and aromatic aerosols and the nitroaromatic gases was determined to account for up to 30 % of the UV irradiance reduction at the monitoring site (1).

Aromatic VOCs are important precursors for particles in polluted atmospheres. These compounds contribute an estimated 25 % of total non-methane VOC

emissions in urban environments and play a vital role in SOA formation from anthropogenic sources (2-9). In a study of the aerosol forming potential of VOCs in Athens, Greece, aromatics were found to be responsible for 90 % of SOA formed from non-methane hydrocarbons (10). Of these aromatic species, nitrophenol-containing SOA comprised the largest portion of SOA measured in Athens. Therefore, nitrophenol compounds have received considerable attention recently (11-15). 2-nitrophenol (2-NP) has a strong absorption at shorter wavelengths (360 nm) in the gas phase; this could lead to similar absorptions in the particle phase and its absorption would be similar to that of brown carbon (BrC). The importance of BrC as an absorber of solar radiation in the troposphere, and the potential contribution of 2-NP to such absorbing SOA, motivate the study of the optical properties of 2-NP.

Nitrophenols are phenols with one or more nitro-substituents attached to the ring. 2-NP, the focus of this chapter, has the nitro group ortho to the OH group, Figure 5.1. 2-NP has been measured at levels of up to μgL^{-1} in rainwater (16). Their high concentrations, good stability and low vapour pressure means they have been detected even in remote sites (17). They are found mostly in and around cities because vehicle exhausts are a common emission source (18; 19). Further information on additional sources, concentrations and health effects of 2-NP has already been described in Chapter 3, and the remainder of this section will focus on 2-NP photolysis and associated SOA formation.

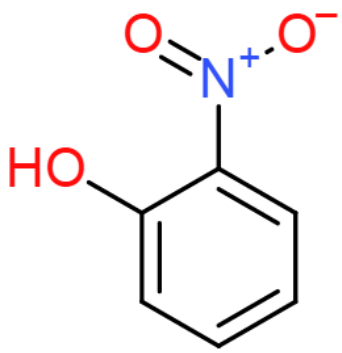

Figure 5.1 Molecular structure of 2-nitrophenol (2-NP).

2-NP absorbs strongly in the near-UV with an absorption maximum near 350 nm (20). As solar radiation extends to 290 nm in the troposphere, photochemical reactions initiated by 2-NP absorption could potentially play a role in the atmosphere. There have been a few studies of the photolysis of 2-, 3- and 4-nitrophenol (21-23). In 2006 Bejan et al. observed that photolysis of 2-NP produced HONO, which they postulated could be a missing HONO source in urban areas (24). HONO levels during the day are up to 64 times higher than at night and this difference cannot be accounted for by known HONO sources (25). HONO is important as a major precursor of the OH radical, which is the dominant oxidant in the atmosphere:

$$\mathrm{HONO} + \mathrm{hv} \rightarrow \mathrm{NO} + \mathrm{OH} \qquad \textbf{(R 5.1)}$$

The formation of the OH radical as a result of 2-NP photolysis was also reported in a 2008 study by Wei et al. (26). A combination of theoretical calculations and laser-induced fluorescence measurements by Cheng et al. found similar formation of OH radicals as a result of 2-NP photolysis (27).

The production of HONO is not the only atmospherically relevant result of 2-NP photolysis. It can also form SOA as a result of photolysis. If these products have sufficiently low vapour pressures they can form particles. Bardini studied the formation of particles due to the photolysis of a number of nitroaromatic species, including 2-NP (28). She determined that 2-NP readily undergoes photolysis and has an atmospheric photolysis lifetime, in the absence of OH radicals, of ca. 1.5 hours. She reported an initial 'burst' of particles with mean diameters of 20-40 nm and a high mass yield for aerosol formation of 0.74.

Photo-Fenton reactions have been used to remove 2-NP from the waste water (29; 30). A Fenton reagent is ferrous iron in a solution of H_2O_2; UV light is used with this to make the reaction Photo-Fenton, which produces high levels of OH radicals which aid in the oxidation and eventual removal of 2-NP from the waste water. One of the proposed initial reaction products is nitrocatechol. Chen et al. studied the photolysis of a number of nitroaromatic species in aqueous solutions (31) and

found that 99.5 % of 2-NP was removed within 80 minutes. The products they reported included hydroquinone, benzoquinone, catechol, nitrocatechol, nitrohydroquinone, resorcinol, and 2- and 3-nitrosophenol (that is, with an NO group in place of the NO_2 in nitrophenol), as well as nitrate and nitrite ions. The three main intermediate species were nitrohydroquinone (NHQ), catechol (CC) and nitrocatechol (NC), with yields decreasing in the order: NHQ > CC > NC. Alif and co-workers detected 2-nitrosophenol during photolysis in acidic solution, while the NC and NHQ have very low vapour pressures, which could lead to the formation of particles (32; 33).Some of these species degraded with further irradiation. Based on the yields for the three different nitrophenol isomers (2,3 and 4), there is an indication that the OH radical plays a role in the photochemical process (31). The reaction pathway for the formation of 3-nitrocatechol suggested by Chen et al. is shown in Figure 5.2. The presence of the OH group on the ring directs the attack of the 2-NP group to either the 2 or 4 positions. The position of the attack dictates the species that would be formed; an attack at the 2 position results in the formation of 3-nitrocatechol while an attack at the 4 position forms nitrohydroquinone.

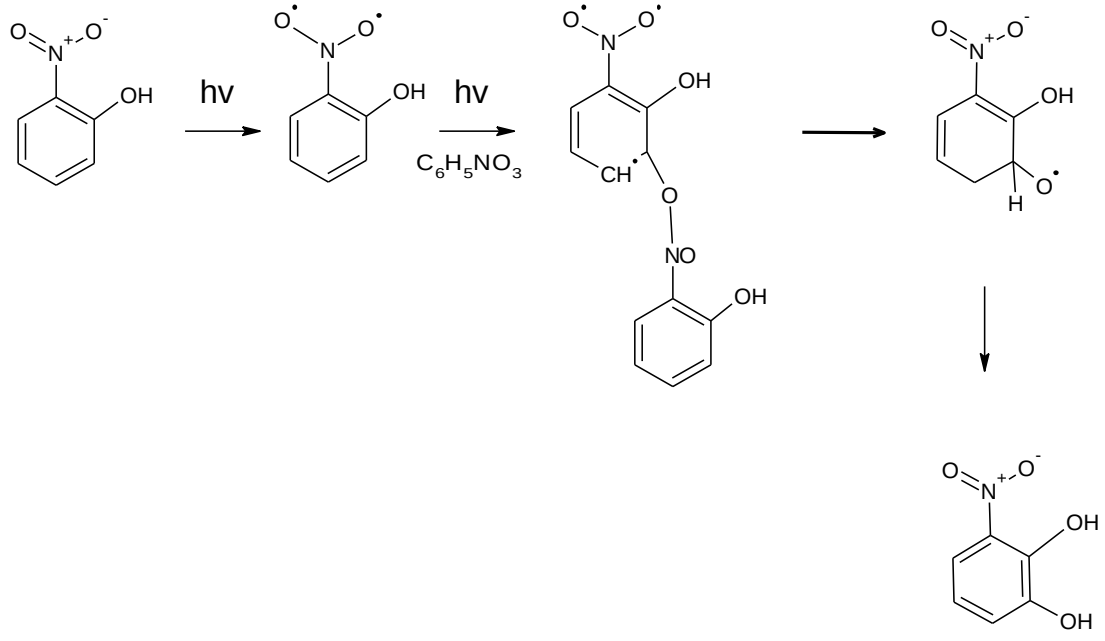

Figure 5.2 Proposed reaction pathway for the formation of 3-nitrocatechol (adapted from the work by Chen et al. (31)).

The aim of this chapter is to characterise the physical and short-wavelength optical properties of SOA formed from photolysis of 2-NP. A reference experiment was performed in which 200 ppbv of 2-NP was illuminated in the chamber. The extinction caused by these particles was monitored over the course of the experiment. Physical properties studied included the mass and number concentration, and mass yield. The work here quantified the extinction and absorption of the particles, as well as the complex refractive index. These quantities allowed the single scattering albedo (SSA) to be determined and the role of 2-NP in particles on the radiative balance to be better understood. As the reaction pathway for the photolysis of 2-NP is not well know, a number of compounds were added to the system to investigate their effect on the SOA. The effects of other reaction conditions on the SOA optical properties were investigated, including the influence of NO_2, and of the presence of OH and criegee intermediate (CI) scavengers.

5.2. Experimental method

In the reference 2-NP SOA experiment, 200 ppbv of 2-NP was introduced into the dark chamber, allowed to stabilise for approx 20 minutes, and then the chamber lamps were turned on. A number of variations on the reference experiment were performed and the results reported here (Table 5.1). In some experiments NO_2, or OH and criegee scavengers were also added to the chamber.

Table 5.1 Experimental conditions for 2-NP photolysis.

Experiment number	2-NP mixing ratio (ppbv)	Additional reactants
1	200	None
2	250	20 ppmv of cyclohexane
3	200	20 ppmv of acetaldehyde
4	234	400 ppbv NO_2

2-NP is a yellow crystal at room temperature and was added to the chamber in the same manner as described previously. However, the vapour pressure of 2-NP (0.11

mmHg) is much lower than that of α-pinene (4.75 mmHg at 25 °C) and it was more difficult to add a consistent amount of 2-NP to the chamber (34; 35). Wall losses were also greater. The chamber lights were turned on to initiate photochemical reactions. 2-NP absorbs strongly in the UV/Vis region (Chapter 3) and is readily photolysed, resulting in the prompt formation of SOA particles.

The sample extinction in the chamber can be determined at any time over the full wavelength range. Due to the absorbing nature of the 2-NP and its moderate volatility, residual absorption structure from 2-NP in the gas phase was also present in the resulting extinction measurements, Figure 5.3. To determine the extinction caused by the particles, gas phase absorption had to be removed. A spectral fitting program was developed in order to remove the absorption of 2-NP and other potential absorbing gases.

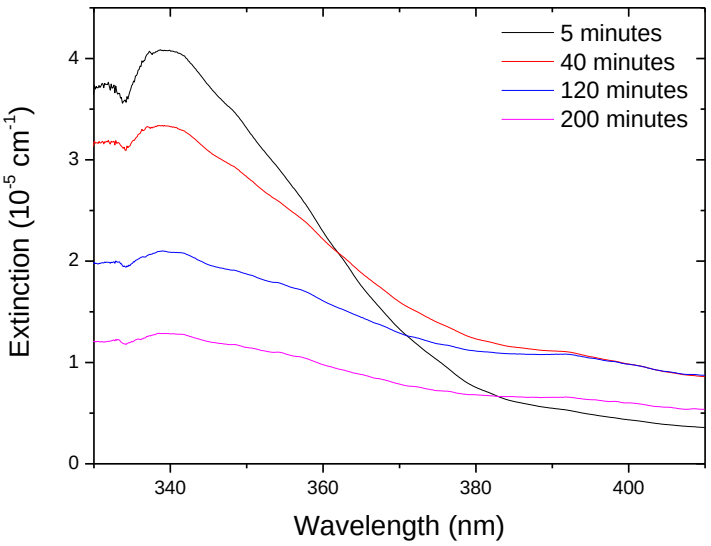

Figure 5.3 Spectral dependence of measured extinction in the chamber at a number of times.

A number of fitting tests were performed with the program. In one test, acetaldehyde was added to the chamber. Acetaldehyde has a structured absorption spectrum which facilitated a robust spectral fit. The retrieved mixing ratio of acetaldehyde from the spectral fit (using the absorption cross section of Schneider and Moortgat (36)) was 24 ppmv, which was 20 % higher than the initial mixing

ratio in the chamber. In a similar test, the mixing ratio of MVK was determined during one of the SOA experiments using the absorption cross section of Giercsak et al. (37). Whereas 5.3 ppmv was added to the chamber, the retrieved mixing ratio was 6.9 ppmv. The fit overestimated the mixing ratio by 26 %. The measured and the calculated extinction for acetaldehyde and its residual are shown in Figure 5.4. The fitted extinction is higher than the measured extinction. When the calculated extinction is removed from the measured extinction the residual is small. This shows that we are able to effectively remove most of the 2-NP gas phase absorption from the measured SOA extinction spectrum.

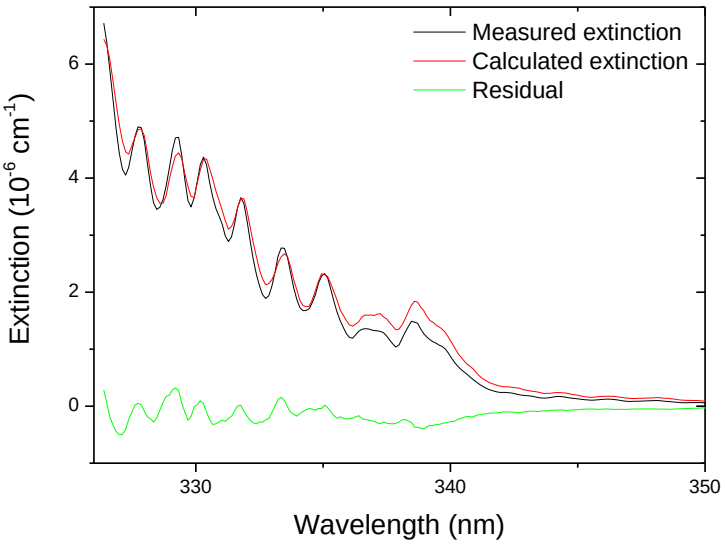

Figure 5.4 The measured and calculated extinction for acetaldehyde and the residual is shown here. The residual mostly arises from the slight differences in the acetaldehyde spectral structure in the extinction measurement and in the reference absorption cross section**.**

Off-line analysis

Filter samples were also collected during the experiment in the same manner as described in Chapter 4. The SOA collected on the filters appeared to have a strong, yellow/brown colour that is similar to the description of brown carbon, Figure 5.5. These particles were extracted into a solvent to measure its absorbance in a UV/Vis spectrometer. As the composition of the particles was unknown, a test was performed to determine the best solvent for the extraction. Brown carbon SOA

species have previously been extracted into dichloromethane, acetonitrile, water, and methanol (38-41). A number of filters from a test experiment were cut in half. Extractions were undertaken in three solvents: methanol, deionised water, and a 1:1 mixture of methanol and deionised water. This combination tested whether the SOA were water-soluble or soluble in organic solvents. A half filter was added to 5 ml of each of the solvents and sonicated for 5 minutes. Sonication of samples has been shown to increase extraction efficiencies (42). After 5 minutes, the filter was removed. The coloured sample SOA was almost entirely removed for each solvent, Figure 5.5. The resulting solvent containing the SOA was passed through a cellulose acetate membrane filter to remove filter debris (43). The absorbance associated with each extracted SOA was measured in a UV/Vis spectrometer. The three solvent options results in approximately equivalent absorbances. The mixture of 1:1 methanol to water was chosen to be the most appropriate solvent for the SOA extraction (Figure 5.16).

Figure 5.5 Left: Filter sample after a 2-NP SOA photolysis experiment. Right: Filter after extraction in methanol, showing that visible absorbing SOA present on the filter had been removed**.**

The chemical composition of the particles formed was also determined by analysing filter samples using ultra high resolution mass spectroscopy. The instrument resolution was sufficiently high to determine the molecular stoichiometry, but not necessarily the identity of the isomer. This analysis was carried out by Dr Ivan Kourtchev in Cambridge.

5.3. Results

The results in this section will be subdivided into different sections. Initially a reference experiment will be presented and discussed. In this instance, the reference experiment was the photolysis of 200 ppbv of 2-NP with no additional species present. The results from this will then be compared to experiments in the presence of an OH scavenger (cyclohexane), and OH and criegee intermediate (CI) scavenger (acetaldehyde) and elevated levels of NO_2. The addition of these species could affect the reaction pathways and influence the extinction potential of the SOA formed.

5.4. Reference experiment

When the 2-NP is added to the chamber, there is an instant increase in extinction at 350 nm but minimal change in the extinction above 400 nm. Figure 5.6 (top) shows the absorption cross section spectrum for 2-NP. When the lights are turned on in the chamber at minute 0 in Figure 5.7, particles begin to form. These particles alter the extinction in the chamber, Figure 5.6 (bottom), with a drop in the extinction at shorter wavelengths when the lights are turned on. This arises because the strongly absorbing 2-NP gas is being removed more rapidly from the system. As 2-NP does not absorb at longer wavelengths (400 nm), the extinction coincides with SOA formation, Figure 5.6 (bottom). The SMPS measurements were corrected by a factor of 2.69, as discussed in Chapter 4.

When the lights in the chamber were turned on, the 2-NP began to react immediately. If the new species produced have sufficiently low vapour pressure, they can form secondary particles. Particles were seen to form as soon as the lights were turned on (Figure 5.7) and immediately contributed to the extinction in the chamber. Not all the 2-NP underwent photodissociation or reaction. When the extinction was determined with the IBBCEAS, 2-NP gas phase absorption was present in the measured extinction. A small spectral feature centred at 385 nm was also observed. The instant formation of particles indicates that photochemical processes were the primary reaction initiator. Moreover, the time rate of change of

extinction responded immediately to turning the lights off and to starting the extraction of particles from the chamber by the filtering process.

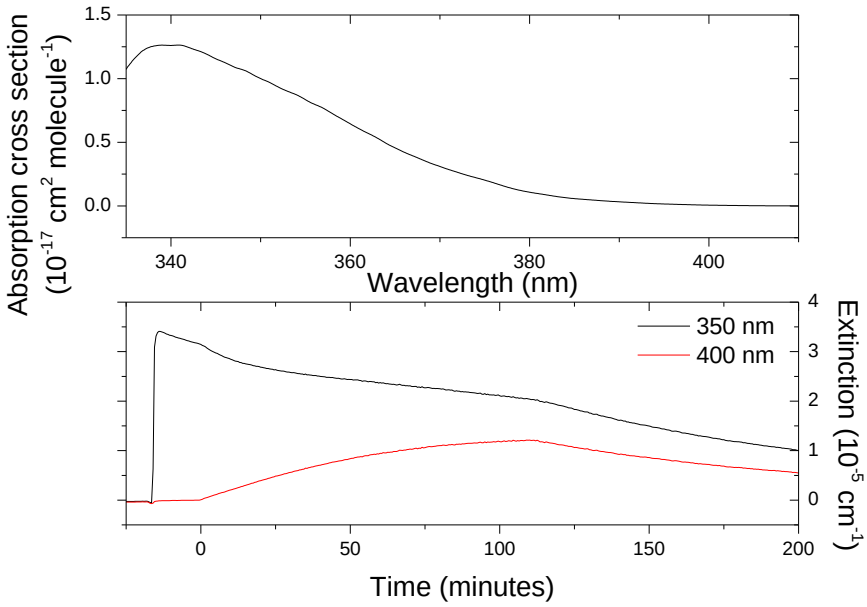

Figure 5.6 Top: Absorption cross section spectrum of 2-NP in the gas phase. Bottom: Extinction time profile at 350 and 400 nm. Chamber lights were switched on at 0 min.

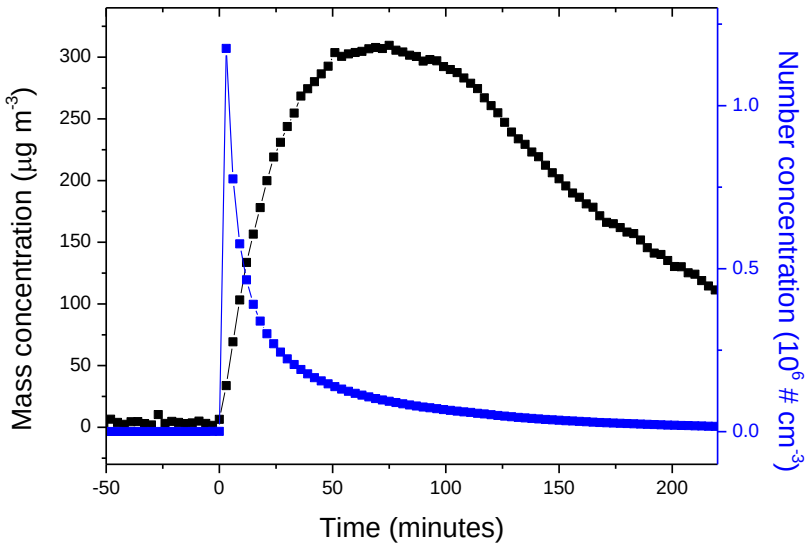

Figure 5.7 Mass and number concentration of SOA formed from the photolysis of 2-NP. The photolysis event starts at 0 min.

The fitting program was used to determine the mixing ratio of 2-NP remaining in the chamber as a function of time (Figure 5.8).The fitting results overestimated the mixing ratio of 2-NP by 18 %, similar to that for MVK and ethanal. The absorption cross section for 2-NP that was recorded earlier was fitted to the measured extinction. This enabled the determination of the mixing ratio of 2-NP present at all times during the experiment and its associated extinction. Being able to determine the mixing ratio of 2-NP throughout the experiment enabled us to investigate the kinetics of the reaction. While photochemistry is its major loss process, 2-NP also deposits to the chamber walls. Wall losses of gas phase species in simulation chambers are well documented and are evident in this experiment by the decrease in extinction between 0 and 900 seconds in Figure 5.8 (44; 45). The first order wall loss rate coefficient, k_{wall}, was determined to be 1.07×10^{-5} s^{-1} for 2-NP during this 'dark' period, i.e. prior to the chamber lights being turned on. This value was used to correct the 2-NP mixing ratio and is also shown in Figure 5.8. The effects of photolysis and other chemical reactions, as well as filter sampling, are evident. The wall loss corrected 2-NP mixing ratios are stable (as they should be) both prior to illuminating the chamber and in the period between switching off the chamber lights and the filter sampling period. Once the filtering process began, both particles and 2-NP gas were removed from the chamber, resulting in a drop in concentration.

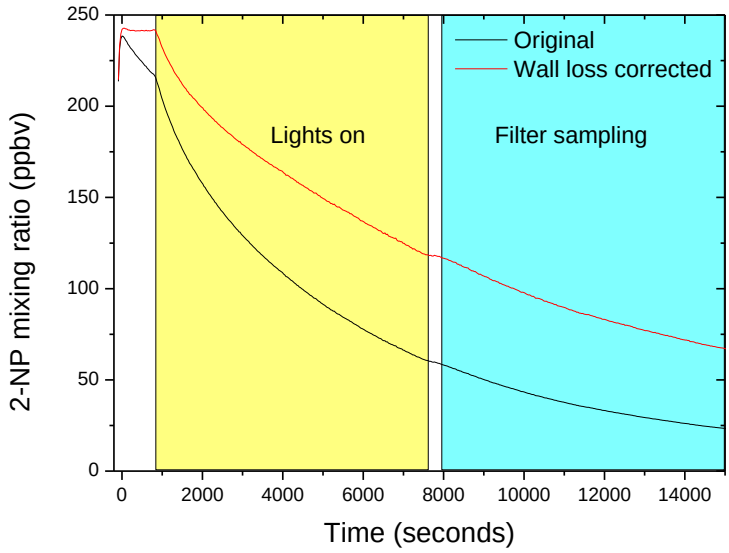

Figure 5.8 Temporal change in 2-NP mixing ratio over the course of the experiment. The calculated concentration of 2-NP is shown in black while a wall loss correction factor has been applied to the red line.

Photolysis is potentially the method through which 2-NP is removed from the system. Photolysis is a first order loss process:

$$J = \frac{\ln\left(\frac{[2-\mathrm{NP}]_0}{[2-\mathrm{NP}]_t}\right)}{t} \qquad \textbf{(5.1)}$$

where *t* is time, *J* is the photolysis rate coefficient, and *[2-NP]*$_0$ and *[2-NP]*$_t$ are the concentrations of 2-NP at time 0 and *t* respectively. An important atmospheric property of a species is its photolysis rate. The photolysis rate coefficient of a species is the product of its absorption cross section, radiative flux and quantum yield (eq. 1.5). We applied Eq. 5.1 to the 2-NP concentration time profile to see if the losses were as a result of a first order reaction. Figure 5.9 shows the resultant plot. Although the fit is generally fair ($r^2$of 0.992), the data deviate significantly from linearity in the first 15 minutes. This could indicate that the loss processes are not determined simply by a first order photolysis mechanism.

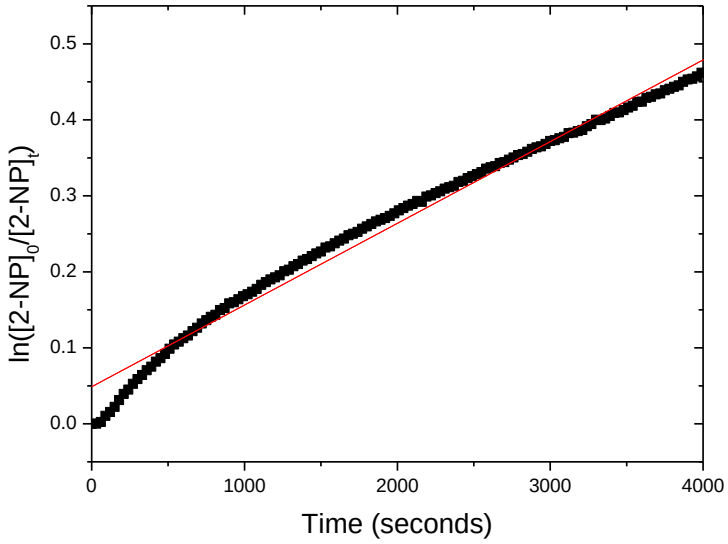

Figure 5.9 Plot of natural log of change of [2-NP] as a function of time. The slope of the line is the photolysis rate constant.

The second order kinetics of [2-NP] concentration was also considered:

$$\frac{1}{[2-\mathrm{NP}]} = \frac{1}{[2-\mathrm{NP}]_0} + \mathrm{kt} \qquad \textbf{(5.2)}$$

where *k* is the second order rate coefficient. This plot (Figure 5.10) better represented the concentration data (r^2 of 0.997) than the first order plot over the entire kinetic data set. This could indicate a number of potential reaction pathways. OH has been supposed to form during the photolysis of 2-NP and these OH radicals could react with other 2-NP molecules to form products. This possibility was investigated in a later experiment through the addition of cyclohexane, an OH radical scavenger. Alternatively, the curvature of Figure 5.9 could be an indicator that there are two first order processes at work. These possibilities aside, a second-order process is consistent with that in the proposed mechanism for the photolysis of 2-NP (Figure 5.2). In this reaction scheme, a 2-NP molecule and a radiatively excited 2-NP molecule react. Despite photolysis processes usually being first order processes, in this case the excited molecule must collide with another 2-NP molecule to react further. This process could account for the second order reaction.

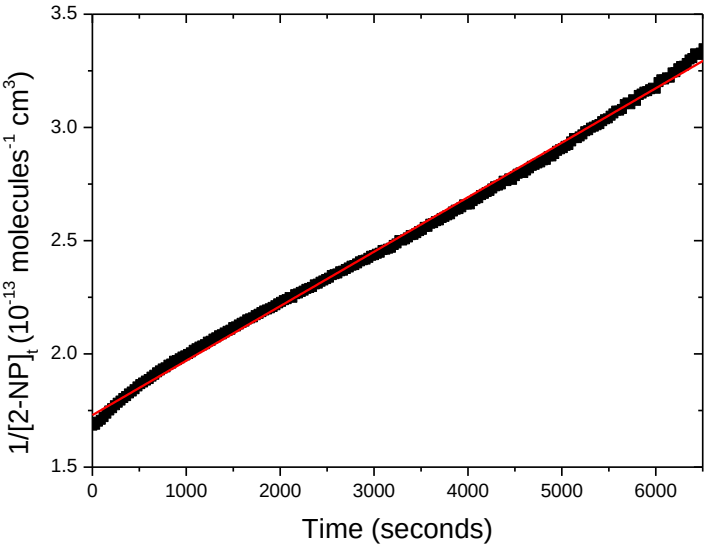

Figure 5.10 Second order reaction plot for the change in 2-NP concentration. This gives a much closer linear fit than the first order plot in Figure 5.9.

After the lights in the system were switched off there was still some 2-NP present. 65 % of the starting concentration of 2-NP remained in the chamber in the gas phase after 200 minutes. The mass concentration of SOA can be determined at any time during the experiment. The SMPS records the volume of particles and uses a user defined density to report the mass concentration. Bardini et al. measured the density for the SOA species formed by the photolysis of 2-NP in the EUPHORE chamber using a tapered element oscillating microbalance (TEOM) and an SMPS (28). By plotting these two values against one another, the density of the particles was determined to be 0.85 ± 0.01 g cm^{-3}. This density changed little over the course of a three hour experiment. The increase in particle formation occurred concurrently with the decrease in 2-NP concentration. The temporal change in gas phase 2-NP mixing ratio and particle mass concentration is shown in Figure 5.11. There are aerosol wall losses starting prior to the filtering processes. However the aerosol loss rate could not be determined with a high enough degree of confidence so this was not accounted for in our data.

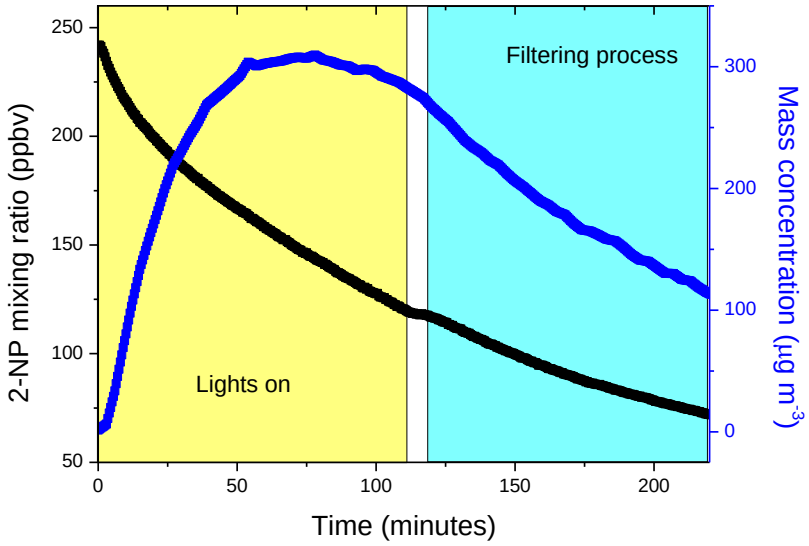

Figure 5.11 Concentration time profile for 2-NP gas phase and SOA particle species. After 117 minutes there is a decrease in mass concentration due to filter samples being taken.

As the concentration of the original 2-NP and the newly formed SOA particles can be determined at any time in the experiment, a yield curve was constructed to determine the overall yield of formation of SOA. The mass concentration of SOA formed was plotted against the amount of 2-NP reacted. The slope of this graph is the mass yield for the experiment. In this case the measured mass yield was 0.70, Figure 5.12, which is similar to the values recorded by Bardini et al. of 0.74. In their study they state that the aerosols formed from 2-NP photolysis are readily lost to the walls of the chamber. Unfortunately no measurements were made of the aerosol loss rate in the study presented here. Such wall losses could be the cause of the slight difference in the measurements.

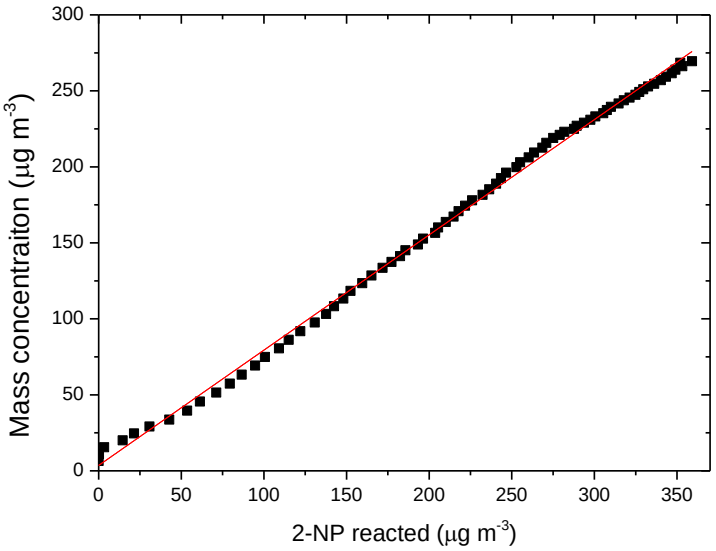

Figure 5.12 Yield plot for the SOA formed from 2-NP photolysis.

2-NP gas phase and artefact removal

As the concentration of 2-NP is now known at any point during the experiment, its gas phase extinction can be removed to determine the remaining extinction. These changes to the spectra are shown in Figure 5.13, where the SOA extinction starts to become clearer. After the 2-NP extinction was removed there was still a strong extinction component present in the chamber. This extinction is due to both scattering and absorption of the SOA.

Besides the prominent 2-NP gas phase absorption, a smaller spectral structure centred at 385 nm is apparent (Figure 5.13). The structure of this feature is inconsistent with the broad spectra associated with Mie scattering, but could indicate the presence of an absorbing species or an experimental artefact. The shape of the absorption was not consistent with any absorbing species that could be identified in this region. To check the latter possibility, the extinction spectra were measured in an empty chamber after turning on the chamber lights. A similar structure at the same position was found to occur in the empty chamber extinction spectra, indicating that the feature was an experimental artefact. In fact, the position of the main structure was located in a reflectivity maximum for the mirror

reflectivity. Fitting a (1-*R*) spectrum to the extinction removed much of this spectral structure entirely. The time dependence of the fit coefficient for (1 – *R*) changes synchronously with the chamber temperature, Figure 5.14. These observations are consistent with small, thermally-induced changes in the alignment of the optical system as the chamber and mirror mounts heat up and cool down. The position of the artefact peaks and the mirror reflectivity peaks can be seen in Figure 5.15. The apparent extinction caused by the mirror reflectivity was therefore removed from the measured extinction based on the (1 – R) fit. The remaining extinction was thus supposed to be due to SOA and gas phase species formed due to 2-NP photolysis.

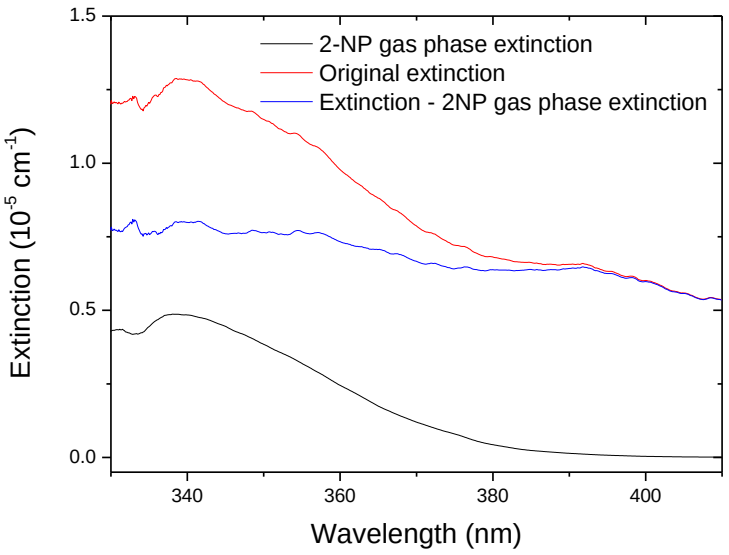

Figure 5.13 Spectra of the measured extinction (red), the fitted2-NP contribution to gas phase absorption (black), and the extinction difference between these spectra (blue). These spectra are based on the original extinction spectra measured after 200 minutes.

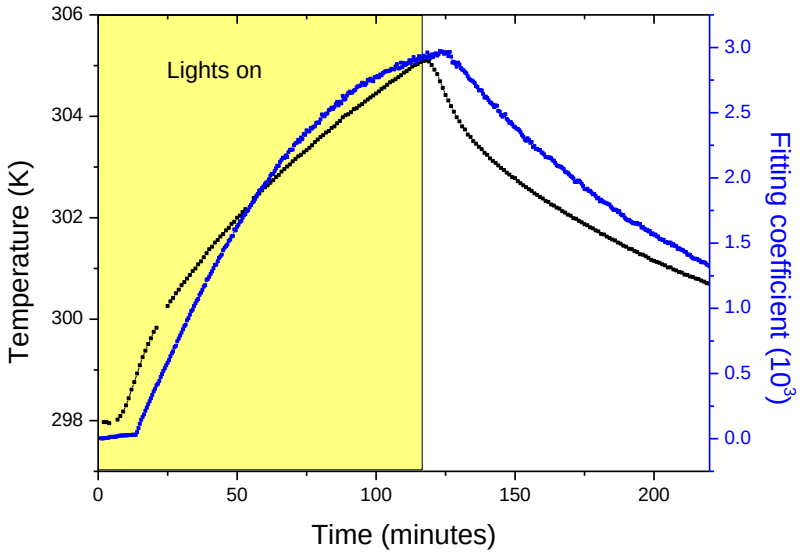

Figure 5.14 Temporal profile of the fit parameter for (1 – R) and the chamber temperature.

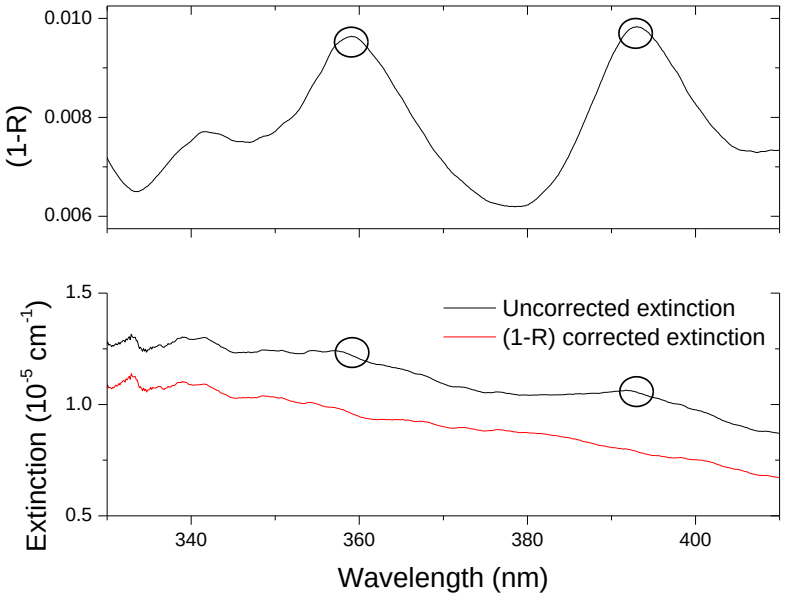

Figure 5.15 Top figure is the spectral structure for (1-R) for the dielectric mirrors. The bottom figure shows the extinction before and after the (1-R) structure is removed. The circles indicate the predominant (1-R) peaks.

Other gas phase species

There have been few studies of the photolysis products of 2-NP. Bardini et al. studied the reaction with an FT-IR spectrometer and observed the formation of NO_2, NO, O_3 and formic acid, while Bejan and co-workers reported the formation of HONO from 2-NP (24; 28). Of these potential gas products NO_2, O_3, and HONO absorb in our region of interest while NO and formic acid do not (46-50). Therefore NO_2, O_3 and HONO were also included in the spectral fit of the extinction spectra. However, the results of these fits were inconclusive and the presence of these species could not be verified. Although the possibility exists that other, semivolatile nitroaromatic reaction products could contribute to the absorption spectra, there was no evidence in the spectra to indicate other gas phase species similar to 2-NP.

5.4.1. SOA optical properties

The optical properties of the SOA can be investigated more closely after removing the underlying 2-NP absorption and the artefact. The extinction can be mass corrected to determine its mass absorption coefficient (MAC) and mass scattering coefficient (MSC). As previously discussed, the IBBCEAS cannot differentiate between scattering and absorption, so the absorption of filter samples was quantified and used as a proxy measure of the SOA absorption.

Off-line analysis

Filter samples were taken after the chamber lights had been turned off and sampling took place over one hour at a flow rate of 20.9 L min^{-1}. The particle mass collected onto the filter was too small to quantify directly by weighing the filter before and after the extraction. The mass was therefore estimated from the measured mass concentration and the total volume sampled. The sample volume was the product of the time and the flow rate, which was measured with an electronic flow meter. The decrease of mass concentration in the chamber was recorded by the SMPS. During the 60 minutes of sampling, the mass concentration in the chamber decreased from 275 to 165 μg m^{-3}. The filters were added to a mixture of 2.5 ml of water and 2.5 ml of methanol and then sonicated to extract the

particles into the solvent. Several assumptions were made about this estimation of the mass concentration: 1) all SOA losses were due to the sampling process, 2) no particles were lost during the extraction process, 3) all of the particles were captured by the filter and 4) the particles dissolved completely in the solvent.

The presence of coloured SOA on the filter indicated that the SOA formed had some visible absorption. Each of the solvent extractions resulted in a similar absorbance structure (Figure 5.16). Extraction efficiency for BrC has been found to be over 90 % when methanol was used as the solvent (43). In order to account for any water-soluble SOA, a 1:1 methanol:water mixture was chosen as the extraction solvent. In contrast to the absorption of gas phase 2-NP, which is negligible above 400 nm, Figure 5.16 shows that the particle absorption extended to much longer wavelengths. There is even appreciable absorption beyond 500 nm. This new, long wavelength absorption suggests that new species cause this absorption.

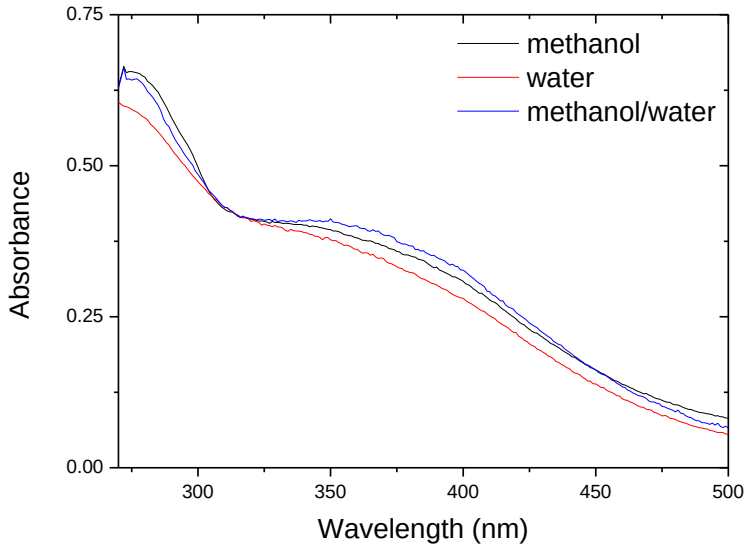

Figure 5.16 Comparison of absorbance spectra resulting from extraction of particles collected from the reference 2-NP SOA experiment into methanol, water, and methanol/water solution.

The absorbance measurements allow the mass absorption coefficient (MAC) and the imaginary part of the complex refractive index of the SOA to be determined. The assumptions underlying the sample mass quantification imply that the

following MAC values should be treated as lower limits. The MAC is calculated from the following formula:

$$MAC = \frac{A_\lambda \ln(10)}{Cb} \quad \textbf{(5.3)}$$

where A_λ is the wavelength dependent absorbance, C is the concentration of the sample (g m^{-3}) and b is the length of the cell (m) (43). The calculated MAC for the reference experiment is shown in Figure 5.17. The values determined range from 0.335 m^2 g^{-1} at 400 nm to 0.664 m^2 g^{-1} at 300 nm.

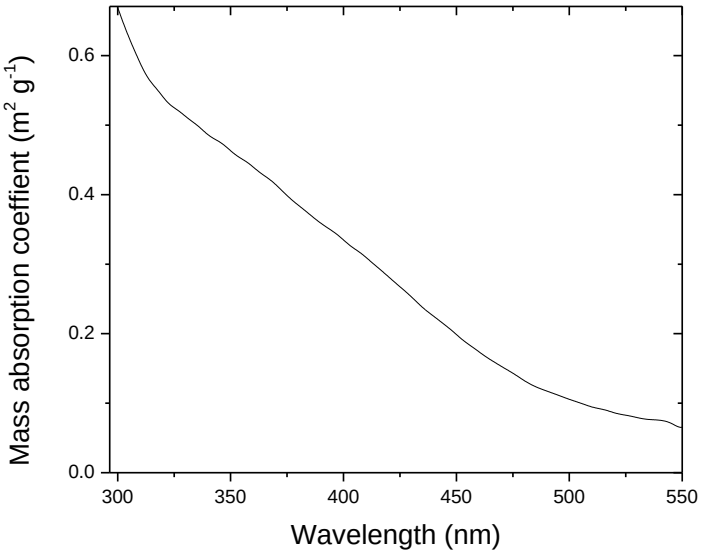

Figure 5.17 Spectral dependence of mass absorption coefficient of particles formed in the reference experiment.

MAC values for various BrC species have been reported and are given in Table 5.2. Values were reported by Chen and Bond, Kirchstetter et al., while Feng and co-workers calculated their MAC to match these other values at 550 nm (43; 51; 52). In our study, the MAC was 0.46 m^2 g^{-1} at 350 nm, which is almost 5 times less than the reported 'moderately absorbing BrC'. This indicates that the particles

formed by 2-NP in the chamber are not particularly strong absorbers in the near-UV. The particle sources and processing were quite different, however. Chen and Bond, and Kirchstetter et al. both studied particles formed directly by wood burning. Kirchstetter and co workers compared the light absorbing potential from particles collected from diesel vehicle emissions with particles from biomass combustion (including wood and savanna burning). Based on the wavelength dependence of absorption they concluded that the vehicle emissions produced BC particles while the biomass particles were a mixture of BC and BrC. Chen et al. investigated the effects of wood type, size, and combustion temperature on BrC formation. They found that increasing the temperature increased the production of BrC. Both of these BrC studies were conducted on particles formed as a result of combustion. These particles would therefore have not undergone extensive exposure to UV light, which could result in photobleaching of some particle constituents. Thus the chemical composition of these studies was likely dissimilar. Also, the density used for the particles in the Kirchstetter paper were reported as 1.2 g cm^{-3} which is almost double the density (0.85 g cm^{-3}) used in the 2-NP experiments. The Chen et al. MAC and CRI was determined with a density of 1.65 g cm^{-3}.

The imaginary part of the refractive index, *k*, is determined from the MAC by:

$$k = \frac{MAC \cdot \rho \cdot \lambda}{4 \cdot \pi} \qquad \textbf{(5.4)}$$

where ρ is the density of the SOA (53). The spectrum of the imaginary part of the CRI is shown in Figure 5.18 and literature values are reported in Table 5.2. Again, these should be treated as lower limits.

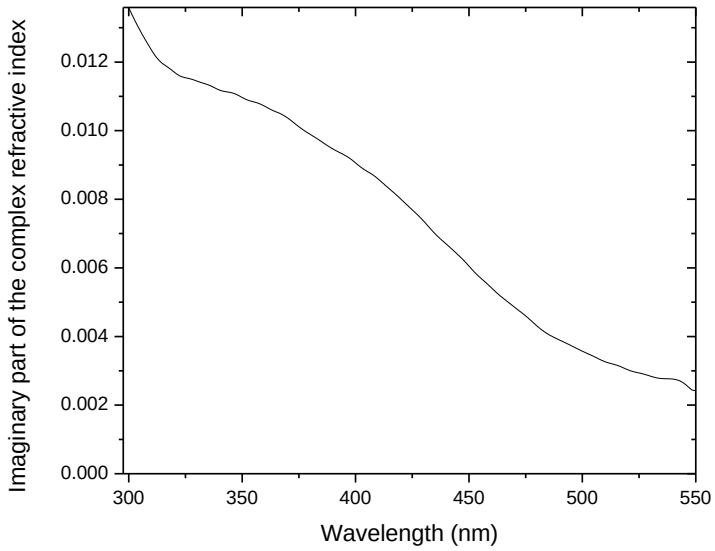

Figure 5.18 Spectral dependence of calculated imaginary part of refractive index of particles formed in the reference experiment.

Table 5.2 The measured and theoretical MAC and imaginary CRI values from a number of studies. This table was adapted from that in Feng et al. (51)**.**

	Imaginary part CRI		MAC (m^2 g^{-1})	
Wavelength	**350 nm**	**450 nm**	**350 nm**	**450 nm**
Moderately absorbing BrC	0.075	0.02	2.25	0.63
Strongly absorbing BrC	0.168	0.063	3.4	1.6
Chen and Bond (43)	0.1	0.02	2.25	0.4
Kirchstetter et al. (52)	0.168	0.0063	5.0	1.5

Single Scattering Albedo (*SSA*)

The mass extinction coefficient (MEC) was determined at several times. The extinction between 5 and 20 minutes was not included due to the rapid change in size and mass of the aerosols within the first 20 minutes. The MAC was subtracted from the average MEC over the filtering period (117-177 minutes) to calculate the MSC. A quadratic fit was applied to the MSC to remove the residual mirror

reflectivity structure. The measured absorption accounts for almost 10 % of total extinction, Figure 5.20, which suggests that the particles are primarily scattering.

The SSA is one of the key properties needed to determine the radiative forcing effect of an atmospheric component, (Section 1.5). The mass corrected values in Figure 5.20 can be used to determine the SSA:

$$\omega_0 = \left(\frac{\mathrm{MSC}}{\mathrm{MSC} + \mathrm{MAC}}\right) \qquad \textbf{(5.5)}$$

The resulting SSA values ranged from 0.89 to 0.90 between 340 and 410 nm. These values are comparable to SSA values measured over a biomass burning event in Southern Africa (0.89 at 550 nm), and to aerosols in semi-polluted locations (54). In these cases, BC is the dominant absorber in the particle phase. A change in the SSA of a particle from 0.9 to 0.8 can cause the sign of the affect to change (55). As the measured SSA value is above 0.8, the 2-NP SOA species likely have a small, negative radiative forcing affect.

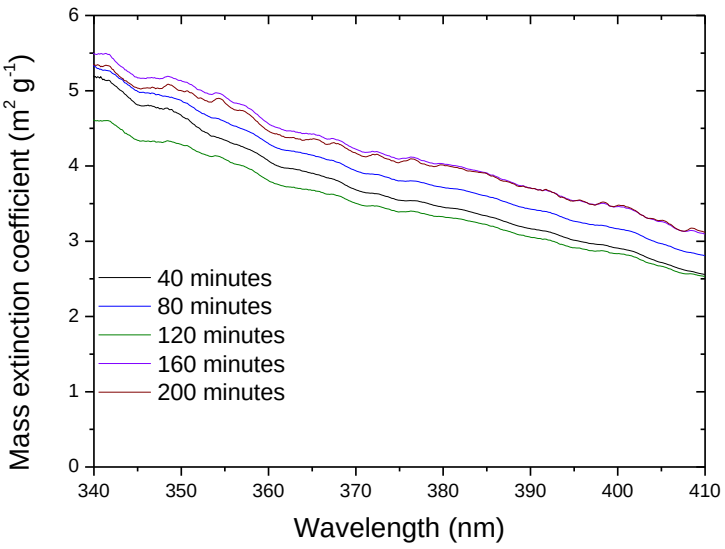

Figure 5.19 Spectral mass extinction coefficient (MEC) at a number of different times. The values converge after 40 minutes.

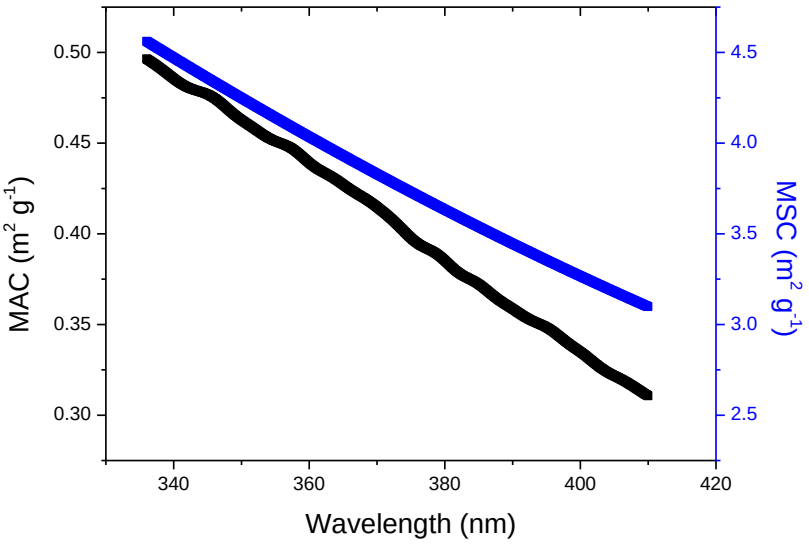

Figure 5.20 Average spectra of the MAC and MSC obtained between 117 and 177 minutes in the reference 2-NP experiment.

Complex refractive index

The real part of the refractive index was determined for the 2-NP SOA in the same manner as described in Chapter 4. For this process, the number distribution of the particles and the imaginary part of the RI are needed. The number distribution was measured with the SMPS, while the imaginary part of the RI was determined from the filter samples as described above. The values for the real RI value were determined at 5 nm intervals, but the time dependence was not investigated because the imaginary RI was determined over a single time period. The spectrum of the real refractive index is shown in Figure 5.21 and increases with decreasing wavelength, as is commonly observed (56). This gives a range of values for the complex refractive index values for 2-NP SOA as a function of wavelength (Table 5.3).

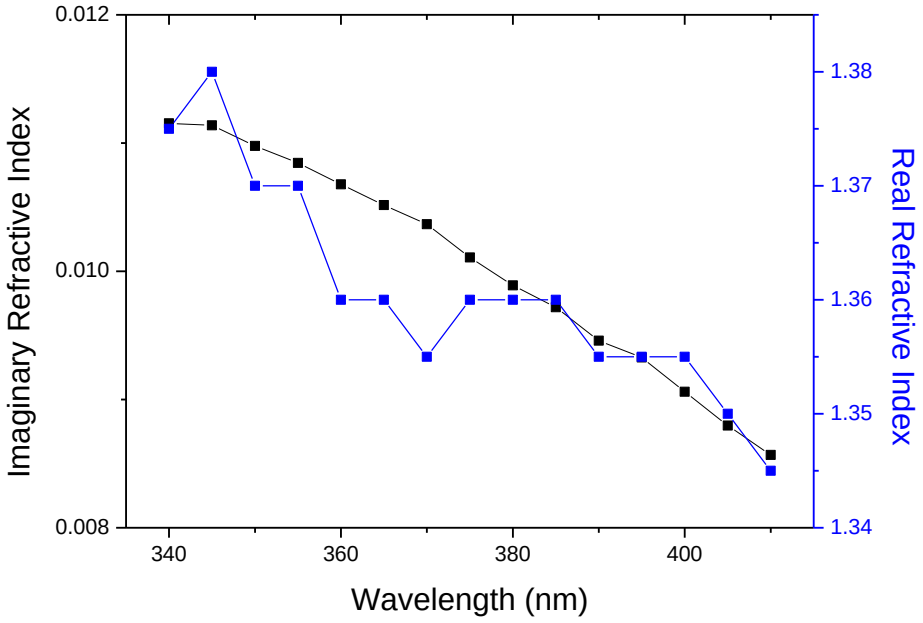

Figure 5.21 Spectral dependence of both imaginary and real components of complex refractive index from the 2-NP reference experiment.

Table 5.3 The complex refractive index of 2-NP SOA from the reference experiment.

Wavelength (nm)	Real	Imaginary
340	1.375	0.01115
345	1.38	0.01114
350	1.37	0.01098
355	1.37	0.01085
360	1.36	0.01068
365	1.36	0.01052
370	1.355	0.01037
375	1.36	0.01011
380	1.36	0.00989
385	1.36	0.00972
390	1.355	0.00946
395	1.355	0.00933
400	1.355	0.00906
405	1.35	0.0088
410	1.345	0.00857

Particle composition

The chemical composition of the SOA was determined using ultra high resolution mass spectroscopy. For the standard experiments the top three masses determined were 155, 184 and 200 based on the molecular mass and the LC retention time. Two species which match the molecular mass of 155 g mol^{-1} are nitrocatechol and nitrohydroquinone, and both species have been found during the photolysis of 2-NP in an aqueous solution (31). Both cases arise from addition of an hydroxyl group to the 2-NP aromatic ring.

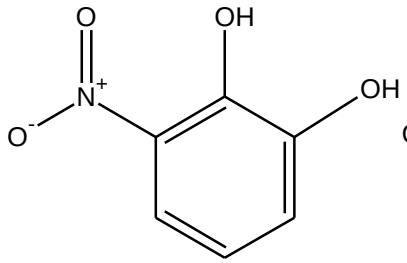

3-nitrocatechol

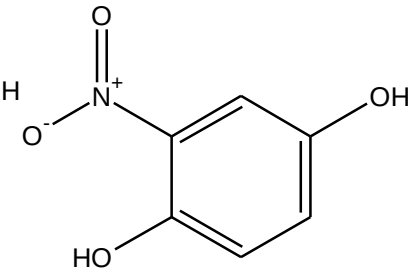

2-nitrohydroquinone

The proposed species with a molar mass of 184 g mol^{-1} mass is 2,5-dinitrophenol. This could arise through the addition of an NO_2 group para to the existing NO_2 group. The final main compound that has been suggested is 3,5-dinitrobenzene-1,2-diol for the 200 group.

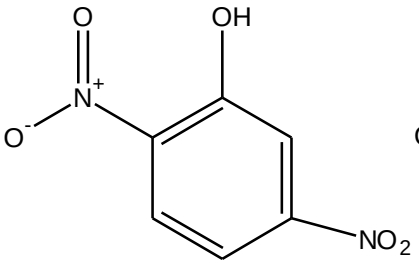

2,5-dinitrophenol

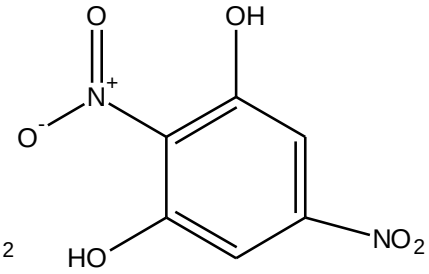

3,5-dinitrobenzene-1,2-diol

5.4.2. Role of OH scavenger

250 ppbv of 2-NP and 20 ppmv of cyclohexane were added to the chamber to test for the effect of the OH radical on the formation of particles. A large excess of cyclohexane was added to the chamber prior to the addition of 2-NP and acted as an OH scavenger by reacting with OH to form cyclohexanone and cyclohexanol (57). Studies involving the ozonolysis of terpenes have shown that the presence of OH scavengers have a significant influence on the SOA yield (58; 59). OH radicals arise from HONO formed on the chamber walls under illuminated conditions. Moreover,

in the 2-NP system considered here, photolysis of 2-NP could also be a direct source of HONO, as Bejan et al. have shown (24).

Physical properties and chemical composition

There was a higher initial concentration of 2-NP added to the chamber compared to the reference experiment, so a higher particle mass concentration would be expected if the OH radicals did not influence SOA formation. Instead, a decrease in the overall mass concentration of the SOA formed was observed (Figure 5.22). The mass yield was determined to be 0.27 and is much lower than that for the reference experiment (0.70) or that reported by Bardini et al. of 0.74 (28). Wall losses of particles were not corrected, but would be too small to account for such a large difference. These observations indicate that OH oxidation plays a significant role in SOA formation in this system, as has been observed in a number of OH scavenger studies (60-62).

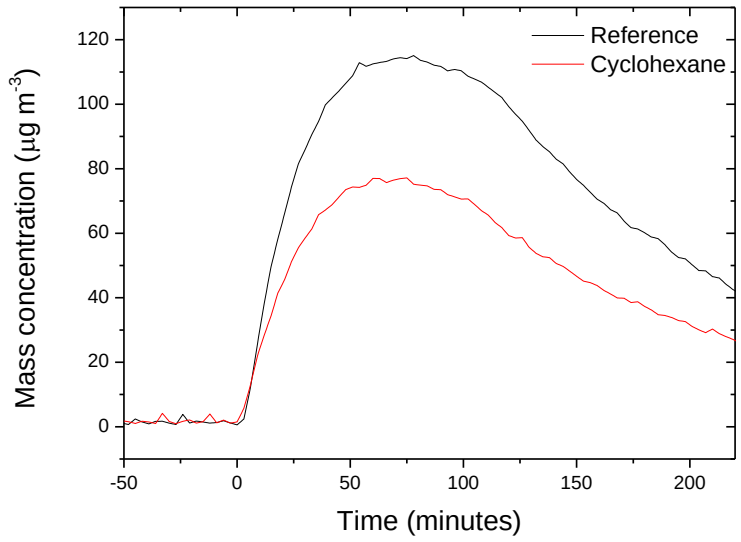

Figure 5.22 Temporal change in mass concentrations for the reference and OH scavenger (cyclohexane) experiments. The role of OH radical in the 2-NP system is indicated by the significant reduction in mass concentration in the presence of cyclohexane.

Kinetics of 2-NP loss

The kinetics of the loss of 2-NP were tested in the same manner as above to investigate the contribution of OH chemistry. Figure 5.23 shows the first and second order fits to the 2-NP-time data. The first order fit was better with cyclohexane present than the reference experiment and the rate was slightly higher (1.5×10^{-4} s^{-1} against 1.0×10^{-4} s^{-1}). The initial kinetics do not diverge as much from later behaviour, as was seen in Figure 5.9 when a scavenger was not present. Nevertheless, the kinetics are again better described by second order kinetics (r^2 0.999) than as a first order loss process (r^2 0.990). The removal of OH radicals in this reaction does not affect the order of reaction significantly, suggesting that OH is not a dominant species in the removal of 2-NP. We therefore must look at the proposed reaction mechanism in (Figure 5.2) to find a more appropriate species for 2-NP reactions. This mechanism indicates the presence of a biradical 2-NP species that reacts with ground state 2-NP. The effect of this reaction on the order of reaction will be investigated in the next section. Bardini and co-workers proposed that as potential reactions with the OH radical were removed by the presence of excess cyclohexane, photolysis was proposed as the primary 2-NP loss process. The ratios of the photolysis of 2-NP to NO_2 was measured as 1.8×10^{-2}. Our first order values for this experiment were 2.27×10^{-2}. However, their data also has a change in slope in the initial photolysis period (0-1000 seconds). This was not addressed in their work and they did not explore the possibility of this being a second order reaction.

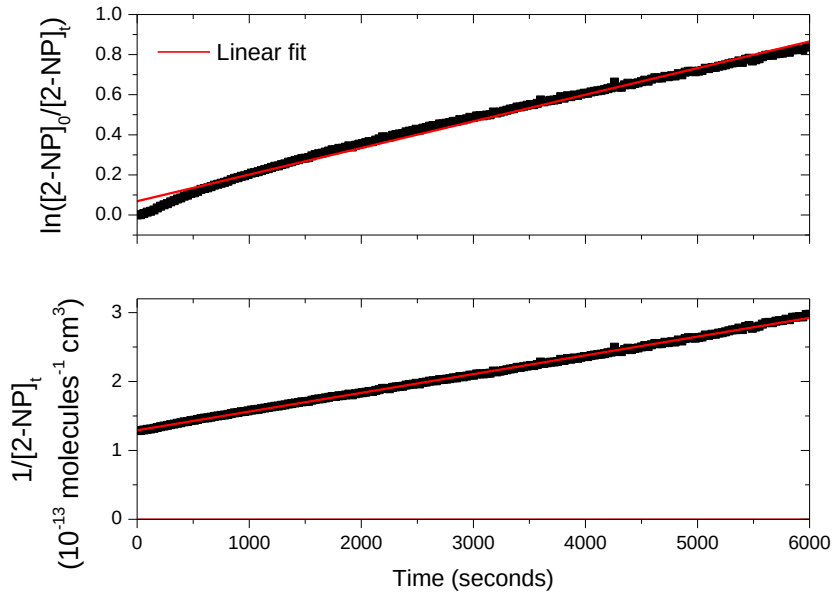

Figure 5.23 Top: First order fit for [2-NP] concentration data. Bottom: Second order fit for the same data set.

Bardini et al. calculated the photolysis rate with the actinic flux, quantum yield and absorption cross section. They found that this over-estimated the photolysis rate constant by almost 1500. As the quantum yield assumed for the calculation was unity, this indicates that this process has a much lower quantum yield.

Optical properties

The effects of the OH scavenger are apparent in a large increase in the MEC (Figure 5.24). This suggests that, despite the large mass concentrations associated with OH oxidation pathways, the products are not so strongly absorbing and scattering. In the same way as before, filter samples were collected after the end of the photolysis period and extracted into water/methanol solution. UV/Vis spectra were then recorded and the MAC calculated. The MAC spectra for the two reactions were quite similar, Figure 5.25.

The SSA was determined using the MAC from the filter extractions and the MEC from the IBBCEAS spectra. The values in this case were 0.96 and relatively constant across the spectrum. This SSA is appreciably higher than the SSA of the reference

experiment, suggesting that the OH radical is somehow associated with the formation of absorbing species.

The imaginary part of the refractive index was calculated from the MAC, Figure 5.26. The imaginary part of the refractive index, the measured extinction and the measured number distribution were again used to determine the real part of the refractive index. The real component of the refractive index (Figure 5.27) was much higher for the OH scavenger experiment, but still within the range expected for many organic aerosols (63-66).

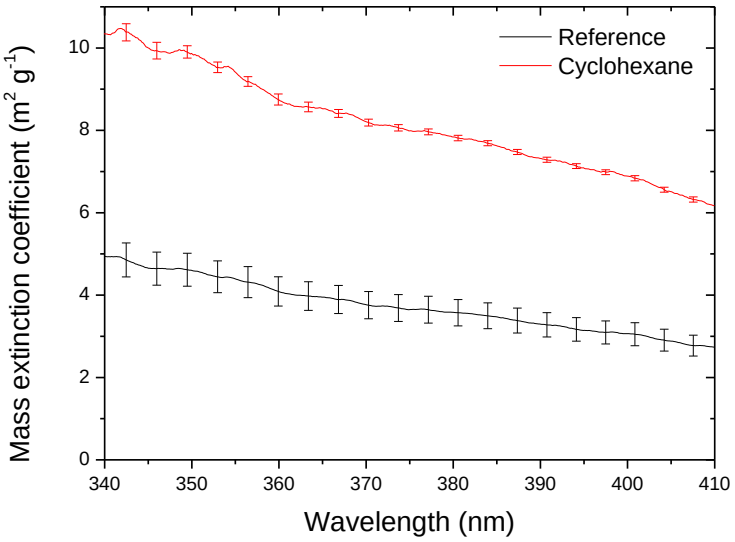

Figure 5.24 Comparison of MEC values for the reference and OH scavenger (cyclohexane addition) experiments. Values for the cyclohexane experiment were both much larger and had smaller uncertainties.

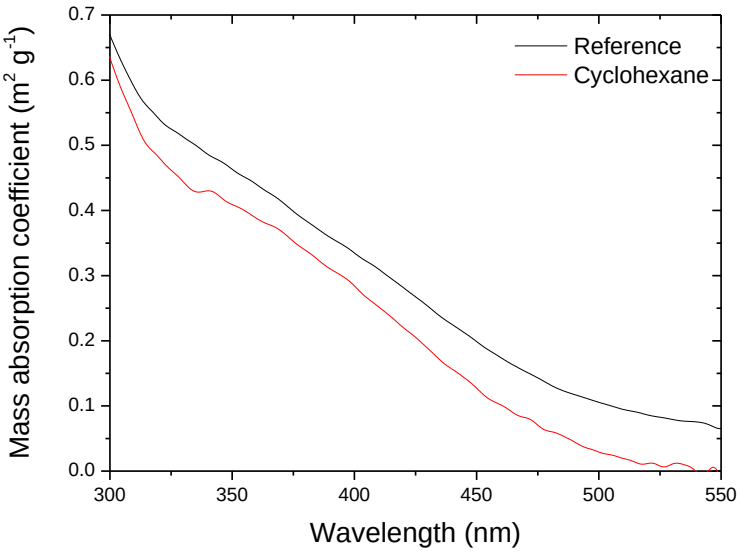

Figure 5.25 Comparison of MAC values for the reference and OH scavenger (cyclohexane addition) experiments.

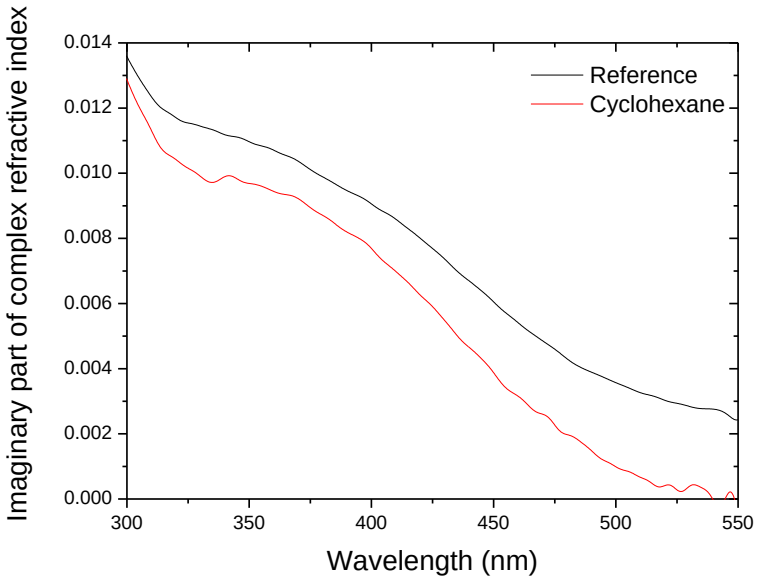

Figure 5.26 Comparison of spectral imaginary component of the CRI for the reference (black) and OH scavenger (red) experiments.

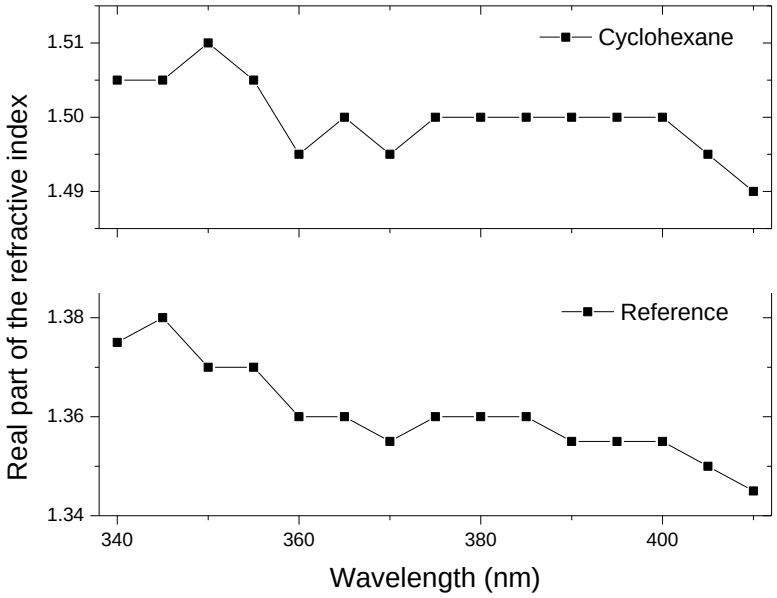

Figure 5.27 Comparison of spectral real component of the CRI for the reference (bottom) and OH scavenged (top) experiment. The real component of the CRI is significantly higher when the OH scavenger is absent.

5.5. Role of OH and Criegee Intermediates

Acetaldehyde was added to the chamber prior the addition of 2-NP. Acetaldehyde is typically used as a scavenger for both OH radicals and criegee intermediates (CI) (62). Although it is unlikely a CI would form as a major intermediate product of the photolysis of 2-NP, biradical species that resemble CI could be formed in the process. As with cyclohexane, acetaldehyde was added in large excess (20 ppmv). The presence of acetaldehyde has a strikingly effect on SOA formation, with complete suppression of particle formation observed. Illuminating the chamber did not produce a change in the mass concentration, size, or the number concentration of particles. The 2-NP concentration was determined over the course of the experiment and it shown in Figure 5.28. 2-NP was lost when the lights were on indicating that the loss of 2-NP is photo-initiated. The mixing ratio data was corrected for wall losses, so once the lights had been turned off there were no 2-NP losses.

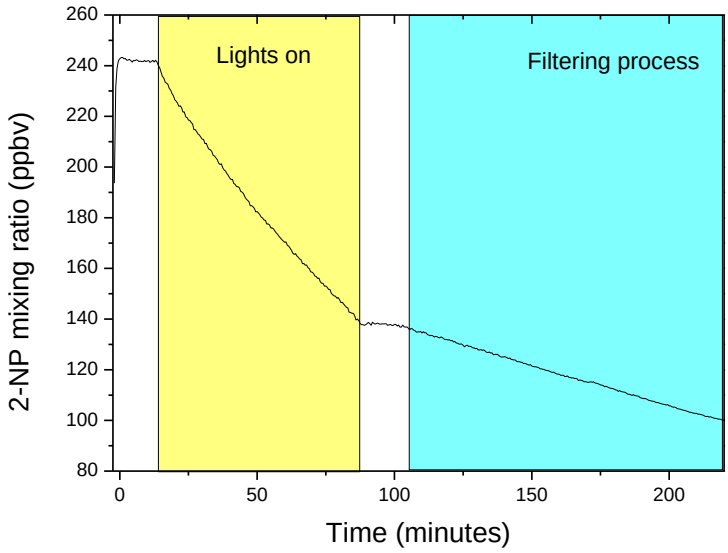

Figure 5.28 The temporal change in 2-NP mixing ratio. The data has been corrected for wall losses. 2-NP is removed when the lights are on, after this there are no further losses until the filtering process begins.

The kinetics of this reaction was once again investigated. First and second order plots were fitting to the data. In contrast to the reference experiment, a first order fit is a much closer fit to the experimental data in this instance. There is a very high degree of linearity with an r^2 value of 0.9995 for the first order fit, while there is an r^2 of 0.9953 for the second order fit, Figure 5.29. As the loss of 2-NP is more closely described by a first order loss process in this experiment we suggest that photolysis is the sole loss process (excluding wall losses). This also indicates that the radicalised form of 2-NP as proposed in Figure 5.2 may be responsible for 2-NP reaction and losses in typical 2-NP photochemical processes.

The calculated extinction due to residual 2-NP and the thermal artefact was removed from the measured IBBCEAS extinction. This enables the extinction from any possible gas phase species or aerosols to be identified. However, as can be seen in Figure 5.30, the residual after the 2-NP and artefact extinction structure is removed is effectively zero.

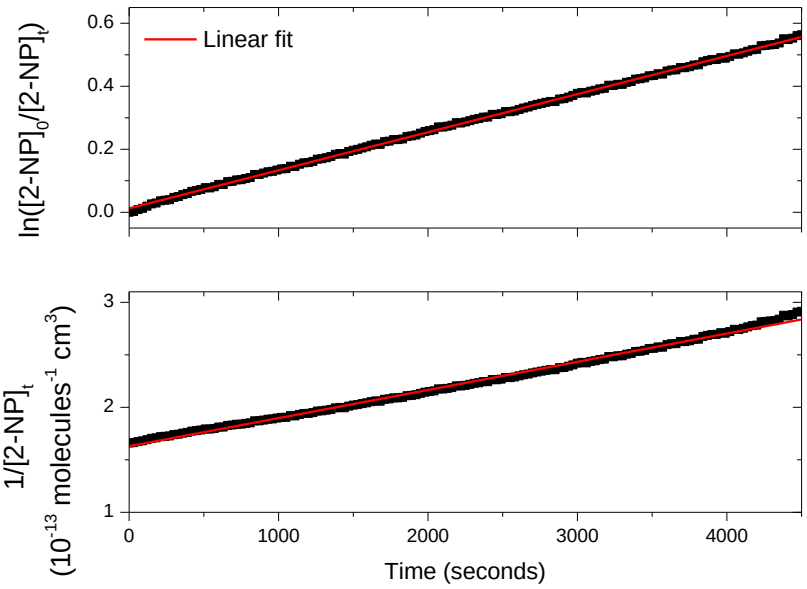

Figure 5.29 Top: First order plot for 2-NP mixing ratio with an r^2 of 0.9995. Bottom: Second order plot for the same data with an r^2 of 0.9952.

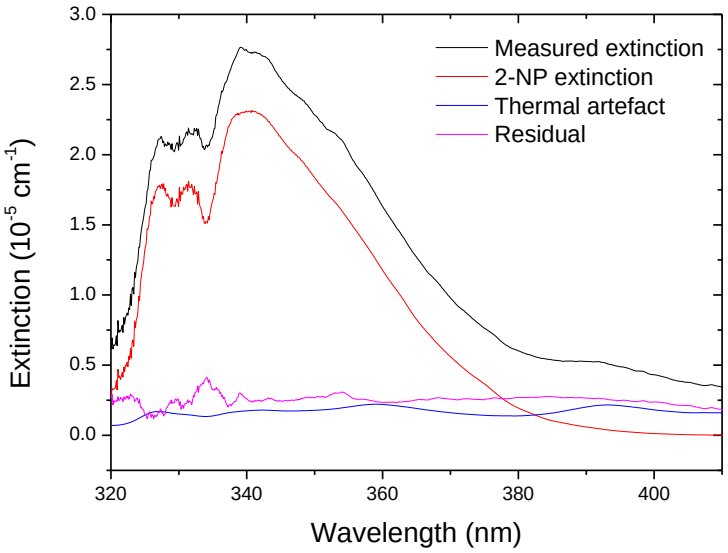

Figure 5.30 Extinction spectra after 100 minutes. Extinction is minimal once the thermal artefact and 2-NP extinction is removed.

Suppression of particle formation was confirmed by analysis of the filter samples solution spectrum, where only minor absorbance was observed at short wavelengths (Figure 5.31). Such absorption could arise from deposition of low volatility species or from secondary reactions on the filter.

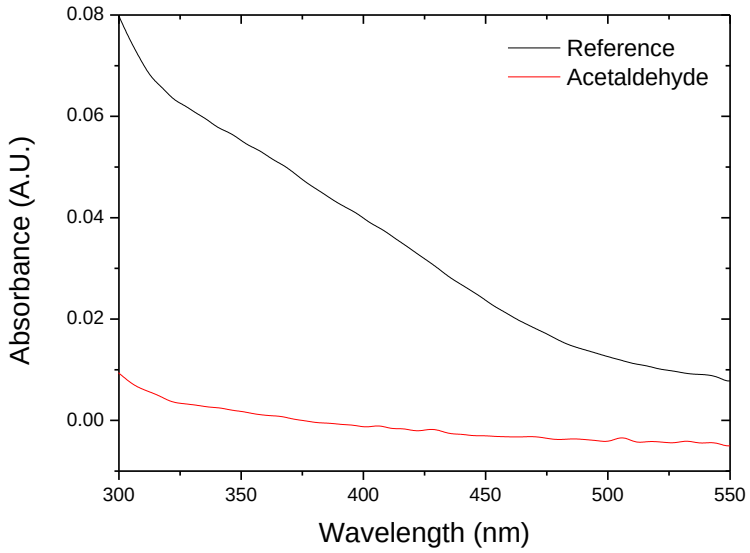

Figure 5.31 Absorption spectrum of filter samples from the reference and acetaldehyde (OH and Cl scavenger) experiments.

Chemical composition

UHRMS analysis of filter samples indicated that 155 was again the dominant species present (3-NC and/or NHQ). However, as the proposed mechanism for the formation of 3-NC proceeds as described in Figure 5.2 then presence of acetaldehyde should inhibit its production. This is also supported by the determination of a first order loss rate for this experiment. There could be potential contamination in the sampling lines from previous experiments. There was no blank filter sample tested so there is no way to rule this out. Both the 200 species, 3,5-dinitrobenzene-1,2-diol, and the 184 species, 2,5-dinitrophenol, were absent from the sample. This could indicate that these two species are responsible for the formation of particulate matter in the reference (and possibly cyclohexane) experiment. The vapour pressures of both species may be low enough to promote particle formation: that of 3,5-dinitrobenzene-1,2-diol could not be quantified, while the vapour pressure of 2,5-dinitrophenol is 1.22 x 10^{-4} mmHg, at 20 °C, indicating that it could readily form particles (67; 68). The IBBCEAS measurements did not show the presence of any extinction causing SOA. The gas phase 2-NP is

removed from the chamber due to photolysis but whatever species are formed do not react further to form SOA.

5.6. Presence of NO_2

NO_2 was added to the system prior to the photolysis of 2-NP to test the influence of photolysis in a nitrated environment. In polluted regions such as those where 2-NP would predominantly be found, elevated levels of NO_2 would be expected, and could alter the physical or optical properties of the SOA and its associated radiative effect.

Physical properties and chemical composition

Prior to addition of 2-NP, ca. 400 ppbv of NO_2 was added to the chamber. Particles formed after the lights were turned on; however, NO_2 also had a suppressing effect on the formation of SOA particles and more than halved the maximum mass concentration (Figure 5.32).

UHRMS analysis of filter extracts indicated that 184 (2,5-dinitrophenol) was the dominant species present in the sample. This compound has two nitro groups, in accordance with expectations that higher nitration would occur in the presence of elevated nitrogen oxides. Filter extracts also contained the 155 and 200 species, and this is the first instance of any of the experiments that 155 was not the most abundant species present.

The formation of SOA particles in high NO_2 studies has been reported previously. In the photochemical oxidation of monoterpenes and mono- and polycyclic species, higher NO_x concentrations were associated with a decrease in SOA yield (6; 69-73). The suppression of SOA formation in high NO_x environments has been attributed to the reaction between peroxy radicals and NO and HO_2 to form volatile products, which prevents their condensation into particles (74). In our experiments, NO would be present in the chamber owing to photolysis of NO_2 below 397 nm.

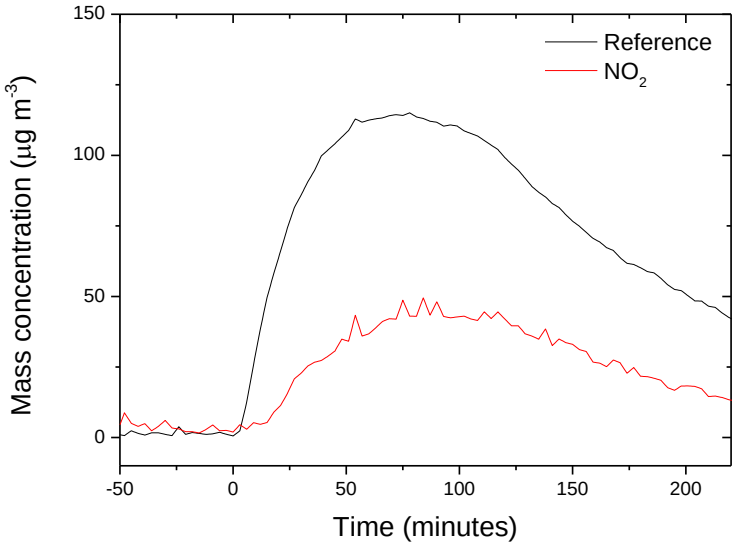

Figure 5.32 Time profile of the SOA mass concentration. Compared to the reference experiment, addition of NO_2 reduces the formation of SOA.

Optical properties

The MAC absorption spectrum of filter extracts shows that, while fewer particles are formed, they have a much larger MAC (Figure 5.33). In particular, the absorption is 4 times greater at the short wavelength limit, but proportionally even larger at longer wavelengths.

2,5-dinitrophenol is the major compound in the filter extracts, which could indicate that this species is responsible for an appreciable portion of the SOA absorption. The increase in the absorbing nature of the SOA could be important in real world environments. 2-NP and NO_x are commonly co-emitted from vehicle exhaust and are both elevated in urban areas. The interaction of these components could increase the absorption of organic particulate matter. As the MAC value is larger in the high NO_2 environment; the imaginary part of the CRI is also greater by over a factor of 3 (Figure 5.34).

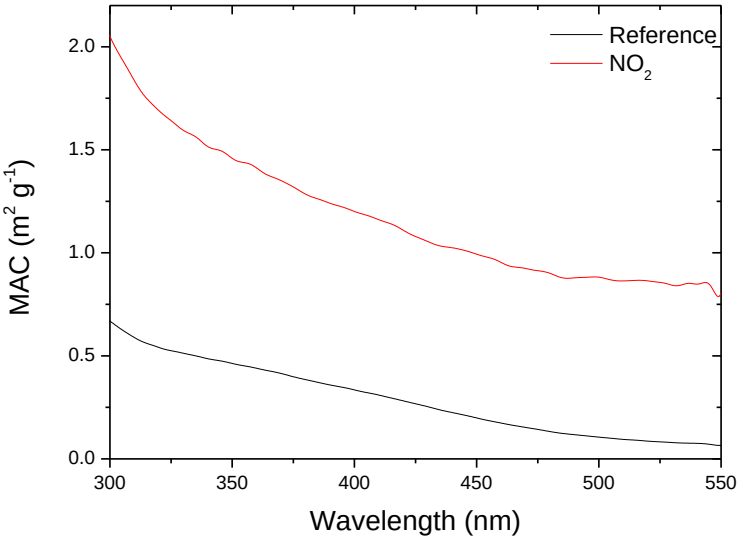

Figure 5.33 Comparison of the MAC spectra for high (red) and low (black) NO_2 environments.

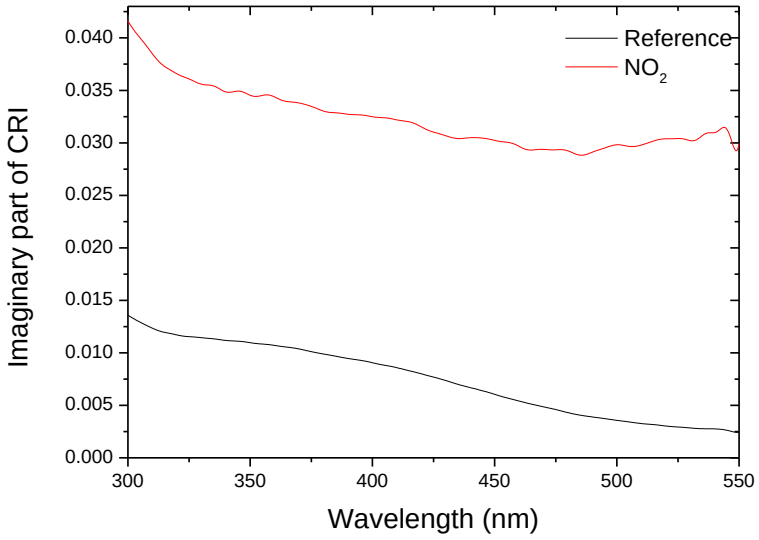

Figure 5.34 Comparison of imaginary part of CRI for species formed in high and low NO_2 environments.

The NO_2 absorption could not be satisfactorily removed from the measured extinction. As such the MSC and the SSA could not be determined. However, as the MAC is over twice as strong across the entire spectral region, it is reasonable to conclude that the SSA values of the 2-NP SOA would be much lower in high-NO_x

rather than low NO_x environments. Compared to particles from the reference experiment, where SSA is close to 0.89, formation of these absorbing organic particles in high NOx environments would likely have a strongly positive radiative forcing.

5.7. Conclusions and atmospheric implications

The absorbing and scattering nature of the SOA formed through the photolysis of 2-NP was investigated. Through the combination of on-line (IBBCEAS) and off-line (UV/Vis spectrometry) techniques the MEC, MSC and MAC values for these particles were determined. The mean value of the SSA value over our measurement spectrum was 0.89, indicating that the SOA formed would have a negative radiative forcing effect. The UHRMS analysis of filter samples identified the most prominent products formed during the photochemical experiments: 3-nitrocatechol, nitrohydroquinine, 2,5-dinitrophenol and 3,5-dinitrobenzene-1,2-diol. Some of these species have previously been found in 2-NP photolysis experiments.

The presence of an OH scavenger (cyclohexane) reduces the mass concentration and imaginary part of the CRI but it increases the real part of the refractive index. This finding may indicate that OH reactions contribute to forming some of the absorbing species. Complete suppression of SOA was seen when acetaldehyde, an OH and criegee intermediate (CI) scavenger, was added to the system. This observation suggests that a biradical or other CI-like species play a key role in the formation of low volatility products in the 2-NP photochemical system. Elevated levels of NO_2 in the chamber produced more absorbing SOA and increased the composition of 2,5-dinitrophenol. This species is likely responsible for a large portion of the absorbing nature of the SOA formed. The increased imaginary part of the CRI indicates that there would be a decrease in the SSA values for particles formed in the presence of high levels of NO_2, which would be associated with many urban environments.

Brown carbon has become an increasingly important area of research owing to their ability to absorb light in the tropospherically relevant UV/Vis region. The SSA values reported here for the standard 2-NP photolysis experiment ranged from 0.89 to 0.9 from 325 to 420 nm. At these values the general radiative forcing (RF) affect of SOA is probably still negative, albeit less so than for purely scattering aerosols. However, elevated levels of NO_2 produced a large increase on the MAC and imaginary part of the CRI. This would reduce the SSA and ensure that the particles have a positive RF effect. Moreover, the absorbing nature of nitrated and aromatic SOA species has been reported as a possible source for reduction in UV light in urban areas (1).

References

1. Jacobson MZ. 1999. Isolating nitrated and aromatic aerosols and nitrated aromatic gases as sources of ultraviolet light absorption. *Journal of Geophysical Research: Atmospheres* 104:3527-42
2. Calvert JG, Atkinson R, Becker KH, Kamens RM, Seinfeld JH, Wallington TH, Yarwood G. 2002. *The mechanisms of atmospheric oxidation of the aromatic hydrocarbons*. Oxford University Press
3. Odum JR, Jungkamp TPW, Griffin RJ, Flagan RC, Seinfeld JH. 1997. The Atmospheric Aerosol-Forming Potential of Whole Gasoline Vapor. *Science* 276:96-9
4. Odum JR, Hoffmann T, Bowman F, Collins D, Flagan RC, Seinfeld JH. 1996. Gas/Particle Partitioning and Secondary Organic Aerosol Yields. *Environmental Science & Technology* 30:2580-5
5. Forstner HJ, Flagan RC, Seinfeld JH. 1997. Secondary organic aerosol from the photooxidation of aromatic hydrocarbons: Molecular composition. *Environmental science & technology* 31:1345-58
6. Hurley MD, Sokolov O, Wallington TJ, Takekawa H, Karasawa M, Klotz B, Barnes I, Becker KH. 2001. Organic aerosol formation during the atmospheric degradation of toluene. *Environmental science & technology* 35:1358-66
7. Grosjean D, Friedlander SK. 1975. Gas-particle distribution factors for organic and other pollutants in the Los Angeles atmosphere. *Journal of the Air Pollution Control Association* 25:1038-44
8. Grosjean D, Seinfeld JH. 1989. Parameterization of the formation potential of secondary organic aerosols. *Atmospheric Environment (1967)* 23:1733-47
9. Novakov T, Penner J. 1993. Large contribution of organic aerosols to cloud-condensation-nuclei concentrations.823-6
10. Kourtidis K, Ziomas I. 1999. Estimation of secondary organic aerosol (SOA) production from traffic emissions in the city of Athens. *Global Nest* 1:33-9
11. Bejan I, Barnes I. Secondary organic aerosol formation during the gas phase photolysis of nitrophenols. *Proc. Geophysical Research Abstracts*, *2006*, 8:07497:
12. Iinuma Y, Mutzel A, Rodigast M, Böge O, Herrmann H. Molecular characterization of nitrogen and sulfur containing compounds in night-time SOA. *Proc. EGU General Assembly Conference Abstracts*, *2014*, 16:5139:
13. Yuan B, Liggio J, Wentzell J, Li S, Stark H, Osthoff H, Roberts J, Gilman J, Lerner B, Li R. Secondary formation of nitrophenols in an oil and gas production region: insights from observations during the Uintah Basin Winter Ozone Study (UBWOS) 2014. *Proc. AGU Fall Meeting Abstracts*, *2014*, 1:3234:
14. Rudolph J, Stupak J. 2002. Determination of aromatic acids and nitrophenols in atmospheric aerosols by capillary electrophoresis. *Journal of chromatographic science* 40:207-13
15. Wilson E, Wenger J, Venables D. Extinction characteristics of SOA formed following the photolysis of 2-nitrophenol: A broadband study in the near-ultraviolet.
16. Leuenberger C, Ligocki MP, Pankow JF. 1985. Trace organic compounds in rain. 4. Identities, concentrations, and scavenging mechanisms for phenols in urban air and rain. *Environmental science & technology* 19:1053-8
17. Lüttke J, Scheer V, Levsen K, Wünsch G, Cape JN, Hargreaves KJ, Storeton-West RL, Acker K, Wieprecht W, Jones B. 1997. Occurrence and formation of nitrated phenols in and out of cloud. *Atmospheric Environment* 31:2637-48

18. Nojima K, Kawaguchi A, Ohya T, Kanno S, Hirobe M. 1983. Studies on Photochemical Reaction of Air Pollutants. X. Identification of Nitrophenols in Suspended Particulates. *CHEMICAL & PHARMACEUTICAL BULLETIN* 31:1047-51
19. Tremp J, Mattrel P, Fingler S, Giger W. 1993. Phenols and nitrophenols as tropospheric pollutants: emissions from automobile exhausts and phase transfer in the atmosphere. *Water, Air, and Soil Pollution* 68:113-23
20. Chen J, Venables DS. 2011. A broadband optical cavity spectrometer for measuring weak near-ultraviolet absorption spectra of gases. *Atmospheric Measurement Techniques* 4:425-36
21. Alif A, Boule P, Lemaire J. 1987. Photochemical behavior of 4-Nitrophenol in aqueous-solution. *Chemosphere* 16:2213-23
22. Alif A, Boule P. 1991. Photochemistry and environment Part XIV. Phototransformation of nitrophenols induced by excitation of nitrite and nitrate ions. *Journal of Photochemistry and Photobiology A: Chemistry* 59:357-67
23. Alif A, Boule P, Lemaire J. 1990. Photochemistry and environment XII: Phototransformation of 3-nitrophenol in aqueous solution. *Journal of Photochemistry and Photobiology A: Chemistry* 50:331-42
24. Bejan I, El Aal YA, Barnes I, Benter T, Bohn B, Wiesen P, Kleffmann J. 2006. The photolysis of ortho-nitrophenols: a new gas phase source of HONO. *Physical Chemistry Chemical Physics* 8:2028-35
25. Kleffmann J, Gavriloaiei T, Hofzumahaus A, Holland F, Koppmann R, Rupp L, Schlosser E, Siese M, Wahner A. 2005. Daytime formation of nitrous acid: A major source of OH radicals in a forest. *Geophysical Research Letters* 32:p. L05818
26. Wei Q, Yin H-M, Sun J-L, Yue X-F, Han K-L. 2008. The dynamics of OH channel in the 266 and 355nm photodissociation of 2-nitrophenol. *Chemical Physics Letters* 463:340-4
27. Cheng S-B, Zhou C-H, Yin H-M, Sun J-L, Han K-L. 2009. OH produced from o-nitrophenol photolysis: A combined experimental and theoretical investigation. *atmosphere* 10:13
28. Bardini P. 2006. *Atmospheric chemistry of dimethylphenols and nitrophenols*. University College Cork
29. Kavitha V, Palanivelu K. 2005. Degradation of nitrophenols by Fenton and photo-Fenton processes. *Journal of Photochemistry and Photobiology A: Chemistry* 170:83-95
30. Goi A, Trapido M. 2002. Hydrogen peroxide photolysis, Fenton reagent and photo-Fenton for the degradation of nitrophenols: a comparative study. *Chemosphere* 46:913-22
31. Chen B, Yang C, Goh NK. 2005. Direct photolysis of nitroaromatic compounds in aqueous solutions. *Journal of Environmental Sciences* 17:598-604
32. Alif A, Pilichowski J-F, Boule P. 1991. Photochemistry and environment XIII: Phototransformation of 2-nitrophenol in aqueous solution. *Journal of Photochemistry and Photobiology A: Chemistry* 59:209-19
33. Booth A, Bannan T, McGillen M, Barley M, Topping D, McFiggans G, Percival C. 2012. The role of ortho, meta, para isomerism in measured solid state and derived sub-cooled liquid vapour pressures of substituted benzoic acids. *RSC Advances* 2:4430-43
34. 2016. *ICSC 0523 - 2-NITROPHENOL*. http://www.ilo.org/dyn/icsc/showcard.display?p_card_id=0523
35. Daubert TE, Danner RP. 1989. *Physical and Thermodynamic Properties of Pure Chemicals: Design institute for physical property data, American institute of chemical engineers. vp*. Hemisphere Publishing Corporation

36. Moortgat WSaGK. 1989. UV/VIS Spectra of Atmospheric Constituents, Version 1. ed. RR Personal communication to E.-P. Röth, G. Moortgat, R. Meller, and W. Schneider
37. Gierczak T, Burkholder JB, Talukdar RK, Mellouki A, Barone S, Ravishankara A. 1997. Atmospheric fate of methyl vinyl ketone and methacrolein. *Journal of Photochemistry and Photobiology A: Chemistry* 110:1-10
38. Zhao R, Lee A, Huang L, Li X, Yang F, Abbatt J. 2015. Photochemical processing of aqueous atmospheric brown carbon. *Atmospheric Chemistry and Physics* 15:6087-100
39. Liu J, Lin P, Laskin A, Laskin J, Kathmann SM, Wise M, Caylor R, Imholt F, Selimovic V, Shilling JE. 2016. Optical Properties and Aging of Light Absorbing Secondary Organic Aerosol. *Atmos. Chem. Phys. Discuss.* 2016:1-36
40. Li K, Wang W, Ge M, Li J, Wang D. 2014. Optical properties of secondary organic aerosols generated by photooxidation of aromatic hydrocarbons. *Scientific reports* 4:4922
41. Kleindienst T, Jaoui M, Lewandowski M, Offenberg J, Docherty K. 2012. The formation of SOA and chemical tracer compounds from the photooxidation of naphthalene and its methyl analogs in the presence and absence of nitrogen oxides. *Atmospheric Chemistry and Physics* 12:8711-26
42. Polidori A, Turpin BJ, Davidson CI, Rodenburg LA, Maimone F. 2008. Organic PM 2.5: Fractionation by polarity, FTIR spectroscopy, and OM/OC ratio for the Pittsburgh aerosol. *Aerosol Science and Technology* 42:233-46
43. Chen Y, Bond T. 2010. Light absorption by organic carbon from wood combustion. *Atmospheric Chemistry and Physics* 10:1773-87
44. Wang J, Doussin J, Perrier S, Perraudin E, Katrib Y, Pangui E, Picquet-Varrault B. 2011. Design of a new multi-phase experimental simulation chamber for atmospheric photosmog, aerosol and cloud chemistry research. *Atmospheric Measurement Techniques* 4:2465-94
45. Grosjean D. 1985. Wall loss of gaseous pollutants in outdoor Teflon chambers. *Environmental science & technology* 19:1059-65
46. Burrows J, Richter A, Dehn A, Deters B, Himmelmann S, Voigt S, Orphal J. 1999. ATMOSPHERIC REMOTE-SENSING REFERENCE DATA FROM GOME—2. TEMPERATURE-DEPENDENT ABSORPTION CROSS SECTIONS OF O_3 IN THE 231–794 NM RANGE. *Journal of quantitative spectroscopy and radiative transfer* 61:509-17
47. Merienne M, Jenouvrier A, Coquart B. 1995. The NO_2 absorption spectrum. I: Absorption cross-sections at ambient temperature in the 300–500 nm region. *Journal of atmospheric chemistry* 20:281-97
48. Bongartz A, Kames J, Schurath U, George C, Mirabel P, Ponche J. 1994. Experimental determination of HONO mass accommodation coefficients using two different techniques. *Journal of atmospheric chemistry* 18:149-69
49. Thompson B, Harteck P, Reeves R. 1963. Ultraviolet absorption coefficients of CO_2, CO, O_2, H_2O, N_2O, NH_3, NO, SO_2, and CH_4 between 1850 and 4000 A. *Journal of Geophysical Research* 68:6431-6
50. Nagakura S, Kaya K, Tsubomura H. 1964. Vacuum ultraviolet absorption spectra and electronic structures of formic acid, acetic acid and ethyl acetate. *Journal of Molecular Spectroscopy* 13:1-8
51. Feng Y, Ramanathan V, Kotamarthi V. 2013. Brown carbon: a significant atmospheric absorber of solar radiation? *Atmospheric Chemistry and Physics* 13:8607-21

52. Kirchstetter TW, Novakov T, Hobbs PV. 2004. Evidence that the spectral dependence of light absorption by aerosols is affected by organic carbon. *Journal of Geophysical Research: Atmospheres* 109:208
53. Bohren CF, Huffman DR. 2008. *Absorption and scattering of light by small particles*. John Wiley & Sons
54. Magi B. 2009. Chemical apportionment of southern African aerosol mass and optical depth. *Atmospheric Chemistry and Physics* 9:7643-55
55. Zhao F, Li Z. 2007. Estimation of aerosol single scattering albedo from solar direct spectral radiance and total broadband irradiances measured in China. *Journal of Geophysical Research: Atmospheres* 112
56. Nakayama T, Sato K, Matsumi Y, Imamura T, Yamazaki A, Uchiyama A. 2012. Wavelength dependence of refractive index of secondary organic aerosols generated during the ozonolysis and photooxidation of α-pinene. *Sola* 8:119-23
57. Malkin T, Goddard A, Heard D, Seakins P. 2010. Measurements of OH and HO_2 yields from the gas phase ozonolysis of isoprene. *Atmospheric Chemistry and Physics* 10:1441-59
58. Gao S, Ng NL, Keywood M, Varutbangkul V, Bahreini R, Nenes A, He J, Yoo KY, Beauchamp J, Hodyss RP. 2004. Particle phase acidity and oligomer formation in secondary organic aerosol. *Environmental science & technology* 38:6582-9
59. Iinuma Y, Böge O, Miao Y, Sierau B, Gnauk T, Herrmann H. 2005. Laboratory studies on secondary organic aerosol formation from terpenes. *Faraday discussions* 130:279-94
60. Keywood M, Kroll J, Varutbangkul V, Bahreini R, Flagan R, Seinfeld J. 2004. Secondary organic aerosol formation from cyclohexene ozonolysis: Effect of OH scavenger and the role of radical chemistry. *Environmental science & technology* 38:3343-50
61. Jenkin M. 2004. Modelling the formation and composition of secondary organic aerosol from α-and β-pinene ozonolysis using MCM v3. *Atmospheric Chemistry and Physics* 4:1741-57
62. Docherty KS, Ziemann PJ. 2003. Effects of stabilized Criegee intermediate and OH radical scavengers on aerosol formation from reactions of β-pinene with O_3. *Aerosol Science & Technology* 37:877-91
63. Guyon P, Boucher O, Graham B, Beck J, Mayol-Bracero OL, Roberts GC, Maenhaut W, Artaxo P, Andreae MO. 2003. Refractive index of aerosol particles over the Amazon tropical forest during LBA-EUSTACH 1999. *Journal of Aerosol Science* 34:883-907
64. Dubovik O, Holben B, Eck TF, Smirnov A, Kaufman YJ, King MD, Tanré D, Slutsker I. 2002. Variability of absorption and optical properties of key aerosol types observed in worldwide locations. *Journal of the atmospheric sciences* 59:590-608
65. von Hoyningen-Huene W, Schmidt T, Schienbein S, Kee CA, Tick LJ. 1999. Climate-relevant aerosol parameters of South-East-Asian forest fire haze. *Atmospheric Environment* 33:3183-90
66. Yamasoe M, Kaufman Y, Dubovik O, Remer L, Holben B, Artaxo P. 1998. Retrieval of the real part of the refractive index of smoke particles from Sun/sky measurements during SCAR-B. *Journal of geophysical research* 103:31
67. 2016. *3,5-Dinitro-1,2-benzenediol | $C_6H_4N_2O_6$ | ChemSpider*. http://www.chemspider.com/Chemical-Structure.3094995.html
68. Hoyer H, Peperle W. 1958. Vapor pressure measurements on organic compounds and their sublimation heats. *Z. Elektrochem* 62:61-6
69. Chan AWH, Kautzman KE, Chhabra PS, Surratt JD, Chan MN, Crounse JD, Kürten A, Wennberg PO, Flagan RC, Seinfeld JH. 2009. Secondary organic aerosol formation

from photooxidation of naphthalene and alkylnaphthalenes: implications for oxidation of intermediate volatility organic compounds (IVOCs). *Atmospheric Chemistry and Physics* 9:3049-60

70. Hatakeyama S, Izumi K, Fukuyama T, Akimoto H, Washida N. 1991. Reactions of OH with α-pinene and β-pinene in air: Estimate of global CO production from the atmospheric oxidation of terpenes. *Journal of Geophysical Research: Atmospheres* 96:947-58
71. Presto AA, Huff Hartz KE, Donahue NM. 2005. Secondary organic aerosol production from terpene ozonolysis. 2. Effect of NO_x concentration. *Environmental Science & Technology* 39:7046-54
72. Zhang Y, Huang JP, Henze DK, Seinfeld JH. 2007. Role of isoprene in secondary organic aerosol formation on a regional scale. *Journal of Geophysical Research: Atmospheres* 112
73. Song C, Na K, Cocker DR. 2005. Impact of the hydrocarbon to NO_x ratio on secondary organic aerosol formation. *Environmental science & technology* 39:3143-9
74. Chan A, Chan M, Surratt JD, Chhabra P, Loza C, Crounse J, Yee L, Flagan R, Wennberg P, Seinfeld J. 2010. Role of aldehyde chemistry and NO_x concentrations in secondary organic aerosol formation. *Atmospheric Chemistry and Physics* 10:7169-88

6. Conclusion

An incoherent broadband cavity-enhanced absorption spectroscopy (IBBCEAS) system was used in conjunction with an atmospheric simulation chamber to study the short-wavelength spectral properties of several atmospherically-relevant systems. In this thesis, the IBBCEAS system was used to measure the absorption cross section of a number of atmospherically relevant species, biacetyl, acetaldehyde, acenaphthylene, 1-nitronaphthalene, 2-nitrophenol and water, two of which had never been reported in the gas phase before. The IBBCEAS was also used to study the optical properties of secondary organic aerosol. Atmospheric particles play an important part in the radiative balance of the earth and a better understanding of their optical properties is necessary to reduce the large uncertainties associated with their influence on radiative forcing (1).

While there have been a number of previous studies with IBBCEAS systems, these have typically been at longer wavelengths and covered much narrower measurement bands Table 1.1. Work at shorter wavelengths is associated with a number of technical challenges, including lower detector efficiencies, lower radiance light sources, and fewer suitable optics. The IBBCEAS system in this work covered a broad spectral region from 325 to 420 nm which is of particular importance for tropospheric photochemistry (2). As part of this work, a procedure was established to ensure the accuracy of the IBBCEAS measurements. To prevent errors associated with misalignment, the procedure included a mirror reflectivity calibration for each experiment using NO_2 and either MVK or biacetyl. The accuracy of the measurements was validated by comparing the absorption cross sections of benzaldehyde and other species measured by IBBCEAS with previously reported literature spectra (3; 4). The good agreement between the measured and literature absorption cross sections gave confidence in the accuracy of the IBBCEAS measurements.

The first part of this work used IBBCEAS to measure gas phase absorption cross section values for biacetyl, 1-nitronapthalene (1-NN), 2-nitrophenol (2-NP), acetaldehyde, acenaphthylene and water. Several of these species have low vapour pressures and are difficult to study as gases. The absorption cross sections in the gas phase differ from those in solution because solution phase spectra are susceptible to peak broadening, peak shifts, and potential artefacts as a results of interactions between solvent and solute. Biacetyl and acetaldehyde showed good agreement with literature values. The absorption cross section of 2-NP has only been reported in the gas phase once before (3). The overall shape of the cross section is similar but the magnitude is lower (ca. 50 %) than the earlier measurement, indicating the challenges associated with the low volatility compounds. Due to the validation steps taken in Chapter 2, we have confidence in our values. Gas phase absorption cross section values for 1-NN and acenaphthylene have not been reported previously. A precise magnitude for the gas phase absorption cross section of 1-NN proved difficult to determine, although the shape of the spectra remained consistent over multiple experiments. Again, this variability was likely due to wall losses associated with the low vapour pressure. In contrast, acenaphthylene was added to the chamber with relative ease and the reproducibility of the acenaphthylene absorption cross section measurements was good. Clear vibronic structure was evident in the acenaphthylene spectra, with two intense peaks centred at 327 and 333 nm, and two much weaker peaks, 339 and 345 nm.

Measurements were also made to determine the absorption of water vapour, one of the most abundant and radiatively important species in the atmosphere. Water is reported to have a structured absorption in the near-UV region (5). Although no absorption by water vapour was observed, upper limit values for the absorption cross section in the near-UV region were determined on the basis of the instrument detection limits. The upper limits reported here are an order of magnitude lower than the values previously reported by Du et al., calling into question the accuracy of their values. Our findings for a much smaller water absorption are supported by theoretical studies which report a theoretical absorption 14-33 times smaller than

our upper limit and 200-600 times smaller than the values reported by Du et al. (6; 7).

The second part of this thesis investigated the optical properties of atmospherically-relevant particles. Aerosols have a strong influence on the earth's radiative balance, although there remain large uncertainties associated with their impact (1). The optical properties of SOA formed by the ozonolysis of α-pinene were investigated in Chapter 4. These SOA species have been widely used as a model for biogenic SOA (8). The refractive index of these SOA particles was determined through a combination of IBBCEAS extinction measurements and SMPS number distributions. The retrieved refractive index values range from 1.40 at 410 nm to 1.43 at 320 nm. These values are broadly similar to, albeit slightly lower than, previously reported values Table 4.2. The broad continuous measurement capabilities allowed us to determine the wavelength dependence of these refractive index values, in contrast to most RI values reported in the literature. Filter extracts of the SOA particles were determined to be non-absorbing in our region of interest, consistent with previous findings (9; 10). Due to the pure scattering nature of the particles in this region, their SSA is 1. Thus, the radiative forcing effect of these particles is negative. The Angstrom exponent (AE) of the extinction spectra was determined and was used as a qualitative measure of particle size. A good correlation was found between the measured AE values and the recorded median particle diameter.

Varying the starting conditions of the ozonolysis reaction allowed an investigation into the effects of a change in precursor concentration, the presence of OH radicals and increased relative humidity (RH) on the optical properties of the SOA. The concentration increased the mass concentration and mass yield; this is to be expected as the increased particle surface area promotes condensation of a greater fraction of low volatility species to the particle phase. The increase in particle size from higher precursor mixing ratios matched the decrease in AE values. The addition of an OH scavenger, in the form of an excess of cyclohexane, was used to determine the influence of OH radicals on the SOA optical properties. OH reacts much faster with α-pinene than ozone does, and the removal of OH by cyclohexane

led to greater loss of ozone. The mass concentration and mass yield also decreased, while the measured extinction and RI values increased in the presence of cyclohexane. The changes in physical and optical properties in the absence of OH radicals show the important role that they play in the production of α-pinene/ozonolysis SOA.

The RH of the simulation chamber was increased to 80 % to investigate the effects of high levels of water on SOA formation. The increased RH levels did not greatly affect the mass concentration, but did double the maximum number of particles formed. Similar results have been seen in some studies, although other studies found that the mass concentration changed with RH. The increase in particle concentration would, depending on size, increase the scattering caused by the particles. This is reflected in the increase in both extinction and RI values for the high RH experiment. As the levels of RH in the real atmosphere would be much higher than the low levels typical of our standard experiment, it is plausible that SOA particles would often have optical properties more similar to those found in the high RH experiment. The values are higher by about 0.1 at every wavelength. As changes in RI from 1.4 to 1.5 for non-absorbing species have been estimated to decrease RF by 12-19 %, the optical properties of SOA formed in high RH experiments is important for real world radiative forcing models (11).

Chapter 5 described an investigation of an important anthropogenic SOA system initiated by photolysis of 2-nitrophenol (2-NP). The potential impact of nitroaromatic SOA species was first proposed by Jacobson and coincided with the rise in attention given to the effect of absorbing SOA species on radiative forcing (12). Solution extracts of 2-NP photolysis SOA filter samples showed that these particles absorb light well into the visible region, with the absorption band extending beyond 500 nm. This is in contrast to the 2-NP precursor, which absorbs almost exclusively in the near-UV. The broad absorption of the SOA could have a substantial impact on light extinction; particularly in urban environments. The SSA of the particles was determined using the mass absorption coefficient and the mass extinction coefficient. The calculated values ranged from 0.89 to 0.90 at 340 and 410 nm, respectively. As the SOA formed here absorb as well as scatter light, we

determined both the real and imaginary parts of the CRI. A list of these values is given in Table 5.3. The mass absorption coefficient and imaginary part of the CRI for these SOA are up to five times weaker than that reported for 'moderately absorbing' brown carbon. However, the MAC is a lower limit as the mass is based on a number of assumptions as discussed in Chapter 5.

The chemical composition of filter particles was analysed using an ultra-high resolution mass spectrometer. As with the previous SOA system, the reaction pathway was altered by adding a number of species to the chamber prior to photolysis: an OH radical scavenger in the form of cyclohexane or acetaldehyde, and increased levels of NO_2. The addition of cyclohexane reduced the mass concentration and yield, resulting in a slightly lower MAC but a much higher MEC. This indicated that reactions with OH radicals produce a large portion of the absorbing particles but do not have much impact on the SOA scattering. In contrast, addition of acetaldehyde completely suppressed particle formation, highlighting the importance of radicals other than OH in the formation of SOA in this system. The presence of high levels of NO_2 increased the MAC almost three-fold. The MAC increase leads to the same level of increase for the imaginary refractive index value, which would lead to a much lower SSA value for these SOA. The increased absorption of these particles would change the radiative forcing effect from negative to positive and thus have an overall heating effect. This effect is important as 2-NP is typically found in polluted urban areas as vehicle emissions are one of its primary sources. These areas typically also have elevated levels of NO_x.

6.1. Future work

There are a number of ways to build on this work which highlights the versatility of IBBCEAS as a technique for measuring both gas and particle phase optical properties. The wavelength range used here is very broad and much shorter than most other optical instruments. However, it would be beneficial to extend this wavelength range even lower to cover all wavelengths of relevance to the troposphere. Extending the spectral coverage to lower wavelengths could also facilitate further measurements of the absorption cross section of VOCs and other

atmospherically relevant species. In addition, a system to reliably add low vapour pressure species to the chamber would be beneficial. The results of this work have shown that increases in RH and NO_x levels drastically change the optical properties of the SOA. Experimental studies of SOA formation approaching more real world conditions could be performed to obtain optical properties more closely resembling what could be found in real environments. Finally, a system similar to this could be constructed for field investigations of atmospheric particles.

References

1. Change IC. 2013. The physical science basis. Contribution of working group I to the fifth assessment report of the intergovernmental panel on climate change. *K., Tignor, M., Allen, SK, Boschung, J., Nauels, A., Xia, Y., Bex, V., Midgley, PM, Eds*:1535
2. Madronich S. 1993. Tropospheric photochemistry and its response to UV changes. In *The role of the stratosphere in global change*:437-61: Springer. Number of 437-61 pp.
3. Chen J, Wenger JC, Venables DS. 2011. Near-ultraviolet absorption cross sections of nitrophenols and their potential influence on tropospheric oxidation capacity. *The Journal of Physical Chemistry A* 115:12235-42
4. Xiang B, Zhu C, Zhu L. 2009. Gas-phase absorption cross sections of 2-nitrobenzaldehyde and benzaldehyde in the 285–400nm region, and photolysis of 2-nitrobenzaldehyde vapor at 308 and 351nm. *Chemical physics letters* 474:74-8
5. Du J, Huang L, Min Q, Zhu L. 2013. The influence of water vapor absorption in the 290–350 nm region on solar radiance: Laboratory studies and model simulation. *Geophysical Research Letters* 40:4788-92
6. Lampel J, Pöhler D, Tschritter J, Frieß U, Platt U. 2015. On the relative absorption strengths of water vapour in the blue wavelength range. *Atmospheric Measurement Techniques* 8:4329-46
7. Lampel J, Pöhler D, Polyansky OL, Kyuberis AA, Zobov NF, Tennyson J, Lodi L, Frieß U, Wang Y, Beirle S. Detection of water vapour absorption around 363 nm in measured atmospheric absorption spectra and its effect on DOAS evaluations. *Proc. EGU General Assembly Conference Abstracts*, *2016*, 18:7312:
8. Hao L, Romakkaniemi S, Yli-Pirilä P, Joutsensaari J, Kortelainen A, Kroll J, Miettinen P, Vaattovaara P, Tiitta P, Jaatinen A. 2011. Mass yields of secondary organic aerosols from the oxidation of α-pinene and real plant emissions. *Atmospheric Chemistry and Physics* 11:1367-78
9. Nakayama T, Matsumi Y, Sato K, Imamura T, Yamazaki A, Uchiyama A. 2010. Laboratory studies on optical properties of secondary organic aerosols generated during the photooxidation of toluene and the ozonolysis of α-pinene. *Journal of Geophysical Research: Atmospheres* 115
10. Schnaiter M, Horvath H, Möhler O, Naumann K-H, Saathoff H, Schöck O. 2003. UV-VIS-NIR spectral optical properties of soot and soot-containing aerosols. *Journal of Aerosol Science* 34:1421-44
11. Kim H, Barkey B, Paulson SE. 2010. Real refractive indices of α-and β-pinene and toluene secondary organic aerosols generated from ozonolysis and photo-oxidation. *Journal of Geophysical Research: Atmospheres* 115
12. Jacobson MZ. 1999. Isolating nitrated and aromatic aerosols and nitrated aromatic gases as sources of ultraviolet light absorption. *Journal of Geophysical Research: Atmospheres* 104:3527-42

Appendix A

The range of values for the absorption cross section for each of the compounds measured in Chapter 3, excluding water, is listed below. Spectra were recorded at 0.12 nm intervals and are presented here in 0.5 nm intervals.

Wavelength (nm)	Biacetyl (10^{-20} cm^2 molecule^{-1})	1-NN (10^{-18} cm^2 molecule^{-1})	2-NP (10^{-17} cm^2 molecule^{-1})	Acetaldehyde (10^{-20} cm^2 molecule^{-1})	Acenaphthylene (10^{-17} cm^2 molecule^{-1})
325	0.40262	-	-	1.05776	1.02553
325.5	0.41237	-	-	0.99313	0.91443
326	0.41871	-	-	0.99476	0.81278
326.5	0.40475	-	-	1.0434	0.92257
327	0.39815	-	-	0.78811	1.84587
327.5	0.4183	-	-	0.72219	1.83464
328	0.3997	-	-	0.74751	1.58068
328.5	0.37522	-	-	0.57601	1.2362
329	0.39068	-	-	0.6755	0.95669
329.5	0.37242	-	-	0.71345	0.7263
330	0.36308	4.88459	1.00863	0.62416	0.56964
330.5	0.36221	4.72526	1.01552	0.69077	0.45535
331	0.38294	4.63009	1.01576	0.56288	0.39664
331.5	0.39918	4.50117	1.02566	0.51696	0.40712
332	0.41808	4.34921	1.00045	0.54592	0.58362
332.5	0.42323	4.21789	0.99109	0.36726	1.55299
333	0.43953	4.08676	0.98547	0.34414	1.57942
333.5	0.44623	4.01544	0.98499	0.43532	1.37795
334	0.44257	3.98403	0.99385	0.31338	1.04171
334.5	0.43918	3.94251	1.01651	0.27702	0.72513
335	0.43008	3.95469	1.04461	0.366	0.49172
335.5	0.42142	3.9389	1.07467	0.29221	0.35347
336	0.41431	3.92729	1.09813	0.20554	0.26973
336.5	0.41538	3.91826	1.1153	0.21529	0.21814
337	0.40143	3.88688	1.13402	0.2198	0.18859
337.5	0.41227	3.83528	1.13944	0.20431	0.17481
338	0.40862	3.77981	1.14451	0.17625	0.17054
338.5	0.41909	3.73562	1.14308	0.24043	0.22452
339	0.41938	3.71193	1.14174	0.21521	0.2355
339.5	0.42972	3.68514	1.13848	0.1778	0.21823
340	0.43854	3.63097	1.13799	0.13607	0.19248
340.5	0.44818	3.50331	1.13473	0.08204	0.167
341	0.45711	3.30616	1.12649	0.04743	0.1489
341.5	0.46762	3.07697	1.11894	0.06137	0.13777
342	0.48522	2.86266	1.11273	0.05081	0.13003
342.5	0.49743	2.6724	1.10476	0.04776	0.12506
343	0.50843	2.51237	1.09381	0.04058	0.12223

343.5	0.52084	2.37656	1.08206	0.03505	0.1199
344	0.53891	2.26198	1.06892	0.03392	0.11853
344.5	0.55388	2.16443	1.05832	0.03391	0.11773
345	0.56668	2.08095	1.04667	0.02803	0.1192
345.5	0.5866	2.00586	1.03027	0.02253	0.1171
346	0.60641	1.93677	1.0143	0.02513	0.11507
346.5	0.62713	1.87885	1.0017	0.02439	0.1129
347	0.65217	1.8278	0.99051	0.02013	0.11124
347.5	0.67526	1.7804	0.97878	0.0201	0.11015
348	0.69716	1.73765	0.96389	0.02151	0.10986
348.5	0.71854	1.695	0.9496	0.02037	0.10974
349	0.74184	1.65411	0.93414	0.01597	0.11057
349.5	0.76311	1.61552	0.91766	0.01449	0.11
350	0.79354	1.57778	0.90301	0.01302	0.10963
350.5	0.8114	1.54333	0.88868	0.01214	0.10843
351	0.83519	1.51148	0.87222	0.01102	0.10762
351.5	0.8559	1.47952	0.85683	0.01011	0.10672
352	0.87719	1.44622	0.84315	0.01072	0.10569
352.5	0.90113	1.41385	0.82947	0.00836	0.10492
353	0.92018	1.384	0.81576	0.00909	0.10417
353.5	0.94086	1.35676	0.80103	0.00866	0.10414
354	0.96527	1.32811	0.7854	0.00744	0.10387
354.5	0.98743	1.30254	0.76852	0.00804	0.10359
355	1.01925	1.275	0.75065	0.00801	0.10289
355.5	1.03981	1.24852	0.73381	0.00745	0.10217
356	1.06757	1.22232	0.71759	0.00769	0.10135
356.5	1.09128	1.19806	0.70016	0.00607	0.10081
357	1.11988	1.17346	0.68332	0.0052	0.10044
357.5	1.14443	1.1506	0.66651	0.00561	0.09995
358	1.17065	1.12637	0.64868	0.00544	0.09955
358.5	1.19658	1.10262	0.62986	0.00417	0.09924
359	1.2229	1.07818	0.6113	0.00368	0.09894
359.5	1.25017	1.057	0.59304	0.00378	0.09856
360	1.28046	1.03656	0.57563	0.00333	0.09842
360.5	1.3139	1.01692	0.55991	0.00238	0.09858
361	1.34853	0.99637	0.54471	0.00256	0.09834
361.5	1.38804	0.97773	0.52876	0.00247	0.09766
362	1.42909	0.95946	0.51256	0.00191	0.09714
362.5	1.47371	0.94114	0.49596	0.00149	0.09627
363	1.52048	0.92357	0.4786	0.00141	0.0955
363.5	1.568	0.90545	0.46106	0.00166	0.0947
364	1.61676	0.8888	0.44378	0.00183	0.09447
364.5	1.66726	0.87091	0.42673	0.00105	0.09488
365	1.71497	0.85193	0.41013	0.00113	0.09545
365.5	1.76431	0.8342	0.39518	6.56576E-4	0.09593
366	1.81373	0.81567	0.38177	1.24122E-4	0.09605
366.5	1.86022	0.7973	0.36849	-	0.09632
367	1.91385	0.77898	0.35465	-	0.09637
367.5	1.9656	0.76109	0.34153	-	0.09623
368	2.01856	0.74268	0.32917	-	0.09535
368.5	2.07619	0.72542	0.31755	-	0.09422

369	2.13233	0.70797	0.30571	-	0.09289
369.5	2.19249	0.69089	0.2936	-	0.09198
370	2.24966	0.67423	0.2821	-	0.0912
370.5	2.30777	0.65827	0.27195	-	0.09068
371	2.36143	0.64301	0.26191	-	0.09076
371.5	2.41305	0.62705	0.25169	-	0.09098
372	2.45768	0.61252	0.24148	-	0.09102
372.5	2.5084	0.59758	0.23135	-	0.09071
373	2.5595	0.5828	0.22184	-	0.09019
373.5	2.60987	0.56866	0.21277	-	0.08919
374	2.6616	0.55428	0.20429	-	0.08815
374.5	2.71672	0.53982	0.19609	-	0.08744
375	2.77207	0.52656	0.18783	-	0.08747
375.5	2.83099	0.51335	0.17876	-	0.08724
376	2.88519	0.50048	0.16873	-	0.08683
376.5	2.94089	0.487	0.15817	-	0.08644
377	2.99653	0.47452	0.1477	-	0.08576
377.5	3.05023	0.46115	0.13781	-	0.08477
378	3.09907	0.44812	0.12881	-	0.08357
378.5	3.14872	0.4349	0.12082	-	0.083
379	3.19781	0.42231	0.11379	-	0.08307
379.5	3.24716	0.40992	0.10755	-	0.08292
380	3.30478	0.39683	0.10179	-	0.08237
380.5	3.36821	0.38479	0.0964	-	0.08147
381	3.43478	0.37227	0.09123	-	0.08032
381.5	3.5109	0.36113	0.08627	-	0.07897
382	3.58748	0.34985	0.08108	-	0.07728
382.5	3.67051	0.33859	0.07592	-	0.07579
383	3.75509	0.32698	0.07109	-	0.0752
383.5	3.84404	0.3161	0.06667	-	0.07615
384	3.93428	0.30537	0.06265	-	0.07702
384.5	4.01952	0.2944	0.05895	-	0.07793
385	4.10468	0.28367	0.05589	-	0.07818
385.5	4.18672	0.27355	0.05319	-	0.07785
386	4.26577	0.26443	0.05073	-	0.07841
386.5	4.33739	0.25499	0.04832	-	0.07897
387	4.41438	0.24594	0.04602	-	0.07888
387.5	4.49151	0.23691	0.04377	-	0.07781
388	4.57576	0.22734	0.04136	-	0.07589
388.5	4.66341	0.21915	0.03919	-	0.07372
389	4.75146	0.21035	0.03706	-	0.07198
389.5	4.85742	0.2025	0.03502	-	0.07063
390	4.95717	0.19405	0.03317	-	0.06928
390.5	5.0572	0.18601	0.03148	-	0.06917
391	5.16176	0.17769	0.02986	-	0.06954
391.5	5.25067	0.17055	0.02822	-	0.07015
392	5.33378	0.1625	0.02648	-	0.07041
392.5	5.39953	0.15414	0.02477	-	0.06992
393	5.44261	0.14726	0.02313	-	0.0686
393.5	5.48432	0.13884	0.02159	-	0.06672
394	5.51484	0.13109	0.02023	-	0.06471

394.5	5.54065	0.12282	0.01901	-	0.06327
395	5.58031	0.11524	0.01799	-	0.06369
395.5	5.62574	0.10766	0.01696	-	0.06476
396	5.67522	0.09998	0.01592	-	0.0652
396.5	5.73775	0.09267	0.01499	-	0.06482
397	5.79657	0.08507	0.01401	-	0.06454
397.5	5.85665	0.0785	0.01304	-	0.06361
398	5.92432	0.07061	0.01206	-	0.06187
398.5	5.98375	0.06383	0.01118	-	0.06001
399	6.05317	0.05692	0.01035	-	0.05906
399.5	6.12945	0.05031	0.00966	-	0.05976
400	6.22767	0.04377	0.00897	-	0.06064
400.5	-	0.03772	0.00844	-	0.06023
401	-	0.03075	0.00789	-	0.059
401.5	-	0.02427	0.00742	-	0.05753
402	-	0.01902	0.00704	-	0.05556
402.5	-	0.01251	0.00649	-	0.05339
403	-	0.00631	0.00608	-	0.05136
403.5	-	0.00116	0.00566	-	0.04986
404	-	-	0.00522	-	0.0494
404.5	-	-	0.00485	-	0.05075
405	-	-	0.00454	-	0.05258
405.5	-	-	0.00427	-	0.05417
406	-	-	0.004	-	0.05497
406.5	-	-	0.00383	-	0.05489
407	-	-	0.00366	-	0.05488
407.5	-	-	0.00352	-	0.05662
408	-	-	0.00335	-	0.05992
408.5	-	-	0.00319	-	0.06101
409	-	-	0.00302	-	0.0603
409.5	-	-	0.00284	-	0.0576
410	-	-	0.00273	-	0.05382
410.5	-	-	0.00254	-	0.05021
411	-	-	0.00246	-	0.04757
411.5	-	-	0.00233	-	0.0457
412	-	-	0.00224	-	0.04459
412.5	-	-	-	-	0.04492
413	-	-	-	-	0.04684
413.5	-	-	-	-	0.04804
414	-	-	-	-	0.04892
414.5	-	-	-	-	0.04957
415	-	-	-	-	0.04889
415.5	-	-	-	-	0.04773
416	-	-	-	-	0.04633
416.5	-	-	-	-	0.04495
417	-	-	-	-	0.04461
417.5	-	-	-	-	0.0455
418	-	-	-	-	0.04785
418.5	-	-	-	-	0.04861
419	-	-	-	-	0.0491
419.5	-	-	-	-	0.04877